MAX-PLANCK-INSTITUT
FÜR PHYSIK

Doctoral Thesis

A Strange and Charming Tale on Hadronic Interactions

Author:
Emma Sophia Chizzali

Supervisor:
Prof. Dr. Laura Fabbietti

A thesis submitted in fulfillment of the requirements
for the degree of Doctor of Natural Sciences
in the
TUM School of Natural Sciences

February, 2024

What we observe is not nature itself,
but nature exposed to our method of questioning.

– *Werner Heisenberg* –

TUM School of Natural Sciences

A Strange and Charming Tale on Hadronic Interactions

Emma Sophia Chizzali

Vollständiger Abdruck der von der TUM School of Natural Sciences der Technischen Universität München zur Erlangung einer

Doktorin der Naturwissenschaften (Dr. rer. nat.)

genehmigten Dissertation.

Vorsitz:	apl. Prof. Dr. Norbert Kaiser
Prüfende der Dissertation:	1. Prof. Dr. Laura Fabbietti
	2. Priv.-Doz. Dr. Oliver Kortner

Die Dissertation wurde am 20.02.2025 bei der Technischen Universität München eingereicht und durch die TUM School of Natural Sciences am 24.03.2025 angenommen.

TECHNISCHE UNIVERSITÄT MÜNCHEN

Abstract

TUM School of Natural Sciences

Doctor of Philosophy

A Strange and Charming Tale on Hadronic Interactions
by Emma Sophia Chizzali

In this thesis, the final state interaction of various systems of hadrons with valence-quark content beyond the light u and d flavors was explored, employing the method of femtoscopy. This technique relates momentum correlations of hadron pairs to their emission source and interaction potential. It provides an alternative, novel approach to accessing information about the residual strong interaction between particles, including unstable ones, that cannot be studied in classical scattering experiments. ALICE at the LHC is the ideal environment for the measurement of such correlation functions due to its excellent particle identification capabilities and high-statistics data sample of pp collisions at $\sqrt{s} = 13$ TeV, where the emission region is ~ 1 fm.

In that setting, the first measurement of the D and light-flavor K and π meson correlation functions of same- and opposite-charged pairs was performed. The raw signals were corrected for background contributions in order to obtain the genuine correlation functions and compare them to the available theoretical predictions of the residual strong interaction. The D–K correlation functions lack statistical precision and are compatible with the different models. The D–π data, on the other hand, clearly favor the Coulomb-only hypothesis and are incompatible with the predictions of the residual strong interaction. The deviation is especially pronounced for the opposite-charge combination. Due to the higher statistical precision, the correlation functions are further used to determine the scattering length of the D–π interaction in the isospin $I = 3/2$ and $I = 1/2$ states, the former of which is shared between the two charge combinations. In a simultaneous fit to the data, where a Gaussian-type potential was used to parametrize the interaction in each isospin state, values consistent with zero within the uncertainties were obtained.

Furthermore, the p–ϕ correlation function, previously measured by ALICE in pp collisions at $\sqrt{s} = 13$ TeV, was re-analyzed. The spin 3/2 component of the interaction was constrained by the LQCD potential, simulated by the HAL QCD collaboration. This made it possible to study the spin 1/2 contribution, which is currently inaccessible on the lattice due to the effect of open channels. It was modeled with a phenomenological complex potential, whose real part was motivated by the parameterization of the LQCD simulation, while the imaginary part, which accounts for inelastic contributions, was modeled by a Yukawa-type potential describing a 2nd-order kaon exchange. The potential parameters were determined by a fit to the data, and the interaction was found to be attractive and strong enough to support a p–ϕ bound state with a binding energy between 12.8 and 56.1 MeV. Furthermore, the scattering parameters for the spin 1/2 interaction were derived for the first time.

Zusammenfassung

In dieser Arbeit wurde die Methode der Femtoscopy angewandt um die Wechselwirkung zwischen verschiedenen Paaren von Hadronen zu untersuchen, einschließlich jener mir einer Valenz-Quark Zusammensetzung jenseits der leichten u und d Flavours. Diese Technik setzt Impulskorrelationen von Hadronenpaaren mit ihrer Emissionsquelle und ihrem Wechselwirkungspotenzial in Beziehung. Sie bietet einen alternativen, neuartigen Ansatz um Informationen über die starke Wechselwirkung zwischen Teilchen zu erhalten, einschließlich instabiler Teilchen, die in klassischen Streuexperimenten nicht untersucht werden können. ALICE am LHC bietet die ideale Voraussetzungen für die Messung solcher Korrelationsfunktionen aufgrund der hervorragenden Teilchenidentifikation und der hohen hochstatistischen Daten von pp Kollisionen mit $\sqrt{s} = 13$ TeV, bei denen der Emissionsbereich ~ 1 fm ist.

In dieser experimentellen Umgebung wurde die erste Messung der Korrelationsfunktionen von D und K bzw. π Mesonen mit gleicher und entgegengesetzt Ladung durchgeführt. Die gemessenen Signale wurden um Hintergrundbeiträge korrigiert und die resultierenden Korrelationsfunktionen mit den verfügbaren theoretischen Vorhersagen der starken Wechselwirkung verglichen. Den D–K Korrelationsfunktionen mangelt es an statistischer Präzision, und sie sind mit den verschiedenen Modellen kompatibel. Die D–π Daten hingegen deuten auf eine reine Coulomb Wechselwirkung hin und sind nicht mit den Vorhersagen über die starke Wechselwirkung vereinbar. Die Abweichung ist besonders ausgeprägt für Paare mit entgegengesetzter Ladung. Aufgrund der höheren statistischen Genauigkeit wurden die Korrelationsfunktionen außerdem zur Bestimmung der Streulänge der D–π Wechselwirkung im Isospin-Zustand $I = 3/2$ und $I = 1/2$ verwendet, wobei ersterer zu beiden Ladungskombinationen beiträgt. In einer simultanen Anpassung an die Daten, bei der die Wechselwirkung in den jeweiligen Isospin-Zuständen mit einem Potential vom Gauß-Typ parametrisiert wurde, wurden Werte bestimmt, die innerhalb der Unsicherheiten mit Null übereinstimmen.

Außerdem wurde die p–ϕ Korrelationsfunktion, die zuvor von ALICE in pp Kollisionen mit $\sqrt{s} = 13$ TeV gemessen wurde, erneut analysiert. Die Spin-3/2 Komponente der Wechselwirkung wurde mit einem LQCD-Potenzial modelliert, welches von der HAL QCD Kollaboration simuliert worden war. Dies ermöglichte die Untersuchung des Spin-1/2 Beitrags, welcher aufgrund des Effekts offener Kanäle derzeit in QCD-Gitter Rechnungen unzugänglich ist. Der Beitrag wurde mit einem phänomenologischen komplexen Potenzial modelliert, wobei für den Realteil eine, der LQCD-Simulation ähnliche Form gewählt wurde, während der Imaginärteil, der die inelastischen Beiträge berücksichtigt, durch ein Potenzial vom Yukawa-Typ modelliert wurde, das einen Kaon Austausch zweiter Ordnung beschreibt. Die Potenzialparameter wurden an die Daten angepasst. Dabei wurde festgestellt, dass die Wechselwirkung attraktiv und stark genug ist, um einen gebundenen p–ϕ Zustand zu bilden, welcher eine Bindungsenergie zwischen $12,8$ und $56,1$ MeV hat. Darüber hinaus wurden zum ersten Mal die Streuparameter der Spin-1/2 Wechselwirkung abgeleitet.

Acknowledgements

This thesis is all but a one-person effort, and I have to thank a lot of people who supported me at every step along the way, the first of whom is, of course, Prof. Dr. Laura Fabbietti, who allowed me to do the PhD in the first place. I still remember meeting you at an event for female physics students at the beginning of my undergraduate studies. After that, I immediately checked out your research and asked if I could join your group as a technical student. I stayed there ever since, which, I guess, speaks for itself. You saw potential in me and pushed me to achieve the most. Moreover, I think hardly any other professor supports the people in their group as much as you do, and I appreciate it a lot. Laura, thank you so much for everything you did for me and for being lenient when I was stubborn at times! I have learned a lot from you, not just about physics, and I am extremely grateful for all the time we spent together!

A big thanks also goes to Raffaele Del Grande. The first time we worked together was back during my masters, when I was trying to finish the $\mathrm{p}\phi$ paper on my own, and you and Laura luckily stepped in to help polish it up and make it ready for publication. I could never have done it myself, and I think it was also the start of a great friendship. We always have an amazing time and a lot of fun together, and you are always there to support and listen! I am also so grateful to Valentina Mantovani-Sarti. The time I spent with you in the same office was just hilarious! You are not just a fantastic person but, of course, also scientist, and literally have answers to everything. Moreover, you always do your best to help everyone in the group, and I cannot even count how often you saved my ass. I also enjoyed our work on $\Lambda\mathrm{K}$ a lot. Next in line is Dimitar Mihaylov. You not only had to endure sharing an office with me but also my constant questions and help requests, which you never turned down. Also, at some point (maybe soon), we will hike up your house mountain in Sofia together. Further, I would like to thank Igor Altsybeev for his incredible help with my service work on ALICE 3 outer tracker simulations.

A BIG thanks also goes to my fellow (ex) PhD colleagues, who made everyday life in Garching more than bearable and were always there to help and support me. Thanks, Daniel, for working together on the charm analysis; your coding skills and knowledge of ML were so helpful! Bhawani, I think I would not have survived the async-QC time without you! Anton, I am not sure if you remember, but you saved my old laptop with all the data during QM preliminaries back in 2022… I can't express my gratitude for that, but also for your help with the ϕNN trigger. Marcel, you are always fun and helpful, and we finally need to go snowboarding this season! Berkin, you are an amazing person (and the best Santa); there is nothing you cannot do! I will always appreciate my (short) time as part of the GEM crew. Maxi, you somehow manage to always remain calm (at least from the outside perspective), and you are extra fun. Also, a huge thanks for always organizing our coffee supply! Without that, I am not sure if I would have survived the long days in the office! Lukas, you always made my stays at CERN much better, especially when Berkin and I were there for some weeks working with you on the ITS3 chip testing; thanks for that! Max, you know so much about physics and are always available to share. I am also very grateful to my Master's thesis supervisor, Andi. You taught me everything about data analysis and how important it is to work clean and precisely. Finally, Laura (Baby), a huge thanks goes to you… you taught Bhawani and me how to do QC and helped me with the trigger alongside Anton, but, moreover, you are a great friend and always there if I need advice or talk about anything. We always had a great time at concerts, and I can't wait to visit you at CERN! Also, all the other people in the TUM group that I haven't named here were amazing!

Moreover, I need to thank Yuki Kamiya, in particular, who provided me with most of the model correlation functions used in this work. Furthermore, I am extremely grateful for the collaboration with Tetsuo Hatsuda, Yan Liu, and Takumi Doi, as well as the rich discussions with Johann Haidenbauer, Albert Feijoo Aliau, Tetsuo Hyodo, and Volker Metag, who helped me a lot, probably without realizing it.

I am also very lucky to be surrounded by a great group of friends and family, and I really wonder why you guys still talk to me even though I ghosted you for days/weeks at the time during stressful periods at work. Anyways, without you, I would never have finished the PhD! I cannot list all of you here, but I'm sure you know who you are... While I'm extremely grateful for all the friends back home who are still in my life, I've also met a lot of special people here in Munich, including Cosi and Dotti, who were my first friends in this city, Tuan, a genuinely good and generous person you can always rely on, as well as Kim and Jez, who are not only amazing friends, but also showed me how important it is to follow your heart and do what makes you happy, no matter how difficult that might be at first. Also, all my mountaineering, ski touring, snowboarding, trail running, climbing, gym, and concert buddies have a special place in my heart, as these things keep me sane and alive. Finally, a big thanks goes to Mum and Dad for their unconditional love, patience, and support during my whole studies, as well as my Aunt Nine, who is basically a second mother to me.

It has been a long and tough road, but I managed to reach the end... I have no idea what the future holds, but I'm ready and looking forward to it!

Contents

List of Figures

List of Tables

Chapter 1

Introduction

The question of what the world is made of has preoccupied mankind for centuries. We have come a long way since Greek philosophers such as Leucippus and his student Democritus first proposed atoms as the indivisible building blocks of matter more than 2000 years ago. Thanks to the rapid technological advances of the last century, we are now able to resolve its smallest, fundamental constituents and study how they interact with each other. Our current understanding of the world and the laws of nature at the most elementary level is embodied in the Standard Model (SM) of particle physics, a well-established and tested theory describing all the known fundamental particles and the forces among them[1].

Quantum quantum chromodynamics (QCD) is the part of the standard model that focuses on the strong interaction between quarks mediated by gluons. Moreover, it governs the spectrum of strongly interacting composite particles, called hadrons[2], which make up almost the entire mass of the tangible universe. Hadrons experience the residual effect of the strong interaction, the most prominent example of which is the nuclear force between protons and neutrons. At the quark level in the high-energy regime, the strong interaction is well described by perturbative QCD (pQCD). At low-energies and subatomic scales, however, where the relevant degrees of freedom are hadronic, it lacks a coherent understanding due to the breakdown of pQCD. Alternative approaches, such as numerical (lattice) calculations, effective field theories, or phenomenological models, are available, but the measurements needed to test or constrain them are limited. While a reasonable amount of nucleon-nucleon scattering data is available, realizing such experiments becomes very challenging to impossible once exotic and unstable particles are involved. In recent years, this gap has been filled by correlation measurements at accelerator facilities such as the LHC. This thesis focuses on studying the residual strong interaction among pairs of unlike hadrons, where one contains strange or charm quarks, applying the femtoscopy method on data measured by ALICE in pp collisions at $\sqrt{s} = 13$ TeV. Before presenting the technique, the experimental apparatus, and the results of the two primary analyses carried out during my doctoral studies in the following chapters, an introduction to the SM and strong interaction, with a special focus on hadrons, is needed.

---

[1] Gravity, which is one of the four fundamental forces, is not included in the SM. However, there are ongoing efforts to provide a quantum theory of gravity and merge it with the SM or find an alternative, unifying theory. However, this is beyond the scope of this thesis. Moreover, gravity is negligible in its relative strength compared to the strong, electromagnetic, and weak forces and is not relevant on a microscopic scale.

[2] Hardons are color-neutral bound states of quarks and gluons.

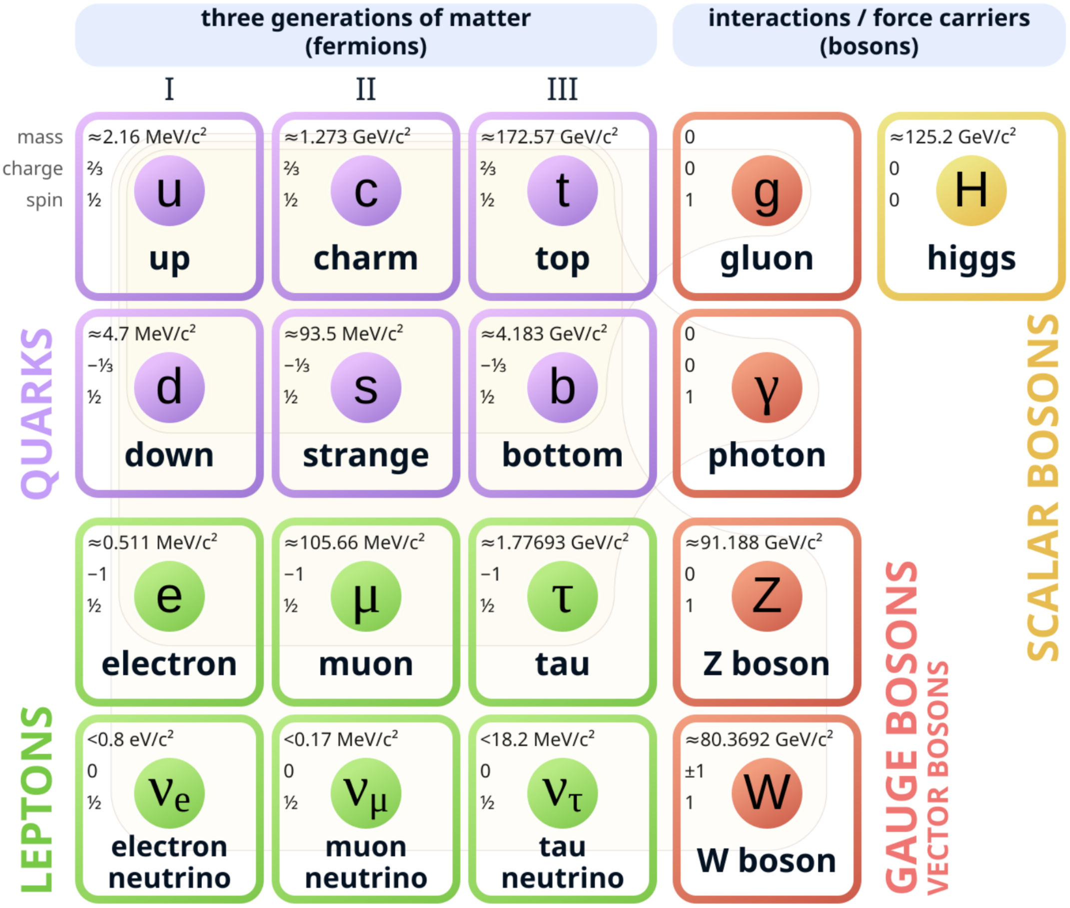

FIGURE 1.1: The elementary particles within the standard model. Figure taken from [1].

1.1 The standard model of particle physics

The standard model of particle physics is the theory describing three of the four fundamental forces: the strong, electromagnetic, and weak interaction. Moreover, it classifies all known elementary particles, as depicted in Fig. 1.1.

The Higgs scalar boson is responsible for the bar mass of the rest of the particles, while the Gauge vector bosons are the force carries. Due to their bosonic nature, they all have full-integer spins. Gluons g mediate the strong interaction and couple to so-called color charge, while photons γ are the exchange particles of the electromagnetic interaction between particles with electric charge. The mediators of the weak force are the Z and W bosons. Charged current interactions, related to W-boson exchange, only involve left-handed particles and right-handed antiparticles, while the neutral current Z bosons do not distinguish between the chirality of particles. Due to the large mass of its exchange particles, the weak interaction has a short range.

The basic building blocks of matter are the quarks and leptons, both fermions with half-integer spin. Each has six different types (flavors), which are grouped in pairs according to their mass, resulting in three generations (families). Additionally, each elementary fermion has a respective anti-particle whose quantum state is interchanged with that of the particle by the combined application of charge conjugation C, parity P, and time reversal T. The mass, spin, and lifetime of an antiparticle are the same as those of a particle. Leptons interact via the weak and, if

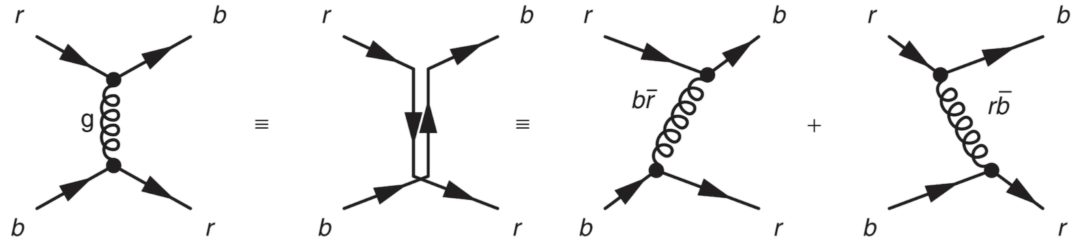

FIGURE 1.2: Illustration of the strong process $rb \to br$. The Feynman diagram, the associated color flow, and the two time-ordered diagrams are shown from left to right. Figure taken from Ref. [2].

electrically charged, the electromagnetic force. Each of the negatively charged e, μ and τ, is associated with a charge-neutral counterpart neutrino, ν_e, ν_μ and ν_τ, of almost vanishing mass. Quarks, on the other hand, have a non-integer electric charge, which distinguishes them from the rest of the SM particles. They are divided into the following families: up-down (ud), charm-strange (cs), and top-bottom (tb). Like leptons, they interact via the weak and electromagnetic forces. However, as the only color-charge-carrying elementary fermions, they also experience the strong interaction. Due to the peculiarities of the strong force, which will be explained in the next section, quarks are never observed in nature as isolated particles but only as color-neutral states bound together by gluons, the hadrons. These subatomic particles are either built from quarks of three different colors (qqq or $\bar{q}\bar{q}\bar{q}$) or the combination of a quark of one color with an anti-quark of the respective anti-color ($q\bar{q}$). The latter are called mesons, while the former are called baryons. The nucleons (N), which are either protons (uud) and neutrons (udd) and the stable building blocks of ordinary matter, are examples of such. However, there exists a much larger variety of hadrons, composed of all possible flavor combinations of quarks and anti-quarks. Their spectrum, as well as the residual interaction among them, are driven by the strong force.

1.2 Quantum Chromodynamics

QCD is the theory of the strong interaction. It is formulated in terms of elementary quark and gluon fields, whose interactions are governed by the principles of relativistic Quantum Field Theory (QFT) with a non-abelian gauge symmetry $\mathrm{SU}(3)_{\mathrm{color}}$, related to the color charges[3] red (r), blue (b) and green (g). Each quark can be assigned to one of the respective color states, which changes when it emits or absorbs a gluon. Gluons, on the other hand, exist in one out of eight possible states of color-anti-color combinations, hence carrying the color difference in strong processes and ensuring the required conservation of color charge. The quark-gluon interaction vertex and associated color flow are shown exemplarily in Fig. 1.2. Since gluons themselves carry color, they can interact not only with quarks but also with one another, allowing for three- and four-gluon vertices. They are depicted in Fig. 1.3, together with the fundamental quark-gluon interaction vertex.

---

[3] In this context, color has nothing to do with the visible light spectrum and is only used to label the three orthogonal states in the $\mathrm{SU}(3)_{\mathrm{color}}$ space.

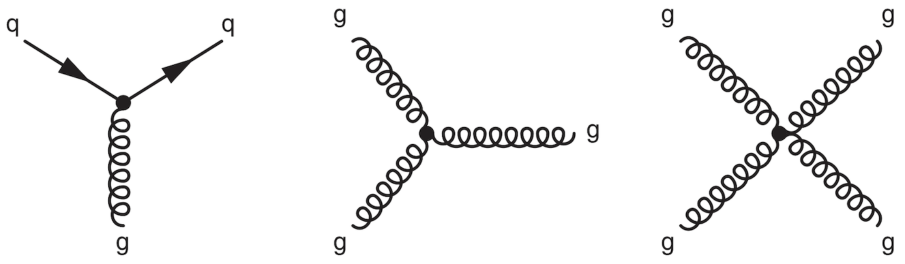

FIGURE 1.3: The three QCD vertices, which arise from the $\mathrm{SU}(3)_{\text{color}}$ local gauge invariance of the theory. Figure taken from Ref. [2].

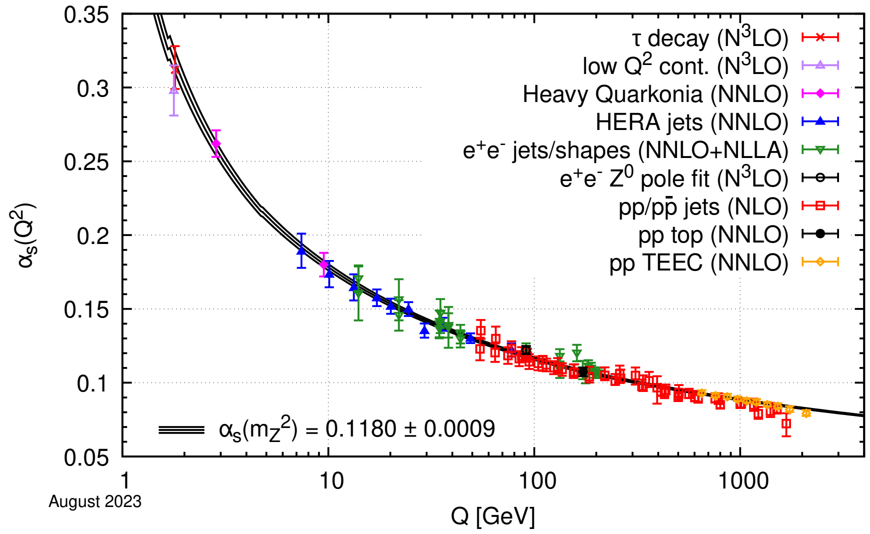

FIGURE 1.4: The measured α_s at different energy scales, expressed in terms of the momentum transfer of the interaction Q, which is inversely proportional to the distance, compared to the running of the coupling, which is computed using the PDG-averaged value $\alpha_s(m_Z^2) = 0.1180 \pm 0.0009$ as input. Figure taken from [4].

The QCD Lagrangian is given by [3]

$$\mathcal{L}_{\text{QCD}} = \sum_f \bar{q}_f \left(i\not{D}_\mu - m_f\right) q_f - \frac{1}{4} G^a_{\mu\nu} G^{\mu\nu}_a . \tag{1.1}$$

The first term accounts for the coupling between quarks and gluons via the gauge covariant derivative $D_\mu = \partial_\mu + igA^a_\mu \frac{\lambda_a}{2}$, where $A^a_\mu(x)$ are the gluon fields, λ_a the Gell-Mann matrices and g the QCD coupling, related to the strong coupling constant via $g^2 = \alpha_s/4\pi$. The term is summed over the six flavors f of quarks with current masses m_f and described by the quark fields $q_f(x)$. The second term incorporates the gluon self-couplings via the gluonic field-strength tensor $G^a_{\mu\nu}(x) = \partial_\mu A^a_\nu - \partial_\nu A^a_\mu - gf^{abd} A^b_\mu A^c_\nu$. The self-interaction of the force-carrying gluons, which is unique to the strong interaction compared to the other forces, leads to an anti-screening of the color charge at short distances and high energies, causing the interaction to weaken and the quarks to behave as quasi-free particles. This phenomenon is also referred to as *asymptotic freedom*, and the corresponding small coupling constant allows for a perturbative treatment of QCD. At large distances and low energies, on the other hand, α_s is large, as can be seen in Fig. 1.4. Quarks and gluons are confined in color-neutral hadrons. This is related to the energy stored in the gluon

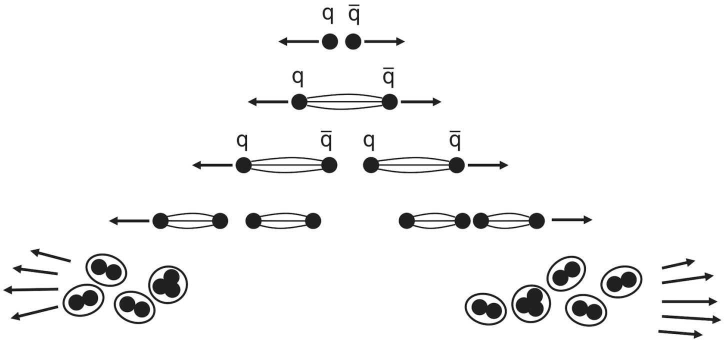

FIGURE 1.5: Simplistic illustration of the hadronization process. Figure taken from Ref. [2].

fields, which increases with the distance between the individual quarks in a quark-anti-quark pair until it is energetically favorable to produce another $q\bar{q}$ pair out of the vacuum, initiating the process of hadronization, which eventually leads to the formation of hadrons, as illustrated in Fig. 1.5.

Notably, hadrons are much heavier than the sum of the masses of their elementary constituents. This missing mass is dynamically generated by the strong interaction among the confined quarks and gluons. It is related to the spontaneous breaking of chiral symmetry, which is respected by the massless QCD Lagrangian[4] but not the ground state of the system, the QCD vacuum. Since the latter is populated by scalar quark-anti-quark pairs that mix left- and right-handed quarks as $q\bar{q} = q_L\bar{q}_R + q_R\bar{q}_L$ [5], it is characterized by a non-zero vacuum expectation value $\langle 0|q\bar{q}|0\rangle \neq 0$, also called chiral condensate. The effects of spontaneous chiral symmetry breaking are most evident in the large mass gap between chiral multiplets, which share all quantum numbers besides parity, e.g., the $\rho(770)$ and $\mathrm{a}_1(1260)$ mesons. Moreover, it leads to the appearance of spinless Nambu-Goldstone bosons [6–8], which are identified as the eight pseudo-scalar mesons $\pi^{\pm}, \pi^0, \mathrm{K}^{\pm}, \mathrm{K}^0, \overline{K^0}$ and η. Notably, they are significantly smaller in mass than the rest of the hadrons.

Coming back to the discussion on the strong coupling constant, the low-energy regime of *color confinement* is still not completely understood due to the complexity of the quark-gluon dynamics at such scales. This prevents an analytic approach, allowing only numerical solutions of QCD obtained through large-scale computations. Alternatively, phenomenological models or effective field theories can be applied where the interaction Lagrangians are formulated in terms of collective, hadronic degrees of freedom. At such energy scales, the residual strong interaction between hadrons becomes relevant, and measurements of the related hadronic observables can provide valuable input for constraining the available theories.

1.3 Hadronic interactions

Although quarks and gluons are the fundamental degrees of freedom of QCD, they are never observed in nature as distinguished particles but only as bound states held

---

[4] Chiral symmetry is explicitly broken when the non-vanishing quark masses are taken into account, as left- and right-handed quark fields get mixed by the mass term in Eq. 1.1. However, the heavy c, b and t quarks can be treated effectively as static in low-energy processes. This leaves the light quarks u, d and s as the only active degrees of freedom whose masses are vanishing. Therefore, chiral symmetry can still be seen as an approximate symmetry of the QCD Lagrangian.

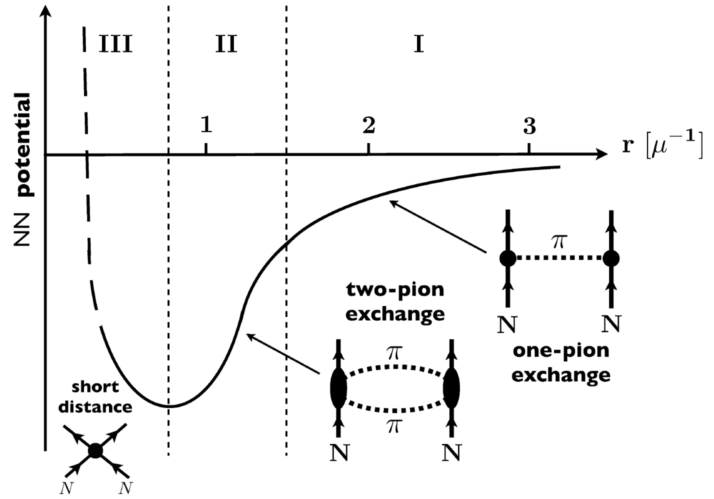

FIGURE 1.6: Phenomenological N–N potential as function of the distance r, given in units of the inverse pion mass $\mu^{-1} \approx 1.5$ fm. The relevant regions characterizing the shape of the potential are highlighted and denoted by roman numbers. Figure taken from [9].

together by the strong force. On the subatomic level, i.e., in the non-perturbative regime of low- and medium-energy physics, hadrons and hadronic interactions, which are the residual long-range effect of the strong force on the quark level, become relevant.

In particular, the N–N interaction, which is responsible for the formation of atomic nuclei and, thus, of the matter that surrounds us, is a main interest of nuclear physics and has been extensively studied both experimentally and theoretically. However, interactions involving hadrons with valence-quark content beyond u and d are also relevant. Strange hadronic matter could, for example, be formed in high-density environments, such as the core region of neutron stars, and studying interactions involving baryons with s-quark content, so-called hyperons (Y), can provide essential information for understanding our universe.

Furthermore, the knowledge of hadronic interactions is crucial to predicting and/or interpreting the hadronic spectrum. Several new exotic states have been discovered in the last decades, especially in the charm sector, whose properties cannot be described by the conventional constituent quark model. This initiated extensive studies on their nature, especially in the context of low-energy QCD. Not only can the measured mass and decay width of such resonances be modified by the interaction between the final scattering states, but most of these exotic states are close to the mass thresholds of pairs of conventional hadrons. They may, therefore, be molecular or bound states (partially) composed of these pairs or their properties subject to the effects of coupled-channel hadron-hadron interactions.

1.3.1 Theoretical Frameworks

Processes of interest to nuclear physics or low-energy hadronic physics occur on the femtometer scale. This corresponds to a small momentum transfer Q and a large coupling constant α_s, which makes it impossible to apply pQCD. However, alternative approaches based on hadronic degrees of freedom have been proven efficient in describing a wide range of low-energy phenomena.

Indeed, in his pioneering work published in 1935, H. Yukawa was the first to develop a theory of the N–N interaction, where the force between nucleons is mediated by a massive boson [10], just as gluons mediate the strong force between quarks. A few years later, in 1947, this exchange boson was finally discovered and identified as pion after initially mistaking it for the muon [11]. **Phenomenological approaches** based on microscopic one or more boson-exchange are still used today. However, more complex potentials are employed, which can be divided into short-, intermediate, and long-range parts, each characterized by different exchange particles, depending on their mass $m \propto 1/r$. An example of such nuclear potential is illustrated in Fig. 1.6. At large distances $r > 2$ fm, corresponding to the region denoted by I in the plot, one-pion exchange leads to an attractive interaction in line with Yukawa's original approach. The intermediate attraction in region II (1 fm $< r <$ 2 fm) is mediated by 2π and/or heavier mesons, like the ρ, ω and σ. The repulsive core at short ranges $r < 1$ fm, i.e., region III, which arises from Pauli-blocking at the quark level, is unresolved at the low-energy scales of nuclear physics. It might, however, be modeled using heavy vector-meson exchange. A prominent example that accurately describes the N–N interaction is the Argonne v_{18} potential, whose 40 adjustable parameters are determined in a direct fit to the Nijmegen pp and np scattering database, low-energy nn scattering parameters, and the deuteron binding energy [12]. Phenomenological approaches based on boson exchange have also been applied to model interactions beyond N–N, such as N–Y [13–17] and Y–Y [18, 19], but also in the charm sector [20, 21].

An alternative theoretical approach is provided by **chiral perturbation theory** (χPT), which is the effective field theory of low-energy QCD. As such, it is a systematic and model-independent approximation method based on scale separation that is able to predict physical phenomena within the low-energy domain without knowing or assuming the full details of the underlying physics. Its principles were first outlined by S. Weinberg [22, 23]. The effective Lagrangian is consistent with the symmetries of low-energy QCD, in particular, the (broken) chiral symmetry. This distinguishes χPT from purely phenomenological models. Each term of the Lagrangian is accompanied by a low-energy coupling constant (LEC), which is to be determined empirically. Further, the terms are ordered by their importance via an expansion in powers of Q/Λ_χ, where Q (soft scale) is given by Nambu-Goldstone boson masses, i.e., m_π or m_K and derivatives (equivalent to momentum). This guarantees that the interactions of Nambu-Goldstone bosons vanish in the chiral limit ($m_\pi \to 0$) and zero momentum transfer ($q \to 0$). $\Lambda_\chi \sim 1$ GeV/c^2 is the chiral symmetry breaking scale (hard scale) and of the size of vector meson masses. The hierarchy of nuclear forces obtained from χPT is shown exemplarily in Fig. 1.7. Depending on the desired accuracy, the relevant interaction diagrams are calculated up to a given order, denoted by leading order (LO), next-to-leading-order (NLO), etc. A detailed discussion on the principles of χPT is provided by Ref. [24]. However, similarly to the phenomenological models, the theory is characterized by several free parameters, the LECs, which have to be determined from fits to experimental data. Therefore, it is essential that enough measurements on a specific interaction are available. Otherwise, they have to be constrained by alternative inputs, such as simulations or data from other hadronic interactions, which can impact the accuracy of the model. While this is of no concern in the nuclear sector, where plenty of data is available, the situation changes once one tries to apply it to other 2-body interactions involving hadrons with valence-quark content beyond u and d, as the number of parameters increases while data are scarce or non-existent.

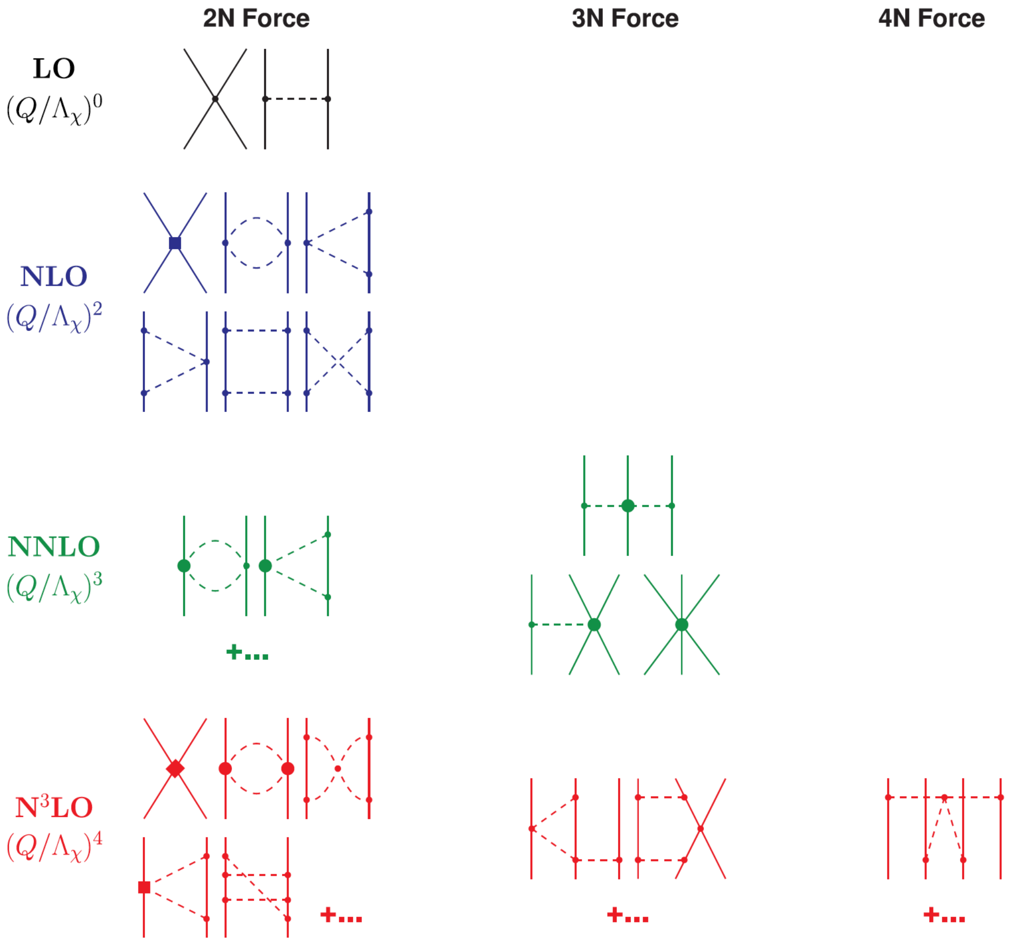

FIGURE 1.7: The hierarchy of Feynman diagrams contributing to the nuclear forces based on Weinberg's power counting scheme. The solid lines represent nucleons, the dashed line pions, and the dots and diamonds are different types of vertices. Figure taken from Ref. [24].

This issue can be avoided by studying hadronic interactions from non-perturbative first principle **lattice QCD** (LQCD) simulations, which are based on the numerical evaluation of path integrals by using Monte Carlo sampling methods. LQCD is a lattice gauge theory proposed by K. Wilson [25]. It is formulated on a hyper-cubic lattice, with gluons and quarks on the links and the sites, respectively, which is characterized by the lattice spacing a and the lattice volume L, as well as the Euclidean time t. By extrapolating the results obtained in the simulations to the continuum limit $a \to 0$ and the thermodynamic limit $L \to \infty$, it is possible to compare them with experimental data [26]. The big advantage of LQCD over the parameter-dependent methods discussed earlier in this section is that hadronic interactions are only controlled by the QCD coupling g and the quark masses. Studying them on the lattice was first proposed by Lüscher [27, 28]. His formalism is based on two hadrons confined in a $L \times L \times L$ box with periodic boundary conditions, whose energy spectrum is characteristic of the force between them. If the lattice volume is sufficiently larger than the interaction range $(L \gg R)$, a direct relation between the energy spectrum and the elastic scattering phase shift can be derived. An alternative approach was developed by Ishii et al. [29] and further advanced within the HAL QCD Collaboration, where the energy-independent non-local interaction potential $U(\vec{r}, \vec{r}')$ is directly determined from the behavior of the equal-time Nambu-Bethe-Salpeter (NBS) amplitude $\psi(\vec{r})$ in the internal region $|\vec{r}| < R$. Scattering phase shifts and other physical observables can then be obtained from the LQCD potential by solving the Schrödinger equation. This allows a broad application of the HAL QCD formalism in nuclear physics. Further details can be found in Ref. [26, 30, 31]. Since low quark masses are computationally more expensive, most simulations in the past have been carried out using non-physical values for quarks and, thus, for all hadrons. However, ongoing technological and numerical advances are already making it possible to perform simulations very close to, or even at, physical masses, and the quality of their results will only improve in the future.

1.3.2 Experimental measurements

Phenomenological models and effective theories, as well as lattice calculations, need empirical constraints, either to determine their free parameters or to validate their predictions. In the following, some of the most commonly used experimental methods for studying hadronic interactions are examined.

Low-energy scattering experiments have been widely used to study both baryon–baryon and meson–baryon interactions, providing over 8000 data points of N–N reactions [32, 33]. However, such measurements become more challenging once strangeness comes into play. While information on the K^-–N interaction can be obtained using secondary kaon beams [34, 35], only few measurements of N–Y scattering are available, mainly involving Λ [36] and Σ hyperons [37, 38], due to their short lifetime and hence unstable beams. Studies based on hypernuclei, which are exotic systems where one or more nucleons are replaced hyperons, are easier to realize [14, 39, 40]. In such experiments, the binding energy of the hyperon inside a specific nucleus is determined in a kinematic analysis of the decay products. However, as the hyperon interacts with multiple neighboring nucleons, effects from many-body interactions are present, and the data cannot be used directly to constrain the N–Y two-body interaction. Exotic atoms, i.e., atoms where an electron is replaced by a negatively charged meson, on the other hand, can be used to study meson–baryon interactions. By measuring the X-ray de-excitation spectrum of pionc [41] and kaonic hydrogen [42], it is possible to determine the complex scattering length of the π^-–p and K^-–p interaction from the width and shift of the respective energy level.

Over the past decade, the femtoscopy technique has become essential for studying interactions between hadrons, especially those with s quark content, providing valuable data with unprecedented statistical precision. The method is based on the measurement of the correlation function of hadron pairs in momentum space, which can be used to infer the two-body interaction potential. An extensive discussion of the theory and experimental method can be found in chapter 2. The ALICE collaboration measured the residual strong interaction between several light-flavor and strange hadrons, including p–p [43], p–$\overline{\mathrm{p}}$ [44], p–$K^{\pm}$ [45], p–Λ [43, 46], p–$\overline{\Lambda}$ [44], p–Σ^0 [47], Λ–Λ [43, 48, 48], Λ–$\overline{\Lambda}$ [44], p–Ξ^- [49, 50], p–Ω^- [50], p–ϕ [51], and Λ–$K^{\pm}$ [52]. Recently, also the first experimental result in the charm sector was obtained by measuring the p–D^- [53] correlation function. Furthermore, the femtoscopic technique has been extended to three-body interactions [54], providing measurements of the p–p–p and p–p–Λ [55] as well as the p–p–$K^{\pm}$ [56] system.

Chapter 2

A novel technique to access the strong interaction

The femtoscopy method relates momentum correlations between particles produced close to each other in momentum and position space to the final state interaction between them, as well as their emission region.

It has its origins in intensity interferometry, which was developed in the early 1950s by Hanbury-Brown and Twiss [57], hence also referred to as HBT interferometry, to determine the angular diameter of astrophysical radio sources. The method is based on the correlation between the signal intensity I_i measured by two independent i receivers at each end of a baseline d, and its relation to the spatial distribution of the emitting source via

$$C(\vec{d}) = \frac{\langle I_1 I_2 \rangle}{\langle I_1 \rangle \langle I_2 \rangle} = 1 + \left| \int d^3 r \rho(\vec{r}) e^{i\left(\vec{k}_1 - \vec{k}_2\right)\cdot\vec{r}} \right|^2 , \tag{2.1}$$

where $\vec{k}_i$ is the wave vector light seen in each detector and $\rho(\vec{r})$ the spatial distribution of the emission points. In particular, the integral whose absolute square value enters in Eq. 2.1 is the Fourier transform of the source distribution.

The method was first used to determine the angular diameter of astrophysical radio sources, but later, in 1956, it was also applied to the visual range [58, 59]. This caused controversy in the community at the time [60], which was resolved by Purcell [61], who explained the approach in terms of quantum mechanics and the relationship between spin, statistics, and the symmetry of a wave function.

In 1959 Goldhaber et al. [62] observed angular correlations for like-sign pion pairs in $\mathrm{p\overline{p}}$ annihilation, which, in contrast to unlike-sign pairs, could not be explained by predictions of the conventional Fermi statistical model. However, by considering the interference of the production amplitudes due to the symmetrization requirement of quantum statistics (QS) for identical mesons, the data could be described qualitatively [63]. The correlation effect was also found to be sensitive to the size of the interaction volume in which the statistical mixing of states takes place. Conceptually this approach is a simplified version of the HBT idea, applied to high-energy particle physics.

The basics of modern femtoscopy were developed in the early 1970s by Kopylov and Podgoretsky [64, 65], who suggested to study correlations as a function of the separation of particles in momentum space and proposed mixing techniques to construct an uncorrelated reference sample. The formalism has been refined by Koonin [66], Pratt [67–69] and Lednicky [70–72], among others, taking into account effects arising from final state interaction (FSI), which become relevant when the particles are emitted close to each other.

Over the past decades, femtoscopy has become a powerful precision tool in high energy physics, linking the momentum correlations of two or more particles with small relative momenta to QS and FSI, which includes both the strong and Coulomb interactions, as well as the spatiotemporal properties of the emission region. Initially, it has been used mainly to study the characteristics of particle production at the 1 fm $= 10^{-15}$ m level, using pairs of known FSI. However, it also provides a unique way to access the strong interaction if the emission process is well understood. This is particularly interesting in the case of exotic particle pairs, for which classical approaches such as scattering experiments are not feasible due to the lack of stable particle beams and/or targets.

A detailed description of the femtoscopy framework, both theoretical and experimental, is given in the following sections, while the last part of this chapter focuses on the two-body interaction in terms of the scattering process. There, the scattering parameters are introduced, which are used to quantify the residual strong interaction and essential to interpret the measured correlation function.

2.1 Femtoscopy

Summarizing the short dive into the history of femtoscopy at the beginning of the chapter, it was found that the relative momentum $\vec{p}_1 - \vec{p}_2$ of two particles, emitted in close proximity with nearly equal momentum, is sensitive to the characteristics of the emission region as well as the FSI, including the strong and Coulomb interaction. In the case of identical particles, also QS, i.e., the symmetrization of the wave function for each spin state, has to be taken into account.

A unique tool to access this information is the two-particle correlation function, which is defined as the ratio of the conditional probability $P(\vec{p}_1, \vec{p}_2)$ of simultaneously observing particles with momenta $\vec{p}_1$ and $\vec{p}_2$ to the probability of finding the particles independently [67];

$$C(\vec{p}_1, \vec{p}_2) = \frac{P(\vec{p}_1, \vec{p}_2)}{P(\vec{p}_1)P(\vec{p}_2)}. \tag{2.2}$$

In the absence of any correlation, the expression equals unity, as the two-particle probability factorizes $P(\vec{p}_1, \vec{p}_2) = P(\vec{p}_1) \cdot P(\vec{p}_2)$. It is further possible to link the observation probabilities to particle emission probabilities under the following main assumptions [69, 71, 72]

1. The mean freeze-out phase space density is sufficiently small that only mutual FSI and QS effects influence the correlation of particle pairs with small relative momentum, and higher-order correlations can be neglected.
2. The particle emission is uncorrelated and independent.
3. The momentum dependence of the single-particle emission probabilities $S_i(p_i, x_i)$ is assumed to be negligible when the particle four-momentum is varied by the amount characteristic for correlations associated with QS and FSI.

These considerations lead to the following expressions

$$P(\vec{p}_i) = \int d^4x_i S_i(p_i, x_i) \tag{2.3}$$

$$P(\vec{p}_1, \vec{p}_2) = \int d^4x_1 d^4x_2 S_1(p_1, x_1) S_2(p_2, x_2) |\psi(p_1, x_1, p_2, x_2)|^2, \tag{2.4}$$

where $S_i(p_i, x_i)$ describes the probability of emitting a particle with momentum p_i from a space-time point $x_i = (t_i, \vec{r}_i)$, hence, containing the all information in the source. The Bethe-Salpeter amplitude $\psi(p_1, x_1, p_2, x_2)$ accounts for the interaction between two particles and $|\psi(p_1, x_1, p_2, x_2)|^2$ is unity for non-interacting particles. Assuming that the two-particle system propagates quasi-free and both particles are emitted at equal times in the pair rest frame[1] it reduces to $\psi(p_1, x_1, p_2, x_2) \to \psi(\vec{k}^*, \vec{r}^*)$, where $\vec{r}^* = \vec{r}_1^* - \vec{r}_2^*$ is the relative distance between the production points of the two particles and $\vec{k}^* = (m_1\vec{p}_1^* - m_2\vec{p}_2^*)/(m_1 + m_2)$ their reduced relative momentum.

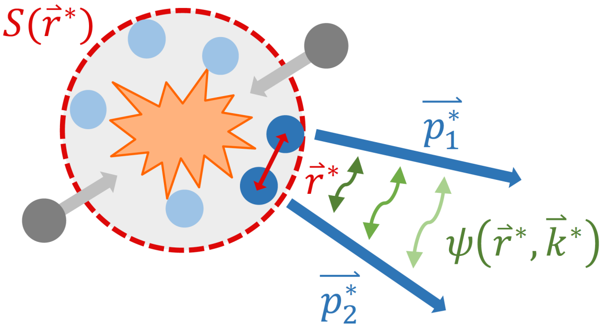

FIGURE 2.1: Illustration of the experimental and theoretical interpretation of the correlation function combined. The two gray circles represent the colliding particles, the blue circles correspond to the particles produced in the collision, and the red circle is the emission source $S(\vec{r}^*)$. If two particles 1 and 2 (dark blue circles) are emitted close to each other, at distance $\vec{r}^*$, with small relative momentum $\vec{k}^* = (m_2\vec{p}_1^* - m_2\vec{p}_2^*)/(m_1 + m_2)$, they experience momentum correlations. These correlations arise from FSI, encoded in the two-particle wave function $\psi(\vec{r}^*, \vec{k}^*)$ and represented by the green arrows, as well as QS in the case of identical particles.

Following these considerations and further simplifications, e.g. no explicit time or momentum dependence of the source, Eq. 2.2 can be rewritten as a convolution of the two-particle source function $S(r^*)$ and the two-particle wave function $\psi(\vec{k}^*, \vec{r}^*)$, also referred to as *Koonin-Pratt Equation* [66, 68],

$$C(k^*) = \int \mathrm{d}^3 r^* S(\vec{r}^*) |\psi(\vec{k}^*, \vec{r}^*)|^2 \xrightarrow{k^* \to \infty} 1, \tag{2.5}$$

thus providing a link between a measurable quantity, the correlation function, and the particle emission and wave function. The latter is associated with the interaction potential via the Schroedinger Equation (SE) and can be calculated numerically using the CATS framework [73], which was developed by Dr. Dimitar Mihaylov and other members in the TUM group. In Femtoscopy, the wave function must satisfy the outgoing boundary condition where the flux of the outgoing wave is normalized. Figure 2.1 illustrates the femtoscopic principle of relating the experimentally measured correlation function to Eq. 2.5. At large k^* the particles separate too quickly to experience QS effects or any kind of FSI, resulting in a flat correlation function equal to unity. The relative momentum range of $k^* < 200$ MeV$/c$, where the particles have

---

[1] The pair rest frame, denoted by the asterisk, is defined as $\vec{p}_1^* - \vec{p}_2^* = 0$

nearly equal momentum and can interact, is also referred to as the femtoscopic region. There, the correlation function is sensitive to possible effects related to the FSI and QS and can deviate from unity.

Assuming a symmetric emission, the two-particle source function $S(\vec{r^*})$ is typically expressed as the convolution of two single-particle Gaussian sources of width r_0

$$S^G(r^*) = \left(4\pi r_0^2\right)^{-3/2} \cdot \exp\left(-\frac{r^{*2}}{4r_0^2}\right). \tag{2.6}$$

Integrating out the angular dependence results in the probability of emitting two particles at a certain relative distance

$$S^G_{4\pi}(r^*) = 4\pi r^{*2} S^G(r^*) = \frac{r^{*2}}{2\sqrt{\pi} r_0^3} \cdot \exp\left(-\frac{r^{*2}}{4r_0^2}\right). \tag{2.7}$$

However, in many physical situations, this approximation is not sufficient since the particle samples from which the experimental correlation functions are built also contain feed-down particles from resonance decays. In particular, those from short-lived, strongly decaying resonances must be considered, as they cannot be removed from the measured particle sample due to experimental limitations. Depending on their lifetime, these resonances either lead to an enhancement of the Gaussian width by adding contributions to the emission duration proportional to their lifetime or introduce a long-range exponential tail [74]. How pronounced the latter is, depends on the particle pair. Figure 2.2 illustrates this effect.

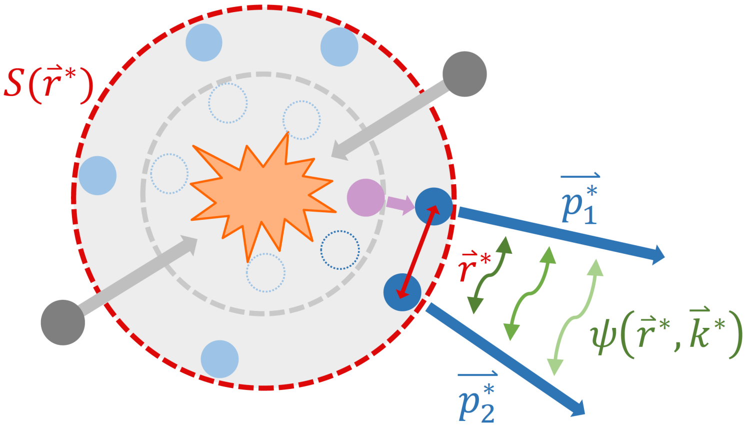

FIGURE 2.2: Illustration of the modification of the source size due to a short-lived, strongly-decaying resonance (lilac circle) feeding into one of the particles of interest (dark blue circles).

While a Gaussian profile is successful in the description of correlation functions like p–p and p–Λ [43], in extreme cases like π–π, a Cauchy/Exponential source function [75] may be used to account for the excessive resonance tail [76–78]. Such an approach, however, does not consider the resonances and their properties explicitly. An alternative is provided by the resonance source model (RMS). It is based on a Gaussian core source from which all primordial particles are emitted and whose width depends on the transverse mass of the pair, and is anchored to experimental data. The effective enhancement of the source size related to feed-down contributions is simulated with EPOS, taking into account the relevant, pair-specific resonances. The resulting source distribution, which is fully constrained from data or simulations, can then be parameterized with a single Gaussian or the weighted sum of several Gaussian's, depending on the extent of the exponential tail. The RSM is discussed extensively in Sec. 3.3. It was successfully employed in several previous femtoscopic analyses [44, 46, 47, 50, 53, 79] and is also used in those presented in this thesis.

The size of the source depends not only on the specific particle pair but also on the system in which it was produced. Typical values for a Gaussian emission source in pp and p–Pb collisions at the LHC are between $1 - 1.5$ fm [43, 49], while for Pb–Pb larger values of $3 - 6$ fm are found [80].

Due to the convolution of the source function with the wave function, the emission size influences the magnitude of the correlation signal at small k^*. This can be understood from Fig. 2.3. The right plot shows a Gaussian source function for two radii r_0, as well as different Yukawa-type strong interaction potentials of the form

$$V(r^*) = \frac{A}{r^*} \exp\left(-m_\pi r^*\right), \tag{2.8}$$

where A[2] is the dimensionless measure for the potential strength and m_π is the mass of the pion, the exchange particle of the nuclear force. The left plot shows the corresponding correlation functions. Notably, the repulsive potential leads to a correlation signal below unity, while the attractive potential results in a correlation function above 1. A larger source size significantly reduces the magnitude and range of the correlation signal, as fewer particles are emitted within the range of the potential and experience the strong FSI. If the attractive interaction is strong enough to support a bound state, this general picture does not hold anymore, and, depending on the source size and characteristics of the potential, the correlation function can assume values below unity in the full or partial k^* range. Bound states are explicitly discussed in Sec. 2.3.3.

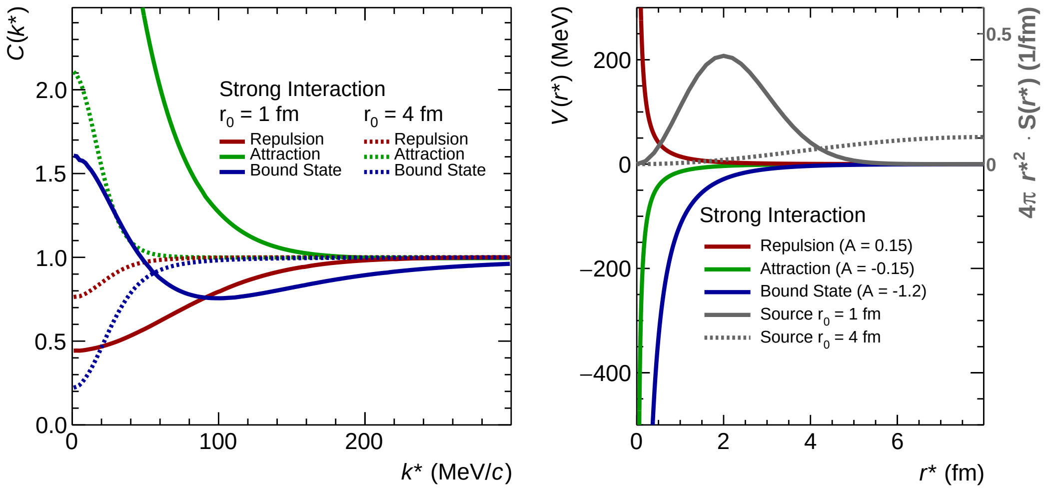

FIGURE 2.3: Correlation functions obtained for different Yukawa-type potentials and Gaussian source radii are depicted on the *left*. The respective potentials and Gaussian source functions are shown on the *right*.

The effect of the emission size on the contributions from QS and the Coulomb interaction is illustrated in Fig. 2.4, again using a Gaussian source parametrization.

---

[2] The values of A used for the potentials shown in Fig. 2.3 have no physical meaning and were chosen at random to exemplary represent an attractive and repulsive interaction, as well as one that could, in theory, support a bound state.

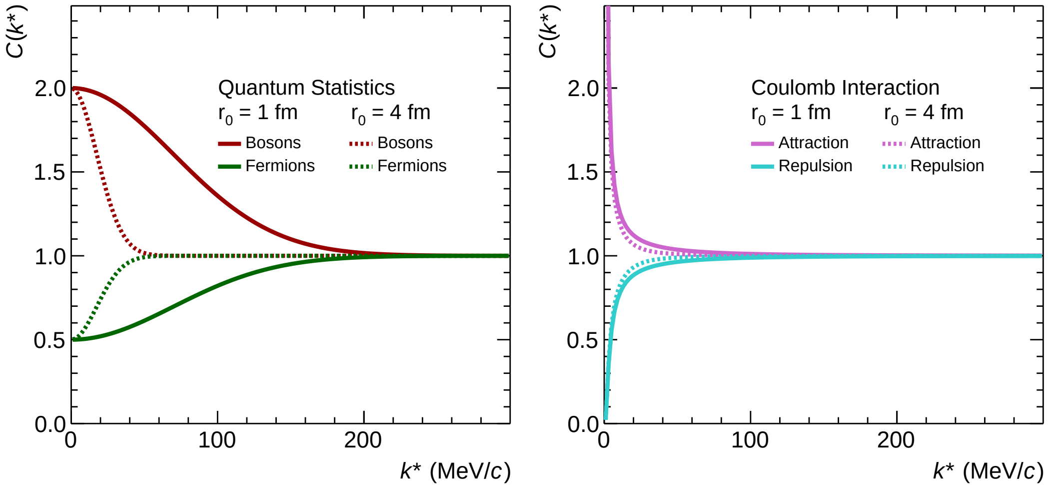

FIGURE 2.4: The correlation function associated with QS effects is depicted on the *left* for different Gaussian source radii. The *right plot* shows the same for the Coulomb interaction.

The left panel shows the correlation signal from quantum statistics. As can be seen, $C_{\mathrm{QS}}^{\mathrm{Bosons}} \xrightarrow{k^*\to 0} 2$ in the case of identical bosons due to the symmetrization requirement of the wave function, while the anti-symmetrization of the wave function for fermions results in $C_{\mathrm{QS}}^{\mathrm{Fermions}} \xrightarrow{k^*\to 0} 0.5$. While the magnitude of the correlation is unaffected by the source size, its range is reduced for a larger source by shifting the signal to a smaller relative momenta. The right panel shows the correlation functions associated with the Coulomb interaction. They are almost independent of the size of the source, which only becomes relevant at very small k^*.

After the contributions from QS, the Coulomb and the strong interaction have been shown individually for different source sizes, the full π–π and p–p correlation functions and their components are shown in Fig. 2.5 for a Gaussian source of $r_0 = 1$ fm. In the case of pions, the strong interaction is negligible, and the correlation signal, shown on the left, arises from a combination of the symmetrization requirement of the wave function and the repulsive Coulomb interaction. The p–p correlation function, shown on the right, is dominated by the strong interaction, which is modeled using the Argonne v_{18} [12] nuclear potential. In the calculation of the full correlation function, the Coulomb repulsion and the anti-symmetrization of the wave function are also considered.

2.2 Experimental correlation function

Having explained the theoretical interpretation of the correlation function in the previous section, the experimental measurement is discussed in the following.

The probabilities in Eq. 2.2 can also be expressed in terms of the Lorentz-invariant one and two-particle spectra [74], leading to the following expression for the correlation function

$$C(\vec{p}_1, \vec{p}_2) = \frac{E_1 E_2 d^6 N / (d^3 p_1 d^3 p_2)}{(E_1 d^3 N / d^3 p_1)(E_2 d^3 N / d^3 p_2)}. \tag{2.9}$$

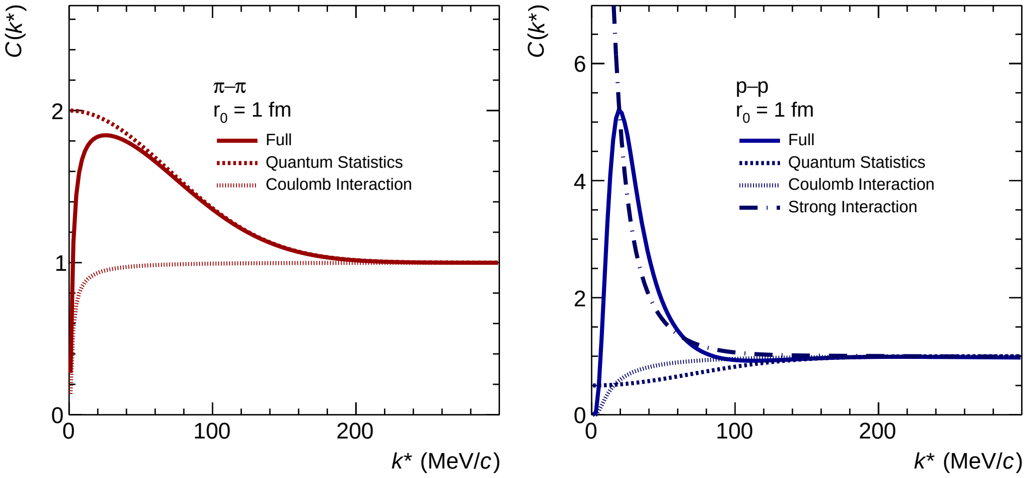

FIGURE 2.5: The full correlation function as well as its individual contributions is shown on the *left* for $\pi\pi$, and on the *right* for pp pairs.

In practice, however, this formal definition of the correlation function is rarely used in high-energy physics. Instead, the correlation between two particles is obtained experimentally as

$$C(k^*) = \mathcal{N} \times \frac{N_{\mathrm{same}}(k^*)}{N_{\mathrm{mixed}}(k^*)}, \tag{2.10}$$

where N_{same} and N_{mixed} are the relative-momentum distributions of two particles emitted in the same (mixed) event[3], and $\mathcal{N}$ is a normalization constant, that ensures $C_{\mathrm{exp}} = 1$ at large k^*, where the femtoscopic signal is absent. The same event distribution is acquired from all possible pair combinations in single collisions. In contrast, the mixed event distribution is obtained from mixing particles emitted in separate collisions, which renders them uncorrelated. Hence, the latter does not include any FSI effects. It reflects the phase space of the underlying event and serves as a reference sample. Due to experimental limitations, the raw correlation signal obtained from Eq. 2.10 is not clean and can be decomposed as

$$C_{\mathrm{raw}}(k^*) = C_{\mathrm{femto}}(k^*) \times C_{\mathrm{non-femto}}(k^*), \tag{2.11}$$

depending on whether or not the final state interaction (FSI) among the reconstructed particles is the underlying mechanism that leads to the measured correlations in k^*, denoted as $C_{\mathrm{femto}}(k^*)$ and $C_{\mathrm{non\text{-}femto}}(k^*)$, respectively. Although the selection criteria are optimized to increase the primary fraction and purity of the candidates, the samples contain a finite amount of secondary and misidentified particles. The FSI among these particles will be different to that involving primary particles only, and hence, results in a different correlation signal. In the case of secondaries, the mother particle is the one involved in the interaction. The femtoscopic correlation function is therefore further decomposed as $C_{\mathrm{femto}}(k^*) = \sum_{\mathrm{i,j}} \lambda_{\mathrm{i,j}} \times C_{\mathrm{i,j}}(k^*)$, where $C_{\mathrm{i,j}}(k^*)$ arises from the FSI between the i-th and j-th component of the reconstructed particle samples. Each contribution $C_{\mathrm{i,j}}(k^*)$ is weighted by a so-called λ parameter, which is computed as $\lambda_{\mathrm{ij}} = p_{\mathrm{i}} p_{\mathrm{j}} f_{\mathrm{i}} f_{\mathrm{j}}$ where $p_{\mathrm{i,j}}$ and $f_{\mathrm{i,j}}$ are the purities and primary (secondary) fractions of the i-th and j-th component of the particle samples, respectively. The individual correlation functions $C_{\mathrm{i,j}}(k^*)$ can be obtained in a data-driven approach or modeled using Eq. 2.5. The different contributions to $C_{\mathrm{femto}}(k^*)$

---

[3] In the context of this thesis events correspond to individual collisions.

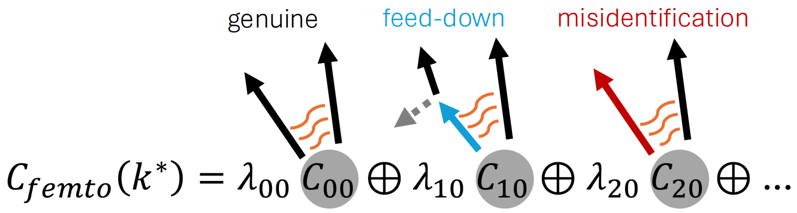

FIGURE 2.6: Illustration of different contributions to the measured femtoscopic correlation signal among two particles. The black arrows represent the primary particles of interest, the blue arrow a resonance, which decays into one of the particles of interest, hence representing the feed-down contribution, and the red arrow corresponds to a fake or misidentified particle.

are illustrated in Fig. 2.6. In particular, the contribution from the interaction of primary particles is also referred to as genuine while feed-down contributions refer to those involving secondary particles from weak decays or longer-lived strong decays. All short-lived, strongly-decaying resonances with $\langle c\tau \rangle < 5$ fm are absorbed in the source function, as discussed in the previouse section.

The residual non-femtosopic background $C_{\text{non-femto}}(k^*)$ is multiplicative as it affects all pairs, independently of their origin, i.e. whether or not they are built, for example, from misidentified, primary or feed-down particles[4]. It can affect the raw correlation function in the full k^* range and arises from energy-momentum conservation effects, biases related to the event mixing, as well as auto-correlations associated with the production of particles within jet-like structures. The latter, also referred to as minijet background, is typically associated with initial hard processes at Parton level [81], which lead to auto-correlated particle pairs that induce long-range structures to the measured correlation function, also affecting the sensitive femtoscopic region. The creation of minijets can be better understood in terms of string fragmentation [82], which is based on the gluonic fields between quarks and anti-quarks that are arranged as color flux tubes (strings) and give rise to a linearly increasing energy as the quarks separate and the tube is stretched [83]. At some point, it is energetically more favorable that the sting breaks, creating less energetic $(q\bar{q})$ pairs from the vacuum. This process continues until the energy is low enough for the quarks to hadronize. If hadrons are produced by a single string, they are collimated, leading to cone-like emission structures, the minijets. $C_{\text{non-femto}}(k^*)$ is typically obtained from Monte Carlo simulated data where the FSI is absent and/or a simple polynomial baseline, depending on how pronounced the minijet contribution is.

The genuine correlation function is the holy grail of any femtosopic analysis, which aims to study the unknown residual strong interaction between a given particle pair. To isolate it, all other contributions to $C_{\text{femto}}(k^*)$, as well as the remaining residual background not related to FSI, $C_{\text{non-femto}}(k^*)$, have to be understood.

---

[4] If the non-femtoscopic background is added with some weight parameter $\lambda_{\text{non-femto}}$, leading to $C_{\text{raw}}(k^*) = \lambda_{\text{non-femto}} C_{\text{non-femto}}(k^*) + (1 - \lambda_{\text{non-femto}}) C_{\text{femto}}(k^*)$, instead of being multiplied, it would mean that it only affects a fraction of pairs, which do not undergo any sort of FSI. As the non-femtosopic background affects all particle pairs in addition to the pair-specific FSI, it is multiplied.

2.3 The two-body interaction

With the femtoscopy framework now in place, the last part of this chapter focuses on its connection to the FSI, in particular, the residual strong interaction. As already discussed, the correlation function directly depends on the two-particle wave function, which is expressed in the relative coordinates k^* and r^* in the center-of-mass frame. The wave function is hence obtained by solving the SE for the respective interaction potential $V(r^*)$, which has a finite range R, is spherically symmetric and invariant under rotation. Considering that only small relative momenta are studied, the problem can be treated non-relativistically. Further, a steady state is assumed, as the interaction between the particles is quick. Therefore, the wave function, which characterizes the system within the potential range, is determined by the time-independent SE

$$E\psi(r^*) = \mathcal{H}\psi(r^*) := \left(-\frac{\hbar^2\nabla^2}{2\mu} + V(r^*)\right)\psi(r^*), \tag{2.12}$$

where $\mu = m_1 m_2/(m_1 + m_2)$ is the reduced mass of the pair. The total energy is given by $E = \frac{\hbar^2 k^{*2}}{2\mu}$ and $\psi(r^*) = \psi_{\vec{k}^*}(r^*, \theta)$ depends only on the relative momentum $\vec{k}^*$ and distance r^* as well as the angle θ due to the symmetry of the potential.

2.3.1 Scattering theory

The interaction between two particles is equivalent to a scattering process, where the initial state of the pair is transformed into a final state due to the action of the two-body interaction potential. The following discussion is based on Ref. [84], which I highly recommend for reading.

The initial state is described by an incident plane wave that moves towards a scattering region. There, the particles interact and the pair transitions into the final state, which at large distance is an outgoing spherical wave. The asymptotic wave function is hence given as

$$\psi(r^*) \xrightarrow[r^* \to \infty]{} \mathcal{N}\left(e^{i\vec{k}^* \cdot \vec{r}^*} + f(\theta)\frac{e^{ik^* r^*}}{r^*}\right), \tag{2.13}$$

where $\mathcal{N}$ is a normalization constant and $f(\theta)$ is the scattering amplitude, which is a measure of how much the incident wave is scattered. The process is illustrated in Fig. 2.7. At large r^*, the exact solution of the SE has to match the asymptotic form of the wave function.

Since angular momentum is conserved for potentials of the form $V(r^*)$, it is convenient to employ *partial wave expansion* and decompose the wave function into components of the angular momentum specified by the quantum number l. For a plane wave, this leads to

$$e^{i\vec{k}^* \cdot \vec{r}^*} = \sum_{l=0}^{\infty} i^l (2l+1) j_l(k^* r^*) P_l \cos(\theta), \tag{2.14}$$

where $P_l \cos(\theta)$ are the Legendre polynomials and $j_l(k^* r^*)$ the spherical Bessel functions, which can be expressed in terms of spherical Hankel functions $h_l^{(1)}(k^* r^*) \xrightarrow{r \to \infty} (-i)^{l+1} \exp(ik^* r^*)/k^* r^*$ and $h_l^{(2)}(k^* r^*) \xrightarrow{r \to \infty} (i)^{l+1} \exp(-ik^* r^*)/k^* r^*$ as

$$j_l(k^* r^*) = \frac{h_l^{(1)}(k^* r^*) + h_l^{(2)}(k^* r^*)}{2} \tag{2.15}$$

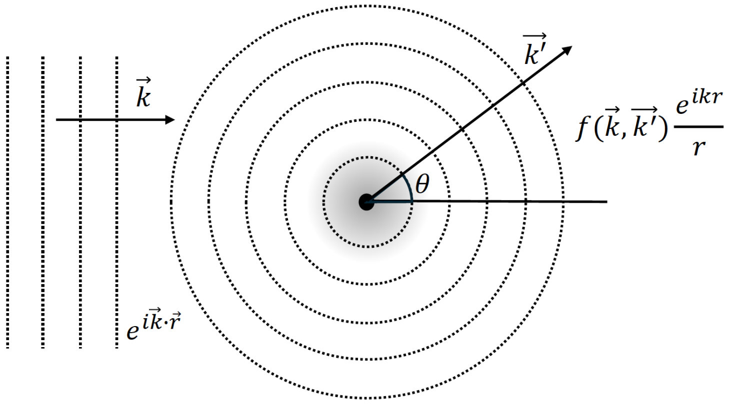

FIGURE 2.7: Schematic picture of the scattering process involving an incident plane wave and an outgoing spherical wave. The gray shaded area illustrates the scattering region, characterized by a central potential. The scattering amplitude $f(\vec{k},\vec{k'})$, which indicates how much of the incident wave is scattered, depends on the initial momentum $\vec{k}$ and the final momentum $\vec{k'}$, with $k = k'$. Due to the symmetry of the potential, $f(\vec{k},\vec{k'}) = f(\theta)$, ultimately only depends on the scattering angle θ.

Motivated by Eq. 2.14, the partial wave expansion of the full wave function is

$$\psi(r^*) = \mathcal{N}\sum_{l=0}^{\infty} i^l(2l+1)R_l(r^*)P_l\cos(\theta) = \mathcal{N}\sum_{l=0}^{\infty} i^l(2l+1)\frac{u_l(r^*)}{r}P_l\cos(\theta), \tag{2.16}$$

where $u_l(r^*)$ is the *reduced radial wave function* which satisfies the SE in spherical coordinates, also called *radial SE*,

$$Eu_l(r^*) = \left(-\frac{\hbar}{2\mu}\frac{\mathrm{d}^2}{\mathrm{d}r^{*2}} + \frac{l(l+1)\hbar^2}{2\mu r^{*2}} + V_l(r^*)\right)u_l(r^*). \tag{2.17}$$

This equation is ultimately solved numerically by frameworks like CATS, and the wave function used to calculate the correlation function. Analogous to Eq. 2.15, the following expression can be used for the radial wave function

$$R_l(r^*) = \frac{u_l(r^*)}{r^*} = c_l^{(1)}h_l^{(1)}(k^*r^*) + c_l^{(2)}h_l^{(2)}(k^*r^*), \tag{2.18}$$

which corresponds to $j_l(k^*r^*)$, if $c_l^{(1)} = c_l^{(2)} = 1/2$. For this specific choice of coefficients and $\mathcal{N} = 1$, Eq. 2.16 reduces to the plane wave solution. Therefore, the ratio of the coefficients can be used to quantify the impact of the scattering potential in terms of the phase shift $\delta_l(k^*)$ and scattering matrix $S_l(k^*)$

$$\frac{c_l^{(1)}}{c_l^{(2)}} = S_l(k^*) = e^{2i\delta_l(k^*)}. \tag{2.19}$$

In the asymptotic limit, Eq. 2.16 can be rewritten as

$$\psi(r^*) \xrightarrow[r\to\infty]{} \mathcal{N}\sum_{l=0}^{\infty}\frac{(2l+1)}{ik^*r^*}c_l^{(2)}\left[e^{2i\delta_l(k^*)}e^{ik^*r^*} - (-1)^l e^{-ik^*r^*}\right]P_l\cos(\theta), \tag{2.20}$$

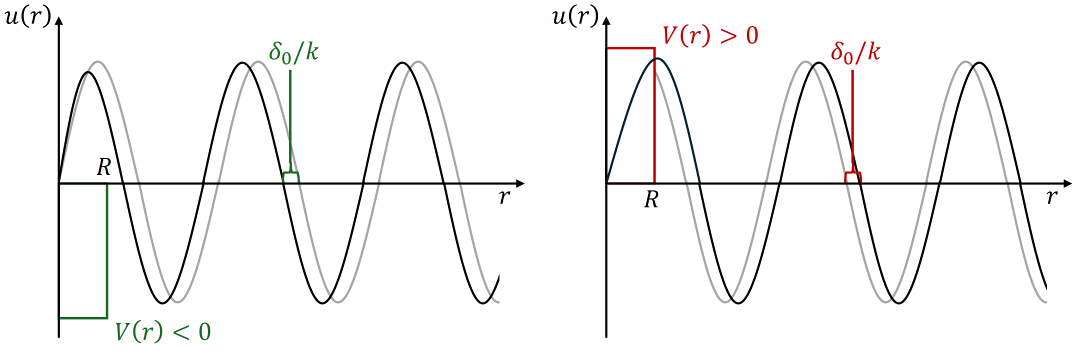

(A) Attractive potential with $\delta_0 > 0$. (B) Repulsive potential with $\delta_0 < 0$.

FIGURE 2.8: Illustration of the effect of the s-wave ($l = 0$) scattering potential on the phase shift δ_0 of the outgoing wave (black line) in comparison to the free incoming wave (gray line).

by considering the behavior of the Hankel functions for $r \to \infty$ and Eq. 2.19. By comparing this expression to Eq. 2.13, with the plane wave replaced with its asymptotic form[5], the scattering amplitude can be extracted as a function of the phase shift

$$f(\theta) = \sum_{l=0}^{\infty}(2l+1)\frac{e^{2i\delta_l(k^*)}-1}{2ik^*}P_l\cos(\theta), \tag{2.21}$$

where the fraction

$$f_l(k^*) = \frac{e^{2i\delta_l(k^*)}-1}{2ik^*} = \frac{1}{k\cot(\delta_l)-ik^*} \tag{2.22}$$

is also referred to as partial wave amplitude and can be related to the scattering matrix via

$$S_l(k^*) = 1 + 2ik^* f_l(k^*). \tag{2.23}$$

To properly match the exact solution to the asymptotic form, the scattering amplitude and, hence, the phase shift of the wave function have to be evaluated. These quantities provide information on the interaction. Physics-wise, the phase shift corresponds to the change in the phase of the outgoing wave function with respect to the incident wave due to the scattering or interaction process. Figure 2.8 illustrates the reduced radial wave function for different interaction potentials. The incoming wave is shown in gray, while the black line corresponds to the scattered outgoing wave in the case of an attractive potential on the left and a repulsive one on the right. Outside the potential range R, the outgoing wave corresponds to the free particle solution, and the observed phase shift is determined within $r^* < R$; an attractive potential leads to $\delta_l > 0$ as it pulls the particles towards each other, while a repulsive interaction pushes them away, leading to $\delta_l < 0$.

2.3.2 Scattering parameters

The s-wave ($l = 0$) scattering parameters are a measure of the strong interaction, commonly predicted by theory and measured in experiments. They are independent of the shape of the potential at low energies. Hence, different potentials can be tuned to result in the same scattering parameters, producing the same phase shift.

---

[5] Eq. 2.20 with $\mathcal{N} = 1$ and $c_l^{(2)} = 1/2$

In the low energy limit $k^* \ll R$, the particles cannot overcome the centrifugal barrier, which is the repulsive l-dependent term in Eq. 2.17. Hence, partial waves with $l > 0$ can be neglected, and the s-wave component of the solution is dominant, for which the centrifugal barrier vanishes. The radial s-wave wave function is given by Eq. 2.18

$$R_0(r^*) = \frac{u_0(r^*)}{r^*} = e^{i\delta_0}\left(\frac{1}{k^*r^*}\sin\left(k^*r^* + \delta_0\right)\right). \tag{2.24}$$

In the zero kinetic energy case, where $k^* \approx 0$, the radial SE, given by Eq. 2.17, reduces to

$$u_0''(r^* > R) = 0, \tag{2.25}$$

outside the potential range, where $V(r^*) = 0$. A possible solution is

$$u_0(r^* > R) = N(r^* + a_0) \propto (r^* + a_0), \tag{2.26}$$

where a_0 is the scattering length and N a normalization constant. Its logarithmic derivative $u'(r^*)/u(r^*)$ has to match the one of the reduced radial wave function $u(r^*)$ in Eq. 2.24 for $k^* \to 0$. This results in

$$\lim_{k^* \to 0} k^* \cot\left(\delta_0\right) = \frac{1}{a_0}, \tag{2.27}$$

for $r^* = 0$. Finally, this implies the following for the s-wave scattering amplitude, which is given by Eq. 2.22,

$$f_0(k^*) = \lim_{k^* \to 0} \frac{1}{k^* \cot\left(\delta_0\right) - ik^*} = a_0. \tag{2.28}$$

Following Eq. 2.26, the scattering length can be interpreted as the negative intercept of the extrapolation of the reduced radial outside wave function. Figure 2.9 shows $u(r^*)$ for the three different Yukawa-type potentials plotted in the left panel of Fig. 2.3, as well as the extrapolation of Eq. 2.26 to $r^* < R$. In the case of an attractive interaction, the scattering length is positive, as the intercept is on the negative side of the r^*-axis. For a repulsive interaction, the opposite is observed, and the scattering length is negative. In the case of a bound-state supporting attractive potential, the intercept is on the positive side, hence, the scattering length is also negative. Notably, the sign convention of the scattering length used in femtoscopy is opposite to the classical one.

Further, the scattering length is related to the low-energy differential cross section via $\mathrm{d}\sigma/\mathrm{d}\Omega = |f_0|^2$. Hence, the scattering cross section $\sigma = 4\pi a_0^2$ can be interpreted as the area of a circle with radius $2a_0$ and the scattering length as *effective size* of the target potential [85, 86].

For finite but small k^*R, the term $k^* \cot\left(\delta_0\right)$ can be expressed in powers of k^*

$$\lim_{k^* \to 0} k^* \cot\left(\delta_0\right) = \frac{1}{a_0} + \frac{1}{2}d_0 k^{*2} + \mathcal{O}(k^{*4}), \tag{2.29}$$

where d_0 is the effective range, which can be understood as the *real range* of the scattering potential [87]. This expression is also referred to as *effective range expansion* and implies the following for the scattering amplitude

$$f_0(k^*) = \lim_{k^* \to 0} \frac{1}{k^* \cot\left(\delta_0\right) - ik^*} \approx \left(\frac{1}{a_0} + \frac{1}{2}d_0 k^{*2}\right)^{-1}. \tag{2.30}$$

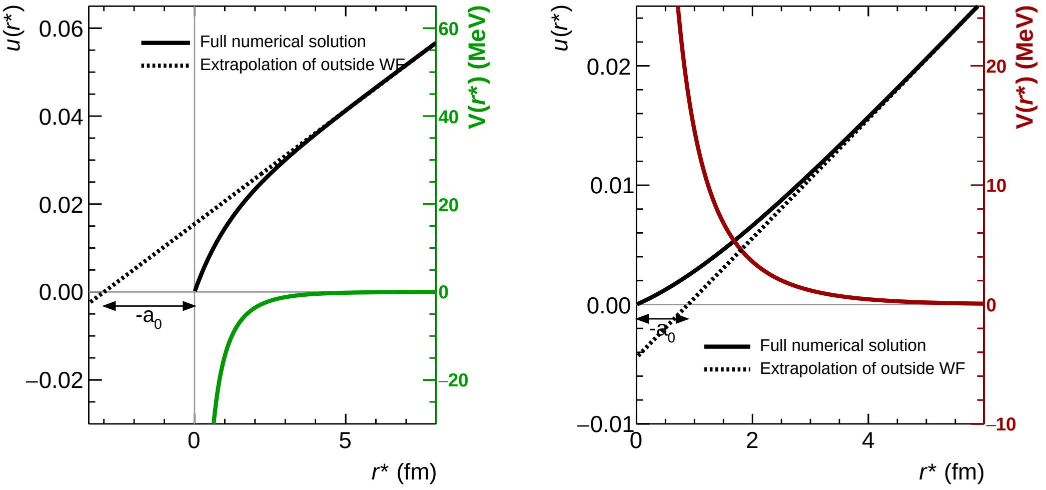

(A) Attractive Yukawa-type potential using $A = -0.15$.

(B) Repulsive Yukawa-type potential using $A = 0.15$.

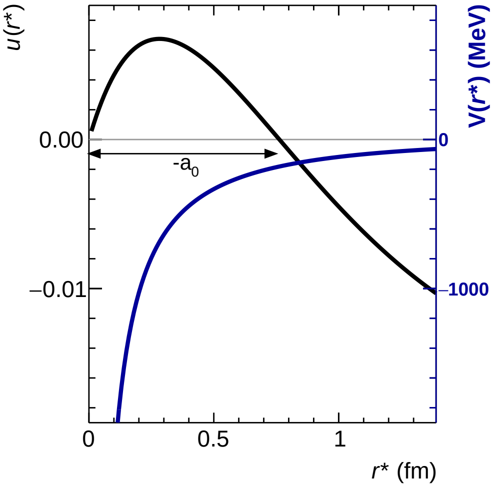

(C) Attractive Yukawa-type potential ($A = -1.20$), which is strong enough to support a possible bound state.

FIGURE 2.9: Reduced radial wave function $u(r^*)$ for different potentials as well as the extrapolation of the outside wave function, given by Eq. 2.26. The intercept corresponds to the negative scattering length in the femtoscopic sign convention.

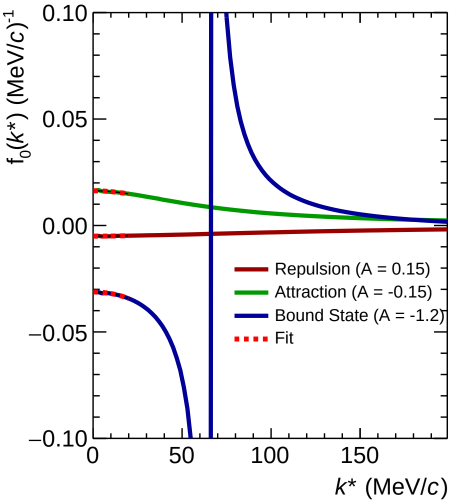

FIGURE 2.10: The scattering amplitude and fit with the effective range expansion, defined in Eq. 2.30, at low k^*.

Potential type	a_0 [fm]	d_0 [fm]
Attractive	3.21 ± 0.12	5.96 ± 0.16
Attractive + Bound state	-6.16 ± 0.02	2.83 ± 0.26
Repulsive	-0.98 ± 0.01	-5.14 ± 4.40

TABLE 2.1: Scattering parameters for different types of potentials.

This function is used to extract the s-wave scattering parameters of a given strong interaction potential. Figure. 2.10 shows the scattering amplitude for the same Yukawa-type potentials used previously in this chapter, as well as a fit with Eq. 2.30 at low k^*. The resulting scattering parameters are listed in Tab. 2.1.

So far, all examples discussed in this section were restricted to the real number set. However, the potentials and scattering parameters are complex and can have a non-negligible imaginary contribution, which accounts for inelastic scattering, decay, or absorption processes.

2.3.3 Bound states and the scattering matrix

This last section focuses on bound states, which are especially relevant for the analysis presented in chapter 5. Following the discussion in the previous sections, a two-body interaction that is attractive enough to support the formation of a bound state is characterized by a negative scattering length $a_0 < 0$. The corresponding correlation function can take values below unity at low k^*, which is the typical behavior expected for repulsive interaction potentials.

In general, two particles can form a bound state if the SE allows for a solution with discrete energy $E < 0$. For $r^* > R$, the radial SE is given by

$$u''(r^*) = -\frac{2\mu E}{\hbar} u(r^*) = \kappa^2 u(r^*). \tag{2.31}$$

A solution that also satisfies the condition that $u(r^* \to \infty)$ is finite, is given by

$$u(r^*) \propto \exp\left(-\kappa r^*\right). \tag{2.32}$$

The inside solution for a bound state with negative but small E is essentially the same as for scattering with zero kinetic energy. Therefore, the logarithmic derivatives of the corresponding outside solutions Eq. 2.32 and 2.26 have to match at $r^* = R$. Hence,

$$-\frac{\kappa e^{i\kappa}}{e^{i\kappa}}\bigg|_{r^*=R} = \frac{1}{r^*+a}\bigg|_{r^*=R}. \tag{2.33}$$

For $R \ll a$, it reduces to $\kappa = 1/a$ and the binding energy is given by

$$E_{\mathrm{BE}} = -\Re(E) = \frac{\hbar^2\kappa^2}{2\mu} \approx \frac{\hbar^2}{2\mu a^2}. \tag{2.34}$$

As there is no incident wave in the case of a bound state, the ratio in Eq. 2.19 is infinite and $S_0(k^*) \to \infty$ leading to a pole in the scattering matrix. From the relation given by Eq. 2.23 it can be seen that the pole appears if the denominator of the scattering amplitude vanishes. From Eq. 2.22 and 2.27 one obtains

$$f_0(k^*) = \frac{1}{1/a_0 - ik^*}, \tag{2.35}$$

resulting in a pole at $k^* = i/a_0 = i\kappa$. Using the effective range expansion Eq. 2.29 instead, one obtains

$$k^* = i\kappa = \frac{i}{d_0}\left(1 \pm \sqrt{1+2\frac{d_0}{a_0}}\right) \tag{2.36}$$

and ultimately a binding energy of

$$E_{\mathrm{BE}} \approx \frac{\hbar}{2\mu d_0^2}\left(1 - \sqrt{1+2\frac{d_0}{a_0}}\right)^2. \tag{2.37}$$

This also restricts the relation between the scattering length and effective range to $d_0 > -a_0/2$. Further, the position of the poles of the scattering matrix in the complex momentum (k^*) and energy (E) plane can be used to identify the nature of composite states. The different classifications are shown in Fig. 2.11. Bound and quasibound states are located on the physical sheet of the energy plane, corresponding to $\Im(k^*) > 0$, and are characterized by $\Re(E) < 0$. In the case of a bound state, $\Im(E) = 0$, as the pole in the scattering matrix appears at $k^* = i\kappa$. Virtual states and resonances, on the other hand, are located on the nonphysical energy sheet with $\Im(k^*) < 0$. Further, resonances have $\Re(E) > 0$. The blue glowing line in the momentum plane, corresponding to real $k^* > 0$, represents physical scattering states.

2.3.4 Coupled channels

Coupled channel dynamics emerge whenever particle pairs with similar mass share the same quantum numbers and can transition from one system to the other on- and off-shell. Depending on the coupling strength, these inelastic channels can have a strong effect on the hadron–hadron interaction and the formation of bound or molecular states as well as resonances, hence, altering the shape of the correlation function. As shown in Ref. [89], below-threshold channels might induce an effective attraction, shifting the correlation function upwards. Above-threshold channels, on the other hand, can lead to a cusp structure close to their opening momentum in the

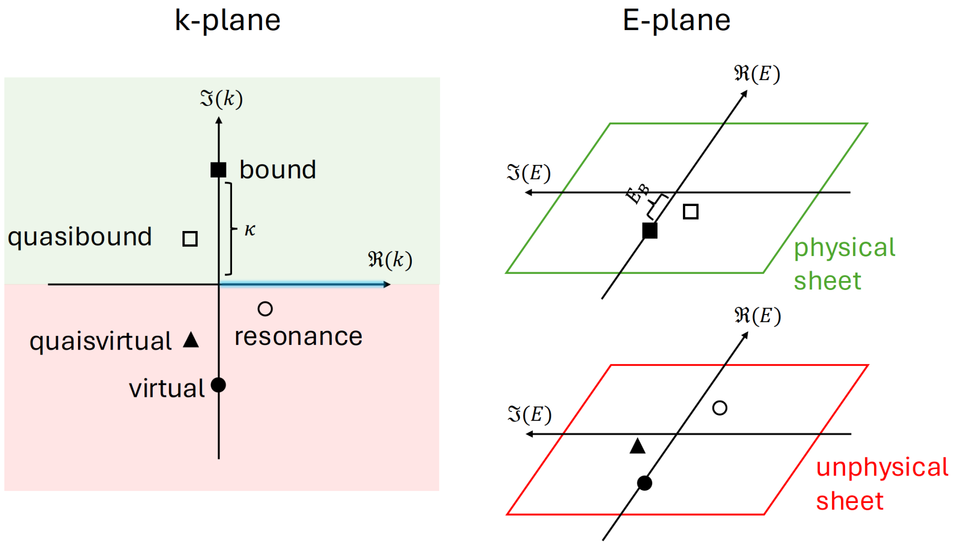

FIGURE 2.11: The complex momentum (*left*) and energy plane (*right*), related via $E = k^{*2}/2\mu$. Figure adapted from a plot seen in Ref. [88].

rest frame of the final state particles, which is given by

$$k^* = \sqrt{\frac{\Delta_i^2 - (m_1 \cdot m_2)^2}{(\tilde{m}_1 + \tilde{m}_2)^2}}, \tag{2.38}$$

where the masses m_j of the particles forming the heavier pair are denoted by tilde and $\Delta_i = \frac{1}{2} \cdot ((\tilde{m}_1 + \tilde{m}_2)^2 - (m_1^2 + m_2^2))$[6]. Therefore, coupled channel dynamics can be crucial to correctly interpreting correlation measurements. For a given pair i in the final state, Eq. 2.5 can be rewritten as

$$C(k^*) = \int d^3r^* S_i(r^*) |\psi_i(\vec{k^*}, \vec{r^*})|^2 + \int d^3r^* \sum_{j \neq i} \omega_j S_j(r^*) |\psi_j(\vec{k^*}, \vec{r^*})|^2, \tag{2.39}$$

where the sum runs over all inelastic channels j, which couple to the final state. Their contribution to the full correlation function is weighted by ω_j, which is determined by the population of the respective initial state. As the relevant coupled channels are close in mass, $S_j(\vec{r^*}) \approx S_i(\vec{r^*})$. The wave functions are constrained by the outgoing boundary condition, where the outgoing wave of the measured channel i is normalized and determined by the coupled-channel Schrödinger equation

$$\begin{pmatrix} \mathcal{H}_{11} & \mathcal{H}_{12} & \dots & \mathcal{H}_{1M} \\ \mathcal{H}_{21} & \mathcal{H}_{22} & \dots & \mathcal{H}_{2M} \\ \vdots & \vdots & \ddots & \vdots \\ \mathcal{H}_{M1} & \mathcal{H}_{M2} & \dots & \mathcal{H}_{MM} \end{pmatrix} \begin{pmatrix} \psi_1(\vec{k^*}, \vec{r^*}) \\ \psi_2(\vec{k^*}, \vec{r^*}) \\ \vdots \\ \psi_M(\vec{k^*}, \vec{r^*}) \end{pmatrix} = E \cdot \begin{pmatrix} \psi_1(\vec{k^*}, \vec{r^*}) \\ \psi_2(\vec{k^*}, \vec{r^*}) \\ \vdots \\ \psi_M(\vec{k^*}, \vec{r^*}) \end{pmatrix}, \tag{2.40}$$

where the elements $\mathcal{H}_{ij}$ of the Hamiltonian matrix give the transition from state i to j. The diagonal terms account for elastic processes, while the off-diagonal elements describe inelastic transitions. A detailed explanation of the formalism can be found in Ref. [89]. Typically, only relevant channels close to the threshold that strongly

---

[6] This formula can also be used to determine the position of resonances, which decay into the final state particle pair by replacing $\tilde{m}_1 + \tilde{m}_2$ with the mass M of the respective resonance.

couple to the final state are considered in the calculation. Furthermore, decay effects related to lower-mass channels, that are not explicitly included within Eq. 2.40, might be accounted for by introducing an imaginary part to the interaction potential.

Chapter 3

Experimental Setup

As discussed in the previous chapter, the method of femtoscopy offers a unique possibility to study the interaction among particle pairs involving unstable, exotic species. The Large Hadron Collider (LHC) provides the ideal experimental environment for such studies due to the large collision energy and luminosity, which results in a large data sample that includes a significant amount of rare and heavy particles. The small emission region of $\sim$1 fm, created in pp collisions at the LHC, is another benefit that allows the study of shallow final state interactions. Additionally, the availability of larger colliding systems, such as heavy ions, makes it possible to extend and deepen such studies.

Located at CERN in Geneva in the tunnel of the former Large Electron-Positron collider, the LHC was successfully commissioned in 2010 with a main focus on the Higgs boson, searching for dark matter as well as deepening the understanding of the standard model of particle physics and beyond. While the former was discovered in 2012 [90, 91], the four major experiments at the LHC, ALICE (A Large Ion Collider Experiment), ATLAS (formerly known as A Toroidal LHC Apparatus), CMS (Compact Muon Solenoid), and LHCb (The Large Hadron Collider beauty) have provided results well beyond the original physics program.

Especially ALICE, on whose data this thesis is based, contributed to a better understanding of several QCD-related topics over the past two decades [92]. Not only did it determine parameters of the quark-gluon plasma (QGP) by measuring, for example, particle yields or momentum anisotropies in heavy-ion collisions and studied the evolution of such collisions starting from the initial state, but also inferred observables related to QCD by investigating, among others, final state hadronic interactions employing femtoscopic correlation techniques. For such studies, excellent particle identification (PID) capabilities, especially at low and moderate transverse momentum, are essential, which are unique to ALICE in comparison to the other main experiments at the LHC.

The following sections of this chapter focus on the essential parts of the experimental setup that provided data for the different studies presented in this work. Technical details on the LHC can be found in Sec. 3.1, while ALICE is intensively discussed in Sec. 3.2. The last Sec. 3.3 introduces the resonance-source model in detail, which is directly anchored to ALICE data.

3.1 The Machine

The LHC [93], also referred to as *the machine*, is the most powerful accelerator so far and is designed for a center-of-mass energy of $\sqrt{s} = 14$ TeV and an unprecedented luminosity of $\mathcal{L} = 10^{34}$ cm^{-2}s^{-1}. The high beam intensities needed to achieve this require the LHC to be a particle-particle collider, which can operate with different colliding systems, i.e., pp, p–Pb, and Pb–Pb. The counter-rotating hadron beams circulate in two separate rings by means of superconducting twin-bore magnets inside the tunnel of the former Large Electron-Positron collider (LEP), which has a circumference of 26.7 km and is located at CERN, the European Organization for Nuclear Research.

Due to an incident in one of the main dipole circuits during the first commissioning in 2008 [94], it was decided to operate the LHC during its first data-taking period, the Run-1, with a reduced center-of-mass energies of $\sqrt{s} = 7 - 8$ TeV for pp collisions. After a long shutdown, where parts of the accelerator were upgraded to ensure safe operation at higher energies [95], the LHC Run-2 started in 2015 with a center-of-mass energy of $\sqrt{s} = 13$ TeV. The collider reached and exceeded its design luminosity by a factor of two during this second data-taking period, which ended in 2018. Following another long shutdown, the upgraded LHC started operating again in 2022 with Run-3 and a collision energy of $\sqrt{s} = 13.6$ TeV, aiming for longer luminosity levellings at $\mathcal{L} = 2 \times 10^{34}\ \mathrm{cm}^{-2}\mathrm{s}^{-1}$ with respect to Run-2 [96]. The integrated luminosity recorded by ALICE in pp collisions during the different runs is listed in Tab. 3.1.

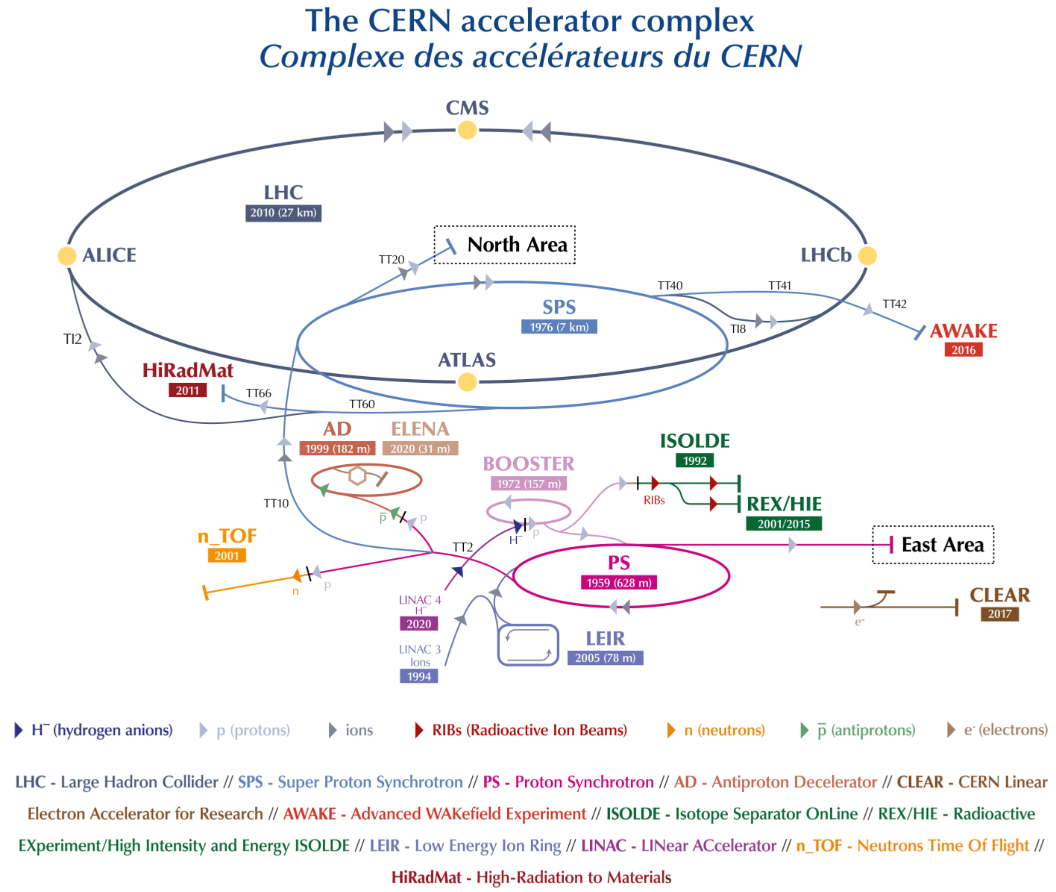

FIGURE 3.1: The CERN accelerator complex with the LHC as the last building block of the injection chain, where protons are accelerated to beam energies of up to 6.8 TeV. Figure taken from Ref. [97].

The large collision energies of the LHC can only be achieved due to a complex accelerator system, which is depicted in Fig. 3.1. Extracted from a hydrogen source via

Run	year	$\sqrt{s}$ (TeV)	$\mathcal{L}_{int}$
1 [98]	2009-2013	0.9	$\sim 200\ \mu\text{b}^{-1}$
		2.76	$\sim 100\ \text{nb}^{-1}$
		7	$\sim 1.5\ \text{pb}^{-1}$
		8	$\sim 2.5\ \text{pb}^{-1}$
2 [98]	2015,2017	5.02	$\sim 1.3\ \text{pb}^{-1}$
	2015-2017	13	$\sim 25\ \text{pb}^{-1}$
3 [99]	2022	13.6	$\sim 19.3\ \text{pb}^{-1}$
	2023		$\sim 9.7\ \text{pb}^{-1}$
	2024		$\sim 45.9\ \text{pb}^{-1}$

TABLE 3.1: Integrated luminosity of pp collision data, collected by ALICE during the different runs.

ionization, protons enter the proton injection chain at the linear accelerator Linac2, which they leave at beam energies of 50 MeV. From there, the particles move through the Proton Synchrotron Booster (PSB) into the Proton Synchrotron (PS), where they are accelerated to energies of 1.4 GeV and 25 GeV, respectively. In the subsequent Super Proton Synchrotron (SPS) the protons reach 450 GeV, before being injected into the LHC. During the magnet ramp, they are accelerated to the final maximum energies required for collisions at the four interaction points (IP), where the produced particles are measured by ALICE, ATLAS, CMS, and LHCb. The proton beams consist of up to 2808 particle packages, so-called bunches, which are spaced by 25 ns and have a maximum proton density of $\sim 1.15 \times 10^{11}$ each.

Lead and other heavy-ions, produced by the electron cyclotron resonance source (ECR), follow a slightly different path upstream of the PS [100], starting with the heavy-ion Linac3 linear accelerator. From there the ions are injected into the Low Energy Ion Ring (LEIR) where they are accumulated and transformed into short, dense bunches before merging with the proton injection chain. Finally, Pb–Pb collisions at $\sqrt{s_{\text{NN}}} = 5.02$ TeV were obtained at the LHC during Run-2, with luminosities of $\mathcal{L} = 10^{27}\ \text{cm}^{-2}\text{s}^{-1}$.

3.2 ALICE

The "dedicated heavy-ion experiment" of the LHC is designed to perform at high particle multiplicities up to $\mathrm{d}N_{ch}/\mathrm{d}\eta \approx 8000$ and cover a wide momentum range, where excellent PID is required. Before Run-3, it operated at lower intensities and readout rates than the high-luminosity LHC experiments ATLAS and CMS. During the last long shutdown, the detector was upgraded, leading to readout rates compatible with those of the other experiments. However, as this thesis is based on data measured during the Run-2, the focus will lie on the corresponding version of the experimental apparatus. Section 3.2.1 concentrates on the detector and its main sub-modules, while the data reconstruction and structure are described in Sec. 3.2.2.

3.2.1 The Detector

The ALICE detector, which has the dimensions $16 \times 16 \times 26$ m^3 and weighs around 10,000 t, is located at IP2 of the LHC in France. It comprises 19 sub-modules, depicted schematically in Fig. 3.2. A detailed description of the apparatus and its performance can be found in Ref. [101–104].

The central barrel part covers pseudorapidities[1] of $|\eta| < 0.9$ and the full azimuth and is enclosed in a large solenoid magnet that delivers a magnetic field up to $\mathrm{B} = 0.5$ T parallel to the beam direction. It includes several detectors, which are radially layered around the beam pipe, starting with the Inner Tracking System (ITS). The ITS is a six-layer silicon detector, which is used to reconstruct the primary collision vertex, as well as tracking and PID. It is followed by a large, gas-filled volume, the Time Projection Chamber (TPC). Together with the ITS it is the main charged-particle tracker of ALICE. Progressing outwards, there is the Transition Radiation (TRD) and the Time of Flight (TOF) detector, which complement the tracking at intermediate momenta and are used for electron and charged-particle PID, respectively. They are followed by the photon spectrometer (PHOS) and the electromagnetic calorimeters (EMCaL), which cover the space in the azimuth and are used to measure jets, photons, neutral mesons, and electrons. Last, there is a High Momentum Particle Identification Detector (HMPID), which extends PID to larger momenta.

While the central barrel detectors measure hadrons, electrons, and photons, muons are detected by means of a large dipole magnet and a set of forward detectors, which cover a pseudorapidity region of $-4.0 < \eta < -2.5$. The Photon Multiplicity Detector (PMD) and Forward Multiplicity Detector (FMD) are also located in the forward direction and are used to measure photons and charged particles. Also, the V0, T0, and two sets of Zero-Degree Calorimeters (ZDC) belong to this category. The former is used for trigger purposes and to characterize an event in terms of multiplicity and centrality; The T0 detector provides information on the timing of the collision as well as its position in beam direction; And the latter is employed to determine the centrality of the collisions and to reject out-of-bunch interactions by detecting spectator neutrons. Finally, the ACORDE scintillators on top of the scintillator are used to trigger cosmic rays.

In the following paragraphs, more detailed information will be provided on the ALICE detectors relevant to this work.

Trigger System

The ALICE trigger system is used to optimize the number of selected events and pick the most interesting collisions to study. It consists of a hardware trigger, called the Central Trigger Processor (CTP), and the software-based High-Level Trigger (HLT) [101, 104].

The trigger decision of the CTP is based on information about the LHC bunch-filling scheme to suppress background, as well as signals from various fast-responding detectors, the most important of which is the V0. This detector consists of two arrays of scintillators located on opposite sides of the nominal vertex (z=0) and segmented into four rings in radial direction. While V0-A lies at $z = 329$ cm, covering backward-pseudorapidities of $-3.7 < \eta < -1.7$, the 4 rings of V0-C are positioned within a range of $z \in [-88, -86]$ cm, leading to a pseudorapidity-coverage

---

[1] The pseudorapidity η is defined as $\eta = -\ln\left[\tan\theta/2\right]$, with θ the polar angle. It is used to describe the angle of a particle relative to the beam axis z.

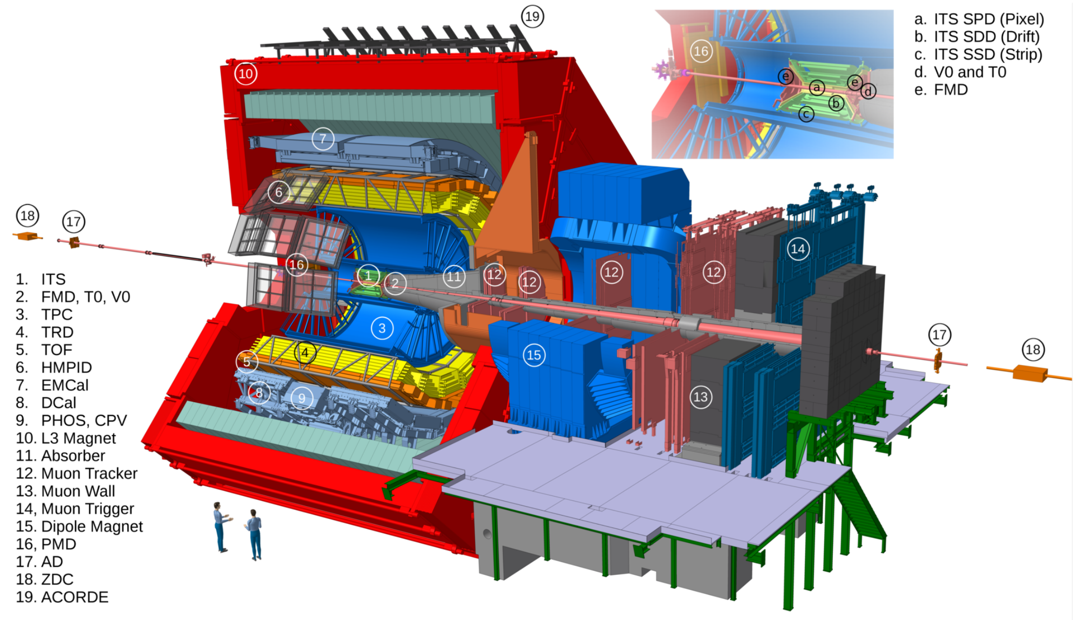

FIGURE 3.2: Schematic representation of the ALICE detector during the LHC Run-2 data-taking period. Figure taken from Ref. [105].

of $2.8 < \eta < 5.1$ [106] in forward direction. The main function of the detector system is being a trigger source, however, it is also used to determine basic event characteristics like charged-particle multiplicity and centrality via the V0 amplitude, which is related to the energy deposit in the scintillators.

The HLT provides online processing to select interesting events and physics regions as well as to reduce their size by means of compression algorithms that are designed to preserve only relevant physics information.

Several trigger classes are available. The minimum-bias (MB) trigger is specifically designed to not introduce a physics bias on the recorded event while ensuring good background rejection. Additionally, a set of rare triggers is available to study special physics cases, which have a much lower rate. The high-multiplicity (HM) trigger for pp collisions is especially interesting for this analysis, as it leads to a larger number of reconstructed particle pairs per event. The triggered events are characterized by on-average 30 charged particles emitted in the pseudorapidity range of $|\eta| < 0.5$ and correspond to the 0.17% of events with the highest V0 amplitude and at least one charged track in the range of $|\eta| < 1$ [50]. Additionally, it was observed that there is enhanced production of particles with hidden and open strangeness as well as charm in events with high particle multiplicities [107, 108].

Inner Tracking System

The ITS is used to determine the primary interaction vertex (PV) as well as the secondary decay vertices of, for example, charm and beauty hadrons with high precision. This is achieved by a low material budget and high spacial resolution both in $r\phi$ and z direction of up to 12 µm and 25 µm [101]. Moreover, it complements the TPC in terms of tracking and PID in the low momentum region, below 200 MeV, improving the resolution of the reconstructed tracks [101, 109].

The ITS surrounds the beam pipe and consists of 3 sets of silicon detectors, each of which is composed of two cylindrical layers located at a radial distance of

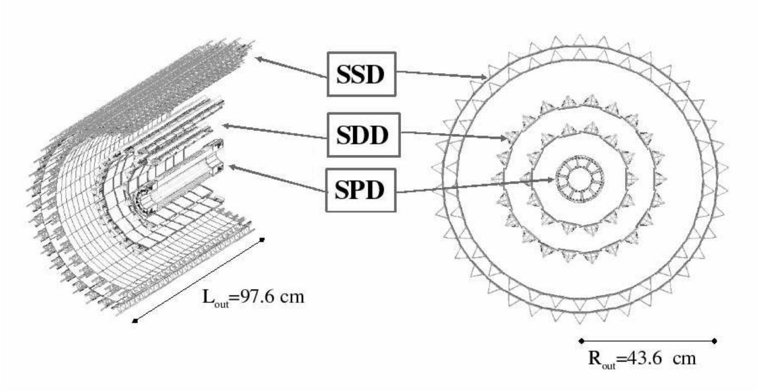

FIGURE 3.3: Schematic view of the ALICE ITS. Figure taken from Ref. [101].

$r = 3.9 - 43.0$ cm [101] from the beam axis. A schematic representation of the detector is shown in Fig. 3.3. The position of the innermost layer is constrained by the size of the beam pipe, while the outermost layer is placed such as to allow efficient track-matching with the TPC. Silicon-pixel detectors (SPD) are chosen as the first two layers to cope with the high particle density in this region. In particular, the first layer has a larger pseudorapidity coverage of $|\eta| < 1.98$ with respect to the other ITS layers and central barrel detectors to provide a continuous coverage for measurements of the charged-particle multiplicity together with the FMD. It is also used as a first-level trigger. The two intermediate layers of the ITS consist of Silicon Drift Detectors (SDD), while the two outer layers are equipped with double-sided Silicon Micro-Strip Detectors (SSD). Both the SDD and SSD layers are used for PID via ionization energy-loss $\mathrm{d}E/\mathrm{d}x$ in the non-relativistic region. In order to cover the full azimuth, the drift and strip detectors slightly overlap.

Time Projection Chamber

The TPC is the main charged-particle tracker of ALICE and provides essential information for PID and good momentum resolution over a large p_{T} range, from 0.1 GeV/c to 100 GeV/c [101]. As a central barrel detector, it covers the full azimuth and pseudorapidities of $|\eta| < 0.9$.

The TPC consists of a field cage, shaped like a hollow cylinder with an inner radius of 85 cm and an outer radius of 250 cm, as well as a length of around 500 cm in beam direction. Its axis is parallel to the magnetic field created by the solenoid magnet. The field cage, depicted schematically in Fig. 3.4, encloses a volume of 90 m^3 and is filled with a Ne–$\mathrm{CO_2}$–$\mathrm{N_2}$ gas mixture [101]. It creates a uniform electrostatic field on either side of the central electrode, which is used to transport electrons from ionization processes caused by charged particles passing through the volume to the respective end plates, where the readout chambers are installed. Each end-plate consists of 18 sectors, radially separated into an inner and outer readout chamber (IROC and OROC, respectively), whose design is based on multi-wire proportional chambers (MWPCs) with pad readout. They consist of a grid of anode wires running in azimuthal direction above a pad plane, followed by a cathode-wire grid and a gating grid. In the vicinity of the anode wire, the field strength increases and the ionization electrons become themselves energetic enough to ionize the surrounding gas, thereby creating an avalanche of electrons and positive ions. While the electrons are immediately absorbed by the anode wire, the slower-drifting ions move towards

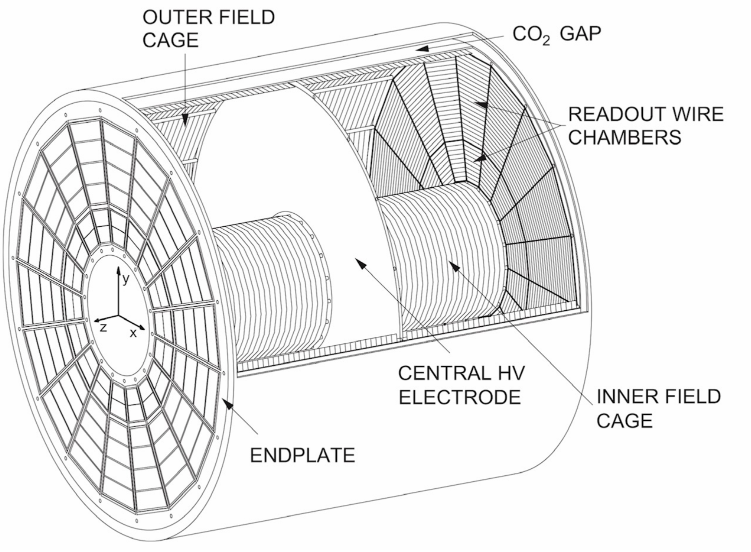

FIGURE 3.4: The layout of the ALICE TPC. Figure taken from Ref. [110]

the cathode grid where they are absorbed as well[2]. As the instantaneous current induced by charge carriers on an electrode depends on their velocity [111, 112], the signal is dominated by ions, which induce mirror charges on the pad plane. If the signals induced on the cells of a given pad row exceed a certain threshold and fulfill the necessary quality criteria, they are combined to form a so-called cluster.

The IROCs and OROCs consist of 63 and 96 pad rows, respectively, which results in approximately 560,000 readout channels. This ensures a low occupancy and sufficient $\mathrm{d}E/\mathrm{d}x$ and position resolution [110].

The particle trajectory in the TPC is reconstructed on the transverse plane from the measured clusters, which can not exceed a total of 159, corresponding to the number of pad-rows in a given TPC sector. By additionally considering timing information, the z-position can be determined, leading to a three-dimensional track.

Particle identification can be performed by simultaneously measuring the momentum p and the specific energy-loss $\mathrm{d}E/\mathrm{d}x$ of a particle of charge ze due to collisions with the drift gas molecules. While p can directly be determined from the bending radius r of the track in the magnetic field B via $r = p/Bze$, the specific energy loss can be obtained from the charge associated with the individual clusters of a track.

Further, the energy-loss is related to the particle velocity β via the Bethe Bloch formula [114]

$$-\frac{\mathrm{d}E}{\mathrm{d}x} = \frac{4\pi n z^2}{m_e c^2 \beta}\left(\frac{e^2}{4\pi\epsilon_0}\right)^2 \left[ln\left(\frac{2m_e c^2\beta^2}{I\cdot(1-\beta^2)}\right)-\beta^2\right], \tag{3.1}$$

where n is the electron number density and I the mean excitation level. Hence, the particle's species can be determined from its mass $M = p/\beta\gamma$ by measuring the momentum and energy loss associated with its track.

Figure 3.5 shows the specific energy loss of different species within the TPC as a function of the momentum, together with a parameterization of the Bethe-Bloch

---

[2] This process can only happen while the gating grid is open for the duration of a drift-time interval of $\sim$ 90 µs upon a trigger signal. Afterwards, the gating grid closes again and ensures that remaining ions cannot drift back into the drift volume, causing severe perturbations of the field.

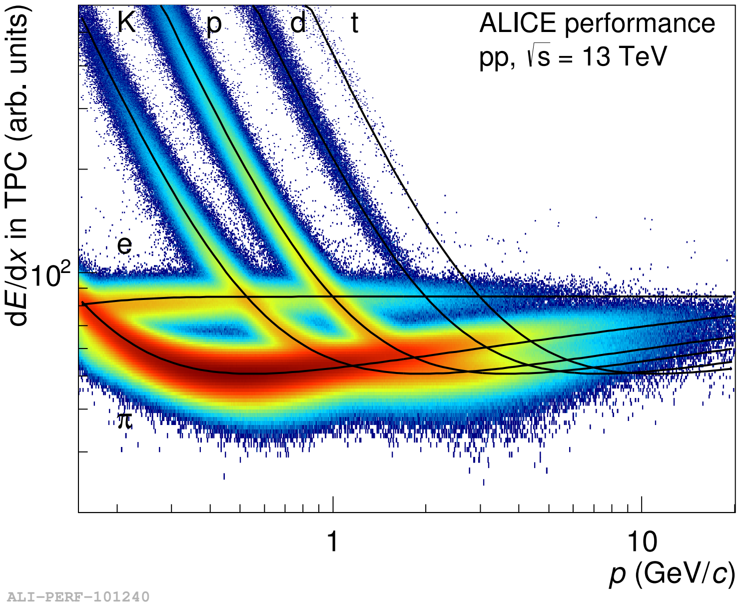

FIGURE 3.5: The energy loss of particles in the TPC as a function of the momentum p, measured in pp collisions at $\sqrt{s} = 13$ TeV. Figure taken from Ref. [113].

formula [115]. The deviation between an experimental measurement and mass hypothesis for particle species in terms of the detector resolution σ defines the so-called $n_{\sigma,i}$ value [104]

$$n_{\sigma,\mathrm{TPC}} = \frac{\mathrm{d}E/\mathrm{d}x_{\mathrm{measured}} - \langle \mathrm{d}E/\mathrm{d}x \rangle_{\mathrm{expected}}}{\sigma}. \tag{3.2}$$

The smaller this value is for a specific mass hypothesis, and the larger it is for the other possibilities, the more likely it is that the particle is correctly identified.

Time of Flight

The TOF is a large area array used for tracking and PID in the intermediate momentum range up to 2.5 GeV/c [101]. It consists of 1593 Multigap Resistive Plate Chambers (MRPC) stacks, which are embedded in a cylindrical shell that surrounds the beam axis and has an inner radius of 370 cm and an outer one of 399 cm. It covers the full azimuth and pseudorapidities $|\eta| < 0.9$ and has a total active area of 141 cm^2.

The MRPCs are composed of two stacks, each of which consists of 6 glass plates, separated by five gas-filled gaps of equal size [101]. The internal resistive plates are electrically floating, while electrodes are placed on the surfaces of the outermost plates of each stack. A high voltage is applied at these electrodes, which leads to a high and uniform magnetic field over the full sensitive gaseous volume of the detector, triggering an immediate electron avalanche from any ionization produced by a traversing charged particle. While the avalanches are confined within the gaps, they create fast signals to which the resistive plates are transparent. Therefore, the induced signal on the external electrodes is the sum of the activities within all the gaps, leading to a high efficiency.

The narrow gap-width of 250 μm leads to a good time resolution of around 80 ps [101] and a precise measurement of the arrival time t_{TOF} of the particles, which makes it suitable for time-of-flight based PID. For this, the event time t_{event} has to be known as well. Ideally, it is provided by the T0, which is part of the forward detectors group of ALICE and consists of two arrays of Cherenkov counters located close to the beam on both sides of the interaction point, covering pseudorapidities of $-3.28 < \eta < -2.97$ and $4.61 < \eta < 4.92$, respectively [101]. However, for a fraction of events, no signal is observed, especially in pp collisions. If there are at least three hits in the TOF, the event time is estimated using an algorithm that compares the measured t_{TOF} with the expected arrival times assuming a common t_{event} [116]. If none of the previous methods is available, an average start time for the run is used.

From the measured time-of-flight, $\tau = t_{\mathrm{TOF}} - t_{\mathrm{event}}$, the mass M of the particle can be determined via [103]

$$M = \frac{p}{\beta\gamma} = p\sqrt{\frac{(c\tau)^2}{L^2} - 1}, \tag{3.3}$$

where L is the reconstructed length of the trajectory and p is the track momentum, which has to be provided by another detector, e.g., the TPC. Figure 3.6 shows the PID capabilities of the TOF; especially at low momentum, a good separation between protons and kaons is obtained. The PID for a specific particle hypothesis is estimated by [116]

$$n_{\sigma,\mathrm{TPC}} = \frac{\tau - t_{\mathrm{expected}}}{\sigma}, \tag{3.4}$$

where σ is the detector resolution.

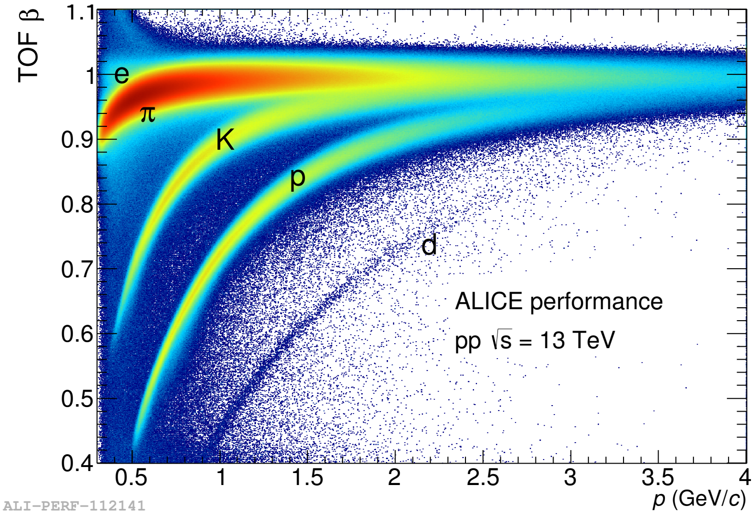

FIGURE 3.6: The velocity β, obtained with the TOF, as a function of the TPC momentum. Figure taken from Ref. [117].

3.2.2 Data reconstruction and structure

The ALICE data flow starts with the detector readout and data recording based on the decision provided by the ALICE trigger system. The raw data is then prepared for track reconstruction by combining signals measured in the individual detectors to clusters with specific positions, amplitudes, etc. [104].

Next, the preliminary vertex of the primary interaction is determined as the point where the largest amount of tracklets, built from clusters in the two innermost layers of the ITS, converge. Then, the track finding is performed by means of the Kalman-filtering approach [118], starting from the outermost layers of the TPC, proceeding

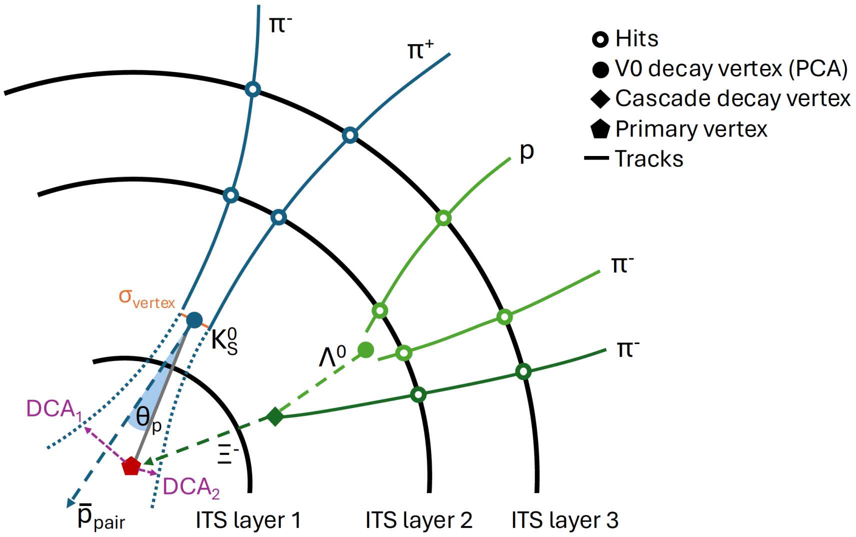

FIGURE 3.7: Illustration of a V_0 ($\mathrm{K}^0_\mathrm{s} \to \pi^+\pi^-$) reconstruction and selection in blue, as well as the reconstruction of a cascade baryon ($\Xi^- \to \Lambda^0\pi^- \to (\mathrm{p}\pi^+)\pi^-$), decaying into a V_0 and another charged particle in green.

inwards, where the reconstructed tracks are matched with clusters in the ITS. As the reconstruction efficiency of the TPC drops significantly for low p_T, an ITS standalone track-finding is performed with the clusters not used in the TPC-ITS matching. Next, the tracks are refitted in the backward direction, using the previously found clusters. When reaching the outermost layer of the TPC, they are matched to TRD tracklets, followed by a matching to clusters in the TOF. The tracks are further propagated and matched with signals in the EMCal, PHOS, and HMPID. Finally, a refit is performed starting at the outer radius of the TPC. During all these steps, starting with the local clusterization, calibration processes are performed to correct the data for detector effects.

The global tracks found with TPC and ITS are used to determine the primary vertex with a higher precision than with SPD tracklets alone.

The event reconstruction proceeds with finding secondary vertices from neutral particle decays such as the K^0_S, which is illustrated in blue in Fig. 3.7. This is done by matching all opposite-sign tracks, which exceed a certain minimum distance to the primary vertex (DCA_1 and DCA_2 in the figure), and calculating their point of closest approach (PCA). Due to their decay topology, these particles are also called V_0 candidates and subject to further selections, such as the position of the PCA, the combined distance of closest approach of the daughter tracks to the PCA (σ_vertex) or the angle between the connection line of primary and secondary vertex, and the total momentum vector of the pair $\vec{p}_\mathrm{pair}$, which is also referred to as pointing angle θ_p.

The event reconstruction process is completed by the search for cascades, which are charged resonances, decaying weakly into a V_0 and another charged particle, such as the Ξ^-, illustrated in green in Fig. 3.7. This is done by matching a V_0 candidate, whose invariant mass lies within a certain window, with another secondary track, applying selections on their mutual distance at the PCA, which, in addition, is required to lie outside of a specific cylindrical volume around the primary vertex. More complex secondary vertices are reconstructed later during the analysis.

The information from the reconstruction process is stored in Event Summary

Data (ESD) files, which are compressed to Analysis Object Data (AOD) files by discarding information that is irrelevant for physics analyses, saving computing resources. The analyses are performed by means of the AliRoot framework [119] on the CERN computing grid.

3.2.3 Monte Carlo simulation

Full-scale Monte Carlo (MC) simulations of the ALICE data are available, where the particles produced in the generated collisions are transported through the detector material and reconstructed following the same algorithm as for raw data. These simulations are anchored to specific data-taking periods in order to reproduce the exact experimental conditions in the simulation.

ALICE provides multiple sets of such simulations. The ones used in this thesis are produced by the event generator PYTHIA 8 [120] with the Monash-2013 tune, while the transport through the detector material is simulated with GEANT 3 [121]. An additional selection on large charged-particle multiplicities is applied to emulate the HM-triggered data sample.

Analyses involving heavy-flavor particles need a specific set of heavy-flavor enriched simulations (HF MC) to obtain a sample with sufficiently large statistics. These simulations require at least one $\mathrm{c\overline{c}}$ or $\mathrm{b\overline{b}}$ pair to be present in each generated pp event. Additionally, the heavy-flavor particles are forced to decay in the hadronic channel of interest for the analysis, which in this case is $\mathrm{D}^+ \rightarrow \mathrm{K}^-\pi^+\pi^+$, with a branching ratio of $\mathrm{BR} = (9.38 \pm 0.15)\%$ [122].

3.3 The resonance-source model

In order to study unknown residual FSI using the femtoscopy method via Eq. 2.5, the particle emission has to be well understood, in particular, the effect of short-lived strongly-decaying resonances.

This section focuses on the resonance-source model (RSM) [123], which is anchored to p–p correlation data, measured with ALICE in HM pp collisions at $\sqrt{s} = 13$ TeV. It is based on the assumption that all primordial particles[3] and resonances are emitted at the same time from a common Gaussian core source. Further, strongly decaying resonances with $c\tau \lesssim \langle 5\ \mathrm{fm}\rangle$ are not expected to live long enough to significantly modify the relative momentum via FSI with other particles.

By considering the different origins of the particles, the source of the two final state particles forming the pair of interest can be decomposed as [123]

$$S(r^*) = \omega_{P_1P_2} \times S_{P_1P_2}(r^*) + \omega_{\tilde{P}_1P_2} \times S_{\tilde{P}_1P_2}(r^*) + \omega_{P_1\tilde{P}_2} \times S_{P_1\tilde{P}_2}(r^*) + \omega_{\tilde{P}_1\tilde{P}_2} \times S_{\tilde{P}_1\tilde{P}_2}(r^*), \tag{3.5}$$

where $\omega_{\tilde{P}_{1(2)}} = 1 - \omega_{P_{1(2)}}$ denotes the fraction of secondary particles $\tilde{P}_{1(2)}$ originating from short-lived resonances and $\omega_{P_{1(2)}}$ the fraction of primordial particles $P_{1(2)}$, both anchored to the yields expected by the Statistical Hadronization model (SHM) [124]. $S_{ij}(r^*)$ denotes the corresponding sources. In particular, $S_{P_1P_2}(r^*)$ is the Gaussian core source, while the others include resonance contributions to one or both final state particles. The $\tilde{P}_1\tilde{P}_2$ case is illustrated in Fig. 3.8. The emission points of the primordial mothers are separated by $\vec{r}^{\,*}_{\mathrm{core}}$, while the final state particles are separated

---

[3] Primordial particles are directly created in the hadronization process, and do not stem from an intermediate decay.

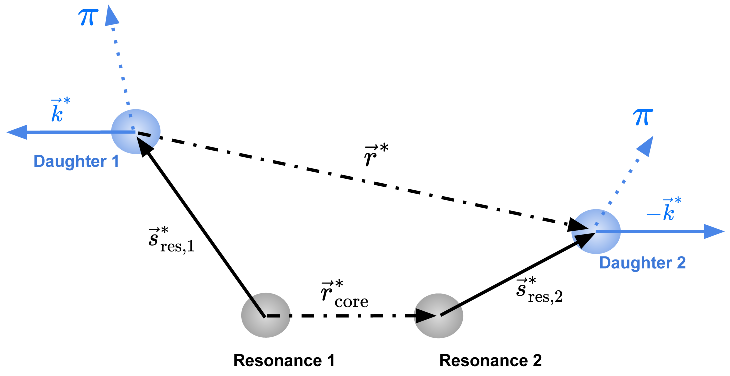

ALI-PUB-483606

FIGURE 3.8: Illustration of the modification of $\vec{r}^*_{\mathrm{core}}$ to $\vec{r}^*$ due to the decay of resonances (gray disks), feeding into the final state particles of interest (blue disks), which have momenta $\vec{k}^*$. The chosen coordinate system is the rest frame of the daughters and marked with an asterisk. Figure taken from Ref. [123].

Pair	FSI		
	strong	Coulomb	QS
pp	Argonne v_{18} [12]	√	√
pΛ	χEFT at LO [127] and NLO [128]	-	-
$\pi^+\pi^+$	-	√	√
K$^+$p	χEFT [79, 129]	√	-

TABLE 3.2: Details on the FSI used to model the correlation functions of the particle pairs that benchmark the RSM.

by $\vec{r}^*$, which is given by

$$\vec{r}^* = \vec{r}^*_{\mathrm{core}} - \vec{s}^*_{\mathrm{res},1} + \vec{s}^*_{\mathrm{res},2}, \tag{3.6}$$

where $\vec{s}^*_{\mathrm{res},1(2)}$ is the distance traveled by each resonance. It is linked to the flight time $t_{\mathrm{res},1(2)}$ of the individual resonance via

$$\vec{s}^*_{\mathrm{res},1(2)} = \vec{\beta}^*_{\mathrm{res},1(2)}\gamma^*_{\mathrm{res},1(2)}t_{\mathrm{res},1(2)} = \frac{\vec{p}^*_{\mathrm{res},1(2)}}{M_{\mathrm{res},1(2)}}t_{\mathrm{res},1(2)}, \tag{3.7}$$

where $\vec{p}^*_{\mathrm{res},1(2)}$ is the momentum and $M_{\mathrm{res},1(2)}$ the mass of the respective resonance. The flight time $t_{\mathrm{res},1(2)}$ is sampled from an exponential distribution based on the lifetime $\tau_{\mathrm{res},1(2)}$ of the resonance, which is obtained from its measured width [122]. In the RSM, the average masses and lifetimes of the resonances feeding into the final state particles predicted by the SHM are used in order to save computation time. Finally, the source of final state particles $S(r^*)$ is obtained from MC simulated collisions and resonance decays with EPOS [125], following simple phase-space rules.

The RSM was then applied in the modeling of the experimental correlation functions of several particle pairs for which the residual strong interaction is well known [123, 126] in order to study the particle emitting core. The investigated pairs are listed in Tab. 3.2 with details on the employed FSI. In the case of π^+–π^+, two different versions of the non-femtoscopic background were tested, namely polynomials of first and second order.

These studies were performed m_{T}-differentially on data measured by ALICE in

HM pp collisions at $\sqrt{s} = 13$ TeV. The resulting r_{core} is shown in Fig. 3.9. In the low-m_{T} region, which can only be accessed with π^+–π^+ correlations, the core radius saturates, while for larger values, a scaling is observed, which is common for the investigated meson-meson, meson-baryon and baryon-baryon pairs. The data points for p–Λ are not shown explicitly in the plot, but the pairs experience the same r_{core} scaling [123]. The observed m_{T} dependence of the particle emission size is already known from HIC and is attributed to the collective expansion of the system. However, the exact reason why the phenomenon is also present in pp collisions is still under investigation. An independent and alternative study could relate it to the radial expansion of the system [130].

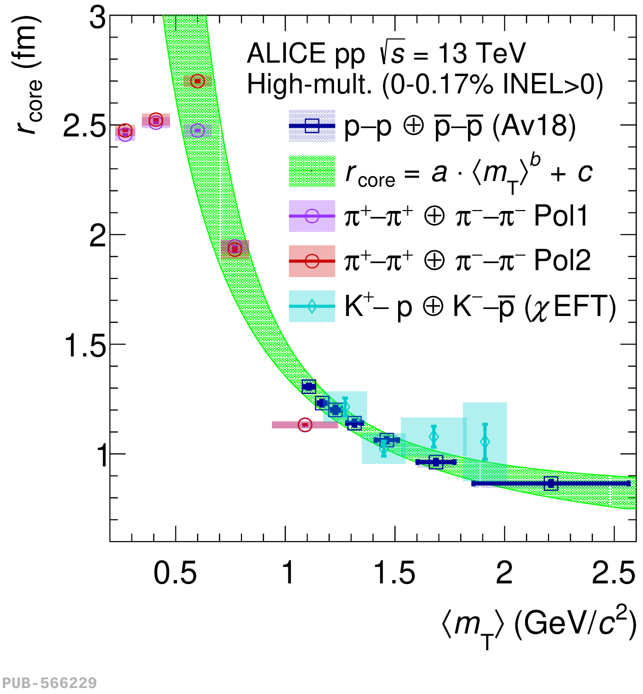

FIGURE 3.9: Radii of the Gaussian core source, extracted by fitting the experimental correlation functions of different particle pairs and transverse masses m_{T}. The green band corresponds to the 3σ spread of the parametrization of the m_{T} scaling of p–p correlations. Figure taken from Ref. [126].

The RMS is essential for femtoscopic analysis performed on pp data measured with ALICE, as it can be used to obtain the effective source of any particle pair by including the relevant resonances in the modeling as well as fixing r_{core} to the value obtained from a parametrization of the p–p data, shown as green band in Fig. 3.9, for the measured pair m_{T}. By constraining the source, the model facilitates experimental access to unknown hadronic interactions by means of the correlation function and femtoscopy method.

Chapter 4

Interaction between D^+ and light-flavor mesons

In the past decades, several new heavy hadron states with charm-quark content have been discovered, some of which cannot easily be accommodated within the quark model [131], like the extremely narrow scalar charm-strange meson $D^*_{s0}(2317)$ [132–134], whose mass lies around 160 MeV$/c^2$ below the prediction. This led to several theories on its nature, some of which propose a tetra-quark state composed of $cq\overline{sq}$ (anti)quarks [135–137]. As it's mass is very close to the DK threshold, the $D^*_{s0}(2317)$ could also be a hadronic molecule with a dominant $D^{(*)}K$ component [138–142], or an admixture of both [143, 144]. Alternatively, the structure can be explained by coupled-channel effects among the $c\bar{s}$ state and the DK continuum [145–151]. To better understand the nature of this exotic state, the D–K scattering has to be studied. Similarly, the properties of the charm-light $D^*_0(2300)$ can be accessed by D–π scattering to shed light on why its mass is close to that of its strange partner $D^*_{s0}(2317)$, although it is expected to be smaller. The same applies to the axial charm-strange $D_{s1}(2460)$ and the non-strange $D_1(2430)$ meson, which also have surprisingly similar masses. Several other heavier exotic hadrons with charm-quark content have been discovered, such as the $\chi_{c1}(3872)$ [152], T^+_{cc} [153, 154], $P_c(4312)$, $P_c(4440)$, and $P_c(4457)$ [146, 155, 156] states. Similar to the $D^*_{s0}(2317)$, these states can be interpreted as compact multiquark states [157–160], or $D\overline{D}^*$, DD^*, or $\Sigma_c\overline{D}$, $\Sigma_c\overline{D}^*$ molecular states due to their proximity to the two-hadron mass threshold, thereby extending beyond the heavy-light-flavor sector.

Besides to better understand the nature of exotic states, the knowledge of the interaction between charm and light-flavor mesons is also relevant for the study of ultrarelativistic heavy-ion collisions (HICs), where a color-confined state of matter, the quark-gluon plasma (QGP), is formed [161–165]. Charm quarks, which are produced in the early stages of collisions in primary hard partonic scattering processes, are ideal probes to infer the properties of the QGP, as they experience the full time evolution of the hot and dense medium. During their propagation in the QGP, they interact with its constituents by exchanging energy and momentum via elastic [166–168] and inelastic processes [169, 170], leaving traces in observables such as the p_T-differential yields, the azimuthal anisotropy or the nuclear modification factor R_{AA} of heavy-flavour hadrons [171, 172]. However, these hadrons will interact with other particles produced in the HIC, which are mainly light-flavor mesons, leading to modifications of their momentum and angular distributions. In order to disentangle such effects from those related to the QGP formation and correctly interpret the data with the available models [173, 174], the interaction between charm and light-flavor mesons, in particular pions and kaons, has to be understood and

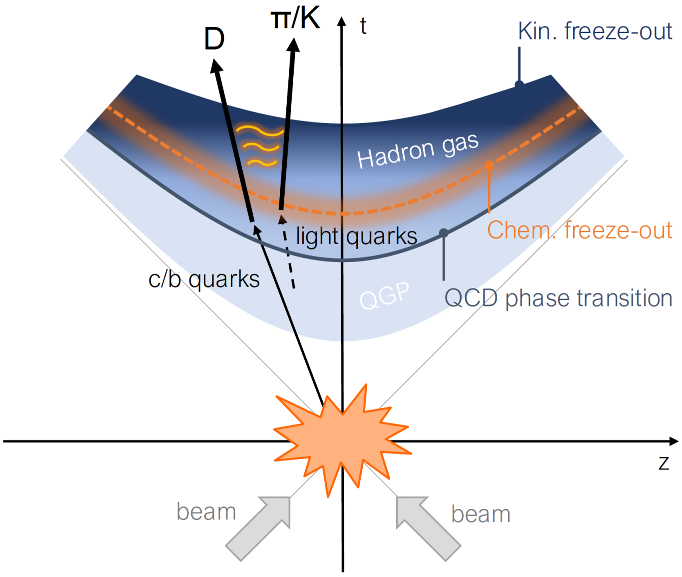

FIGURE 4.1: Illustration of the evolution of a heavy-ion collision with focus on the production of charm quarks in the initial phase of the collision, the subsequent hadronization to D^+ mesons, and their FSI with light-flavor mesons.

the scattering parameters determined. Figure 4.1 illustrates these processes at different stages of the evolution of the HIC, starting with the initial collision at the origin of the *zt*-plane. It is followed by the formation of the QGP, which expands while cooling down until a transition to the hadron gas phase takes place, where hadrons materialize out of quarks and gluons. After the hadronization, the particles can interact inelastically until chemical freeze-out, where the particle composition is settled. Elastic interactions, including rescattering, are, however, still allowed and cease at kinetic freeze-out. After this, the particle momenta are fixed, and the free-streaming hadrons propagate towards the detector.

On the theoretical side, scattering processes involving charm and light-flavour mesons have been extensively studied in the framework of χPT [141, 175, 176]. However, scattering observables such as phase shifts have not yet been measured, as the realization of such experiments is hindered by the extremely short lifetime of hadrons containing heavier quarks. For the time being, the unknown parameters of the theory have to be constrained by simulated LQCD data. In recent years, however, femtoscopy has emerged as a unique method to study such interactions experimentally. In particular, the measurement of the pD^- correlation function [53] marks its first application to the charm sector, demonstrating the feasibility of such studies.

In the following, the first experimental results on the interaction of D^+ mesons with pions and kaons are presented for both the same- and opposite-charge configuration in pp collisions at $\sqrt{s} = 13$ TeV. In Sec. 4.1, the different steps of the data analysis are discussed, with focus on the event and particle selection, followed by Sec. 4.2, where the experimental correlation functions are presented. The decomposition of the raw data is discussed in Sec. 4.3 and Sec. 4.4 focuses on the pair emission. The final results are discussed in Sec. 4.5 and the summary and conclusion can be found in Sec. 4.6. Details on the systematic uncertainties are given in the respective sections.

Selection criterion	Value
Trigger	HM
Physics selection	default
Incomplete DAQ	check
z vertex	$\|vtx_z\| < 10\,\mathrm{cm}$
Contributors to track vertex	$N_{\mathrm{contrib,track}} > 1$
Contributors to SPD vertex	$N_{\mathrm{contrib,SPD}} > 0$
Distance between track and SPD vertex	$d_{\mathrm{vtx,track-SPD}} < 0.5\,\mathrm{cm}$
SPD vertex z resolution	$\sigma_{\mathrm{SPD},z} < 0.25\,\mathrm{cm}$
Pile-up rejection	`AliVEvent::IsPileUpFromSPD()` `AliEventUtils::IsSPDClusterVsTrackletBG()`

TABLE 4.1: Event selection criteria.

4.1 Data Analysis

The analysis is conducted on a data set obtained in pp collisions at $\sqrt{s} = 13$ TeV with ALICE from 2015 to 2018, during the Run-2 data-taking period. The events are selected employing the HM trigger, which is discussed in detail in Sec. 3.2.1. For quality assurance, standard selections on the event properties are applied, which are summarized in Tab. 4.1. The default physics selection rejects events of poor quality and background from the interaction of beam protons with beam pipe material or residual gas present in the pipe. To further ensure the quality of the selected events, the check flag for incomplete data acquisition (DAQ) in AliRoot is required. The distance between the primary vertex reconstructed from at least one SPD tracklet with a resolution below 0.25 cm in z-direction, and the primary vertex obtained from at least two global tracks, which need both ITS and TPC clusters, has to be below 5 mm. Uniform detector coverage is ensured by requiring the primary vertex to lie within 10 cm of the nominal interaction point along the beam direction. Additionally, in order to reject pile-up events, only one primary vertex is allowed to be reconstructed in the SPD. This results in approximately 9.1×10^8 events available for the analysis and the selection of possible pair candidates.

4.1.1 Particle selection

Light-flavor mesons

The selection criteria for pion and kaon candidates are summarized in Tab. 4.2. Global tracks are used for pions, while TPC-only tracks are employed for kaons to increase the yield of reconstructed particles. As shown in [104], the momentum resolution of TPC-only tracks is comparable to that of globally reconstructed tracks since the track fitting is constrained by the primary vertex, which is reconstructed independently. As a cross-check to assess any bias that may arise from this choice, the D–K correlation functions are also studied using global tracks, leading to compatible results within the uncertainties.

A selection on the reconstructed TPC clusters is applied to ensure a good track quality and p_{T}-resolution at large momenta as well as to remove fake tracks from the sample. Tracks for both species are required to be reconstructed from more than 80 clusters in the TPC and have crossed at least 70 out of the total 159 pad rows.

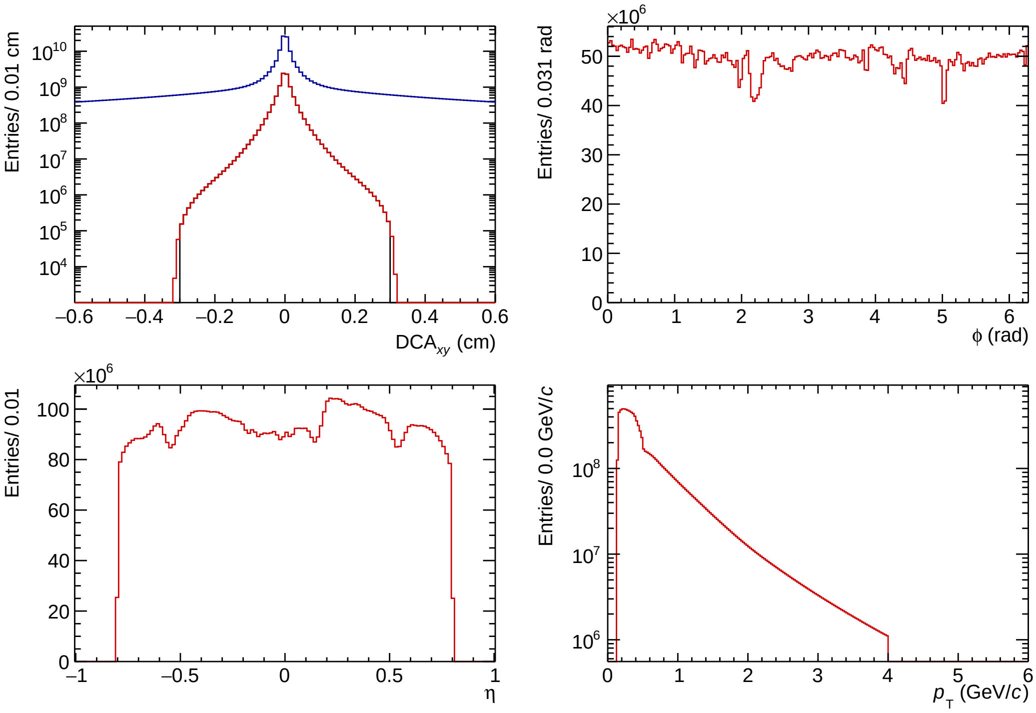

FIGURE 4.2: The *top left plot* shows hte distance of closest approach in the xy-plane for pions. The blue line shows the distribution without any DCA selection, the red one includes the selection on the DCA in beam direction, $|\mathrm{DCAz}\ | < 0.3$ cm, whereas the black one additionally includes $|\mathrm{DCA}xy\ | < 0.3$ cm, which corresponds to the full DCA selection applied on the sample. The *other* histograms show the φ, η, and p_{T} distributions of pion candidates in red, which are needed to construct the particle 4-vector.

Additionally, kaon candidates are rejected if the associated track shares clusters with another one, and the ratio between the number of crossed rows and the number of clusters that can potentially be found has to be larger than 0.8.

To minimize unwanted effects related to the detector acceptance, the light-flavor candidates are selected within $|\eta| < 0.8$. A low transverse-momentum cutoff of $p_{\mathrm{T}} > 0.14$ GeV$/c$ for pions and $p_{\mathrm{T}} > 0.15$ GeV$/c$ for kaons is applied to reduce the number of candidates stemming from interactions with the detector material. An upper limit of $p_{\mathrm{T}} < 4$ GeV$/c$ is imposed to enhance the purity of the candidates, as the separation power for different particle species in the TPC and TOF decreases for large p_{T}. To suppress contributions from weak decays or interactions with the detector material, a selection on the distance of closest approach (DCA) of the tracks to the primary vertex in both the transverse plane xy and z direction along the beam axis is applied. For pions it is $\mathrm{DCA}_{xy,z} < 0.3$ cm, while for kaons it is $\mathrm{DCA}_{xy} < 0.1$ cm and $\mathrm{DCA}_z < 0.2$ cm. The resulting DCA_{xy} distribution is shown in the top left plot of Fig. 4.2 and 4.3, for pions and kaons, respectively.

For particle identification (PID), information provided by the TPC and TOF detectors is used. The selections are based on n_σ, the number of standard deviations of the measured to the expected signal for a specific particle hypothesis at a given momentum, which is described in more detail in Sec. 3.2.1. Depending on the momentum of the candidates and the separation power between different particles hypothesis in the detectors, a selection on $n_{\sigma,\mathrm{TPC}}$ is sufficient, or the combined $n_{\sigma,\mathrm{comb}} = \sqrt{(n_{\sigma,\mathrm{TPC}})^2 + (n_{\sigma,\mathrm{TOF}})^2}$ is used.

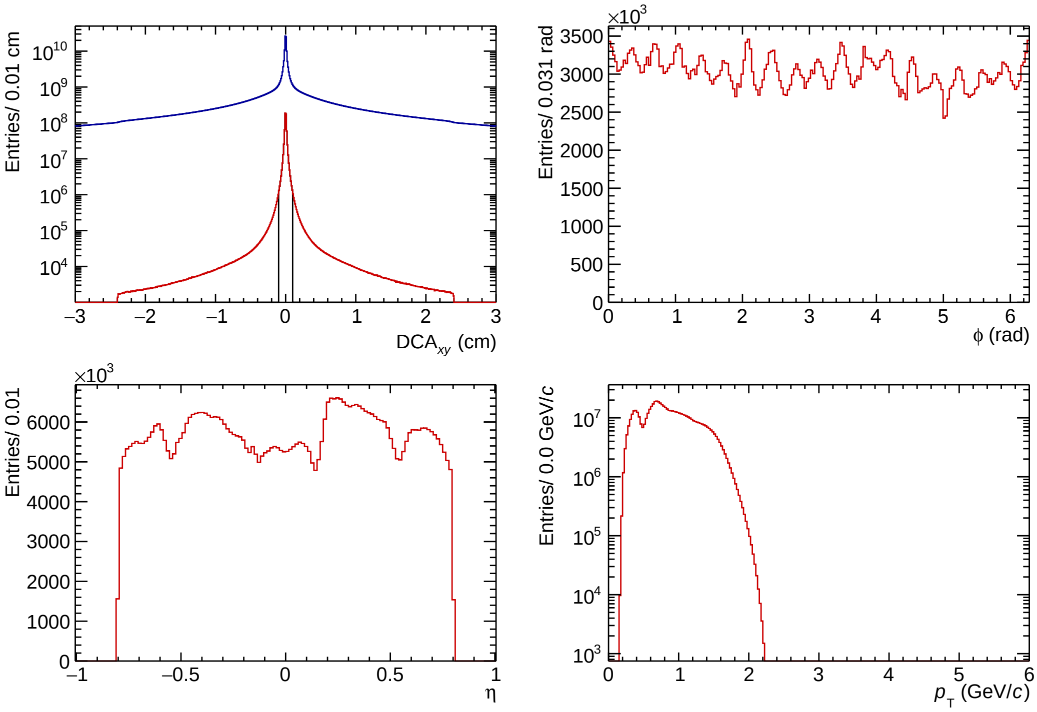

FIGURE 4.3: The *top left plot* shows the distance of closest approach in the xy-plane for kaons. The blue line shows the distribution without any DCA selection, the red one includes the selection on the DCA in beam direction, $|\mathrm{DCA}z\ | < 0.3\,\mathrm{cm}$, whereas the black one additionally includes $|\mathrm{DCA}xy\ | < 0.3\,\mathrm{cm}$, which corresponds to the full DCA selection applied on the sample. The *other* histograms show the φ, η, and p_{T} distributions for kaon candidates in red, which are needed to construct the particle 4-vector.

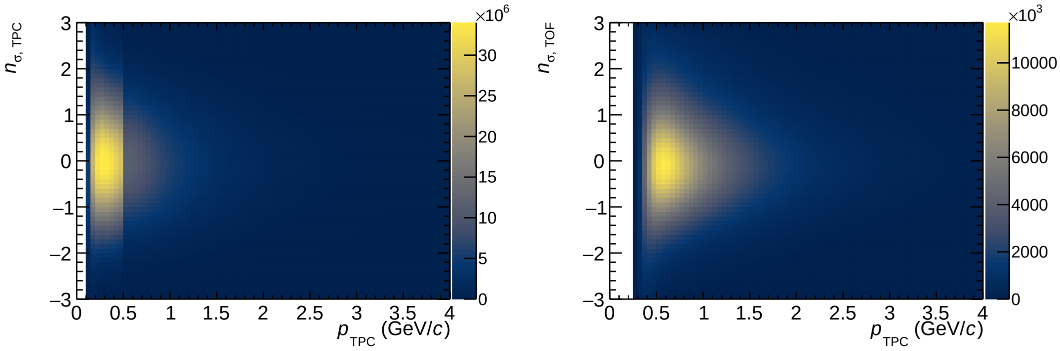

FIGURE 4.4: Particle identification for pions. For $p < 0.5$ GeV/c the specific energy loss information provided by the TPC in form of deviations from the theoretical expectation value is used (n_σ). For $p > 0.5$ GeV/c also, the time-of-flight information provided by the TOF is employed. The *left plot* depicts $n_{\sigma,\mathrm{TPC}}$, while the *right* one shows $n_{\sigma,\mathrm{TOF}}$, both as a function of the momentum measured in the TPC, p_{TPC}.

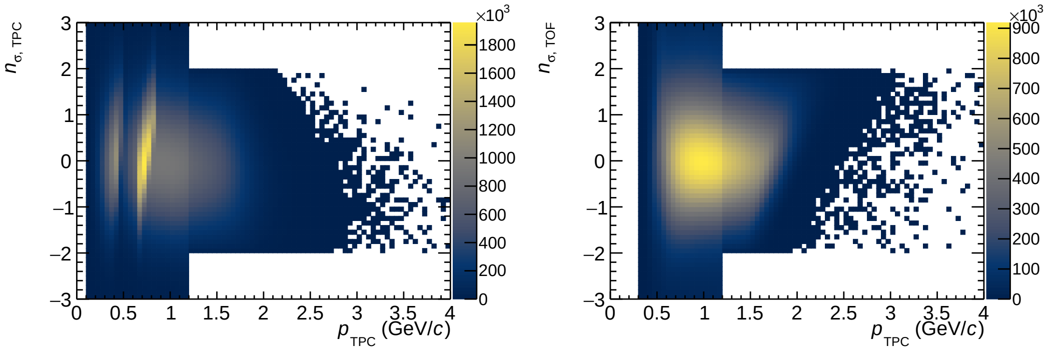

FIGURE 4.5: Particle identification for kaons. The *left plot* depicts $n_{\sigma,\mathrm{TPC}}$ for kaons while the *right* one shows $n_{\sigma,\mathrm{TOF}}$, both as a function of the momentum measured in the TPC, p_{TPC}. They are both used for particle identification.

As can be seen in Fig. 3.5, pions with $p < 0.5\,\mathrm{GeV}/c$ can be well identified from their energy-loss in the TPC with $|n_{\sigma,\mathrm{TPC}}(\pi)| < 3$. For larger momenta, $|n_{\sigma,\mathrm{comb}}(\pi)| < 3$ is required, additionally relying on information on the TOF β. The resulting n_σ distributions in the TPC and TOF are shown in Fig. 4.4.

For kaon identification, a more complex set of selections is applied to increase the yield while maintaining a sufficient purity of the sample. Two different identification methods are used; *Method 1* exclusively relies on the TPC, while *Method 2* also uses the TOF. In order to be accepted, a kaon candidate has to pass any of the two methods. The selections are tuned to minimize contamination from other particle species, in particular electrons ($\mathrm{e}^\pm$), protons (p), and pions (π), and are motivated by the energy-loss curves of different particle species in the ALICE TPC, depicted in Fig. 3.5, as well as the TOF β, shown in Fig. 3.6.

Method 1 is only applied for momenta $p < 0.85$ GeV/c, due to the worsening kaon separation power of the TPC for larger momenta and requires $|n_{\sigma,\mathrm{TPC}}(\mathrm{K})| < 3$. Additionally, the region $p \in [0.5, 0.65]$ GeV/c, where the electron energy-loss curve crosses the kaon curve, is excluded. A possible contamination from pions and electrons is accounted for by requiring $|n_{\sigma,\mathrm{TPC}}(\pi)| > 3$ for $p > 0.5$ GeV/c and

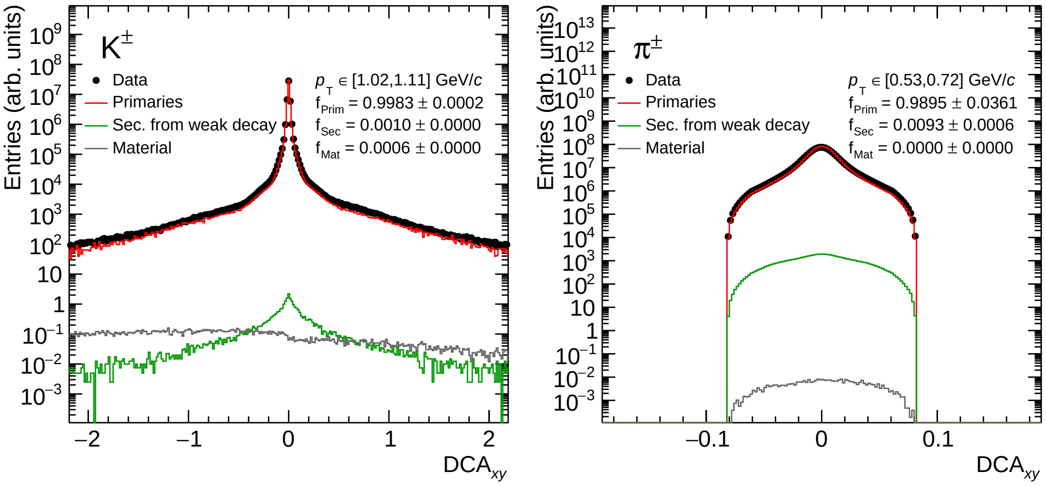

FIGURE 4.6: MC template fit results to the measured DCA_{xy} distribution of K^+ candidates with $p_{\mathrm{T}} \in [1.02, 1.11]$ GeV/c shown on the *left*. The same is shown for π^+ candidates with $p_{\mathrm{T}} \in [0.53, 0.72]$ GeV/c on the *right*.

$|n_{\sigma,\mathrm{TPC}}(\mathrm{e}^{\pm})| > 3$ for $p > 0.3$ GeV/c, which are the momentum regions where the energy-loss curves of the two species approach the kaon curve, as can be seen in Fig. 3.5. *Method 2* uses the combined PID information of TPC and TOF, requiring $|n_{\sigma,\mathrm{comb}}(\mathrm{K})| < 3$ for kaons in the full momentum region. For $p > 1.2$ GeV/c, where the separation power between kaons and pions decreases in the TOF, a tighter selection of $|n_{\sigma,\mathrm{comb}}(\mathrm{K})| < 2$ is applied, while additionally requiring $|n_{\sigma,\mathrm{comb}}(\pi)| < 6$. Figure 4.5 displays the resulting distributions of n_σ. The structure visible around $p_{\mathrm{TPC}} \sim 0.8\,\mathrm{GeV}/c$ in the $n_{\sigma,\mathrm{TPC}}$ histogram arises from the momentum-overlap of *Method 1* and *Method 2*.

The η, ϕ, and p_{T}-distributions of the light-meson candidates, which are the quantities needed to reconstruct the four-momentum, are displayed in Fig. 4.2 and 4.3 after the selections of Tab. 4.2 are applied.

Even though the selections are chosen such as to maximize the amount of primary particles[1], additional contributions from weak decays or interactions with the detector material are present in the light-flavor sample. Information on the origin of the selected π and K is obtained by fitting MC templates of the DCA distributions of the different contributions to the experimental data. These fits are performed for several p_{T} intervals and example plots are shown in Fig. 4.6. The resulting fractions as a function of p_{T} are presented in Fig. 4.7. As can be seen, the fractions only mildly depend on the transverse momentum of the candidates and they are almost identical between particles and antiparticles. Also, the dominant contribution to the sample is primary particles, with $> 99\,\%$.

The purity of the selected particles is obtained from the ratio of correctly identified candidates to misidentified ones, using MC information on the true particle species, and is shown in Fig. 4.8 for both kaons and pions. For kaons, it remains high over the full p_{T} range, while it drops for low-p_{T} pions.

---

[1] According to ALICE definition [177], primary particles are either produced directly in the interaction or in decays of particles with $\tau < 1$ cm/c, excluding particles produced in interactions with the material. By this definition, feed-down from strongly decaying resonances is also part of the primary fraction.

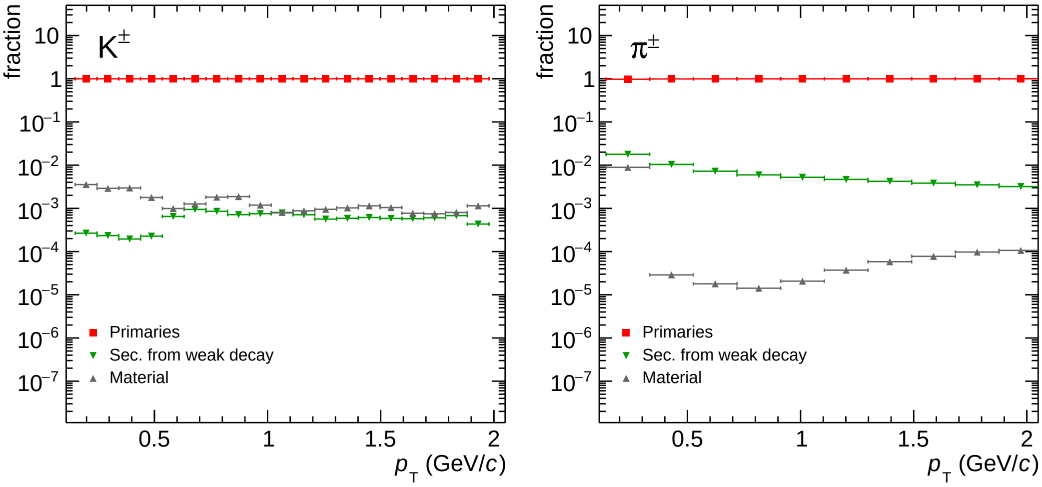

FIGURE 4.7: Contributions from the primary vertex, weak decays and material to the kaon sample on the *left* and to the pion sample on the *right*, shown as function the transverse momentum.

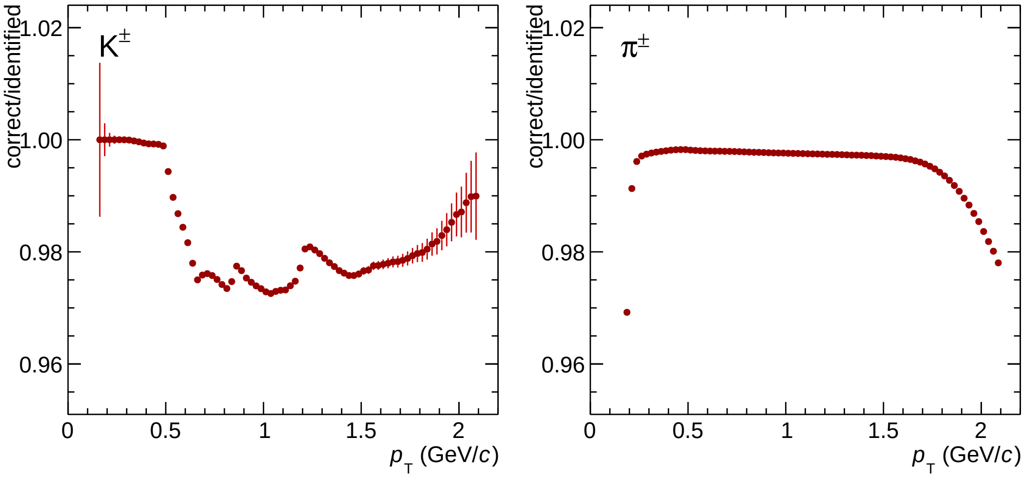

FIGURE 4.8: The purity of the K^+ candidates as function of p_T is depicted on the *left*, while the one of π^+ is shown on the *right*.

Selection criterion	π selections	K selections
Track-type	Global tracks	TPC-only tracks
Pseudorapidity	$\|\eta\| < 0.8$	$\|\eta\| < 0.8$
Transverse momentum	$0.14 < p_{\mathrm{T}} < 4.00\,\mathrm{GeV}/c$	$0.15 < p_{\mathrm{T}} < 4.00\,\mathrm{GeV}/c$
TPC cluster	$n_{\mathrm{TPC}} > 80$	$n_{\mathrm{TPC}} > 80$
Crossed TPC pad rows	$n_{\mathrm{crossed}} > 70$	$n_{\mathrm{crossed}} > 70$
Tracks with shared clusters	n.a.	reject
Ratio crossed rows	n.a.	0.8
DCA xy	$\|\mathrm{DCA}_{xy}\| < 0.3\,\mathrm{cm}$	$\|\mathrm{DCA}_{xy}\| < 0.1\,\mathrm{cm}$
DCA z	$\|\mathrm{DCA}_{z}\| < 0.3\,\mathrm{cm}$	$\|\mathrm{DCA}_{z}\| < 0.2\,\mathrm{cm}$
Particle identification	– $\|n_{\sigma,\mathrm{TPC}}(\pi)\| < 3$ for $p_{\mathrm{T}} < 0.5\,\mathrm{GeV}/c$ – $\|n_{\sigma,\mathrm{comb}}(\pi)\| < 3$ for $p_{\mathrm{T}} > 0.5\,\mathrm{GeV}/c$	*Method 1 (TPC only PID)*: – $p < 0.85$ GeV/c – $p \notin [0.5, 0.65]$ GeV/c – $\|n_{\sigma,\mathrm{TPC}}(\mathrm{K})\| < 3$ – $\|n_{\sigma,\mathrm{TPC}}(\mathrm{e}^{\pm})\| > 3$ for $p > 0.3$ GeV/c – $\|n_{\sigma,\mathrm{TPC}}(\pi)\| > 3$ for $p > 0.5$ GeV/c **OR** *Method 2 (TPC and TOF combined PID)*: – $\|n_{\sigma,\mathrm{comb}}(\mathrm{K})\| < 3$ – $\|n_{\sigma,\mathrm{comb}}(\mathrm{K})\| < 2$ and $\|n_{\sigma,\mathrm{comb}}(\pi)\| > 6$ for $p > 1.2$ GeV/c

TABLE 4.2: Light-flavor meson selection criteria.

TABLE 4.3: Track selection criteria for the D^+-meson daughters.

Selection criterion	Value
Pseudorapidity	$\lvert\eta\rvert < 0.8$
Transverse momentum	$p_{\mathrm{T}} > 0.3$ GeV/c
Crossed TPC pad rows	$n_{\mathrm{crossed}} > 70$ (out of 159)
Findable TPC clusters	$n_{\mathrm{crossed}}/n_{\mathrm{findable}} > 0.8$
χ^2 per TPC cluster	$\chi^2/n_{\mathrm{clusters}} < 4$
ITS hits	at least two and at least one in the SPD layers
Particle identification	$\lvert n_{\sigma,\mathrm{TPC}}(\mathrm{K}/\pi)\rvert < 3$ **OR** $\lvert n_{\sigma,\mathrm{TOF}}(\mathrm{K}/\pi)\rvert < 3$

TABLE 4.4: Preselections used for the reconstruction of D^+ mesons, which depend on the transverse-momentum of the candidates.

Selection criterion	p_{T} interval (GeV/c)	
	$[1,5]$	$[5,10]$
σ_{vertex} (μm)	< 400	< 600
Decay length (μm)	> 300	> 300
$\cos\theta_{\mathrm{p}}$	> 0.85	> 0.75
$\cos\theta_{\mathrm{p}}^{\mathrm{xy}}$	> 0.80	> 0.70

D^+ mesons

The D^+-meson selection follows the approach used in Ref. [53] and developed within the heavy-flavor group of ALICE. The charm particles are reconstructed via the $\mathrm{D}^+ \to \mathrm{K}^-\pi^+\pi^+$ decay channel and its charge conjugate, which have a branching ratio of $\mathrm{BR} = 9.38 \pm 0.16\%$ [122]. In a first step, three correctly charged tracks, which pass the loose preselections reported in Tab. 4.3, are combined to build a D^+ candidate. These tracks are reconstructed with both the ITS and TPC, requiring a minimum of two hits in the ITS, with at least one in the innermost layers, the SPS, to ensure a good pointing resolution. Moreover, selections on the track quality in the TPC are applied and tracks have to fulfill $\lvert\eta\rvert < 0.8$ and $p_{\mathrm{T}} > 0.3$ GeV/c. For particle identification, TPC or TOF information is used, employing a cut of 3σ on the difference between the measured and expected signal for the daughter species. Triplets are rejected if the oppositely charged track is not associated to a kaon candidate. Additional preselections on the decay-vertex topology are applied, most of which have already been introduced in the discussion on V_0 candidates in Sec. 3.2.2. They are listed in Tab. 4.4 and depend on the p_{T} of the reconstructed D^+-meson candidates.

The so obtained sample of D^+-meson candidates includes three different types of contributions

- The *combinatorial background* consists of uncorrelated pions and a kaons
- *Prompt* D^+ mesons directly originate from the hadronization of a charm quark (i.e. primary D^+ mesons) or the decay of charmonium and excited open-charm states, such as D^* mesons.
- *Non-prompt* D^+ mesons come from the decay of beauty hadrons, e.g. B mesons.

As the mean proper decay length of D^+ mesons is $c\tau \approx 300$ μm, while the one of D^* mesons is $c\tau \approx 2000$ fm, hence, negligible in comparison, it is the main contributor to the displacement of the decay vertex of prompt D^+ mesons. The mean proper decay

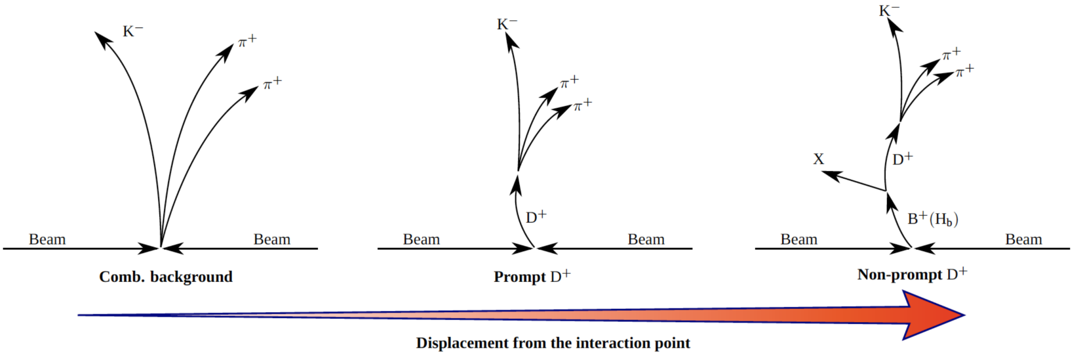

FIGURE 4.9: Illustration of the decay topologies of the different contributions to the D^+-meson sample. Image by the courtesy of my colleague D. Battistini.

length of beauty hadrons, on the other hand, is about $c\tau \approx 500$ µm, resulting in a significantly larger displacement of the decay vertex of non-prompt D^+ mesons with respect to that of prompt candidates. The different decay-vertex topology, illustrated in Fig. 4.9, can be used to distinguish not only between combinatorial background and D^+ mesons but also between the non-prompt and prompt contribution to the sample.

A multi-class machine learning (ML) algorithm based on boosted decision trees (BDT), provided by the XGBOOST library [178], is employed to efficiently categorize the sample into contributions from the combinatorial background, as well as prompt and non-prompt D^+ mesons. It is based on weak learners (decision trees), which classify the training data sample by recursively splitting it based on specific features and attributes. In this analysis, different variables related to the decay-vertex topology, such as the decay length, $\cos\theta_\mathrm{p}$ or σ_vertex, as well as PID information on the daughter candidates are used. Combining many weak learners subsequently (boosting) results in one strong classifier, which extends traditional cut-based (rectangular) particle selection. The model is trained on a sample of prompt and non-prompt D^+ mesons obtained from the HF MC simulations, while the one of the combinatorial background is taken from a small fraction of the HM events used in the analysis, selecting invariant-mass intervals outside the resonance peak region (sidebands). The training is performed in different p_T intervals[2] and the hyper-parameters used to configure the learning process during the training were chosen with a Bayesian optimization procedure [179] with a 5-fold cross-validation [180] implemented in the HIPE4ML package [181]. The model is tested on analogous but independent datasets to those used for training. Figure 4.10 shows the resulting BDT output scores, which represent the probability of belonging to one of the three classes of D^+-meson candidates, in two of the p_T intervals used for training. As can be seen, there is good agreement between the distributions obtained from applying the model to training and test data, respectively. Moreover, the probability distribution is close to unity for the respective true class, while the other two classes approach zero. The shape of the combinatorial background distributions clearly differs from the others, indicating that the algorithm is more efficient in separating the combinatorial background from the signal than in distinguishing between prompt and non-prompt D^+

---

[2] The p_T intervals range from $p_\mathrm{T} \in [1, 10]$ GeV/c and have a width of 1 GeV/c except for the last interval, which is twice as wide for statistical purposes. Hence, they are defined as $[1, 2]$ GeV/c, $[2, 3]$ GeV/c, $[3, 4]$ GeV/c, $[4, 5]$ GeV/c, $[5, 6]$ GeV/c, $[6, 7]$ GeV/c, $[7, 8]$ GeV/c and $[8, 10]$ GeV/c, respectively.

mesons.

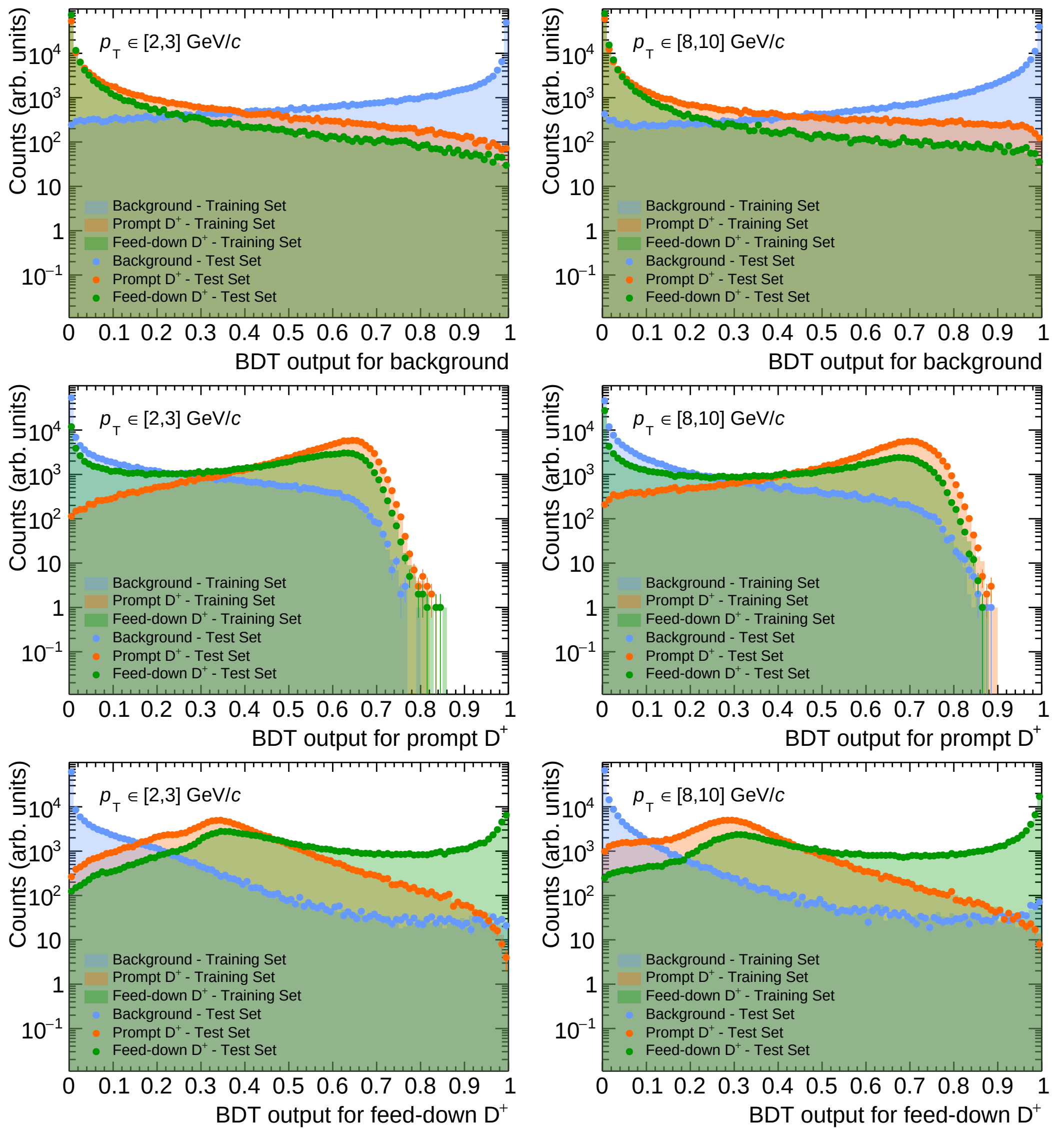

FIGURE 4.10: Distributions of ML output scores for combinatorial background candidates (*top panels*), prompt D$^+$ mesons (*middle panels*), and non-prompt D$^+$ mesons (*bottom panels*), obtained from the training and test samples in the $p_T \in [2,3]$ GeV/c (*left column*) and $p_T \in [8,10]$ GeV/c (*right column*) intervals.

Further, the performance of the model can be assessed by considering the area under the Receiver Operating Characteristic curve (ROC AUC), which plots the true positive rate, corresponding to the signal selection efficiency, as a function of the false positive rate, which is equivalent to the background selection efficiency. A value of 1 indicates a perfect discrimination between two classes, while 0.5 corresponds to a random classification. Figure 4.11 shows the ROC curves obtained from the training sets for all possible pairs of classes of D$^+$ mesons, trained in the p_T intervals $p_T \in [2,3]$ GeV/c and $p_T \in [8,10]$ GeV/c.

A scan of the BDT output scores for the background and the non-prompt D$^+$ mesons is performed, and the expected statistical significance and signal-over-background ratio, the efficiency for prompt and non-prompt D$^+$ mesons, as well

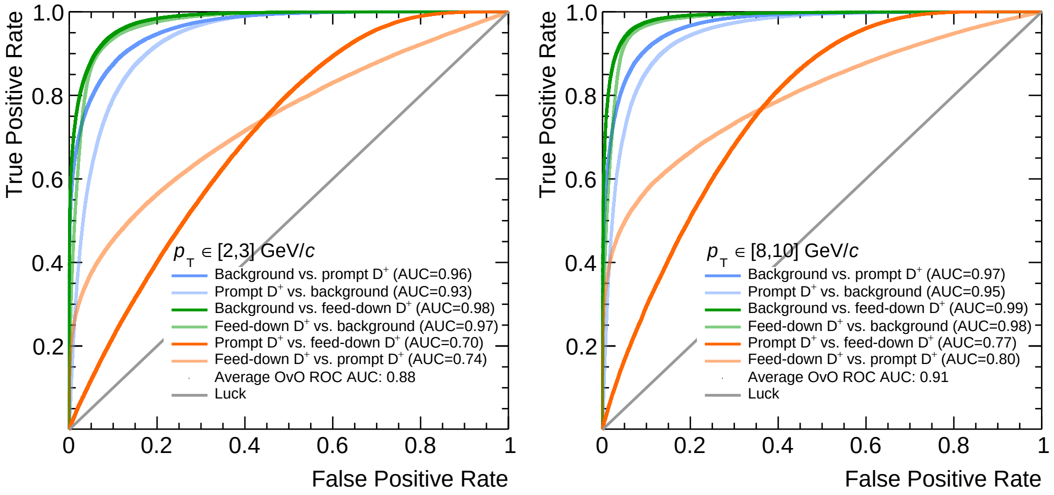

FIGURE 4.11: ROC curves for the models trained for D^+ mesons in the $p_T \in [2,3]$ GeV/c (*left panel*) and $p_T \in [8,10]$ GeV/c (*right panel*) relative-momentum intervals.

p_T interval (GeV/c)	prob to be bkg $<$	prob to be prompt $>$
$[1,2]$	0.0025	0.30
$[2,3]$	0.0025	0.30
$[3,4]$	0.0030	0.30
$[4,5]$	0.0080	0.30
$[5,6]$	0.0100	0.30
$[6,7]$	0.0250	0.30
$[7,8]$	0.0300	0.30
$[8,10]$	0.0200	0.30

TABLE 4.5: ML selection criteria applied in the different p_T intervals for the selection of prompt D^+ mesons.

as the prompt and non-prompt fractions evaluated in order to find a set that enhances the contribution from prompt D^+ mesons to the sample, while keeping a high statistical significance. The resulting selections on the output scores are listed in Tab. 4.5,

Finally, the model is applied to the data to select D^+ candidates. The resulting invariant-mass distribution is fitted in p_T intervals of 200 MeV/c from 1 to 10 GeV/c, using a Gaussian distribution for the signal and an exponential function for the combinatorial background. An example distribution and the fit result are shown in the left panel of Fig. 4.13 for the p_T interval $p_T \in [2,3]$ GeV/c. Finally, the D^+-meson candidates are selected within $2\sigma(p_T)$ around the mean value of the D^+-meson mass $M_D(p_T)$, obtained from the fit. In each p_T interval, the purity of the candidates is calculated as the ratio $S/(S+B)$ of the signal candidates S over the total raw yield, which also includes the combinatorial background B, obtained from the fit-functions within the D^+ selection window. The resulting distribution is shown in Fig. 4.12. A clear p_T dependence is visible as the purity of D^+ mesons with $p_T < 3$ GeV/c drops drastically. As the training of the ML model is performed in intervals of p_T, a staggered behavior can be observed, with jumps at the interval borders.

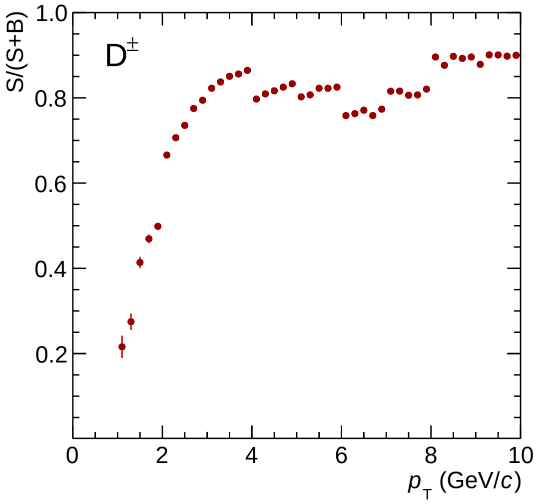

FIGURE 4.12: The p_{T}-differential purity of the D^+-meson candidates.

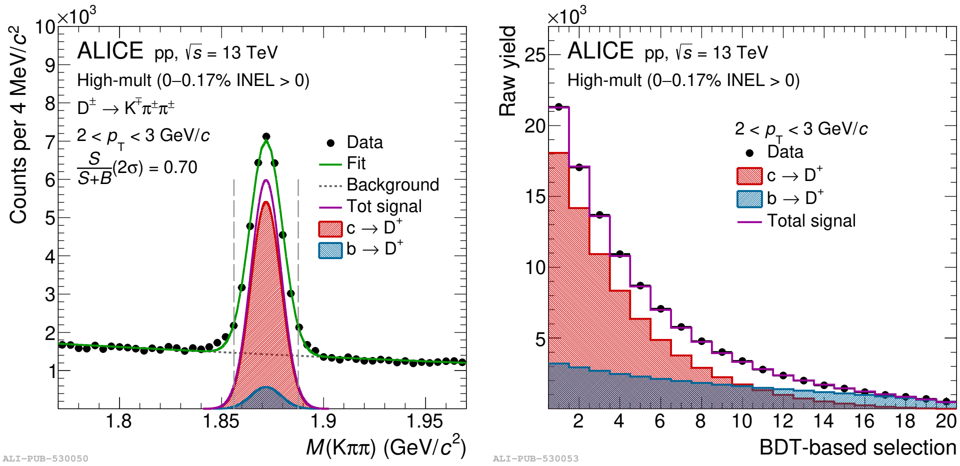

FIGURE 4.13: The *left panel* shows the invariant-mass distribution of D^+ mesons, reconstructed from the decay $\mathrm{D}^+ \rightarrow \mathrm{K}^-\pi^+\pi^+$ in the $p_{\mathrm{T}} \in [2, 3]$ GeV/c interval. The green solid line represents the total fit function, composed of both signal (violet solid line) and combinatorial background contributions (gray dotted line). The gray dashed vertical lines correspond to the selection interval for D^+-meson candidates. The red shaded area represents the prompt contribution to the signal, which originates from charm quark hadronization, while the blue shaded area represents the non-prompt contribution from beauty-hadron decays. The extracted raw yield of the candidates is shown in the *right panel* as a function of the BDT-based cut selection for the same p_{T} interval. It is obtained from the minimization procedure used to determine the fraction of non-prompt D^+ mesons in the sample.

The remaining non-prompt contribution to the sample is estimated using a data-driven procedure adopted from Ref. [182], which exploits the fact that the prompt selection efficiencies change differently to the non-prompt ones when changing the selection on the ML scores. For each selection i, the raw yield Y_i of D^+ candidates can be extracted from the fit to the invariant-mass, as explained before, and can be related to the corrected yields of prompt and non-prompt D^+ mesons, denoted by

N_{prompt} and $N_{\mathrm{non\text{-}prompt}}$, respectively, via

$$\delta_i = Y_i - (\mathrm{Acc} \times \epsilon)_{\mathrm{prompt},i} \times N_{\mathrm{prompt}} - (\mathrm{Acc} \times \epsilon)_{\mathrm{non\text{-}prompt},i} \times N_{\mathrm{non\text{-}prompt}}, \tag{4.1}$$

where $(\mathrm{Acc} \times \epsilon)_{\mathrm{prompt/non\text{-}prompt},i}$ is the product of the acceptance and efficiency for each selection and δ_i a residual that accounts for possible uncertainties in the equation. By performing a χ^2 minimization of the overdetermined system of equations, the corrected yields are obtained for each set of selections individually. More details can be found in Ref. [182]. The right panel of Fig. 4.13 shows an example of a raw-yield distribution as a function of the BDT-based selection used in the minimization procedure for D^+ mesons with a transverse momentum of $2 < p_{\mathrm{T}} < 3\,\mathrm{GeV}/c$. When moving from left to right, the BDT-based selection associated with the probability of a candidate being a non-prompt D^+ meson becomes stricter and the raw yield in the last bin consists almost exclusively of non-prompt D^+ mesons (blue shaded area) with negligible contribution from prompt D^+ mesons (red shaded area).

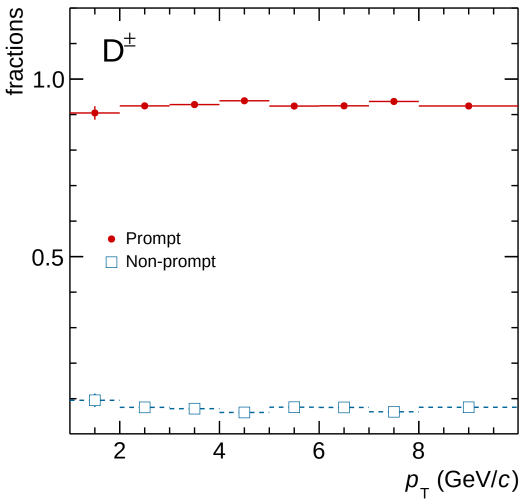

FIGURE 4.14: Prompt and non-prompt fraction of D^+-meson candidates as a function of p_{T} for the default set of selections.

The resulting p_{T}-differential non-prompt fraction is shown in blue if Fig. 4.14. Only a mild dependence on the transverse momentum is visible. The dominant prompt component to the D^+-meson sample, shown in red in the same figure, includes feed-down contributions from excited charm states, mainly D^{*+} mesons, via the $\mathrm{D}^{*\pm} \rightarrow \mathrm{D}^{\pm} + \pi^0$ and $\mathrm{D}^{*\pm} \rightarrow \mathrm{D}^{\pm} + \gamma$ decays, with branching ratios of $\mathrm{BR} = (30.7 \pm 0.5)\%$ and $\mathrm{BR} = (1.6 \pm 0.4)\%$, respectively [122].

Due to the short lifetime of such states, $c\tau \approx 2000$ fm, it is not possible to experimentally separate them from the rest using the decay topology. Their contribution is estimated from the p_{T}-differential production cross sections of D^+ and D^{*+} mesons measured in pp collisions at $\sqrt{s} = 5.02$ TeV [182, 183], shown as green and blue points in the left panel of Fig. 4.15, following the procedure presented in Ref. [53]. The D^{*+} data is extrapolated to $p_{\mathrm{T}} = 0\,\mathrm{GeV}/c$, by fitting it with a power-law function, represented by the blue line in the same figure. D^{*+} mesons are then sampled from this function and decayed via $\mathrm{D}^{*\pm} \rightarrow \mathrm{D}^{\pm} + \mathrm{X}$ using PYTHIA 8, which results in the red distribution in the left panel of Fig. 4.15. Finally, the fraction as a function of p_{T} is obtained from the ratio between the experimental D^+ production cross-section and the simulated $\mathrm{D}^+ \leftarrow \mathrm{D}^*$ cross-section and shown in the right panel of Fig. 4.15.

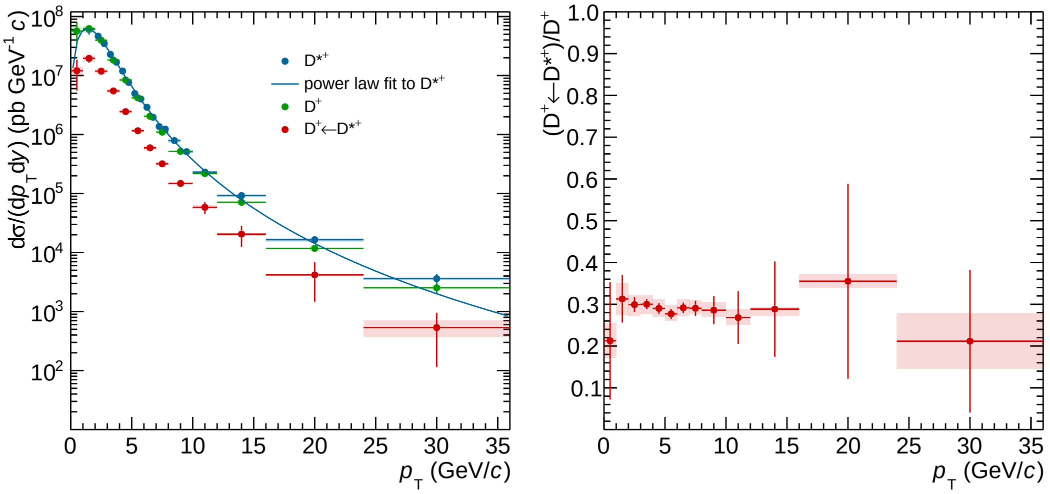

FIGURE 4.15: The *left panel* shows the measured D$^+$ and D* cross sections, the power-law fit to the D^{*+} cross section, and the D$^+ \leftarrow$ D* cross section obtained with PYTHIA 8 as function of p_{T}. The *right panel* shows the resulting fraction of D$^+$ mesons originating from D^{*+} decays as a function of p_{T}.

TABLE 4.6: Total number of pairs in the full k^* range as well as number of pairs with small relative momenta, where final state effects become relevant.

Pair	Total	$k^* < 200$ MeV/c
$\mathrm{D}^+\pi^+ \oplus \mathrm{D}^-\pi^-$	3.0×10^6	2.0×10^5
$\mathrm{D}^+\pi^- \oplus \mathrm{D}^-\pi^+$	2.9×10^6	2.1×10^5
$\mathrm{D}^+\mathrm{K}^+ \oplus \mathrm{D}^-\mathrm{K}^-$	1.7×10^5	1.9×10^3
$\mathrm{D}^+\mathrm{K}^- \oplus \mathrm{D}^-\mathrm{K}^+$	1.6×10^5	2.2×10^3

4.1.2 Pairing

The reconstructed D$^+$ and light-flavor mesons are paired, and their relative momentum k^* is calculated in order to build the experimental raw correlation function. Both the same- and opposite-charge combination is investigated in this analysis. As the D$^+$ candidates are reconstructed from their decay to charged pions and kaons, it is essential not to pair mother- and daughter-particles to avoid auto-correlations. Therefore, pairs are rejected if the track of a light-flavor meson candidate is also used as a daughter track in the reconstruction of a D$^+$ meson. The resulting number of particle pairs available for building the correlation functions is displayed in Tab. 4.6.

4.2 The raw correlation function

As discussed extensively in Sec. 2.2, the experimental correlation function is obtained from the ratio of the k^* distribution of pairs emitted in the same collision, $N_{\mathrm{same}}(k^*)$, and a reference sample of uncorrelated pairs from different collisions, $N_{\mathrm{mixed}}(k^*)$. Following Eq. 2.10, it is further multiplied by a normalization constant, $\mathcal{N}$, which ensures that $C(k^*) = 1$ for large k^* values. It is chosen such that the mean value of the correlation function is equal to one for $k^* \in [1.5,\ 2.0]$ GeV/c for DK

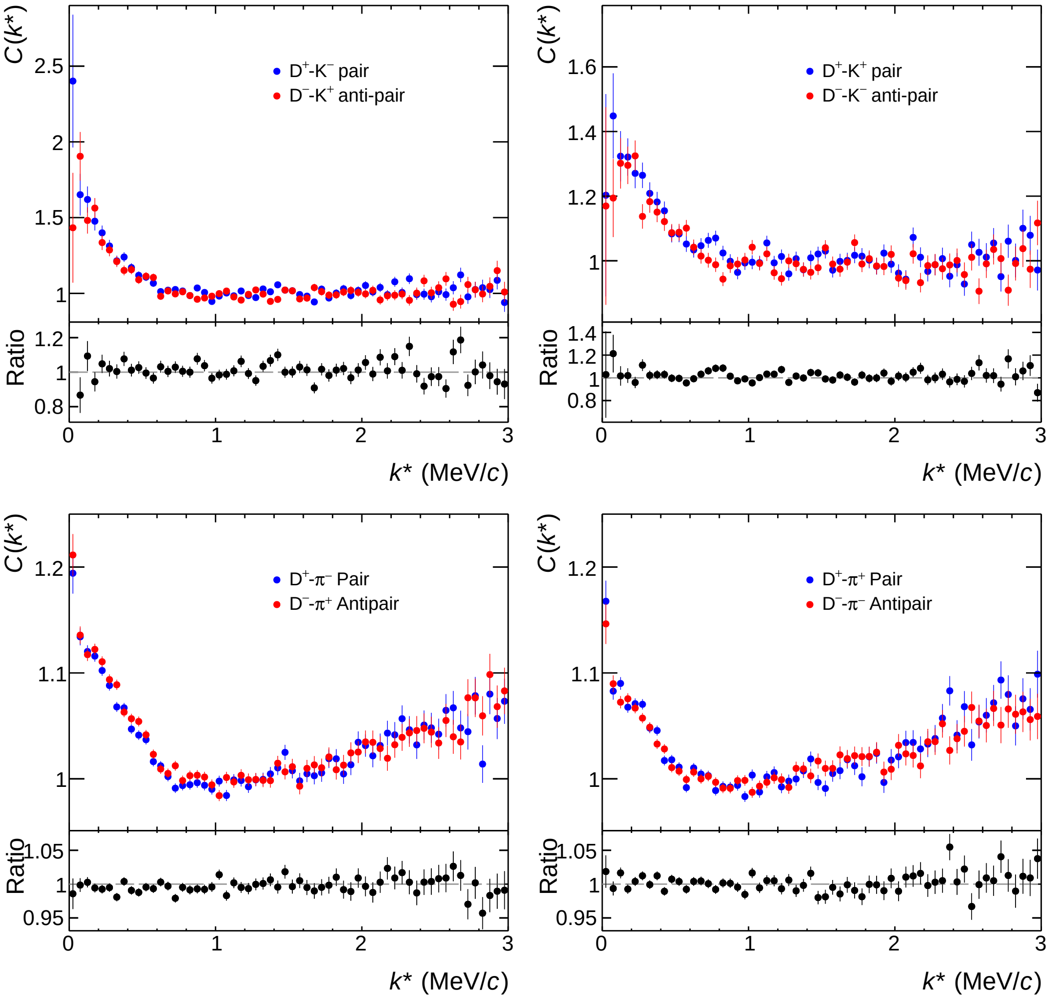

FIGURE 4.16: The correlation function of DK (*upper row panels*) and Dπ pairs and anti-pairs (*lower row panels*) are depicted for both the opposite- (*left column panels*) and same-charge combination (*right column panels*), as well as their ratio.

pairs and $k^* \in [1.0,\ 1.5]$ GeV$/c$ for Dπ pairs. These intervals correspond to kinematic regions, where the correlation functions are flat, and no femtoscopic signal is present. The mixed-event distribution $N_{\text{mixed}}(k^*)$ is obtained from event-mixing techniques, pairing single particles from separate collisions. To avoid possible bias due to acceptance effects of the detector system and to ensure the quality of the reference sample, only particles from events with similar multiplicity and z position of the primary vertex are paired [184]. Further, $N_{\text{mixed}}(k^*)$ is re-weighted in each multiplicity bin in order to have the same statistical weight as $N_{\text{same}}(k^*)$. More information on the mixing can be found in Appendix B.1 and B.2. Furthermore, the impact of the finite momentum resolution of the ALICE detector on the correlation functions was investigated and found to be negligible. Therefore, no unfolding is performed to correct for it. Details are provided in Appendix B.3.

The correlation functions of pairs and anti-pairs, evaluated in 50 MeV$/c$ wide k^* intervals, as well as their ratio, are shown in Fig. 4.16. As they are compatible within the uncertainties, they are combined to enhance the statistical significance of the results. In the following, same-charge $\mathrm{D}^{(*)}$X refers to the combined $\mathrm{D}^+\mathrm{X}^+ \oplus \mathrm{D}^-\mathrm{X}^-$ pairs, while opposite-charge DX refers to $\mathrm{D}^+\mathrm{X}^- \oplus \mathrm{D}^-\mathrm{X}^+$, where X is a placeholder

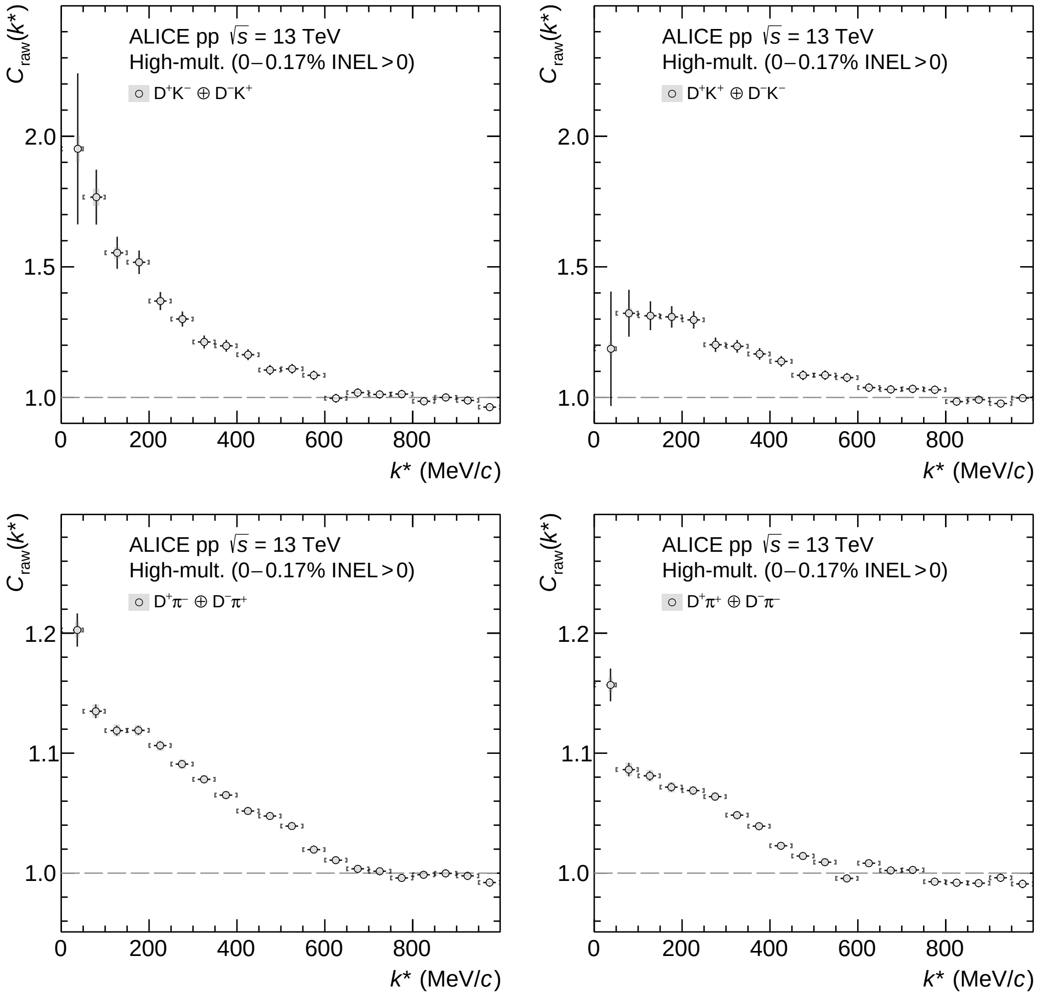

FIGURE 4.17: The raw opposite- (*left column panels*) and same-charge (*right column panels*) D–K correlation functions with statistical (bars) and systematic uncertainties (gray shaded boxes) depicted in the *upper row panels*, while the same is shown for D–π pairs in the *lower row panels*.

for either K or π mesons. The resulting raw correlation functions for DK and Dπ pairs in both charge combinations are shown in Fig. 4.17. The horizontal position of each data point corresponds to the mean k^* in the mixed-event distribution within the respective relative-momentum interval, taking into account a possible shift with respect to the bin center, which is most prominent in the low-k^* region, where the correlation is sensitive to the strong FSI interaction.

As can be seen from the plots, the correlation functions deviate from unity up to $k^* \sim 800$ MeV$/c$, well outside the femtoscopic region where the signal from FSI is expected. This is related to the presence of several background contributions to the raw correlation signal, which mainly arise from non-femtoscopic contributions but also the finite purity and primary fraction of the D^+ and light-flavor mesons. In order to study the residual strong interaction between D^+ and light-flavor mesons, the raw correlation function must first be decomposed into its constituent parts and the genuine signal, which includes only primary light-flavor mesons and signal D^+ mesons, extracted.

TABLE 4.7: Variations of the kaon selection criteria.

Selection criterion	Default	Loose	Tight
p_T (GeV/c)	0.15	0.1	0.2
$\lvert\eta\rvert$	0.8	0.75	0.85
$\lvert n_{\sigma,\mathrm{comb}}(\mathrm{K})\rvert < n^{\mathrm{thr}}_{\sigma,\mathrm{comb}}$ $p < 1.2$ GeV/c or $\lvert n_{\sigma,\mathrm{comb}}(\mathrm{K})\rvert < 2$ or $\lvert n_{\sigma,\mathrm{comb}}(\pi)\rvert > 6$	$n^{\mathrm{thr}}_{\sigma,\mathrm{comb}} = 3$	$n^{\mathrm{thr}}_{\sigma,\mathrm{comb}} = 3.3$	$n^{\mathrm{thr}}_{\sigma,\mathrm{comb}} = 2.7$
n_Cluster	80	70	90

TABLE 4.8: Variations of the pion selection criteria.

Selection criterion	Default	Loose	Tight
p_T (GeV/c)	0.14	0.12	0.15
$\lvert\eta\rvert$	0.8	0.7	0.9
$\lvert n_{\sigma,\mathrm{TPC}}(\pi)\rvert < n^{\mathrm{thr}}_{\sigma}$ for $p_\mathrm{T} < 0.5\,\mathrm{GeV}/c$ $\lvert n_{\sigma,\mathrm{comb}}(\pi)\rvert < n^{\mathrm{thr}}_{\sigma}$ for $p_\mathrm{T} > 0.5\,\mathrm{GeV}/c$	$n^{\mathrm{thr}}_{\sigma} = 3$	$n^{\mathrm{thr}}_{\sigma} = 3.3$	$n^{\mathrm{thr}}_{\sigma} = 2.7$
n_Cluster	80	70	90

Systematics

The choice of the selection criteria used to identify the light-flavor and D$^+$-meson candidates determines their single-particle properties. Therefore, it affects the distributions of pairs obtained from the same and mixed events and ultimately impacts the raw correlation function. The corresponding systematic uncertainty is estimated by varying the selections for pions and kaons as reported in Tab. 4.8 and 4.7, respectively, as well as the selection on the BDT output score related to the probability of a D$^+$ being a background candidate, as reported in Tab. 4.9. These variations are randomly combined into 20 sets to account for possible correlations, and for each set, the raw correlation function is recomputed. The systematic uncertainty of the individual data points is then obtained in a conservative manner via $[C_\mathrm{max}(k^*) - C_\mathrm{min}(k^*)]/\sqrt{12}$, considering the full spread of the correlation function values obtained from the different sets of selections. This leads to a relative systematic uncertainty below 3% in the case of DK pairs and below 1% in the case of Dπ pairs.

p_T interval (GeV/c)	Loose 1	Loose 2	Tight 1	Tight 2
$[1,2]$	0.0026	0.0028	0.0024	0.0023
$[2,3]$	0.0026	0.0028	0.0024	0.0023
$[3,4]$	0.0032	0.0036	0.0029	0.0028
$[4,5]$	0.0085	0.0088	0.0076	0.0072
$[5,6]$	0.0105	0.0115	0.0095	0.0085
$[6,7]$	0.0275	0.0300	0.0225	0.0200
$[7,8]$	0.0325	0.0350	0.0275	0.0250
$[8,10]$	0.0250	0.0300	0.0175	0.0150

TABLE 4.9: Variation of the upper limit of the probability of a D^+ being a background candidate for the individual p_T intervals, which is part of the ML selection criteria.

4.3 Decomposition of the correlation function

Following the discussion in Sec. 2.2, the raw correlation functions can be decomposed as in Eq. 2.11, separating contributions related to FSI, which are part of $C_\mathrm{femto}(k^*)$, from the residual non-femtosopic background $C_\text{non-femto}(k^*)$. In order to study the residual strong interaction among DK and Dπ pairs, the genuine correlation function $C_\mathrm{gen}(k^*)$, which arises from the interaction of primary and signal particles, has to be extracted from the raw data. This is, however, only possible if all other contributions to $C_\mathrm{femto}(k^*)$, as well as $C_\text{non-femto}(k^*)$, are well understood. The former are individually discussed in Sec. 4.3.1, while the latter is studied in Sec. 4.3.2, and the resulting decomposition of the correlation function is presented in Sec. 4.3.3.

4.3.1 Contributions from final state interaction

There are several other contributions to $C_\mathrm{femto}(k^*)$, besides $C_\mathrm{gen}(k^*)$, due to the limited purity of the candidates used to construct the experimental correlation functions, as well as the presence of feed-down particles in the sample. Each particle combination leads to a different FSI and the resulting contributions are either directly obtained in a data-driven approach or modeled using the Koonin-Pratt formalism defined by Eq. 2.5. Furthermore, as discussed in Sec. 2.2, each component is weighted by a λ parameter, which is calculated from the purity and relevant single particle fractions, respectively.

The values used to determine these parameters are obtained by reweighing the p_T-differential distributions of the purities and fractions, shown in Sec. 4.1, with the p_T distribution of the single particles, which form DK and Dπ pairs with $k^* < 200$ MeV/c, hence, contribute to the correlation signal in the sensitive femtoscopic region. The only exception are the light-flavor meson fractions obtained from the DCA template fits, which are computed as average over the full p_T range instead, due to their mild dependence on the particle transverse momentum. The resulting primary fractions of pions (kaons) are found to be 99.49 % (99.80 %), while the remaining 0.51 % (0.20 %) of the total yield is associated to weak decays of resonances and contributions from interactions with the detector material. Following Ref. [126], the so obtained primary fractions have to further be corrected for strongly decaying resonances with $\langle c\tau \rangle \gtrsim 5$ fm[3]. The associated fractions $f_\text{sec,strong}$ cannot be accessed

---

[3] Resonances with a smaller decay length are absorbed in the particle emitting source, as it is assumed that they do not live long enough to induce a significant correlation signal from FSI.

		DK	Dπ
D^+	p	71.5%	71%
	$f_{\text{primary}} = 1 - f_{\mathrm{D}^* \leftarrow \mathrm{D}} - f_{\text{non-prompt}}$	$\sim 65.53\%$	$\sim 65.50\%$
	$f_{\mathrm{D}^* \leftarrow \mathrm{D}}$	$(27.35 \pm 0.70)\%$	$(27.30 \pm 0.60)\%$
	$f_{\text{non-prompt}}$	$(7.15 \pm 0.20)\%$	$(7.20 \pm 0.20)\%$
K/π	p	98%	99%
	$f_{\text{primary}} = 1 - f_{\text{sec,weak+mat}} - f_{\text{sec,strong}}$	$\sim 93.81\%$	$\sim 87.55\%$
	$f_{\text{sec,weak+mat}}$	0.20%	0.51%
	$f_{\text{sec,strong}}$	5.99%	12.20%

TABLE 4.10: The p_{T}-integrated values of the purity and fractions of the light-flavor and D^+-meson samples.

experimentally due to the short lifetime of the strongly decaying resonances. Therefore, they are estimated with the THERMALFIST SHM [185]. For kaons, a value of 5.99 % is found, with ϕ meson decays as the main contributor. This results in a corrected primary fraction of 93.81 %. A total of 12.20 % of pion candidates is associated with the decay of short-lived, strongly decaying resonances, mainly the ω and η mesons [126], leading to a corrected primary fraction of 87.55 %.

The fractions and purities used to determine the λ parameters of the D–K and D–π correlation functions are summarized in Tab. 4.10 and the corresponding λ parameters are listed in Tab. 4.11. As can be seen, the main contribution to the correlation signal arises from the genuine FSI among primary particles, followed by the one from fake D^+ mesons from the combinatorial background as well as prompt D^+ mesons from the decay of excited charm states, interacting with light-flavor mesons. The other components of $C_{\text{femto}}(k^*)$ are either not expected to lead to correlations or scaled by such a small λ parameter that any correlation signal is washed out. They are approximated by a flat correlation function $C_{i,j}(k^*) = 1$ and include contributions from pairs involving non-primary or misidentified light-flavor mesons, as well as non-prompt $\mathrm{D}^{(*)+}$ mesons. The latter is discussed in Appendix B.4. The individual non-flat contributions to $C_{\text{femto}}(k^*)$ are discussed in detail in the following, with the exception of $C_{\text{gen}}(k^*)$, which is presented in Sec. 4.5.

Contribution from misidentified D^+ mesons

Due to the limited purity of the reconstructed D^+ mesons, which is about $\sim 71\%$, contributions associated with the combinatorial background must be considered. These include all pair combinations involving $\tilde{\mathrm{D}}$ in Tab. 4.11 and contribute with a total of $\sim 29\%$ to $C_{\text{femto}}(k^*)$. Such correlation signals arise from residual two-body interactions between the particles used to build fake D^+ mesons and the light-flavor candidates [54]. They are accessed in a data-driven approach, where candidates outside the D^+-meson reconstruction region in the invariant-mass distribution are paired with π and K candidates, respectively. The sideband intervals are chosen to be as close to the resonance region as possible while avoiding the tails of the signal, in order to minimize kinematic effects while keeping the fake sample clear from real D^+ mesons. Therefore, the sidebands start at $5\sigma_{\mathrm{D}^+}$ away from the nominal mass of the D^+ and extend for 200 MeV/c^2 to the left and right, respectively, where σ_{D^+} corresponds to the width of the Gaussian function describing the signal and is determined by the fit to the p_{T}-differential invariant-mass distribution, depicted in Fig. 4.18. The red shaded area corresponds to the region within which the D^+ candidates are selected, while the regions highlighted in gray correspond to the

Pair	λ (%)		Treatment
	$\mathrm{m} = \mathrm{K}$	$\mathrm{m} = \pi$	
Dm	43.06	40.30	Gauss+Coulomb
$\mathrm{Dm}_{\mathrm{sec,weak+mat}}$	0.09	0.23	Flat
$\mathrm{Dm}_{\mathrm{sec,strong}}$	2.75	5.50	
$\mathrm{D}\tilde{\mathrm{m}}$	0.94	0.47	
$\mathrm{D}_{\mathrm{non-prompt}}\mathrm{m}$	4.70	4.43	Flat
$\mathrm{D}_{\mathrm{non-prompt}}\mathrm{m}_{\mathrm{sec,weak+mat}}$	0.01	0.03	
$\mathrm{D}_{\mathrm{non-prompt}}\mathrm{m}_{\mathrm{sec,strong}}$	0.30	0.60	
$\mathrm{D}_{\mathrm{non-prompt}}\tilde{\mathrm{m}}$	0.10	0.05	
$\mathrm{D}_{\mathrm{D}\leftarrow\mathrm{D}^*}\mathrm{m}$	17.98	16.80	Coulomb
$\mathrm{D}_{\mathrm{D}\leftarrow\mathrm{D}^*}\mathrm{m}_{\mathrm{sec,weak+mat}}$	0.04	0.10	Flat
$\mathrm{D}_{\mathrm{D}\leftarrow\mathrm{D}^*}\mathrm{m}_{\mathrm{sec,strong}}$	1.15	2.29	
$\mathrm{D}_{\mathrm{D}\leftarrow\mathrm{D}^*}\tilde{\mathrm{m}}$	0.39	0.19	
$\tilde{\mathrm{D}}\mathrm{m}$	26.20	25.14	Sideband
$\tilde{\mathrm{D}}\mathrm{m}_{\mathrm{sec,weak+mat}}$	0.06	0.14	
$\tilde{\mathrm{D}}\mathrm{m}_{\mathrm{sec,strong}}$	1.67	3.43	
$\tilde{\mathrm{D}}\tilde{\mathrm{m}}$	0.57	0.29	

TABLE 4.11: Individual components of the femtoscopic DK and Dπ correlation functions and their relative contribution quantified by λ parameters, as well as their treatment in the analysis. Particles denoted by a tilde correspond to misidentifications.

left and right sideband intervals. A contamination from D^{*+} mesons is expected in the right sideband sample due to the $\mathrm{D}^{*+} \to \mathrm{D}^0\pi^+$ and subsequent $\mathrm{D}^0 \to \mathrm{K}^-\pi^+$ decays. Therefore, the interval $[1.992, 2.028]$ MeV/c around the nominal D^{*+} mass of $(2010.26 \pm 0.05)\mathrm{MeV}/c^2$ [122] is excluded.

The correlation functions obtained from the left and right sideband are normalized in the same range as the correlation functions from the signal region and are found to be compatible within the uncertainties for all pairs and charge combinations, as can be seen in Fig. 4.19. To properly describe the combinatorial background in the signal region, they are combined as

$$C_{\mathrm{SB}}(k^*) = w_{\mathrm{left}} \cdot C_{\mathrm{left}}(k^*) + (1 - w_{\mathrm{left}}) \cdot C_{\mathrm{right}}(k^*), \tag{4.2}$$

where $w_{\mathrm{left}} = 0.51$ corresponds to the p_{T}-averaged relative amount of background present in the left half of invariant mass interval used for the selection of D^+-mesons candidates. The value is obtained by integrating the function used to describe the combinatorial background in the parametrization of the invariant mass distribution within an interval of $[M_{\mathrm{D}^+} - 2\sigma_{\mathrm{D}^+}, M_{\mathrm{D}^+}]$ in each p_{T} interval and re-weighting the resulting distribution with the p_{T} distribution of the D^+-meson background candidates in the left sideband interval. The resulting correlation function is shown in blue in Fig. 4.19.

As it is obtained from experimental data, $C_{\mathrm{SB}}(k^*)$ is also a raw signal and, therefore, composed of a femtoscopic and non-femtoscopic contribution, as stated in Eq. 2.11. This has to be taken into account in the modeling of the raw DK and Dπ correlation functions.

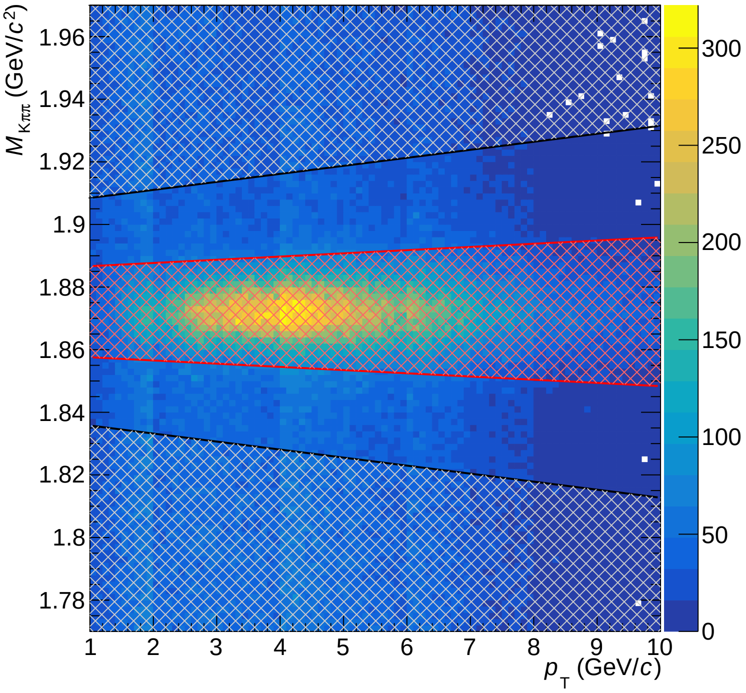

FIGURE 4.18: Invariant mass distribution as a function of the transverse momentum. The region highlighted in red corresponds to the $2\sigma_{D^+}$ interval around the mass of the D^+ meson and represents the selection applied to reconstruct D^+ candidates. The lower and upper regions highlighted in gray correspond to the left and right sidebands, respectively. They start at $5\sigma_{D^+}$ away from the peak of the D^+ resonance. The region rejected in the right sideband due to the contamination of D^{*+} is not shown, as it lies outside of the depicted invariant mass region.

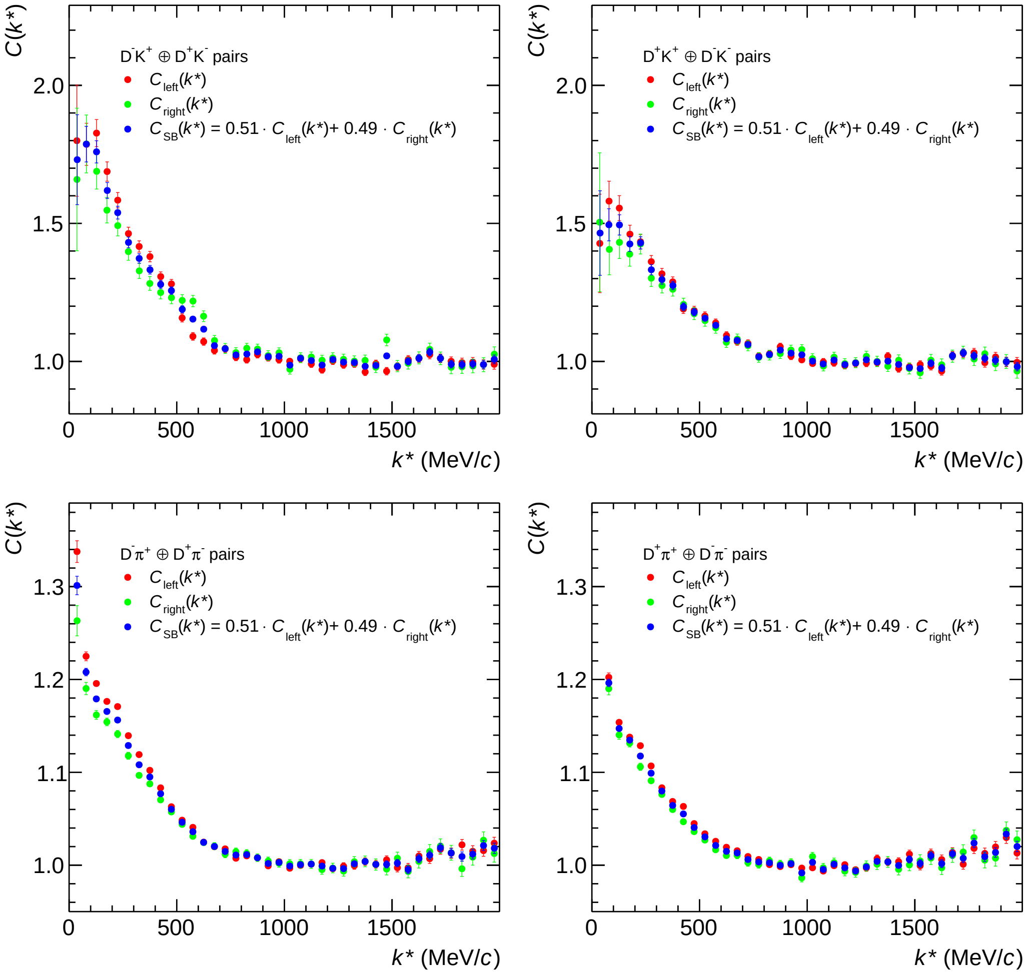

FIGURE 4.19: Correlation functions of the left (red) and right sideband (green), as well as the weighted sum of the two (blue), for opposite- (*left column panels*) and same-charge (*right column panels*) DK pairs depicted in the *upper row panels* and for Dπ pairs in the *lower row panels*.

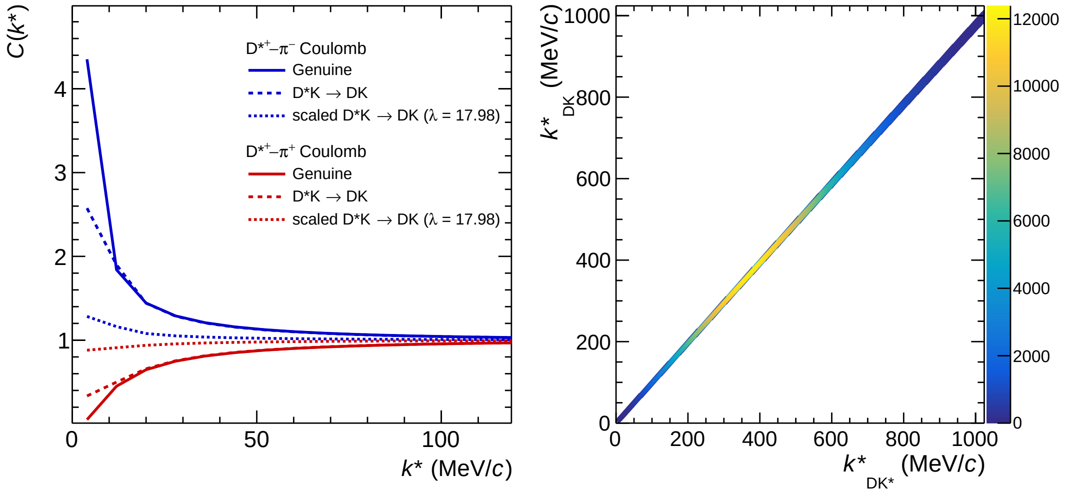

FIGURE 4.20: The *left panel* depicts the D*–K correlation function modeled using the Coulomb potential (solid line), as well as the same correlation function after the transformation to the DK system (dashed line) and additional re-weighting by $\lambda = 17.98\%$ (dotted line), for same- (red) and opposite-charge (blue) pairs. The *right panel* shows the momentum transformation matrix.

Contribution from excited charm states

A significant fraction of D^+-meson candidates is produced in the decay of charm-hadron resonances. In particular, contributions from D^{*+} mesons make up $\sim 30\%$ of the sample, while feed-down from the decays of other excited charm states is expected to be negligible, due to the small branching ratios [122]. Since D^{*+} mesons have a finite lifetime of $c\tau \approx 2000$ fm, they will interact with light-flavor mesons before decaying into D^+. This initial interaction leads to a correlation signal in the final state, which is smeared according to the decay kinematics.

The genuine D*–K and D*–π correlation functions are modeled using the Koonin-Pratt formalism, Eq. 2.5 with the effective source parametrization, discussed in Sec 4.4. The wave function is obtained by solving the Schrödinger equation with the CATS framework, taking into account only the Coulomb potential, as D^{*+} mesons interact with light-flavor mesons mainly electromagnetically [186]. A brief discussion of the associated experimental results is given in Sec. 4.5.3. The resulting genuine correlation functions are shown as solid lines in the left panels of Fig. 4.20 and 4.21 for DK and Dπ pairs. They are subsequently mapped into those of $(D^{*+} \to D^+)$K and $(D^{*+} \to D^+)\pi$ pairs via a transformation to the DK and Dπ momentum basis. This is done using GENBOD phase-space simulations [187] of the $D^{*\pm} \to D^{\pm}\pi^0$ decay. The resulting correlation functions are depicted as dashed lines in the left panel of Fig. 4.21 and 4.20 and the transformation matrices are shown in the right panel. The dotted lines in the left panel show the same correlation function $C_{D \leftarrow D^*}(k^*)$, properly scaled by the λ parameters, which are given by the $D_{D \leftarrow D^*}$m pair contribution in Tab. 4.11. Notably, the overall magnitude of the correlation function is significantly reduced, even though the λ parameters of $\sim 17 - 18\%$ are seizable.

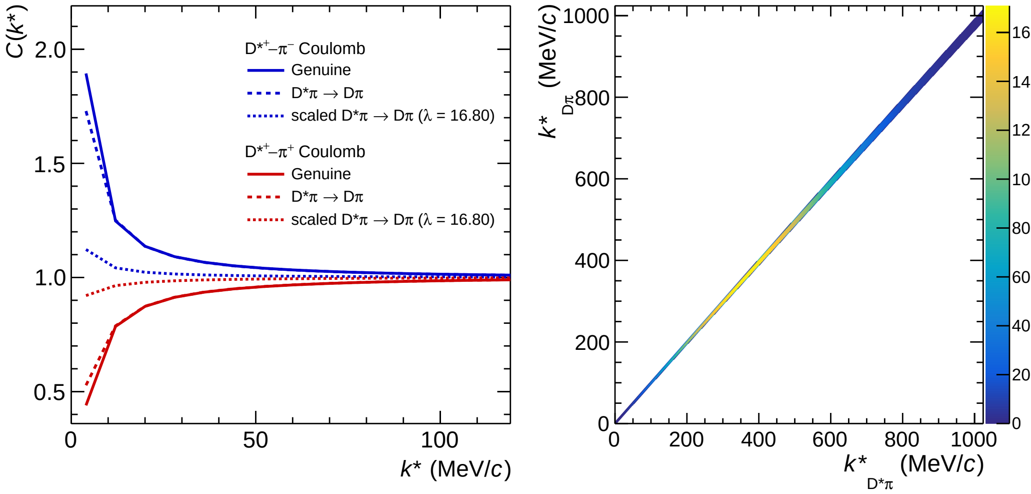

FIGURE 4.21: The *left panel* depicts the D*–π correlation function modeled using the Coulomb potential (solid line), as well as the same correlation function after the transformation to the Dπ system (dashed line) and additional re-weighting by $\lambda = 16.80\%$ (dotted line), for same- (red) and opposite-charge (blue) pairs. The *right panel* shows the momentum transformation matrix.

4.3.2 Residual contributions

The residual background $C_{\text{non-femto}}(k^*)$ consists of contributions from several different sources, which are not related to FSI. In the case of DK and Dπ pairs, the dominant contribution comes from minijets, which induce long-range structures to the raw correlation function at low to intermediate k^* and also affect the sensitive femtosopic region. Such minijet background has previously been observed in other meson-meson [43, 188–191], but also meson-baryon [45, 51] and baryon-antibaryon [44] femtoscopic analyses, while baryon-baryon pairs are unaffected. This is consistent with the sting fragmentation picture introduced in Sec. 2.2 in the context of minijets. As shown in Ref. [190, 191], the background is well reproduced by MC simulated data[4], where FSI is absent. In this analysis, the HF MC sample is used due to the increased number of D$^+$ mesons. However, to account for the correct fractions of prompt and non-prompt D$^+$ mesons found in nature, the contribution has to be modeled as

$$C_{\text{MC}}(k^*) = f_{\text{non-prompt}} C_{\text{D}\leftarrow\text{b}}(k^*) + (1 - f_{\text{non-prompt}}) C_{\text{D}\leftarrow\text{c}}(k^*), \tag{4.3}$$

combining the correlation function $C_{\text{D}\leftarrow\text{b}}(k^*)$, which only involves non-prompt D$^+$ mesons originating from b quarks, with $C_{\text{D}\leftarrow\text{c}}(k^*)$, which is build from prompt D$^+$ mesons from the hadronisation of c quarks, using the non-prompt D$^+$-meson fraction given in Tab. 4.10 as weight. The resulting correlation functions are shown in Fig. 4.22b and 4.22a. As a crosscheck, the analysis was also performed, using a correlation function obtained from standard HM MC data as $C_{\text{MC}}(k^*)$, which already includes the correct relative amount of prompt and non-prompt D$^+$ mesons. The final results were found to be independent of the choice of the MC simulation and in agreement within the uncertainties. Hence, the correlation function from HF MC is used, as it has higher statistical precision.

---

[4] The fragmentation in PYTHIA is based on the Lund string model [82, 192].

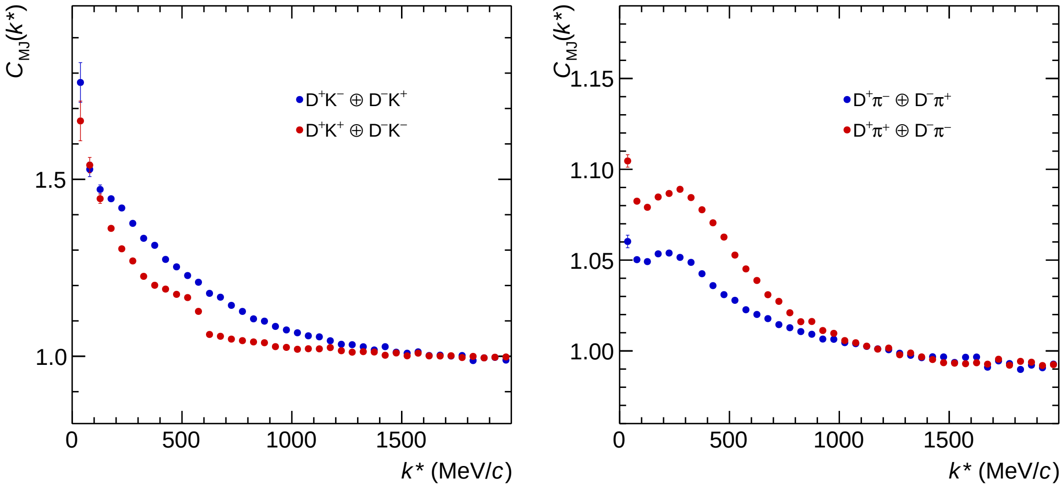

(A) D–K (B) D–π

FIGURE 4.22: Correlation functions obtained from the HF MC data sample, used to describe the minijet background of the raw correlation functions, for the same- (red) and opposite-charge configuration (blue) of DK (*left panel*) and Dπ pairs (*right panel*).

$C_{\mathrm{MC}}(k^*)$ is further multiplied by a free parameter N that accounts for a possible bias due to the choice of the normalization range of the raw data. In the case of Dπ, a baseline is added to the MC correlation function to better describe the enhancement of $C_{\mathrm{raw}}(k^*)$ at intermediate to large k^*, which is visible in Fig. 4.16 and most probably related to energy-momentum conservation. A polynomial of the form $p(k^*) = ak^{*2}$ is chosen, which is 0 and flat at $k^* = 0$ MeV/c, in order not to bias the shape of the correlation function in the femtoscopic region, sensitive to the FSI. The baseline introduces another free parameter a to the residual background of Dπ pairs.

The residual background is finally obtained as

$$C_{\text{non-femto}}(k^*) = \begin{cases} N \times C_{\mathrm{MC}} & \text{for DK} \\ N \times \left[C_{\mathrm{MC}} + ak^{*2}\right] & \text{for D}\pi, \end{cases} \tag{4.4}$$

where the free parameters are determined by a fit to the raw correlation function.

4.3.3 Modeling of the correlation function

In order to isolate the genuine correlation function $C_{\mathrm{gen}}(k^*)$ from the raw data, a model is built according to Eq. 2.11, taking into account all background contributions discussed in the previous sections

$$C_{\mathrm{raw}}(k^*) = \lambda_{\mathrm{SB}} C_{\mathrm{SB}}(k^*) + C_{\text{non-femto}}(k^*)\left[\lambda_{\mathrm{gen}} C_{\mathrm{gen}}(k^*) + \lambda_{\mathrm{D}\leftarrow\mathrm{D}^*} C_{\mathrm{D}\leftarrow\mathrm{D}^*}(k^*) + \lambda_{\mathrm{flat}}\right], \tag{4.5}$$

where $C_{\mathrm{SB}}(k^*)$ arises from the combinatorial background of the reconstructed D^+ mesons, $C_{\text{non-femto}}(k^*)$ accounts for residual correlations not associated to FSI and is dominated by minijet background, $C_{\mathrm{D}\leftarrow\mathrm{D}^*}(k^*)$ describes correlations involving D^* mesons, feeding into the D^+ sample, and λ_{flat} accounts for all the other femtoscopic background contributions described by a flat correlation signal $C_{\mathrm{flat}} = 1$. In particular, $C_{\mathrm{SB}}(k^*)$ is derived from a data-driven method and is therefore not multiplied

TABLE 4.12: Weight parameters of the components of the D–K and D–π model correlation functions.

Parameter	Value (%)	
	DK	Dπ
λ_{gen}	43.06	40.30
λ_{SB}	28.50	29.00
$\lambda_{\mathrm{D}\leftarrow\mathrm{D}^*}$	17.98	16.80
λ_{flat}	10.46	12.72

by $C_{\text{non-femto}}(k^*)$ as it already includes residual contributions, not related to FSI. The respective λ parameters are listed in Tab. 4.12, properly combining the individual values given in Tab. 4.11. The free parameter(s) of the model describing the D–K (D–π) raw signals are part of $C_{\text{non-femto}}(k^*)$, which dominated the intermediate k^* region. They are determined by employing a background model, which only takes into account the background contributions to the measured $C_{\text{raw}}(k^*)$ by imposing $C_{\text{gen}}(k^*) = 1$ in Eq. 4.5. The background model is fitted to the raw data in the range of $k^* \in [100, 600]$ MeV/c for Dπ pairs and $k^* \in [200, 400]$ MeV/c for DK pairs, where no femtoscopic correlations from the genuine FSI are expected.

The fit results are depicted in Fig. 4.23 for the D–π and D–K raw correlation functions. The violet bands depict the background model and the blue bands show $C_{\text{non}-\text{femto}}(k^*)$, with parameters determined by the fit. The other fit-independent contributions to the raw signal are shown as well, with the orange bands representing the combinatorial background $C_{\text{SB}}(k^*)$, and the red bands depicting the contribution arising from the feed-down of D^{*+} to D^+, $C_{\mathrm{D}\leftarrow\mathrm{D}^*}(k^*)$. The deviation between the data and the background model at low k^* is small, indicating a shallow contribution from the genuine FSI. After the fit, the genuine correlation function can be obtained by rearranging Eq. 4.5 in terms of $C_{\text{gen}}(k^*)$ and removing all background contributions from the raw data.

Systematics

The systematic uncertainties of the background model fit arise from the combined systematic uncertainties of its components, the fit procedure, as well as the raw data, each of which are estimated as follows;

- The systematic uncertainties of the raw correlation function as well as $C_{\text{SB}}(k^*)$ are estimated by extracting the experimental correlation function for different sets of selection criteria on the single D^+ and light-flavor mesons, as discussed in the part on systematics in Sec. 4.2.
- The systematic uncertainty of the model correlation function $C_{\mathrm{D}\leftarrow\mathrm{D}^*}(k^*)$ is estimated by varying the effective source parameters within the uncertainties given in Tab. 4.13.
- The uncertainties on the λ-parameters are dominated by those on the fraction of non-prompt D^+ mesons as well as prompt D^+ mesons from the decay of excited charm states, the purity of the D^+ candidates, as well as the fraction $f_{\text{sec,strong}}$ of light-flavor mesons. They are estimated by varying the D^+-meson

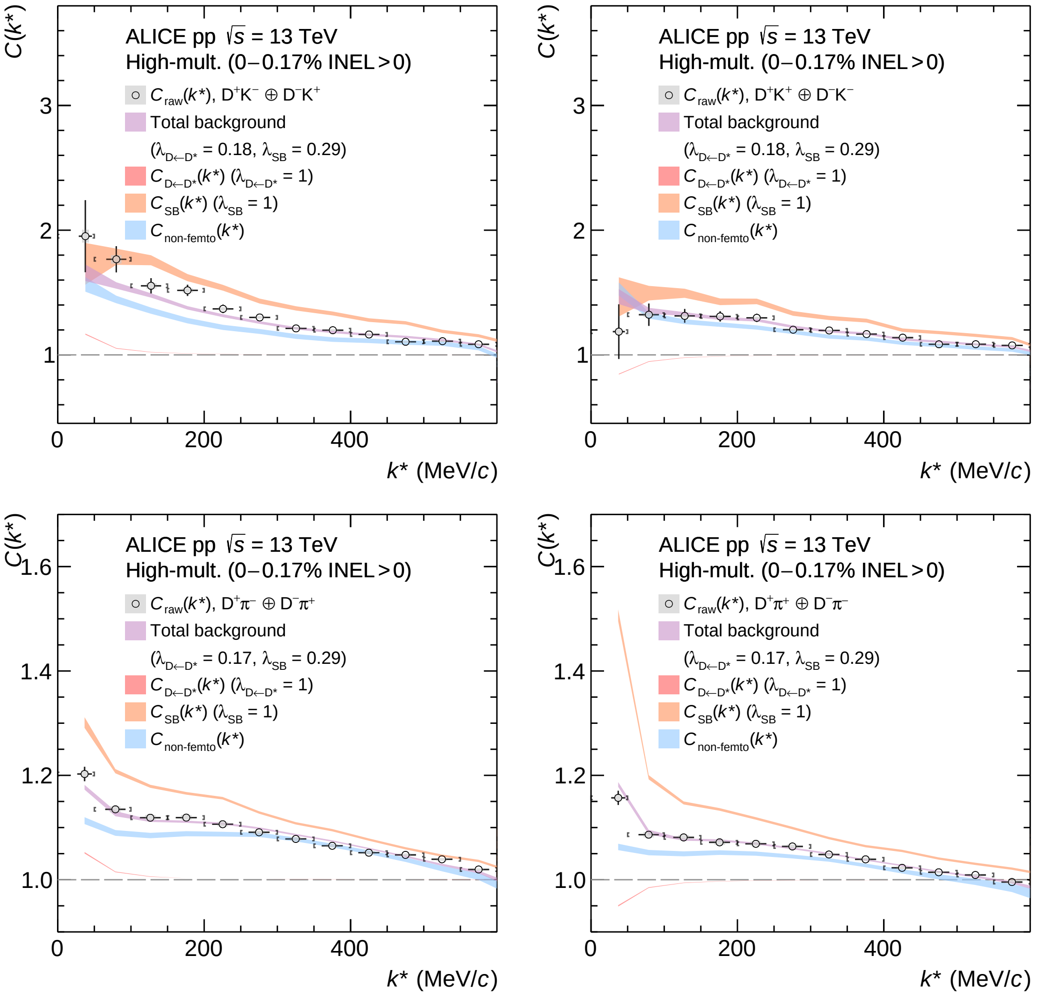

FIGURE 4.23: Experimental D–K (*upper row panels*) and D–π (*lower row panels*) raw correlation functions ($C_{\mathrm{raw}}(k^*)$) for opposite-charge (*left column panels*) and same-charge (*right column panels*) pairs with statistical (bars) and systematic uncertainties (gray shaded boxes), as well as background contributions. The width of the bands corresponds to the total uncertainty $\sigma_{\mathrm{tot}} = \sqrt{\sigma^2_{\mathrm{stat}} + \sigma^2_{\mathrm{syst}}}$. The violet band in each panel describes the total background, fitted to the data, and used to extract the genuine correlation function from the raw signal. It consists of several contributions, scaled by the appropriate λ parameter, which are shown individually and unscaled in the same figure.

candidate fractions according to the uncertainties stated in Tab. 4.10, their purity by 2% [53] and $f_{\mathrm{sec,strong}}$, by 10%, following [126], to account for the uncertainty related to the hadronic cocktail obtained from the SHM. This results in a $\sim$ 10% variation of the λ-parameter values.

- The upper limit of the range used to perform the background model fit is varied by ±50 MeV/c in order to account for possible systematic effects related to the fitting procedure.

The width of the curves in Fig. 4.23, which corresponds to the total uncertainty σ_{tot} and includes statistical and systematic errors, is obtained from a combined application of the bootstrap method and the systematic variations listed above. The background fit is performed repeatedly, each time randomly sampling the individual data points of the raw and sideband correlation functions from Gaussian distributions, whose widths and means correspond to the statistical errors and values of the points. If sufficient iterations (> 1000) are performed, a reliable distribution of fit results is obtained, whose mean and standard deviation correspond to the default fit result and statistical uncertainty σ_{stat}, respectively. By additionally including systematic variations in each iteration, σ_{tot} can be derived as the standard deviation of the resulting distribution. Assuming that statistical and systematic uncertainties are uncorrelated, i.e. $\sigma_{\mathrm{tot}} = \sqrt{\sigma^2_{\mathrm{stat}} + \sigma^2_{\mathrm{syst}}}$, it is further possible to assess the systematic uncertainties σ_{syst}.

4.4 Source

In this section, the particle emitting source of DK and Dπ pairs, which is one of the two ingredients of the Koonin-Pratt equation, defined in Eq. 2.5 and used to model femtoscopic correlations, is determined. As discussed in Sec. 3.3, it is constrained from the RSM [123], which is based on the hypothesis of a common emission source of all primordial hadrons [126] and is anchored to p–p correlation data, collected by ALICE in pp collisions at $\sqrt{s} = 13$ TeV.

The width of the Gaussian core r_{core} for DK and Dπ pairs is obtained from parametrization of its m_{T}-dependence, presented in Sec. 3.3, and the measured m_{T} of the reconstructed pairs with $k^* < 200$ MeV/c. The values can be found in Tab. 4.13.

The effective source is then determined by considering the effect of short-lived, strongly decaying resonances, feeding into the particles, which form the pairs of interest, thereby enlarging the source size. They are characterized by $\langle c\tau \rangle \lesssim 5$ fm, which is much smaller than the typical distance at which decays of excited charm and beauty hadrons into D^+ mesons occur. Therefore, only resonances feeding into the light-flavor mesons have to be considered, such as K^{*0} and $\mathrm{K}^{*\pm}$. These resonances induce an exponential tail to the Gaussian core source and the resulting effective source distributions of DK and Dπ pairs obtained from the model are shown as black dots in Fig. 4.24a and 4.24b. In order to properly account for the enhancement at large r^*, the distribution is parametrized by two Gaussian sources of width r^i_{eff} and combined with weight w, leading to

$$S_{\mathrm{eff}}(r^*) = wS^G_1(r^*) + (1-w)S^G_2(r^*). \tag{4.6}$$

The fit results are depicted as black solid lines in Fig. 4.24a and 4.24b, while the red dashed lines depict the two Gaussian distributions, which constitute $S_{\mathrm{eff}}(r^*)$. The source parameters obtained from the fit are listed in Tab 4.13.

TABLE 4.13: The m_{T} of the measured particle pairs and the corresponding core radius r_{core}, as well as the parameters of the effective source $S_{\mathrm{eff}}(r^*)$, which is given by two Gaussian distributions of width r^i_{eff} and combined with a weight w.

Pair	$\langle m_{\mathrm{T}} \rangle$ [GeV/c^2]	r_{core} [fm]	w	r^1_{eff} [fm]	r^2_{eff} [fm]
$\mathrm{D}^+\mathrm{K}^+ \oplus \mathrm{D}^-\mathrm{K}^-$	2.68	$0.81^{+0.08}_{-0.07}$	$0.78^{+0.02}_{-0.01}$	$0.86^{+0.09}_{-0.07}$	$2.03^{+0.19}_{-0.12}$
$\mathrm{D}^+\mathrm{K}^- \oplus \mathrm{D}^-\mathrm{K}^+$	2.63				
$\mathrm{D}^+\pi^+ \oplus \mathrm{D}^-\pi^-$	2.54	$0.82^{+0.07}_{-0.07}$	$0.66^{+0.03}_{-0.02}$	$0.97^{+0.09}_{-0.08}$	$2.52^{+0.36}_{-0.20}$
$\mathrm{D}^+\pi^- \oplus \mathrm{D}^-\pi^+$	2.55				

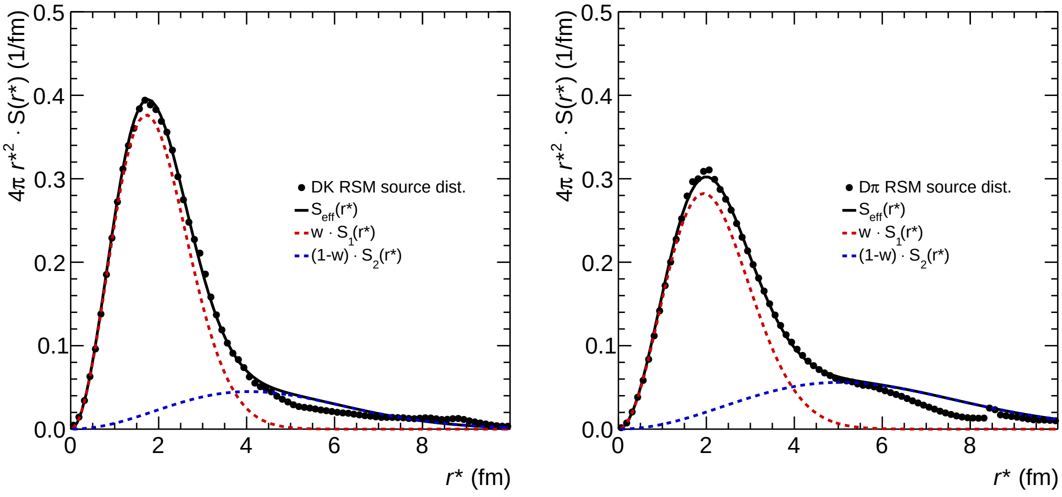

(A) DK source

(B) Dπ source

FIGURE 4.24: The effective DK and Dπ source distribution obtained from the RSM and parametrized with $S_{\text{eff}}(r^*)$. The dashed lines represent the individual single Gaussian distributions that constituent $S_{\text{eff}}(r^*)$.

Employing $S_{\text{eff}}(r^*)$ as source function in Eq. 2.5 ultimately leads to two correlation functions with the respective Gaussian sources, $S_1^G(r^*)$ and $S_2^G(r^*)$, which are properly combined by the weight w.

4.5 Results

The genuine correlation functions of DK and Dπ pairs for the same- and opposite-charge configuration are presented in Fig. 4.26. They are extracted from the raw data, following the procedure described in Sec. 4.3.3. In the femtoscopic region of $k^* < 200$ MeV/c the genuine correlation functions are sensitive to both the Coulomb and strong force. As can be seen from the plots, the correlation signals for all pairs and charge combinations only slightly deviate from unity in the low k^* region, indicating a shallow FSI. Notably, an enhancement at low k^* is visible for the opposite-charge combinations, pointing to an attractive interaction, while for the same-charge pairs, a depletion can be observed, indicating a repulsive interaction, as expected from the Coulomb force.

The data is further used to obtain information on the strong interaction by extracting the scattering length from a fit and/or comparing it to predictions by theory. This is done by means of model correlation functions, which are obtained from the Koonin-Pratt equation (Eq. 2.5) using the parametrization of the effective source $S_{\text{eff}}(r^*)$, presented in Sec. 4.4. The wave function is obtained by numerically solving the Schrödinger equation, considering both the residual electromagnetic and strong interaction. While the former is modeled using the well-understood Coulomb potential, the latter is parametrized by a Gaussian potential[5] of the form

$$V(r) = V_0 \exp\left(-m_\rho^2 r^2\right), \tag{4.7}$$

---

[5] The scattering length is independent of the shape of the strong interaction potential at low energies. Therefore, a Gaussian potential is used in the modeling, as it is perhaps the most generic phenomenological potential available.

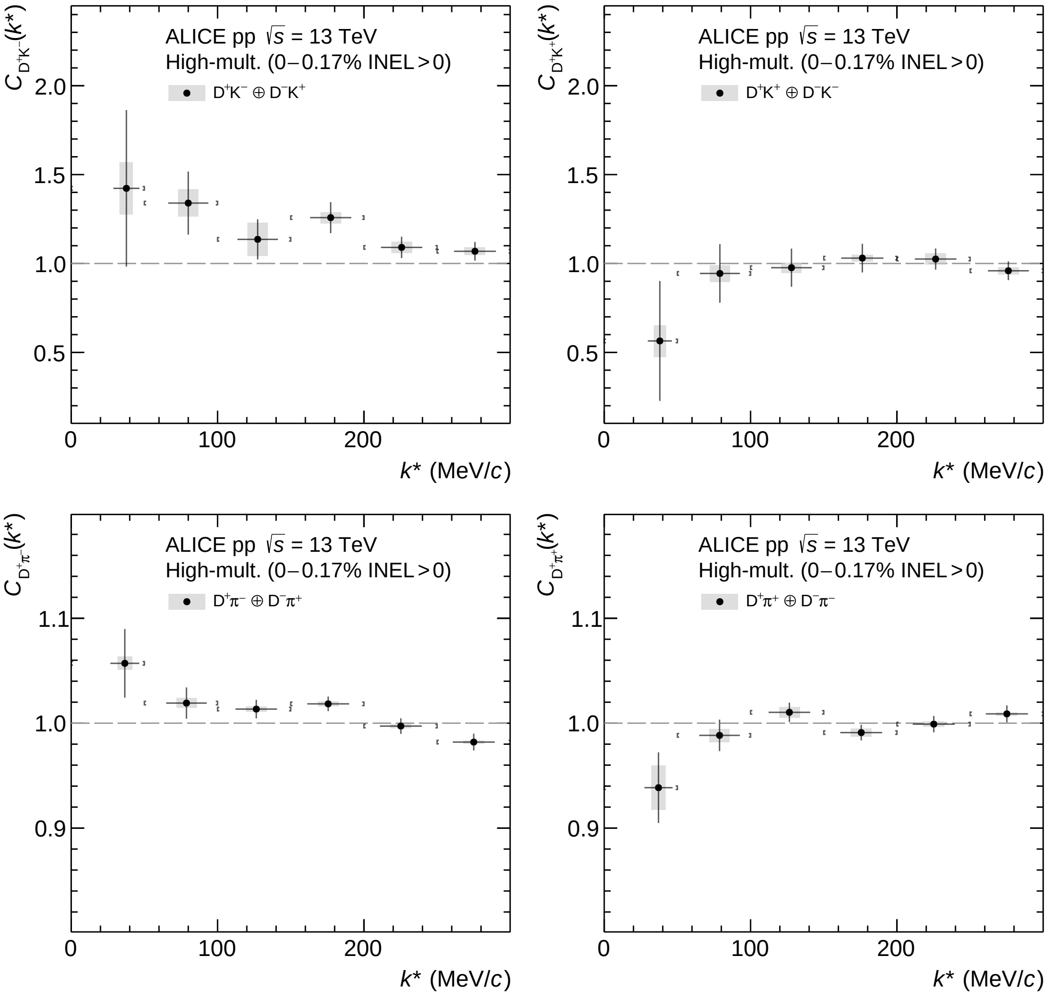

FIGURE 4.25: Genuine correlation functions with statistical (bars) and systematic uncertainties (gray shaded boxes) of DK (*upper row panels*) and Dπ pairs (*lower row panels*) for the opposite- (*left column panels*) and same-charge (*right column panels*) combination.

where V_0 is the variable potential strength and m_ρ is the parameter that controls the range of the potential, which is fixed by the mass of the lightest exchangeable meson, the ρ meson. The corresponding scattering parameters, which only depend on the free parameter V_0, can then be extracted by fitting the scattering amplitude of the potential at low momentum using the effective range expansion, as explained in detail in Sec. 2.3.2.

Since the strong interactions depends on the specific state of a system, it is classified by the relevant quantum numbers, in this case isospin I and strangeness S, leading to $\mathrm{D\overline{K}}(I = 1, 0)$, with $S = -1$, $\mathrm{DK}(I = 0)$, with $S = +1$, and $\mathrm{D}\pi(I = 3/2, 1/2)$ with $S = 0$, respectively. From an experimental point of view, however, the interactions can only be studied based on the charge of the involved particles. While the same-charge combination corresponds to a pure isospin state, the opposite-charge combination is an admixture of two isospin states[6]. In the particular case of Dπ, the

---

[6] The same-charge DK correaltion function consists of the isospin $\mathrm{DK}(I = 1)$ contribution only, while for the opposite-charge both the $\mathrm{D\overline{K}}(I = 1)$ and $\mathrm{D\overline{K}}(I = 0)$ ispspin states contribute with 50% each. The some-charge Dπ correaltion function only consists of the isospin $\mathrm{D}\pi(I = 3/2)$ contribution,

isospin state $I = 3/2$ is shared between the same- and opposite-charge configuration, as the net strangeness of the system is zero. Moreover, for the opposite-charge pairs, the coupled-channel source contribution of the $\mathrm{D}^0\pi^0$ and the $\mathrm{D}^0\overline{K^0}$ channels are accounted for and the correlation functions accessed by solving the coupled-channel Schrödinger equation for two isospin components, which are combined with the proper Clebsch-Gordan coefficients.

In the following sections, the D–K and D–π genuine correlation functions are compared to the available theory predictions, and the scattering length of the D–π strong interaction is extracted for the two isospin states $I = 3/2$ and $I = 1/2$, as the data is statistically more precise than in the D–K case.

Systematics

As the genuine correlation function is extracted from the raw data by removing all background contributions, using Eq. 4.5, its systematic uncertainty is obtained from the propagates uncertainty of the individual contributions as well as the raw data. Both have been discussed extensively in the previous Sec. 4.3.3. This leads to a relative systematic uncertainty below 1% for opposite-charge Dπ pairs, below 2% for same-charge Dπ pairs, below 10% for same-charge DK pairs, and below 15% for opposite-charge DK pairs, which is largest in the low k^* region. The difference between the relative systematic uncertainty of the D–K and D–π genuine correlation functions arises from the overall larger propagated uncertainty of the D–K raw correlation functions, which is related to the variation of the kaon selection criteria.

4.5.1 Comparison to model predictions

The genuine correlation functions are compared to model correlation functions based on the theoretical predictions available for the D–π and D–K scattering length [193–197]. The calculations, which employ χPT to extrapolate the available LQCD data to the physical mass, are briefly introduced in the following

- **L. Liu *et al.*** [193]: Lüscher's finite volume technique is employed to calculate the S-wave scattering lengths $a_0^{\mathrm{D}\pi}(I = 3/2)$, $a_0^{\mathrm{D}\overline{\mathrm{K}}}(I = 0)$, and $a_0^{\mathrm{D}\overline{\mathrm{K}}}(I = 1)$ on the lattice, which relates the scattering phase shift to the shift of the total energy ΔE of two interacting hadrons, confined within a finite box. The simulations are performed at four different unphysical light quark masses and extrapolated to the physical point by means of an expansion scheme based on SU(3) unitarized χPT at NLO. The free low-energy constants (LECs) are determined by a fit to the lattice data and also used to predict the scattering lengths of the $a_0^{\mathrm{D}\pi}(I = 1/2)$ and $a_0^{\mathrm{DK}}(I = 1)$ channels, for which no simulation was performed. The results support a molecular nature of $\mathrm{D}_{\mathrm{s}0}^*(2317)$, with DK as the major component.
- **X. Y. Guo *et al.*** [194]: The extrapolation of charm-meson masses is studied using a SU(3) chiral extrapolation scheme at N^{3}LO with unitarisation in coupled channels. The LECs are determined by a global fit to several sets of LQCD simulations of D$^+$-meson masses and scattering observables from Ref. [193] and others to impose additional constraints. Based on the fit results, the scattering lengths of the channels $\mathrm{D}\pi(I = 3/2)$, $\mathrm{D}\overline{\mathrm{K}}(I = 1)$, and $\mathrm{D}\overline{\mathrm{K}}(I = 0)$ are predicted

---

while the opposite-charge is an admixture of the $\mathrm{D}\pi(I = 3/2)$ and $\mathrm{D}\pi(I = 1/2)$ states, contributing with 66% and 33%, respectively.

at physical mass. For the other relevant channels $\mathrm{D}\pi(I=1/2)$ and $\mathrm{DK}(I=1)$, the scattering lengths are deduced from the phase shift predictions, published in the paper, where the former is directly constrained by LQCD data.

- **Z. H. Guo *et al.*** [195]: Unitarized SU(3) χPT at NLO is employed to study the scattering between light-flavor and D^{+} mesons. The free parameters of the theory are constrained by fitting LQCD simulations of the finite-volume spectra and scattering lengths of different channels, including the ones obtained in Ref. [193]. A chiral extrapolation scheme is used to predict the scattering lengths at the physical point. The calculation is performed on different sets of data, denoted by Fit-1B and Fit-2B, respectively. While $\mathrm{D}_{\mathrm{s0}}^{*}(2317)$ is a bound state in Fit-2B, the results of Fit-1B imply a virtual state.

- **B. L. Huang *et al.*** [196]: By fitting the LQCD simulation of scattering lengths and D^{+}-meson masses from Ref. [193], as well as using the lattice values of f_{π} and f_{K}, the LECs of a Lagrangian formulated within SU(3) heavy-meson χPT at N^{3}LO are determined. Two different formulations of the scattering length are used in the fitting, the perturbative and the iterated, respectively. The latter is based on a Lippmann-Schwinger equation with a cutoff range scale to obtain a finite result. Both approaches are used to predict the scattering length at physical masses, and in the fit that employs the iterated formulation of the scattering length, the LQCD simulation of $a_0^{\mathrm{DK}}(I=0)$ [198] is included as well. Notably, the values obtained from applying the perturbative method do not seem to converge properly for the DK and $\mathrm{D}\overline{\mathrm{K}}$ systems, and in this thesis, results from the iterated method are used. The results support a physical $\mathrm{D}_{\mathrm{s0}}^{*}(2317)$ bound state.

- **J. M. Torres-Rincon *et al.*** [197]: The correlation functions of $\mathrm{D}\pi$ and DK pairs are calculated in both charge configurations. The two-particle wave function is derived from an off-shell T-matrix calculation in a coupled-channel basis, employing unitarized χPT at NLO. The corresponding LECs are taken from Fit-2B in Ref. [195]. Within the framework, the $\mathrm{D}_{0}^{*}(2300)$ and $\mathrm{D}_{\mathrm{s0}}^{*}(2317)$ states are dynamically generated as double-pole structure and meson-meson bound state, respectively. The lower pole of the former leads to a depletion in the opposite-charge D–π correlation function at ~ 240 MeV/c.

The scattering lengths predicted by these models are collected in Tab. 4.14 and 4.15. Besides in the $\mathrm{D}\overline{K}(I=0)$ channel, the values are rather small, especially in comparison to the N–N scattering length of $a_0^{\mathrm{NN}} \sim 16-19$ fm [199–201] in the $^{1}S_{0}$ channel. Further, while most of the models predict similar scattering lengths, the calculation of B. L. Huang *et al.* results in a much larger attraction in the $\mathrm{D}\overline{K}(I=0)$ and arguably also the $\mathrm{D}\pi(I={}^{1}\!/_{2})$ channel. It is performed in heavy-meson χPT, which, in contrast to the other approaches, is not unitarized.

The authors of Ref. [197] have directly provided the correlation functions for the different charge combinations in a private communication, using the effective source parametrization presented in Sec. 4.4. The correlation functions for the other models were calculated by Dr. Yuki Kamiya and built following the procedure explained in the beginning of this section, i.e., tuning the strength V_0 of the Gaussian potential (Eq. 4.7) such as to reproduce the predicted scattering lengths [159].

The resulting theoretical correlation functions, which account for the strong interaction between D^{+} and light-flavors mesons predicted by the various models, as well as the Coulomb interaction, are compared to the measured genuine correlation

TABLE 4.14: Scattering lengths of the available theoretical models for the D–π interaction. The values are reported separately for the two isospin states $I = 1/2$ and $I = 3/2$. Values denoted with * are deduced from the published phase shifts.

Model		a_0 (fm)	
		D$\pi(I = 3/2)$	D$\pi(I = 1/2)$
L. Liu *et al.* [193]		-0.100 ± 0.002	$0.37^{+0.03}_{-0.02}$
X. Y. Guo *et al.* [194]		-0.11	0.33^*
Z. H. Guo *et al.* [195]	Fit-1B	$-0.101^{+0.005}_{-0.003}$	$0.31^{+0.01}_{-0.01}$
	Fit-2B	$-0.099^{+0.003}_{-0.004}$	$0.34^{+0.00}_{-0.03}$
B. L. Huang *et al.* [196]		-0.06 ± 0.02	0.61 ± 0.11
J. M. Torres-Rincon *et al.* [197]		-0.101	0.423

functions in Fig. 4.26. The difference between the data and the predictions is quantified by the number of standard deviations n_σ and reported in the figure legends. Each n_σ is calculated from the p-value in the range of $k^* < 200$ MeV/c, taking into account the total uncertainty of both the data and the predictions.

As a reference, also the correlation function obtained from the Coulomb-only hypothesis (gray curve) is shown in the figures and any deviation from the experimental data is associated with the presence of a residual strong force among the particles. It can be seen that the correlation functions of all the analyzed pairs are adequately described by the Coulomb interaction alone, indicating a shallow strong interaction between the D^+ and light-flavor hadrons. The $n_\sigma = 2.72$ reported for the Coulomb-only hypothesis in the case of $\mathrm{D}^+\mathrm{K}^- \oplus \mathrm{D}^-\mathrm{K}^+$ pairs is related to the fluctuating data point at $k^* \sim 180$ MeV/c. By only considering data points with smaller k^*, the n_σ value reduces to 1.76, indicating that the Coulomb interaction adequately describes the measurement in the sensitive region.

The current statistical precision of the D–K data is not sufficient to distinguish between the individual models of the residual strong interaction, as well as the

TABLE 4.15: Scattering lengths of the available theoretical models for the D–K interactions. The values are reported separately for the different strangeness and isospin states, which are $S = -1$, corresponding to D$\overline{\mathrm{K}}$, and $S = +1$, corresponding to DK, as well as $I = 0$, and $I = 1$, respectively. The real and imaginary components are associated with elastic and inelastic processes. Values denoted with * are deduced from the published phase shifts.

Model		a_0 (fm)		
		DK$(I = 1)$	D$\overline{\mathrm{K}}(I = 1)$	D$\overline{\mathrm{K}}(I = 0)$
L. Liu *et al.* [193]		$0.07 \pm 0.03 + 0.17^{+0.02}_{-0.01}i$	-0.20 ± 0.01	$0.84^{+0.17}_{-0.22}$
X. Y. Guo *et al.* [194]		$-4.87 \cdot 10^{-2*}$	-0.22	0.46
Z. H. Guo *et al.* [195]	Fit-1B	$0.06^{+0.05}_{-0.03} + 0.30^{+0.09}_{-0.05}i$	$-0.18^{+0.01}_{-0.01}$	$0.96^{+1.44}_{-0.44}$
	Fit-2B	$0.05^{+0.04}_{-0.03} + 0.17^{+0.02}_{-0.03}i$	$-0.19^{+0.02}_{-0.02}$	$0.68^{+0.17}_{-0.16}$
B. L. Huang *et al.* [196]		-0.01 ± 0.03	-0.24 ± 0.02	1.81 ± 0.48
J. M. Torres-Rincon *et al.* [197]		$-0.027 + 0.083i$	-0.233	0.399

Coulomb-only hypothesis. For the $\mathrm{D}^+\mathrm{K}^+ \oplus \mathrm{D}^-\mathrm{K}^-$ system, no tension with theory is observed, which is reflected by small n_σ values. The overall larger deviations reported for the $\mathrm{D}^+\mathrm{K}^- \oplus \mathrm{D}^-\mathrm{K}^+$ system are again associated with the fluctuation of the fourth data point. The D–π correlation functions, on the other hand, deviate significantly from the curves that account for the residual strong force and are incompatible with all the available theoretical predictions, reflected by large n_σ values. The data clearly favor the Coulomb-only hypothesis. In the case of $\mathrm{D}^+\pi^+ \oplus \mathrm{D}^-\pi^-$ pairs, the deviation between data and models is not as pronounced as for $\mathrm{D}^+\pi^- \oplus \mathrm{D}^-\pi^+$, where the predicted attraction is enhanced by seizable coupled-channel effects mainly arising from the transition $\mathrm{D}^+\pi^- \leftrightarrow \mathrm{D}^0\pi^0$. However, also in that case the Coulomb-only hypothesis is preferred. Since most of the models predict very similar scattering parameters, the corresponding correlation functions are close to each other or even overlap, resulting in comparable n_σ values. An exception is the

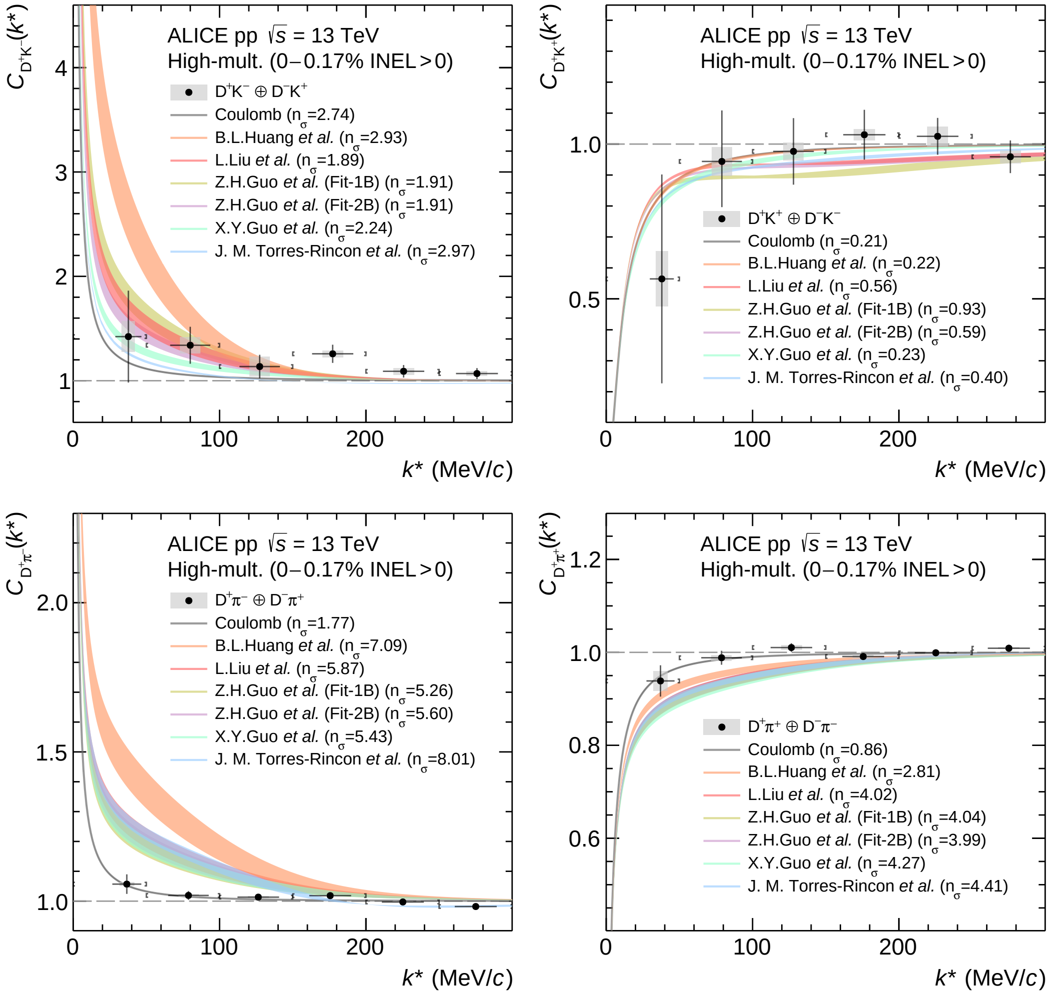

FIGURE 4.26: Measured genuine correlation functions in comparison to the theoretical model predictions (colored bands), listed in Tables 4.14 and 4.15, and the Coulomb-only hypothesis (gray band). The width of the bands represents the uncertainty related to the source. The number of standard deviations n_σ is reported in the legend for each model. The results are shown for DK (*upper row panels*) and Dπ (lower row panels) pairs for the opposite- (*left column panels*) and same-charge (*right column panels*) combinations.

model correlation function obtained from the scattering parameters provided by B. L. Huang *et al.*. Notably, the model performs worse with respect to the others in the opposite-charge case, as it predicts larger scattering lengths for the $\mathrm{D}\pi(I = 1/2)$ and $\mathrm{D}\overline{K}(I = 0)$ channel, respectively. In the same-charge case, the opposite is observed, and the slightly less repulsive model correlation function is closer to the data. It should also be mentioned, that the model of J. M. Torres-Rincon *et al.* is the least compatible with the data. This is, however, mostly related to the small uncertainties of the predicted correlation functions, which are considered in the calculation of the n_σ reported in the figures. Moreover, it is the only model that reproduces the depletion in the measured opposite-charge D–π correlation function at $k^* \sim 240$ MeV/c, which is ascribed to the lower pole of the $\mathrm{D}_0^*(2300)$ state. In summary, the D–K correlation functions do not put constraints on the theory due to the limited statistics of the data, while the D–π data is incompatible with the available predictions of the residual strong interaction. All measurements are well described by the Coulomb interaction.

4.5.2 Scattering length of the strong interaction

The D–π genuine correlation functions are used to extract the S-wave scattering length a_0 of the strong interaction for both isospin states $I = 1/2$ and $I = 3/2$. The strong force is parametrized by the Gaussian potential, given in Eq. 4.7. As the isospin $I = 3/2$ state is shared among both charge combinations, the corresponding potential strength $V_0^{I=3/2}$ is a common fit parameter of the two correlation functions. A simultaneous χ^2 minimization within $k^* < 250$ MeV/c is performed to determine $V_0^{I=3/2}$ and $V_0^{I=1/2}$ and the corresponding scattering lengths. The available parameter ranges are $V_0^{1/2} \in [-2000, 5000]$ MeV and $V_0^{3/2} \in [-3000, 4000]$ MeV, and the step size is 100 MeV for both[7]. Figure 4.27 shows the correlation functions obtained from the combined fit to the data as red bands. The corresponding χ^2/ndf is 0.7 within $k^* < 250$ MeV/c.

The scattering lengths of the Dπ system are found to be

$$\begin{aligned} a_0^{\mathrm{D}\pi}(I = 3/2) &= (0.01 \pm 0.02\ (\mathrm{stat.}) \pm 0.01\ (\mathrm{syst.}))\ \mathrm{fm}, \\ a_0^{\mathrm{D}\pi}(I = 1/2) &= (0.02 \pm 0.03\ (\mathrm{stat.}) \pm 0.01\ (\mathrm{syst.}))\ \mathrm{fm}. \end{aligned} \tag{4.8}$$

The correlation between the two is shown in Fig. 4.28, where the dark (light) violet-shaded area represents the confidence intervals for a 68% (95%) probability. Within the uncertainties, the scattering lengths of the residual strong interaction between D^+ and light-flavor mesons are compatible with zero. They are further compared to the theoretical values reported in Tab. 4.14. In the $I = 1/2$ channel, the deviation between the fit result and the predictions by theory, which cover values between ~ 0.3 and ~ 0.6 fm, is significant. Depending on the model, $5 - 13\sigma$ are obtained. Tension with the predictions is also observed in the $I = 3/2$ channel, which is shared between the same- and opposite-charge D–π correlation function. With deviations of $2 - 5\sigma$, it is, however, smaller and less significant than in the $I = 1/2$ channel.

---

[7] The model correlaion functions for the different potnetial strenghts were calculated by Dr. Yuki Kamiya.

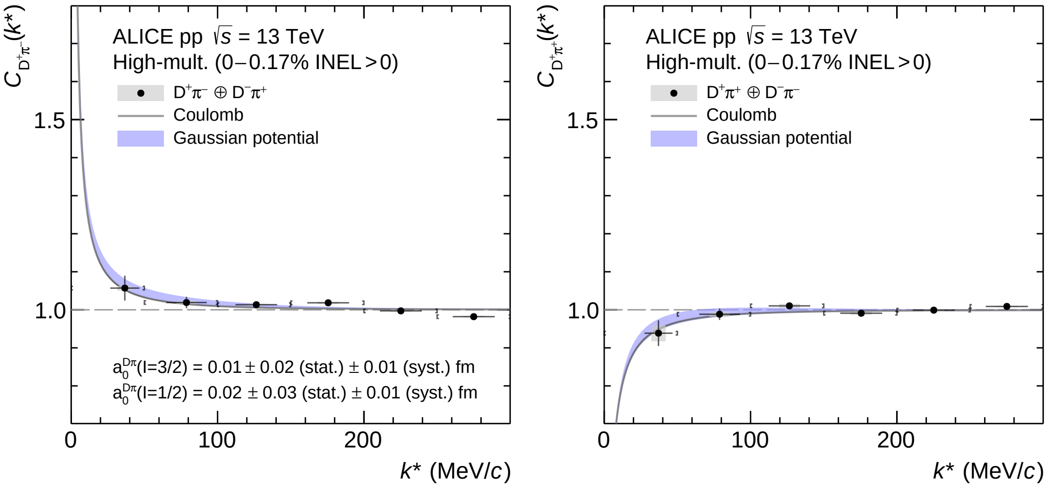

FIGURE 4.27: Comparison of the D–π genuine correlation functions of opposite- (*left panel*) and same-charged (*right panel*) pairs with the results of the χ^2 minimization using a Gaussian potential to parameterize the strong interaction (violet band). The correlation functions obtained from the Coulomb-only assumption are depicted as well (gray band). The width of the bands corresponds to the total uncertainty.

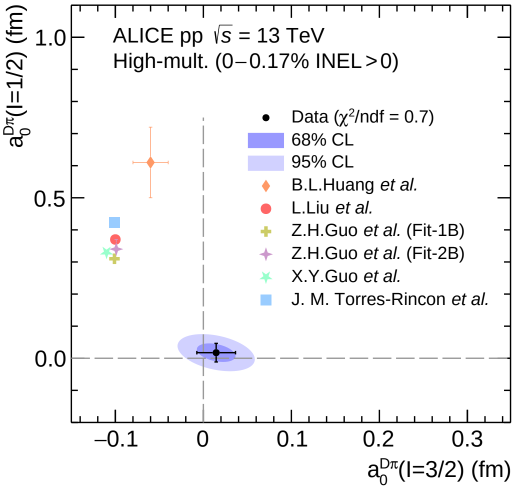

FIGURE 4.28: Scattering length of the two Dπ isospin states, extracted from a simultaneous χ^2 minimization to the experimental correlation functions. The dark (light) violet-shaded areas represent the resulting confidence intervals for a 68% (95%) probability. The dashed lines correspond to the Coulomb-only hypothesis, which is characterized by a vanishing scattering length. The available theory predictions [193–197], listed in Tab. 4.14, are shown as comparison.

Systematics

The scattering lengths of the strong FSI of the Dπ system are extracted by fitting model correlation functions to the data. To properly estimate the statistical uncertainties σ_{stat} the bootstrap method is applied, which has already been introduced in Sec. 4.3.3. By additionally accounting for the systematic uncertainty of $C_{\mathrm{gen}}(k^*)$

in the sampling of the data, varying the parameters of the effective source according to the uncertainties reported in Table 4.13, as well as changing the fit range by ±50 MeV/c in each bootstrap iteration, the total error σ_{tot} is obtained. The systematic error σ_{syst} is then derived by assuming that statistical and systematic uncertainties are uncorrelated, i.e., $\sigma_{\mathrm{tot}} = \sqrt{\sigma^2_{\mathrm{stat}} + \sigma^2_{\mathrm{syst}}}$. The uncertainty on the source represents the largest contribution to systematic uncertainties of the scattering length.

4.5.3 Consistency check with measurements involving D^*mesons

Form heavy-quark spin symmetry [202, 203], it is expected that the interaction of light-flavor mesons with pseudoscalar (D^+) or vector (D^{*+}) charm mesons is the same at leading order. In Ref. [186], the correlation functions of $\mathrm{D}^*\pi$ and $\mathrm{D}^*\mathrm{K}$ pairs are studied in parallel to $\mathrm{D}\pi$ and DK, following the similar analysis procedure as presented in this chapter. Equivalent results are obtained, however, with lower statistical precision. All genuine correlation functions involving D^{*+} and light-flavor mesons are compatible with the Coulomb-only hypothesis and the scattering lengths of the $\mathrm{D}^*\pi$ system

$$\begin{aligned} a_0^{\mathrm{D}^*\pi}(I = 3/2) &= (0.05 \pm 0.04\ (\mathrm{stat.}) \pm 0.02\ (\mathrm{syst.}))\ \mathrm{fm}, \\ a_0^{\mathrm{D}^*\pi}(I = 1/2) &= (-0.03 \pm 0.05\ (\mathrm{stat.}) \pm 0.02\ (\mathrm{syst.}))\ \mathrm{fm}, \end{aligned} \tag{4.9}$$

are consistent with the ones extracted for $\mathrm{D}\pi$, given in Eq. 4.8. Furthermore, the experimental results disagree with the only available values directly calculated in this channel and predicted by the model of Z. W. Liu *et al.* [204], which are $a_0^{\mathrm{D}^*\pi}(I = 3/2) = (-0.13 - 0.00036i)$ fm and $a_0^{\mathrm{D}^*\pi}(I = 1/2) = (0.27 - 0.00036i)$ fm, respectively. Figure 4.29 shows the correlation between the scattering lengths for the two isospin states obtained from the fit to the data, as well as those obtained in the $\mathrm{D}\pi$ channel. The agreement between the two channels strengthens the experimental results obtained for $\mathrm{D}\pi$ pairs.

4.5.4 Possible explanations for discrepancies between data and predictions

The discrepancy between the experimental data and the predictions by theory in the $\mathrm{D}\pi$ channel is puzzling. It could be diminished by a much larger effective source size, which leads to a less pronounced correlation signal for a given interaction strength. However, there is no obvious motivation for assuming a breaking of the universal m_{T} scaling of the core radius [123, 126] for pairs that involving charm mesons, especially as the resonance–source model was already successfully used in the analysis of the experimental pD^- correlation function [53]. However, it could be that heavy-flavor particles hadronize earlier than light-flavor mesons, similar to the early production of charm quarks in HIC that was mentioned in the introduction of this chapter. A MC study, shown in Fig. 4.30, hints at such behavior. If the D^+ meson is indeed produced prior to kaons and pions, it will propagate by a certain amount before any FSI with light-flavor mesons can take place. This could lead to modifications of the $\mathrm{D}\pi$ and DK source core radius, not accounted for in the RSM.

Alternatively, other complex structures not taken into account by the theory models considered in this analysis could explain the deviations. In Ref. [205] the molecular nature of the two axial resonances $\mathrm{D}_1(2430)$ and $\mathrm{D}_1(2420)$ are studied using a hidden gauge formalism and implementing unitarization in coupled channels.

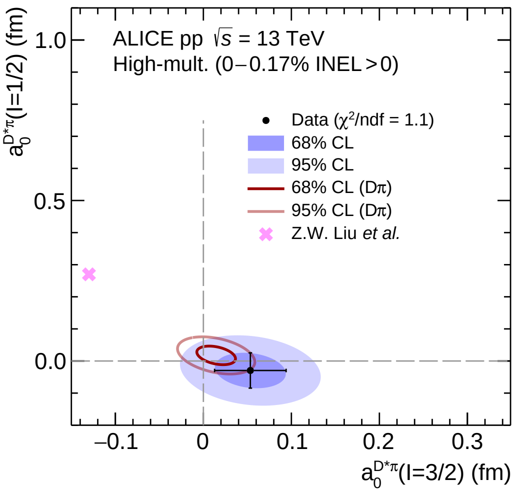

FIGURE 4.29: Scattering length of the two $\mathrm{D}^*\pi$ isospin states, extracted in Ref. [186] from a simultaneous χ^2 minimization to the experimental correlation functions of. The dark (light) violet-shaded area represents the resulting confidence interval for a 68% (95%) probability. The dashed lines correspond to the Coulomb-only hypothesis, which is characterized by a vanishing scattering length. The available theory prediction [204] is shown as a comparison. The 68% (95%) CL from the fit to the D–π data is also depicted as the area enclosed by the dark (light) red line.

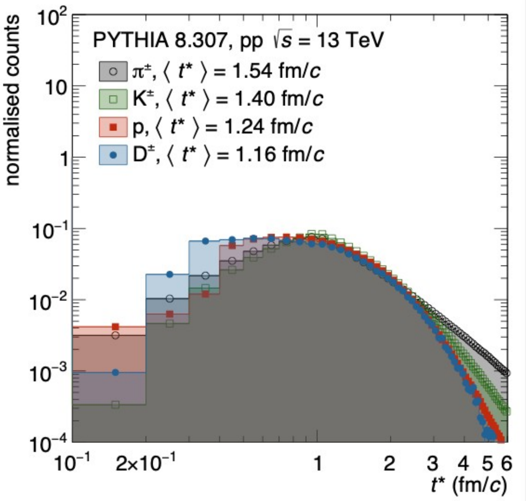

FIGURE 4.30: The hadronization time distribution for several species, studied with PYTHIA 8.307. Figure by the courtesy of F. Grosa.

The scattering amplitude of D$^*\pi$ and Dρ, which are part of the meson−baryon basis considered in the work, are determined by explicitly adding a bare quark-model pole structure. By tuning the parameters of the pole such as to better accommodate D$_1$(2430) within the experimental observations [206, 207] (denoted as Model B in their publication), a scattering length of $a_0^{\mathrm{D}^*\pi}(I = 1/2) = 0.1$ fm is obtained, which is much closer to the value of $a_0^{\mathrm{D}\pi}(I = 1/2) = (0.02 \pm 0.03\ (\mathrm{stat.}) \pm 0.01\ (\mathrm{syst.}))$ fm obtained for D–π in this chapter. Using arguments of heavy-quark spin symmetry, the authors expect a similar scattering length for the Dπ system. Using a different set of parameters, scattering lengths in agreement with theory predictions are obtained (denoted as Model A in their publication). Such findings challenge the current understanding of the residual strong interaction among charm mesons and pions.

4.6 Conclusions

The residual strong interaction of D$^+$ and the light-flavor π and K mesons is studied using the femtoscopy technique, providing the first experimental results for these channels. The correlation functions of same- and opposite-charge particle pairs are measured in HM pp collisions at $\sqrt{s} = 13$ TeV using data collected by ALICE at the LHC. The raw data is further corrected for background contributions, and the genuine D–K and D–π correlation functions are compared to the available theoretical predictions of the strong interaction, also taking into account the Coulomb force, shown in Fig. 4.26. Within the current limited statistical precision of the DK data, no preference is observed between the different models and the Coulomb-only hypothesis. In the case of Dπ, the data is more precise and suggests that the theoretical predictions overestimate the residual strong interaction. The Coulomb interaction alone is sufficient to describe the data. The Dπ correlation functions are further used to determine the scattering length of the two isospin states $I = 1/2$ and $I = 3/2$ of the system by a simultaneous fit to the data of same- and opposite-charge pairs, as both have contributions from the isospin $I = 3/2$ state. A Gaussian potential with variable strength is used to parameterize the strong interaction for each state. The scattering lengths, extracted from the scattering amplitude of the potential using the effective range expansion, are found to be small and compatible with zero. Figure 4.28 shows the experiential values compared to the ones predicted by theory. Especially in the $I = 1/2$ channel, a significant disagreement of $> 5\sigma$ is observed. These findings challenge the current understanding of the residual strong interactions of D$^+$ and pions, especially as similar experimental results were obtained in the D$^*\pi$ channel [186] using the same analysis method, which is expected by heavy-quark spin symmetry.

The results are also relevant for the interpretation of heavy-ion observables related to D$^+$ mesons, which are used to infer the properties of the QGP, as discussed at the beginning of this chapter. Since the strong interaction is found to be shallow, the rescattering of D$^+$ with light-flavor mesons during the hadronic phase of the system might also be smaller than expected.

Future studies using the large data set collected during the current LHC Run 3 data-taking period will make it possible to measure the correlation functions with higher precision. This is especially relevant for studying the DK system. Additionally, further studies regarding the emission of charm mesons might be useful, as an earlier hadronization with respect to light-flavor mesons could affect the source function of the pairs. A significant increase in the mean relative distance of the pairs would wash out signals from FSI and lead to a more shallow correlation function compatible with the data. Larger data sets will also facilitate studying the correlation functions of other particle pairs involving charm hadrons. This is essential, as for now, there is no alternative experimental approach available to study the strong interaction among pairs that include charm particles.

Chapter 5

Spin-dependent p–ϕ interaction

Nucleons (N) and ϕ mesons ($s\bar{s}$) do not have common flavor valence quarks. Hence, the Pauli exclusion principle, which leads to a repulsive core in the N–N interaction potential, does not apply. Furthermore, the diagram depicting the N–ϕ interaction process is characterized by disconnected quark lines and can be separated into two disconnected diagrams by removing the gluon lines. Therefore, the N–ϕ interaction is expected to be suppressed because of the Okubo-Zweig-Iizuka (OZI) rule [208–210]. However, the QCD van der Waals force, characterized by multigluon instead of quark-exchange, could lead to a considerable attractive interaction [211–213]. At long ranges, where the dominant degrees of freedom are the lightest hadronic states and gluons hadronize into pions, the major contribution to the interaction between the two particles is associated with the two pion exchange (TPE) [214–217]. Within the constituent quark model, the attraction arises mainly from σ exchange [218], which is a one-boson exchange and similar to the TPE [219]. Further, if inelastic channels such as $\mathrm{N}\phi \rightarrow \mathrm{K}^{*}\Lambda(\mathrm{K}^{*}\Sigma)$ are taken into account, the interaction can proceed via OZI allowed couplings, e.g. via kaon exchange.

Precise knowledge of the p–ϕ interaction is of particular interest because of the possible existence of a ϕ-mesic bound state with nucleons, which has been predicted by various models [212, 213, 218, 220–225], however, never tested on data or observed experimentally. First theoretical investigations followed a study on nuclear-bound charmonium ($c\bar{c}$) where an effective Yukawa-type potential was used to describe the QCD van der Waals force [226]. The potential parameters were estimated by relating the vector-exchange parts of the high-energy hadron-nucleon scattering amplitude in the forward direction to the vector contribution of the multigluon-exchange potential at low energies. The same type of potential was used to model the N–ϕ interaction and was found to be fully attractive and strong enough to bind a ϕ meson onto a nucleon inside a nucleus, thus forming a bound state [213]. This potential was used to model the N–ϕ interaction in later studies of A-body systems involving ϕ mesons and nucleons [212, 222], also resulting in a bound state. A quasi-bound N–ϕ state was predicted in a study based on an extension of the constituent quark model, where the coupling between the N–ϕ and Λ–K* channel was taken into account and found to be considerable [218]. The model parameters were obtained by a fit to the N–N scattering data. Similarly, a unitary coupled-channel approach, anchored to the experimental scattering length of the p–ϕ interaction determined by ALICE [51], leads to a two-pole structure in the scattering amplitude, where one of the two poles could be associated with a possible pϕ bound state [225].

However, several other theoretical calculations of the N–ϕ interaction do not support a bound state formation. Studies of the vector-meson–baryon interaction, based on extensions of chiral Lagrangians, where vector mesons are accommodated within a coupled channel unitary scheme [227–230], lead to dynamically generated resonances, which mostly couple to the K*–Σ and K*–Λ channels, but no bound

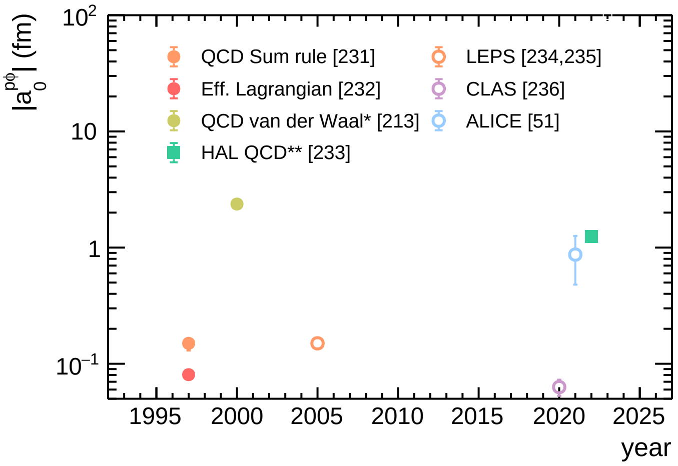

FIGURE 5.1: The spin-averaged, absolute value of the p–ϕ scattering length obtained from the available theoretical calculations and simulations (listen in the left column of the legend) as well as measurements (listen in the right column of the legend) in chronological order.
* The value is not directly provided in Ref. [213] but extracted from the published potential via the effective range expansion of the corresponding scattering amplitude, given by Eq. 2.30.
** The value depicted in the plot is the one estimated at physical masses, for which no uncertainties are given in the Ref. [233].

states. For some of these resonances, the coupling to the pϕ channel is seizable [228]. A direct calculation of the spin-averaged N–ϕ scattering length within the framework of the QCD sum rule resulted in a value of $a_0^{p\phi} = (0.15 \pm 0.02)$ fm [231]. In Ref. [232] the N–ϕ scattering amplitude was modeled by an effective Lagrangian that combines chiral SU(3) dynamics with vector meson dominance (VMD)[1] and a scattering length of $a_0^{p\phi} = (0.01 - i \cdot 0.08)$ fm was obtained [232]. The dominant imaginary part is mainly associated with the inelastic channels N–ϕ → KΛ, KΣ included in the calculation. From the Yukawa-type potential describing an attractive QCD van der Waals force between ϕ and nucleons in Ref. [213], a scattering length of $a_0^{p\phi} \approx 2.37$ fm is estimated. On the lattice, only the spin 3/2 channel of the N–ϕ interaction is available for the moment since the spin 1/2 contribution shows signs of open channels. A scattering length of $a_0^{p\phi}(s = 3/2) \approx 1.25$ fm was estimated for physical masses [233]. Details of the LQCD simulation can be found in Sec 5.2.

---

[1] VMD is used to describe the interaction of energetic photons with hadronic matter, assuming that a physical photon can fluctuate into a virtual vector meson that subsequently scatters elastically on the target proton via multigluon exchange.

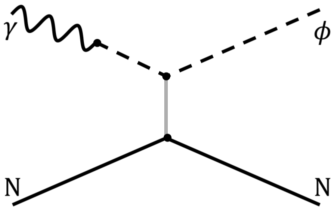

It is used to interpret the differential cross section of near-threshold vector meson V photoproduction, linking γp → Vp to Vp → Vp

On the experimental side, only spin-averaged p–ϕ scattering parameters are available. The LEPS collaboration measured the differential cross section of ϕ-meson photoproduction from protons, using a beam of linearly polarized photons from the threshold energy of $E_\gamma = 1.57$ GeV up to 2.37 GeV [234]. The data at the threshold were found to be in qualitative agreement with the value calculated from the scattering length of ~ 0.15 fm predicted in Ref. [231] assuming VMD and using the optical theorem [235]. Similarly, the total ϕ cross-section in $\gamma\text{p} \rightarrow \phi\text{p}$ reactions with near-threshold photons of $E_\gamma = 1.63 - 2.82$ GeV has been measured by the CLAS collaboration. Again, the data were interpreted using the VMD model, and a scattering length of $|a_0| = (0.063 \pm 0.010)$ fm was obtained [236].

The most recent experimental result was obtained by the ALICE collaboration in a measurement of the p–ϕ correlation function in pp collisions at $\sqrt{s} = 13$ TeV [51]. Details on the analysis procedure can be found in Sec. 5.1. The data were modeled using the simplistic Lednický–Lyuboshits approach, which is explained in Appendix A. A spin-averaged scattering length of $a_0^{\text{p}\phi} = (0.85 \pm 0.34(\text{stat.}) \pm 0.14(\text{syst.}) + i \cdot 0.16 \pm 0.10(\text{stat.}) \pm 0.09(\text{syst.}))$ fm was extracted. The scattering length is much larger than the values obtained from ϕ-photoproduction measurements. Possible explanations are given in Ref. [237]. The ϕ meson scattering off the nucleon in ϕ-photoproduction is not at equilibrium, and the N–ϕ interaction may be suppressed near the threshold as the $s\bar{s}$ pair in a point-like configuration lacks time to form a complete ϕ wave function. Hence, the proton interacts with this smaller "young", undressed ϕ meson. This effect is known as the young meson effect [238]. More recent studies of the VMD based on calculations with Dyson Schwinger equations found that conclusions based on VMD involving heavy mesons are unreliable [239]. This can be seen as a more formal alternative explanation of the young meson effect. Finally, since the virtual ϕ mesons from the conversion of the incident photons are off-shell, it may be difficult to determine the scattering length phenomenologically by using VMD [237].

Figure 5.1 depicts the scattering length of the p–ϕ interaction obtained from the various aforementioned theoretical calculations and experimental measurements. An additional study has been carried out to pin down the spin 1/2 component of the p–ϕ interaction by a fit to the experimental correlation function published by ALICE and constraining the spin 3/2 contribution from the published LQCD potential. Details on the experimental input can be found in Sec. 5.1, while Sec. 5.2 focuses on the LQCD simulated potential of the spin 3/2 channel. The analysis and the evaluation of the systematic uncertainties are discussed in Sec. 5.3 and Sec. 5.4, respectively, and the results presented in Sec. 5.5, which precedes a final conclusion in Sec. 5.6.

5.1 The experimental correlation function

The genuine p–ϕ correlation function, which is re-analyzed in this chapter, was obtained as a result of my master thesis project [51, 240] from HM pp collision data at $\sqrt{s} = 13$ TeV, collected by ALICE from 2016 to 2018 during the LHC Run-2.

Events are selected using the same cuts as listed in Tab. 4.1 and discussed in detail in Sec. 4.1, which include the standard quality selections by ALICE. Moreover, to minimize the pronounced contribution from minijets, which have already been introduced in Sec. 2.2, and additional cut on the transverse sphericity [2] of $0.7 < S_T < 1.0$ is applied to select rather spherical events and reduce jet-like contributions. The proton selection follows Ref. [43], and the resulting candidates have a purity of 99%, with a primary fraction of 82%. The ϕ mesons are reconstructed from their hadronic decay to charged kaons $\phi \rightarrow K^+K^-$ with a branching ratio of $\mathrm{BR} = (49.2 \pm 0.5)\%$ [122]. The selection of the kaon daughters is tuned to produce a large ϕ sample while maintaining a high purity. Details on the selection criteria can be found in Ref. [51]. Two oppositely charged daughter candidates are then combined to calculate the $K + K^-$ invariant mass, where the ϕ candidates are selected within a window of $\pm 8\,\mathrm{MeV}/c^2$ around their nominal mass. The resulting p_T-integrated spectrum is depicted in Fig. 5.2. The purity and yield of the ϕ candidates are extracted by fitting the resonance peak with a Voigt function (blue line), which is the convolution of a relativistic Breit-Wigner and a Gaussian. The former describes the natural line width and depends on the mass of the resonance M_ϕ, while the latter accounts for the detector resolution, given by its width σ. The combinatorial K^+K^- background is described by a quadratic polynomial (red line), and the result of the combined signal and background fit to the measured $K + K^-$ invariant mass is shown in green. The extracted $M_\phi = 1019.550 \pm 0.002\ \mathrm{MeV}/c^2$ is consistent with the literature value of $M_{\phi,\mathrm{PDG}} = (1019.461 \pm 0.016)\ \mathrm{MeV}$ [122] within the detector resolution $\sigma = 1.44\ \mathrm{MeV}/c^2$. By integrating the total fit function over the ϕ selection interval, a yield of 5.8×10^6 candidates is estimated. Similarly, the purity is obtained as $S/(S+B)$, the ratio of signal candidates S over the total yield $S + B$, which also includes the combinatorial background B. It is found to be 66%. Further, the ϕ mesons are assumed to be 100% primary particles, as the amount of secondaries is negligible [122].

The raw correlation function is obtained from Eq. 2.10 and normalized in the region $k^* \in [800, 1000]\ \mathrm{MeV}/c$. A total of 4.17×10^4 pϕ and 3.61×10^4 $\overline{\mathrm{p}}\phi$ pairs with $k^* < 200\,\mathrm{MeV}/c$ contribute to the respective N_{same} distribution. Both correlation functions are combined, as they are compatible within the uncertainties, and the resulting raw correlation function is shown in the left panel of Fig. 5.3. Due to the limited statistical precision, the correlation function is evaluated in rather large k^* intervals of 40 MeV/c. Therefore, the k^* value of each data point is determined by the average $\langle k^* \rangle$ of the N_{mixed} distribution in the corresponding interval. The systematic uncertainties are obtained by simultaneously varying the selection criteria of protons and kaons as well as the lower limit of sphericity. A detailed discussion can be found in Ref. [240].

Following the discussion in Sec. 2.2, the raw p–ϕ correlation function is decomposed as

$$C_{\mathrm{raw}}(k^*) = \lambda_{\mathrm{SB}} C_{\mathrm{SB}}(k^*) + C_{\mathrm{non-femto}}(k^*)\left[\lambda_{\mathrm{gen}} C_{\mathrm{gen}}(k^*) + \lambda_{\mathrm{flat}}\right], \tag{5.3}$$

---

[2] The event shape can be classified by its transverse sphericity S_T, which is defined in terms of the eigenvalues λ_1 and λ_2 of the transverse momentum matrix [241]

$$\mathbf{S_{xy}} = \frac{1}{\sum_j p_{T_j}} \sum_i \frac{1}{p_{T_i}} \begin{bmatrix} p_{x_i}^2 & p_{x_i} p_{y_i} \\ p_{y_i} p_{x_i} & p_{y_i}^2. \end{bmatrix} \tag{5.1}$$

The transverse sphericity is calculated as

$$S_T = \frac{2\lambda_2}{\lambda_1 + \lambda_2}, \tag{5.2}$$

where $\lambda_1 > \lambda_2$. A spherical event is characterized by $S_T = 1.0$, while $S_T = 0$ corresponds to a jet-like event.

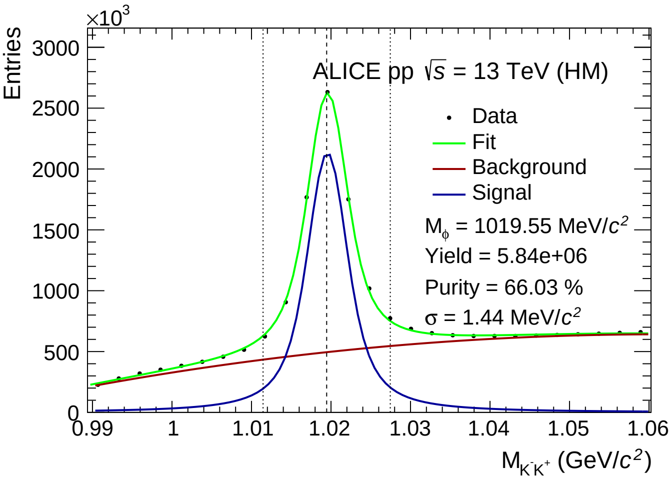

FIGURE 5.2: The K^+K^- invariant mass distribution is shown, together with the total fit to the data in green. The latter is composed of a Voigt function (blue line), describing the signal, and a quadratic polynomial (red), accounting for the background. The dotted lines represent the $M_\phi \pm 8$ MeV/c^2 selection window, used to reconstruct the ϕ candidates, and the dashed line marks the nominal ϕ mass.

where $C_{\mathrm{SB}}(k^*)$ describes the contribution associated with the combinatorial K^+K^- background that contaminates the yield of ϕ candidates, C_{gen} is the genuine contribution from signal ϕ mesons and primary protons, λ_{flat} considers the negligible effects from weak decays feeding into protons and misidentified ones, that contribute with a flat correlation signal $C_{\mathrm{flat}}(k^*) = 1$, and $C_{\mathrm{non-femto}}(k^*)$ describes the residual non-femtoscopic background. The λ parameters listed in Tab. 5.1 are obtained from the single-particle purity and fractions. Instead of using the p_{T}-integrated ϕ purity in the calculation, its distribution is reweighed with that of ϕ candidates forming pairs with protons at low $k^* < 200$ MeV/c, hence contributing to the correlation signal. This leads to a significantly smaller value of 57% and results in $\lambda_{\mathrm{gen}} = 46.3\%$.

The similarity between Eq. 5.3 and Eq. 4.5, which describes the decomposition of the D and light-flavor meson correlation functions discussed in chapter 4 is evident and the process of extracting the genuine correlation function from the raw data also closely follows the approach used in the charm analysis.

$C_{\mathrm{SB}}(k^*)$ arises from fake ϕ mesons, i.e., Kaons from the combinatorial background, which interact with protons via the Coulomb and strong force. This contribution is evaluated in a data-driven approach employing the sidebands of the K^+K^- invariant mass, corresponding to the intervals $0.995 - 1.011$ GeV/c^2 and $1.028 - 1.044$ GeV/c^2 on both sides of the resonance, instead of the signal region for the ϕ candidate selection. The resulting correlation functions are combined as a weighted sum, where the weights correspond to the relative amount of background present in each half of the interval used for ϕ selection, and parametrized with a double Gaussian and a quadratic polynomial. A residual amount of 8.6% real ϕ mesons is present in the sideband intervals due to the tail of the ϕ resonance, which leads to a 7% contribution to the experimental $C_{\mathrm{SB}}(k^*)$. This is accounted for in the modeling by a rescaling of the λ parameters. The resulting correlation function is depicted as orange band in the left panel of Fig. 5.3. Since $C_{\mathrm{SB}}(k^*)$ is obtained from data, it already includes the non-femtoscopic background and, hence, is separated from the other contributions in Eq. 5.3.

TABLE 5.1: Weight parameters of the individual components of the p–ϕ correlation function.

Parameter	Value (%)
λ_{gen}	46.3
λ_{SB}	43.3
λ_{flat}	10.4

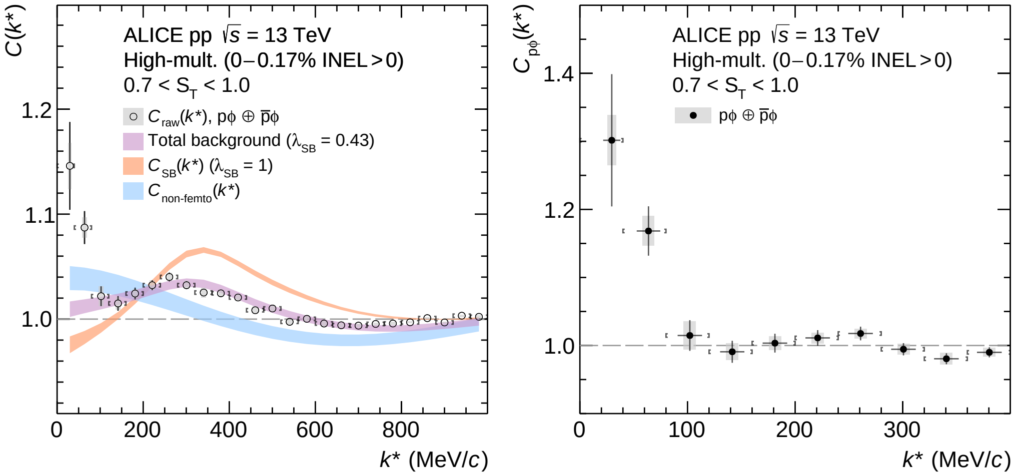

FIGURE 5.3: The left panel shows the raw p–ϕ correlation function $C_{\mathrm{raw}}(k^*)$ with statistical (bars) and systematic uncertainties (boxes). The violet band describes the fitted total background, which consists of several contributions, scaled by the appropriate λ parameter and shown individually and unscaled in the same figure. The with of the bands corresponds to the total uncertainty $\sigma_{\mathrm{tot}} = \sqrt{\sigma^2_{\mathrm{stat}} + \sigma^2_{\mathrm{syst}}}$. The total background is used to extract the genuine correlation function from the raw data, which is shown in the right panel.

The non-femtoscopic background is decomposed as

$$C_{\mathrm{non-femto}}(k^*) = N \times \left[C_{\mathrm{MC}}(k^*) + \left(a + bk^{*2}\right)\right], \tag{5.4}$$

where N is a normalization constant and $C_{\mathrm{MC}}(k^*)$ describes the dominant contribution from the residual minijet background. Similarly to the charm and light-flavor case discussed in Sec. 4.3.2, the latter is obtained from MC-generated events. The additional second-order polynomial baseline accounts for further correlations at large k^* from energy-momentum conservation effects, which are not properly reproduced by PYTHIA. The free parameters a, b and N of Eq. 5.3 are determined by fitting the raw data with a background model (Eq. 5.3 with $C_{\mathrm{gen}}(k^*) = 1$) within $k^* \in [200, 800]$ MeV/c. The resulting total background, as well as the non-femtoscopic background, are depicted as violet and blue bands in Fig. 5.3.

Finally, the genuine p–ϕ correlation function is extracted from the raw data by subtracting all background contributions according to Eq. 5.3. It is shown in the right panel of Fig. 5.3. At low k^* a deviation from unity is visible, with a significance of $4.7 - 6.6\,\sigma$. For $k^* > 200$ MeV/c, the genuine correlation function is flat.

The systematic uncertainty of the genuine correlation function is attributed to the systematic error of the raw correlation function and the total background. The latter is estimated by varying the fit range and the order of the polynomial assumed for the baseline and also considers the systematic error of the sideband correlation function. A relative systematic uncertainty of 2.8% is found at low k^*.

The effective pϕ source is determined using the RSM, which is extensively discussed in Sec. 3.3 as well as Sec. 4.4, where it is applied to determine the DK and Dπ emission. The measured m_T of the pϕ pairs contributing to the correlation signal in the femtoscopic region of $k^* < 200$ MeV$/c$ is $\langle m_\mathrm{T} \rangle = 1.66\,\mathrm{GeV/c^2}$. This corresponds to a core radius of $r_\mathrm{core} = 0.98 \pm 0.04$ fm. The effective source distribution is obtained by explicitly considering the strong decays feeding the proton candidates and is parametrized by a Gaussian source function with $r_\mathrm{eff} = 1.08 \pm 0.05$ fm

5.2 The spin 3/2 channel

The HAL QCD collaboration has published the N–ϕ interaction potential for the spin 3/2 channel, also denoted by $^4\mathrm{S}_{3/2}$[3] [233], whose coupling to the two-body open channels Λ-K ($^2\mathrm{D}_{3/2}$) and Σ-K ($^2\mathrm{D}_{3/2}$) is kinematically suppressed due to the difference in the orbital angular momentum state. Three or more particle decays are also expected to be suppressed by the small phase space.

The calculation of the spin 3/2 potential is performed in a large volume of $L^4 = 96^4$ and small lattice spacing of $a = 0.0846$ fm, leading to $La = 8.1$ fm. It is based on a (2+1)-flavor simulation with nearly physical quark masses, resulting in a slightly larger $m_\pi = 146.4$ MeV$/c^2$ in comparison to the experimental $m_\pi = 139.6$ MeV$/c^2$ [122]. Also, the mass of the kaon is enhanced by around 6%, while it is 3%(2%) larger for the ϕ (N). Therefore, the kinematic decay $\phi \to \mathrm{K}\overline{\mathrm{K}}$ is forbidden. The potential, shown in Fig. 5.4, is calculated at different Euclidean times t. No time dependence is observed as the potentials agree within the statistical uncertainties of the LQCD simulation, indicating that elastic scattering states dominate the interaction channel. The spin 3/2 potential is attractive in the full range, and at a large distance, it is characterized by an attractive tail dominated by TPE. The simulated LQCD potential can be parametrized by

$$\mathrm{A}: \quad V_{3/2}(r^*) = \sum_{i=1,2} a_i e^{-(r^*/b_i)^2} + a_3 m_\pi^4 f(r^*, b_3) \frac{e^{-2m_\pi r^*}}{r^{*2}} \tag{5.5}$$

$$\mathrm{B}: \quad V_{3/2}(r^*) = \sum_{i=1,2,3} a_i e^{-(r^*/b_i)^2}, \tag{5.6}$$

where a_i and b_i are free parameters and $f(r^*, b_3)$ is a form-factor. Function A is motivated by the TPE tail, which has a strength $\propto m_\pi^4$ [214] and is described by a Yukawa-type potential squared. Function B serves as a comparison and has a purely phenomenological Gaussian shape. Two types of form-factors are examined for fit A, namely the Nijmegen- $f_\mathrm{erfc}(r^*, b_3)$ and Agronne-type $f_\mathrm{exp}(r^*, b_3)$, defined as

$$f_\mathrm{erfc}(r^*, b_3) = \left[\mathrm{erfc}\left(\frac{m_\pi}{\Lambda} - \frac{\Lambda r^*}{2}\right) - e^{2m_\pi r^*}\mathrm{erfc}\left(\frac{m_\pi}{\Lambda} - \frac{\Lambda r^*}{2}\right)\right]^2 \tag{5.7}$$

$$f_\mathrm{exp}(r^*, b_3) = \left[1 - e^{-(r^*/b_3)^2}\right]^2, \tag{5.8}$$

---

[3] The channel notation is $^{2s+1}\mathrm{L}_\mathrm{J}$, where s is the total spin, L the orbital angular momentum and J the total angular momentum.

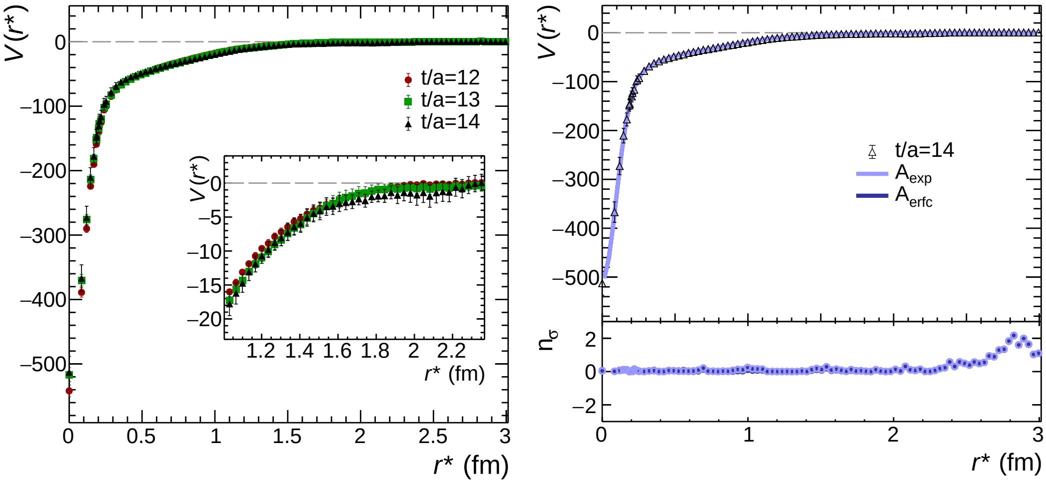

FIGURE 5.4: The *left plot* shows the N–ϕ interaction potential for $s = 3/2$ as function of the distance r^*, calculated at different euclidean times t. The *right plot* depicts the results of the fit with model A using the two different types of form factors $f_{\text{erfc}}(r, b_3)$ and $f_{\text{exp}}(r, b_3)$. The lower panel shows the number of standard deviations n_σ between data and the fit results A$_{\text{exp}}$ and A$_{\text{erfc}}$, respectively. The LQCD potential data are taken from Ref. [233].

m_π (MeV/c^2)	$a_0^{p\phi}(s = 3/2)$ (fm)	$d_0^{p\phi}(s = 3/2)$ (fm)
146.4	$1.43 \pm 0.23(\text{stat.})^{+0.06}_{-0.36}(\text{syst.})$	$2.36 \pm 0.10(\text{stat.})^{+0.02}_{-0.48}(\text{syst.})$
138.0	~ 1.25	~ 2.49

TABLE 5.2: The scattering parameters characterizing the N–ϕ interaction in the spin 3/2 channel for different pion masses.

where $\Lambda = 2/b_3$ and $\text{erfc}(x) = \int_x^\infty e^{-z^2} dz$. All functions give an equally good description of the LQCD simulated data, using the lattice pion mass of $m_\pi = 146.4$ MeV/c^2 in the fit. The parameterization of the potential can be used to extract physical observables, such as the phase shift, from which the scattering parameters can be obtained from the effective range expansion, given by Eq. 2.29. The resulting values are listed in Tab. 5.2, using $t/a = 14$ and A_{erfc} as defaults. The systematic uncertainties are estimated from the different fit functions at different Euclidean times t. An estimate at the physical mass is made by changing the pion mass to the physical value $m_\pi \sim 138.0$ MeV/c^2 for $r > 1$ fm, the region dominated by TPE, while keeping the other potential parameters fixed. The resulting scattering parameters are also listed in Tab. 5.2. As can be seen, the overall attraction is weaker at the physical mass, even though the TPE range increases, due to the m_π^4 dependence of the TPE term in fit A.

The authors of Ref. [233] also investigated the spin 1/2 potential (^{2}S$_{1/2}$) of the N–ϕ interaction. However, a clear t-dependence was observed, which is expected from the S-wave decays into Λ-K (^{2}S$_{1/2}$) and Σ-K (^{2}S$_{1/2}$). Therefore, at the moment, no reliable information can be obtained from lattice calculations, and other methods have to be used to study the N–ϕ interaction in the spin 1/2.

5.3 Pinning down the interaction in the spin 1/2

The spin-averaged experimental p–ϕ correlation function [51] presented in Sec. 5.1 and the LQCD spin 3/2 potential [233] discussed in Sec. 5.2 are combined to study the interaction in the spin 1/2 channel, which is currently not accessible on the lattice due to effects from open channels. Also, no other predictions by theory are available. Hence, the spin 1/2 channel determined in this re-analysis is described by a phenomenological potential, whose shape is based on the findings of the HAL QCD collaboration [233].

5.3.1 Potential parametrization

As discussed in the previous section, the N$\phi(^2S_{1/2})$ state can couple to the ΛK$(^2S_{1/2})$ and ΣK$(^2S_{1/2})$ channels via S-wave fall apart-decays [233]. Such processes introduce an imaginary part to the potential and can be described by the exchange of kaons. The TPE tail observed in the spin 3/2 potential at large distance is expected to also be present in the spin 1/2 channel, as the exchange of two pions in a scalar-isoscalar state is independent of the total spin of the system. Therefore, the N–ϕ interaction potential describing the spin 1/2 channel should consist of a long-range attractive TPE tail, a phenomenological term at short distances, and an imaginary part described by a 2nd-order kaon exchange. Motivated by these considerations as well as the parametrization of the LQCD spin 3/2 potential, given by Eq. 5.5, the spin 1/2 potential of the N–ϕ interaction is modeled as

$$V_{1/2}(r^*) = \beta\left(\sum_{i=1,2} a_i e^{-(r^*/b_i)^2}\right) + a_3 m_\pi^4 f(r^*;b_3)\frac{e^{-2m_\pi r^*}}{r^{*2}} + i\gamma\frac{f(r^*;b_3)}{m_\mathrm{K}}\frac{e^{-2m_\mathrm{K} r^*}}{r^{*2}}, \tag{5.9}$$

where the free parameters β and γ are determined by a fit to the experimental data. The former can be any real number, and if positive, results in a short-range attraction, while a negative β corresponds to a short-range repulsion. The parameter γ is restricted to negative values corresponding to absorption processes. All other parameters have already been introduced when discussing the parametrization of the spin 3/2 potential in Sec. 5.2. The free parameters a_i and b_i are obtained from a fit to the LQCD spin 3/2 potential and are shared between the two channels, and $f(r^*, b_3)$ is a form factor. For $\beta = 1$ and $\gamma = 0$, Eq. 5.9 is equivalent to Eq. 5.5, used to parameterize the spin 3/2 potential [233].

5.3.2 Fit to the data

The measured p–ϕ correlation function is a spin averaged observable. To pin down the interaction in the spin 1/2 channel, the data is modeled as

$$C^{(\beta,\gamma)}_{\mathrm{model}}(k^*) = \frac{2}{3}C_{3/2}(k^*) + \frac{1}{3}C^{(\beta,\gamma)}_{1/2}(k^*)\,, \tag{5.10}$$

where the dependence on the free parameters (β, γ) of the phenomenological potential, given by Eq. 5.9, are explicitly indicated. They are to be determined by a fit to the data. The individual spin contributions are evaluated via the Koonin-Pratt formalism Eq. 2.5, considering the potential parametrization Eq. 5.5 and Eq. 5.9 for spin 3/2 and 1/2, respectively. The particle emission is modeled by a Gaussian source with an effective size of $r_\mathrm{eff} = 1.08 \pm 0.05$ fm, equivalent to the one found in the analysis

Parameter	Value
a_1 [MeV]	-392(10)
b_1 [fm]	0.128(3)
a_2 [MeV]	-145(9)
b_2 [fm]	0.284(7)
$a_3 m_\pi^4$ [MeV · fm^2]	-83(1)
b_3 [fm]	0.582(6)

TABLE 5.3: Values and statistical uncertainties of the parameters of the spin 3/2 potential parametrization, obtained by a fit to the lattice simulation for the spin 3/2 channel at $t/a = 12$ [233]. They are also used in the phenomenological potential, describing the spin 1/2 channel.

of the ALICE data [51]. The weights of the contributions in Eq. 5.10 correspond to the respective spin multiplicity of the channel.

The potential parameters a_i and b_i, common for both spin channels, are determined by fitting the LQCD potential at $t/a = 12$, using Eq. 5.5 with the Argonne-type form factor defined in Eq. 5.8. To be conservative, a smaller Euclidean time is chosen over the default $t/a = 14$ in Ref. [233], as it corresponds to the least attractive potential in the spin 3/2 channel, hence, also to the weakest potential in the spin 1/2. The choice of the form factor is arbitrary, as it gives equivalent results to the ones obtained with the Nijmegen-type, given by Eq. 5.7. A nonphysical pion mass of $m_\pi = 146.4$ MeV/c^2, corresponding to the settings of the LQCD simulation, is used in the fit. The resulting parameter values are listed in Tab. 5.3, and the fit result is depicted as green band in Fig. 5.5, together with the LQCD potential at $t/a = 12$.

The spin 3/2 correlation function $C_{3/2}(k^*)$ is obtained by employing the CATS framework [73] and changing the pion mass in the potential parametrization to its physical value $m_\pi \sim 138$ MeV/c^2 in the full range, while keeping the other parameters fixed. The resulting modified potential is shown as orange band in Fig. 5.5. As can be seen, the potential is most affected by the mass change in the intermediate range and is slightly less attractive overall.

The spin 1/2 contribution $C_{1/2}^{(\beta,\gamma)}(k^*)$ is calculated for different β and γ parameters of the complex spin 1/2 potential in steps of 0.1 and 0.2, respectively[4]. The resulting full correlation functions $C_{\text{model}}^{(\beta,\gamma)}(k^*)$ are compared to the data to determine the best-fitting parameter combination in a χ^2 minimization, with the χ^2 defined as

$$\chi^2(\beta,\gamma) = \sum_{j=1}^{N} \left(\frac{C_{\text{data}}(k_j^*) - C_{\text{model}}^{(\beta,\gamma)}(k_j^*)}{\sigma_{\text{data}}(k_j^*)} \right)^2 , \tag{5.11}$$

where $N = 5$ is the number of data points in the femtoscopic region $k^* < 200$ MeV/c, and $\sigma_{\text{data}}(k_j^*)$ is the uncertainty of the j-th data point.

The resulting χ^2 distribution is shown in Fig. 5.6, taking into account the statistical uncertainties of the measured correlation function. The red lines correspond to the 1-,2- and 3-σ contours with respect to the minimum $\chi^2_{\text{min}} = 6.85$ ($n_\sigma = 1.77$) at $\beta = 6.9$ and $\gamma = 0.0$, and the green dashed line shows the 99% CI.. Notably, the $\beta < 0$ region, which corresponds to a repulsive core of $\Re(V_{1/2})$, is excluded by more

---

[4] The spin 1/2 correlaion functions $C_{1/2}^{(\beta,\gamma)}(k^*)$ were calculated by Dr. Yuki Kamiya.

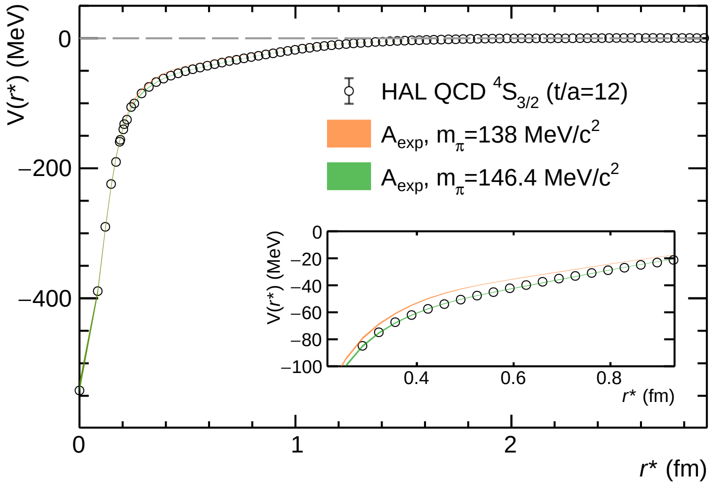

FIGURE 5.5: The ${}^4S_{3/2}$ potential of the N–ϕ interaction obtained from LQCD simulations at $t/a = 12$, which are performed at nearly physical quark masses of $m_\pi = 146.4$ MeV$/c^2$, with its statistical uncertainties is shown as function of the hadron distance r. The green band represents the fit result using the parametrization A$_{\text{exp}}$. An estimate at physical mass is made by using $m_\pi = 138$ MeV$/c^2$ in the fit function instead, while keeping the other parameters fixed and is shown in orange. The width of the bands corresponds to the total uncertainties $\sigma_{\text{tot}} = \sqrt{\sigma^2_{\text{stat}} + \sigma^2_{\text{syst}}}$.

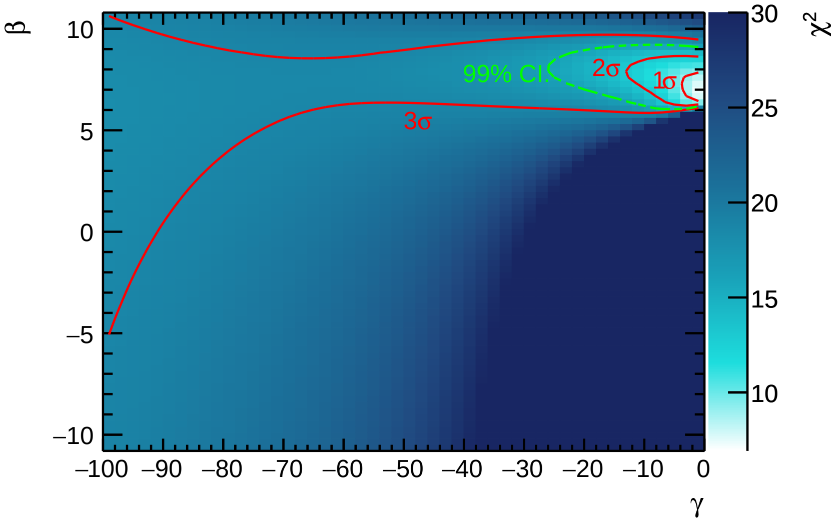

FIGURE 5.6: The χ^2 distribution in the (β, γ) plane, evaluated within $k^* \in [0, 200]$ MeV$/c$ considering the statistical uncertainties of the data. The red lines correspond to the 1-, 2- and 3-σ contour with respect to the minimum $\chi^2_{\text{min}} = 6.85$ ($n_\sigma = 1.77$) at $\beta = 6.9$ and $\gamma = 0.0$, and the green dashed line shows the 99% CI.

TABLE 5.4: Variations of the analysis inputs, used to estimate the systematic uncertainties of the p–ϕ interaction potential in $^2S_{1/2}$ channel.

Input	Default	Variation 1	Variation 2
r_{eff}	1.08	1.13	1.03
$^4S_{3/2}$ potential from LQCD	$V(r)_{\mathrm{LQCD}}$	$V(r)_{\mathrm{LQCD}} + \sigma_{\mathrm{stat}}$	$V(r)_{\mathrm{LQCD}} - \sigma_{\mathrm{stat}}$
t/a	12	13	14
χ^2 evaluation range	$[0, 200]$ MeV/c	$[0, 250]$ MeV/c	$[0, 150]$ MeV/c

than 3σ in the largest part of the phase-space down to a region of $\gamma \approx -90$ and within 99% CI. in the full tested region.

5.4 Systematics

The systematic uncertainty on the $^2S_{1/2}$ potential parameters is estimated by considering different sources of uncertainty at the various steps of the analysis. They include the effective source size r_{eff}, the LQCD simulated potential for the spin 3/2 channel as well as the fit procedure used to determine the spin 1/2 potential. Both the total uncertainty of the effective source size r_{eff} and the statistical uncertainty of the lattice potential are accounted for by varying their values to their extremes within the uncertainties. Different Euclidean times $t/a = 12, 13, 14$ of the $^4S_{3/2}$ potential are considered [233]. A possible bias from the fit procedure is estimated by varying the upper limit of the interval used to evaluate the χ^2 by ±50 MeV/c, which changes the number of degrees of freedom by ±1. The variations are summarized in Tab. 5.4. The analysis is performed by changing one input at a time, and the best-fitting β and γ values are extracted. To be conservative, the systematic errors are estimated from the width of the resulting parameter distributions.

5.5 Results

The parameters of the $^2S_{1/2}$ potential, determined by the minimum χ^2 method explained the previous Sec. 5.3, are found to be $\beta = 6.9^{+0.9}_{-0.5}(\mathrm{stat.})^{+0.2}_{-0.1}(\mathrm{syst.})$ and $\gamma = 0.0^{+0.0}_{-3.6}(\mathrm{stat.})^{+0.0}_{-1.8}(\mathrm{syst.})$. The statistical uncertainty of the parameters is determined by the 1-σ contour of the χ^2 distribution, with respect to the minimum, and the systematic uncertainties are obtained following the procedure discussed in Sec. 5.4. The corresponding model correlation function is shown in blue in Fig. 5.8, together with the individual spin contributions unscaled. A good agreement with the data is obtained. Considering the total uncertainty on both data and model leads to a $\chi^2 = 3.44$ and $n_\sigma = 0.98$ within $k^* \in [0, 200]$ MeV/c. The real and imaginary parts of the spin 1/2 potential are depicted in Fig. 5.7. It can be seen that the real part is strongly attractive, making the imaginary part seem negligible in comparison. At large distance, $\Re(V_{1/2})$ overlaps with the potential of the $^4S_{3/2}$ channel, shown in the same figure for comparison, since the TPE tail is common to both spin states. Furthermore, the attractive core, which is part of the real $^2S_{1/2}$ potential, is much stronger than it is for spin 3/2 due to the large β.

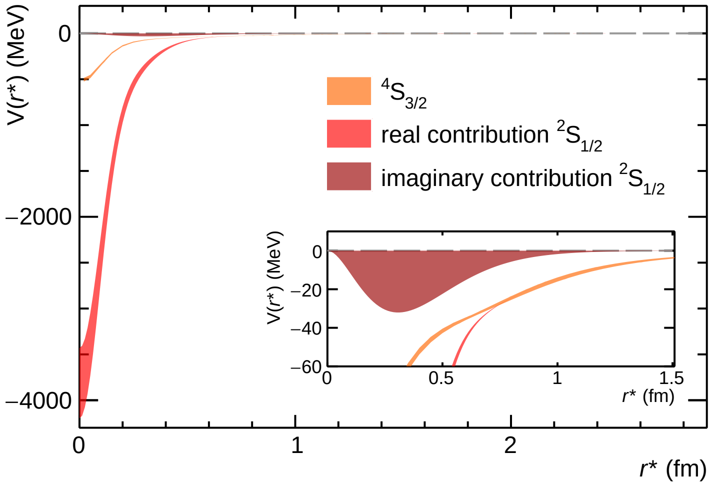

FIGURE 5.7: The parametrization of the N–ϕ lattice potential for the ${}^4S_{3/2}$ channel, estimated at physical masses (orange band), is shown together with the real (light red band) and imaginary (dark red band) part of the complex phenomenological potential for the ${}^2S_{1/2}$ channel, determined by a fit to the experimental correlation function. The width of the bands represent the total uncertainty $\sigma_{\text{tot}} = \sqrt{\sigma^2_{\text{stat}} + \sigma^2_{\text{syst}}}$.

Multiplying the potentials by the Jacobian factor and comparing them with the effective source function, as depicted in Fig. 5.9, shows that even though a vanishing γ value best describes the data, a sizable $\Im(V_{1/2})$ can not be excluded. This is particularly evident at distances $r^* \sim 1$ fm where a considerable amount of pϕ pairs are emitted. Such non-vanishing imaginary contribution to the potential is expected from the LQCD studies in the spin 1/2 channel, mentioned in Sec. 5.2, as well as other theoretical calculations [228]. Furthermore, it becomes clear that the shape of the potential at small r is not relevant since a negligible amount of pϕ pairs are emitted at such distance. Therefore, the influence of the extreme core of $\Re(V_{1/2})$ on the results is diminished.

The scattering length a_0 and effective range d_0 of the ${}^2S_{1/2}$ channel, extracted from the effective-range expansion of the scattering amplitude, given by Eq. 2.30, are found to be

$$\begin{aligned}
\Re\left(a_0^{\mathrm{p}\phi}(s=1/2)\right) &= -1.54^{+0.53}_{-0.53}(\text{stat.})^{+0.16}_{-0.09}(\text{syst.})\ \text{fm},\\
\Im\left(a_0^{\mathrm{p}\phi}(s=1/2)\right) &= \ \ 0.00^{+0.35}_{-0.00}(\text{stat.})^{+0.16}_{-0.00}(\text{syst.})\ \text{fm},\\
\Re\left(d_0^{\mathrm{p}\phi}(s=1/2)\right) &= +0.39^{+0.09}_{-0.09}(\text{stat.})^{+0.02}_{-0.03}(\text{syst.})\ \text{fm},\\
\Im\left(d_0^{\mathrm{p}\phi}(s=1/2)\right) &= \ \ 0.00^{+0.00}_{-0.04}(\text{stat.})^{+0.00}_{-0.02}(\text{syst.})\ \text{fm}.
\end{aligned} \tag{5.12}$$

They are of the same order of magnitude as the scattering parameters of the ${}^4S_{3/2}$ channel, obtained from the LQCD simulation [233], as well as the ones published in the original analysis of the experimental p–ϕ correlation function [51]. However, they are much larger than the ones obtained within the VMD model from ϕ-meson photoproduction measurements by the CLAS and LEPS collaboration. All scattering

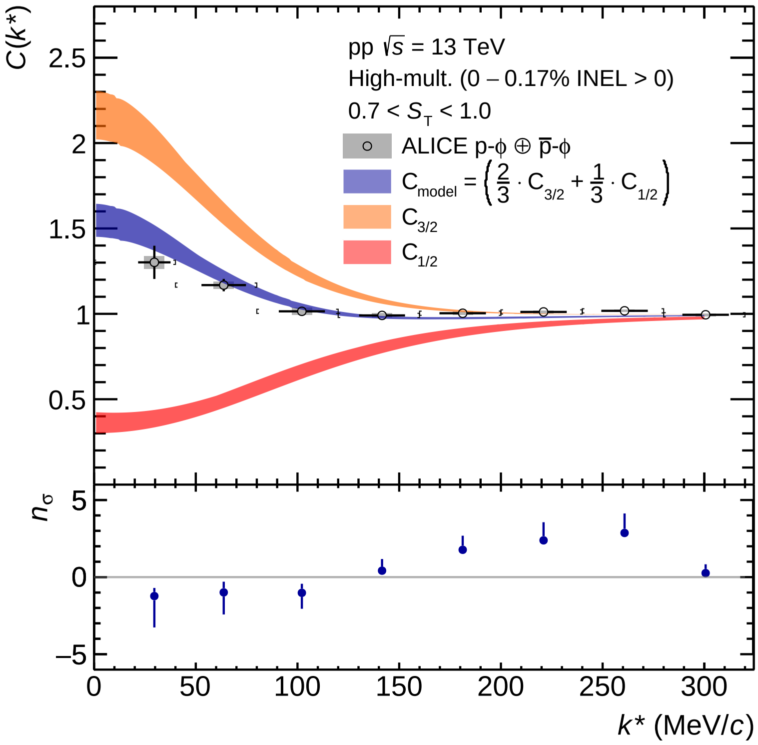

FIGURE 5.8: The upper panel shows the experimental p–φ correlation function with statistical (bars) and systematic uncertainties (gray shaded boxed) and together with the spin averaged model correlation function (blue band) and the unweighted $^4S_{3/2}$ (orange band) and $^2S_{1/2}$ contributions (red band). The width of the bands corresponds to the total error, which includes the systematic uncertainty via $\sigma_{\text{tot}} = \sqrt{\sigma^2_{\text{stat}} + \sigma^2_{\text{syst}}}$. The number of standard deviations n_σ between C_{model} and data is shown in the lower panel.

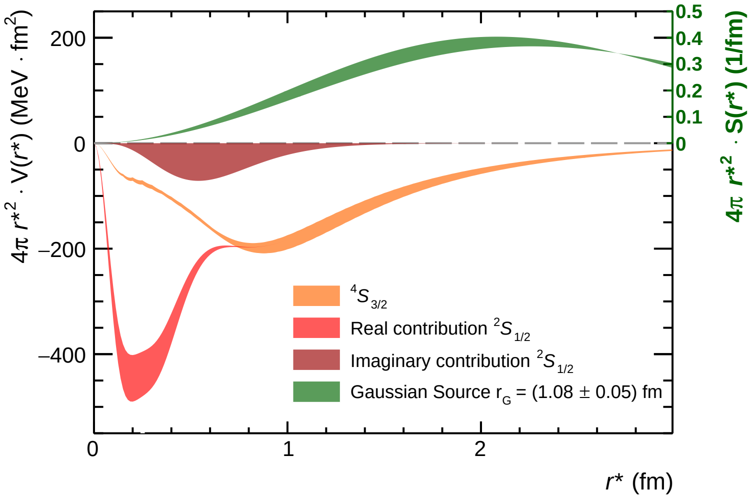

FIGURE 5.9: The probability density distribution for the hadron distance $4\pi r^{*2} \cdot S(r^*)$ is depicted (green band) together with the $^4S_{3/2}$ and $^2S_{1/2}$ potentials, multiplied by the Jacobian term $4\pi r^{*2}$ to emphasize the range of sensitivity of the correlation function measurement to the potential. The width of the band corresponds to the $\sigma_{\text{tot}} = \sqrt{\sigma^2_{\text{stat}} + \sigma^2_{\text{syst}}}$.

J^P	E_B (MeV)
$\frac{1}{2}^-, \frac{3}{2}^-$	1.8 [213]
	9.0 [225]
	9.3(ϕn), 9.23(ϕp) [212]
	9.47 [222]
$\frac{1}{2}^-$	1.0-3.0 [218]
$\frac{3}{2}^-$	6.0-9.0 [218]
	1.6-10.1 [224]

TABLE 5.5: Predicted binding energies of a pϕ bound state with spin-parity J^P. Values obtained from spin-independent potentials apply for both $\frac{1}{2}^-$ and $\frac{3}{2}^-$.

length values and a possible explanation of the deviation are given in the introduction to this chapter.

In summary, the p–ϕ interaction in the spin 1/2 is characterized by an attractive interaction in the full range, excluding negative β values within 99% CI., as well as $\Re(a_0) < 0$ and a correlation function below unity in the low k^* range. This information combined hints at the possible existence of a pϕ bound state. Details leading to such a conclusion can be found in Sec. 2.3.3. Solving the Schrödinger equation with Eq. 5.9 leads to an eigenenergy of $E = -23.8^{+10.7}_{-32.2}(\text{stat.})^{+2.7}_{-2.8}(\text{syst.}) - i \cdot 0.0^{+0.0}_{-16.4}(\text{stat.})^{+0.0}_{-6.6}(\text{syst.})$ MeV, indicating a quasi-bound state due to its position on the complex energy plane. The binding energy E_B corresponds to $-\Re(E)$, which leads to $E_B = 12.8$-56.1 MeV. Alternatively, the approximate formula Eq. 2.34 can be used, which results in $E_B \simeq 10.7$-120.5 MeV, considering the total uncertainty on the scattering parameters.

These values are comparable to or even larger than previous model calculations, which were mentioned in the introduction to this chapter and listed in Table 5.5. In the following, they are described in detail.

- The interaction between two color singlet hadrons with no common quarks might be dominated by QCD van der Waals forces, mediated by gluon exchange. The corresponding attractive force, modeled by a Yukawa-type potential following previous investigation of nuclear-bound quarkonium [226], is strong enough to form a N–ϕ bound state inside the nucleus, with a binding energy of $E_{\mathrm{B}} = 1.8\ \mathrm{MeV}/c^2$ [213].
- A a unitary coupled-channel approach is used to calculate the N–ϕ scattering length [225]. The value published by ALICE [51] can only be reproduced by an attractive potential, which results in a two-pole structure in the scattering amplitude. One pole is detected around 1970 MeV, above the pϕ threshold, and is, hence, interpreted as resonance that could correspond to the N(1895) or N(1875) [122]. The lower mass pole at around 1950 MeV can be associated with a pϕ bound state with $E_B = 9$ MeV.
- Using the phenomenological N–ϕ potential of Ref. [213], a variational method is employed to estimate the binding energy of thee-body ϕNN systems [212]. $E_{(\phi\mathrm{n})\mathrm{p}} = 10.03$ MeV and $E_{(\phi\mathrm{n})\mathrm{p}} = 17.45$ MeV are obtained. Seizable binding energies of 9.3 for n–ϕ and 9.23 MeV for p–ϕ are also reported in the two-body case [212].
- In [222] a two-variable integro-differential equation is employed to study the ϕ– and ϕ ϕ–nuclear systems. Similar to [212], the attractive two-body N–ϕ interaction provided by [213] is used in the calculation and a binding energy of 9.47 MeV is found for N–ϕ , while much larger values up to $E_{\phi\mathrm{NN}} = 39.84$ MeV and $E_{\phi\phi\mathrm{NN}} = 124.59$ MeV are obtained for A-body systems.
- The extended SU(3) chiral quark model is used to dynamically study structures of N–ϕ states with spin-parity $J^P = \frac{3}{2}^-$ and $J^P = \frac{1}{2}^-$, considering the channel coupling of N–ϕ and ΛK* [218]. The N–ϕ interaction of both spin states is found to be attractive in the medium range, resulting in a binding energy of 1-3 MeV for spin-1/2, while much larger values of 6-9 MeV are obtained for spin-3/2.
- Employing the resonating-group method within the quark delocalization color screening model, a bound state with $J^P = \frac{3}{2}^-$ and mass between 1948.9 and 1957.4 MeV/c^2 is found, whose main component is N–ϕ . The corresponding binding energy is in the range of $[1.6, 10.1]$ MeV [224].

The results obtained in this re-analysis of the p–ϕ correlation function might inspire direct searches for a pϕ bound state. Possible decay channels are $\Lambda\mathrm{K}^+$ or $\Sigma\mathrm{K}^+$, both fall-apart decays in the S-wave. For now, experimental evidence is missing. The recent ALICE measurement of the $\Lambda\mathrm{K}^+ \oplus \overline{\Lambda}\mathrm{K}^-$ correlation function [52], where the pϕ bound state would appear as structure in the region $k^* \in [479, 517]$ MeV/c, given the binding energy obtained in this work, shows no sign of its existence. However, the signal might be washed out, and/or other decay channels favored. Also, no cusp at the opening of the pϕ channel is found at $k^* \sim 529$ MeV/c, indicating a shallow coupling between the two channels. Details can be found in Appendix C.

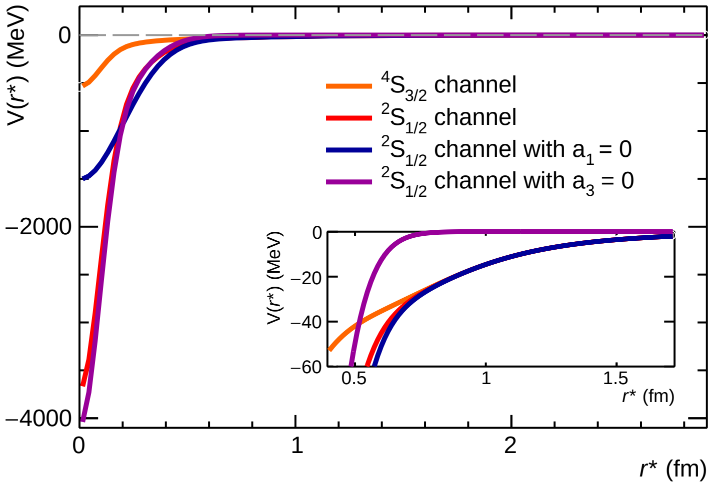

FIGURE 5.10: A modified version of the spin 1/2 potential without the strongly attractive core ($a_1 = 0$) is depicted in blue for the best-fitting parameter combination ($\beta = 10.4, \gamma = 0.0$). Another version without the TPE tail is shown in magenta for ($\beta = 7.6, \gamma = 0.0$), which yields the best description of the data. The spin 3/2 and default 1/2 potential with ($\beta = 6.9, \gamma = 0.0$) is shown for comparison. All potential parametrizations are obtained using $m_\pi = 138$ MeV/c^2.

5.5.1 Cross-check with other potential shapes

To test the stability of the results, the same analysis is performed using the Nijmegen-type form factor f_{erfc} defined in Eq. 5.7 for both the spin 1/2 and 3/2 potential and the physical pion mass only at $r > 1.0$ fm, as done in Ref. [233]. Even though the resulting spin 1/2 scattering length is found to be in agreement with the one extracted from the standard fit, listed in Eq. 5.12, and the β parameter is always significantly larger than zero, the model does not well reproduce the data. The best-fitting parameter combination is $\beta = 15.0$ and $\gamma = -0.2$, corresponding to a scattering length of $a_0^{\mathrm{p}\phi}(s = 1/2) = (-1.62 + i \cdot 0.02)$ fm. However, this variation of the model correlation function can be excluded due to the large $\chi^2_{\mathrm{min}} = 21.6$. Also, using only the imaginary part of the spin 1/2 potential ($\beta = 0$) with standard settings, combined with the default spin 3/2 potential parametrization, leads to a model correlation function insufficient in describing the data, with $\chi^2_{\mathrm{min}} = 15.40$ for $\gamma = -6.6$. Furthermore, the sensitivity to the extremely attractive short-range part of the spin 1/2 potential is studied by setting $a_1 = 0$ in Eq. 5.9, which reduces the potential strength by about 60% in the region $r^* < 0.3$ fm. The modified version (blue) is shown in Fig. 5.10 together with the $^4S_{3/2}$ (orange) and default $^2S_{1/2}$ potential parametrization (red). A scattering length of $a_0^{\mathrm{p}\phi}(s = 1/2) = (-1.56 + i \cdot 0.00)$ fm, consistent with those found from the standard fit, is found for $\beta = 10.4$ and $\gamma = 0.0$, with $\chi^2_{\mathrm{min}} = 6.90$, also compatible with the standard fit result. Finally, a simple double-Gaussian form of the real part of the spin 1/2 potential is tested by setting $a_3 = 0$ in Eq. 5.9. Hence, $\Re(V_{1/2})$ is attractive or repulsive in the full r^*-range, and the TPE tail, found in the spin 3/2 channel [233], is removed. The best-fitting potential is characterized by $\beta = 7.6$ and $\gamma = 0$ with a $\chi^2_{\mathrm{min}} = 4.99$ and is depicted as well in Fig. 5.10 (magenta). The corresponding scattering length is $a_0^{\mathrm{p}\phi}(s = 1/2) = (-1.40 + i \cdot 0.00)$ fm is consistent with the result obtained from the standard fit with the TPE tail.

These studies demonstrate the stability of the results and confirm the possible existence of a pϕ bound state below the threshold.

5.6 Conclusions

The experimental p–ϕ correlation function [51], obtained from ALICE HM pp collision data at $\sqrt{s} = 13$ TeV, is re-analyzed, constraining the spin 3/2 contribution with a recently published LQCD potential [233]. This facilitates the study of the unknown spin 1/2 channel of the p–ϕ interaction, which is currently inaccessible on the lattice due to effects from open channels. A phenomenological complex potential, whose shape is motivated by the LQCD simulation, is used for the unknown contribution. The potential parameters are partially shared with the parametrization of the spin 3/2 potential and fixed from a fit to the lattice data. The remaining free parameters are determined by fitting the ALICE data with a model correlation function that correctly takes into account both the 1/2 and 3/2 spin contributions to the p–ϕ interaction. Figure 5.8 shows the resulting model correlation functions for both spin states individually, as well as combined, in comparison to the measurement.

The scattering parameters are calculated from the effective range expansion of the scattering amplitude of the spin 1/2 potential. The scattering length is found to be

$$a_0^{\mathrm{p}\phi}(s = 1/2) = \left(-1.54^{+0.53}_{-0.53}(\mathrm{stat.})^{+0.16}_{-0.09}(\mathrm{syst.}) + i \cdot 0.00^{+0.35}_{-0.00}(\mathrm{stat.})^{+0.16}_{-0.00}(\mathrm{syst.})\right)\ \mathrm{fm}$$

and the effective range is

$$d_0^{\mathrm{p}\phi}(s = 1/2) = \left(0.39^{+0.09}_{-0.09}(\mathrm{stat.})^{+0.02}_{-0.03}(\mathrm{syst.}) + i \cdot 0.00^{+0.00}_{-0.04}(\mathrm{stat.})^{+0.00}_{-0.02}(\mathrm{syst.})\right)\ \mathrm{fm}.$$

The imaginary part of the potential is vanishing, however, within uncertainties, it does not exclude the possibility of inelastic contributions expected by theory [228]. The real part of the spin 1/2 potential is attractive and strong enough to support the formation of a pϕ bound state, as predicted by several previous theoretical calculations [212, 213, 218, 222, 224, 225]. A binding energy in the range between 12.8 and 56.1 MeV is obtained. These results motivate a direct search for the pϕ bound state and a lattice QCD simulations of the $^2S_{1/2}$ channel. Additionally, calculations that properly consider coupled channel effects, which can have a strong impact on the p–ϕ FSI, are called for, such as the ones performed in Ref. [242]. However, the results obtained in this study demonstrate the importance of correlation functions for the study of bound and exotic states as an alternative to classical approaches, such as invariant mass measurements, especially as they provide a powerful tool to access information in the strange and charm sector.

In the future, the p–ϕ correlation function will be measured with higher statistical precision on data collected during the LHC Run-3. Figure 5.11 shows the ϕ resonance, obtained from applying the same selections as in Ref. [51] on a subsample of MB data from pp collisions at $\sqrt{s} = 13.6$ TeV, obtained during the 2022 period. The limited data set of 3.2×10^9 events results in a ϕ yield similar to that obtained with the full Run-2 HM data. In addition, the first steps towards measuring the 3-body ϕNN correlation function have been taken, with the development of a ϕNN trigger in ALICE, which has been active during data acquisition since September 2024.

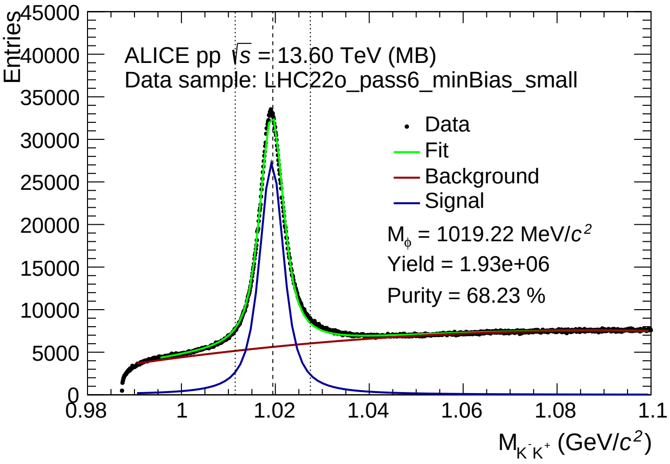

FIGURE 5.11: The K^+K^- invariant mass spectrum with the ϕ resonance peak, obtained from a subsample of the LHC22o data, collected in 2022 during the LHC Run-3.

Chapter 6

Summary

The work presented in this thesis concerns the study of hadronic interactions, especially the residual strong force among hadrons with valence quark content beyond the light u and d quarks. While various theoretical predictions are available for such systems, the measurements needed to constrain and test the models are limited. Since classical scattering experiments with unstable hadrons have proven difficult to impossible, the femtoscopy technique provides a unique tool to probe hadronic final state interactions via correlations in momentum space. The technique is based on the modification of the relative momentum of a pair of particles emitted close to each other and with similar momentum, i.e., small relative momentum, which is induced by the interaction between them. Since the measured correlation signal also depends on the pair emission and is more pronounced if particles are emitted at a short relative distance, colliding systems such as pp provide the ideal environment for this kind of study. The corresponding small emission region of ~ 1 fm makes it possible to even obtain information on shallow interactions.

The first topic discussed in this thesis was the measurement of the correlation function of light-flavor (π and K) and D^+ mesons in pp collisions at $\sqrt{s} = 13$ TeV, recorded with the ALICE detector at the LHC, which provides excellent particle identification capabilities needed for these kinds of studies. The raw correlation functions of same- and opposite-charge DK and Dπ pairs were corrected for all known background contributions related to the finite purity and fraction of primary signal particles to the single-particle samples, as well as auto-correlations from pairs emitted in jet-like structures. The resulting genuine correlation functions provide first experimental results in the charm sector, preceded only by the measurement of the pD^- correlation function [53]. They were compared to the available theoretical predictions of the strong interaction, which are all based on chiral effective field theory and constrained by LQCD simulations. In the D–K case, the data lack the statistical precision to discriminate between the different models. The D–π correlation functions, on the other hand, are well described by the Coulomb-only interaction and are incompatible with the predictions of the residual strong interaction. Moreover, taking advantage of their relatively good statistical precision, the correlation functions were also used to determine the scattering length of the $\mathrm{D}\pi(I = 1/2)$ and $\mathrm{D}\pi(I = 3/2)$ channels, respectively. Since the latter contributes to both the same- and opposite-charge combination, a simultaneous χ^2 minimization was performed, parameterizing each channel with a Gaussian-type potential of variable depth. The scattering lengths were derived from the scattering amplitude of the resulting potentials using the effective range expansion. They were found to be negligible in both isospin channels, and a deviation of $> 5\sigma$ from the predicted values was observed in the $I = 1/2$ channel. As expected from heavy-quark spin symmetry, similar results were obtained in an analogous and independent analysis of the same- and opposite-charge correlation functions involving D^* and light-flavor mesons, strengthening the experimental results on the D–K and D–π interaction presented in this thesis. However, possible explanations for the discrepancy with theory were also explored, including a much larger source size for pairs involving charm mesons in comparison to only light-flavor particles, which would lead to a more shallow measured femtoscopic signal for a given interaction strength. Nevertheless, the experimental results challenge the current understanding of the interaction of charm and light-flavor mesons and motivate more measurements in the sector as well as new theoretical approaches. Moreover, the data can be used to constrain the free parameters of the available models, which are currently sloley derived from LQCD simulated results.

The second topic of this thesis was the re-analysis of the p–ϕ correlation function measured by ALICE in pp collisions at $\sqrt{s} = 13$ TeV and obtained as a result of my master thesis. The spin 3/2 state of the p–ϕ interaction was constrained by the corresponding simulated LQCD potential [233] in order to obtain information about the spin 1/2 state of the interaction, which is currently inaccessible on the lattice due to the effects from open channels. The simulated potential is characterized by an attractive two-pion exchange tail at medium to large distances and an attractive core. A similar shape was used for the real part of the complex phenomenological interaction potential of the spin 1/2 state, consisting of a Gaussian core of variable depth $\beta \in \mathbb{R}$ as well as an attractive two-pion exchange tail, identical to the one observed in the spin 3/2 state. The imaginary part, which accounts for possible inelastic contributions mediated by a 2nd-order kaon exchange, was parametrized by a Yukawa-type potential scaled by $\gamma < 0$. Both spin contributions were properly combined into a model correlation function and compared to the data in order to determine the free parameters β and γ of the spin 1/2 potential in a χ^2 minimization. A strongly attractive Gaussian core, i.e., a fully attractive real part of the potential, as well as a vanishing imaginary part of the potential were found to best describe the measured correlation function. This potential is strong enough to support the formation of a pϕ bound state, predicted by various theoretical models. The binding energy was determined to be between 12.8 and 56.1 MeV. Furthermore, the stability of the result was tested by applying several modifications to the spin 1/2 potential shape, including the removal of the Gaussian core or the two-pion exchange tale, respectively. Since $\Lambda\mathrm{K}^+$ is a possible decay channel of the bound state, the corresponding correlation function was investigated in the relevant k^* region, where the bound state would appear as structure. However, no sign was found, motivating a direct search for it in other channels, for example, by means of invariant-mass measurements. Moreover, a LQCD simulation of the interaction potential in the $^2S_{1/2}$ channel is called for.

The results of these works show the importance and relevance of femtoscopic analyses in deriving information on the FSI of pairs that cannot be studied experimentally by other means, even providing clues to the possible existence of exotic states. Experimental correlation functions are essential to constrain and test the available theoretical models and to help advance the field of hadronic physics. Especially in the charm sector, there is great potential as the statistical precision of the data is improving and more exotic systems become accessible.

Appendix A

The Lednický–Lyuboshits approach

The Lednický–Lyuboshits approach [70] is an established and simplistic method to derive the scattering parameters of the strong interaction analytically, assuming an isotropic particle emission with a Gaussian profile. The s-wave scattering amplitude $f(k^*)$ that enters into the asymptotic wave function is expressed in terms of the effective range expansion, Eq. 2.30, and the Koonin-Pratt Eq. 2.5 can be solved analytically. For uncharged non-identical particles this results in

$$C_{LL}(k^*) = 1 + \frac{1}{2}\left|\frac{f(k^*)}{r_0}\right|^2 \left(1 - \frac{d_0}{2\sqrt{\pi}r_0}\right) + \frac{2\Re f(k^*)}{\sqrt{\pi}r_0}F_1(2k^*r_0) - \frac{\Im f(k^*)}{r_0}F_2(2k^*r_0), \tag{A.1}$$

where $F_1(2k^*r_0)$ and $F_2(2k^*r_0)$ denote analytical functions from the Gaussian approximation of the source and are defined as

$$F_1(z) = \frac{1}{z}e^{-z^2}\int_0^z e^{x^2}dx \tag{A.2}$$

and

$$F_2(z) = \frac{1}{z}(1 - e^{-z^2}). \tag{A.3}$$

The term $\left(1 - \frac{d_0}{2\sqrt{\pi}r_0}\right)$ is a correction factor, that was introduced by Lednický in order to account for small sources and enable the use of the model of outside HI physics.

Appendix B

Additional material on the analysis of the interaction among D^+ and light-flavor mesons

B.1 Event-mixing

The event-mixing, used to obtain N_{mixed}, is conducted only among events with similar z position of the primary vertex and multiplicity [184], to avoid a possible bias from acceptance effects of the detector system.

For the z vertex position, a bin width of 2 cm is chosen, and the multiplicity is grouped in classes of $[1-4]$, $[5-8]$, $[9-12]$, $[13-16]$, $[17-20]$, $[21-24]$, $[25-28]$, $[29-32]$, $[33-36]$, $[37-40]$, $[41-44]$, $[45-48]$, $[49-52]$, $[53-56]$, $[57-60]$, $[61-64]$, $[65-72]$, $[65-72]$, $[73-76]$, $[77-80]$, $[81-84]$, $[85-88]$, $[89-92]$, $[93-96]$, $[97-100]$, $[>101]$. The latter is estimated by using the reference multiplicity Ref08 $|\eta| < 0.8$, which is shown in the left panel of Fig. B.1. The distribution of the z vertex position is shown on the right panel of the same figure.

B.2 Weighting of the mixed-event distribution

In order to account for the different multiplicity-dependence of the number of pairs in the same- and mixed event, the mixed-event distributions are re-weighted in each multiplicity bin to have the same statistical weight as the same-event distribution. The top left panel of Figs. B.2, B.3, B.4 and B.5 shows the amount of $\mathrm{D^-K^+}$, $\mathrm{D^+K^+}$, $\mathrm{D^-\pi^+}$ and $\mathrm{D^+\pi^+}$ pairs with $k^* \in [0.2, 0.9]$ GeV/c per multiplicity bin for

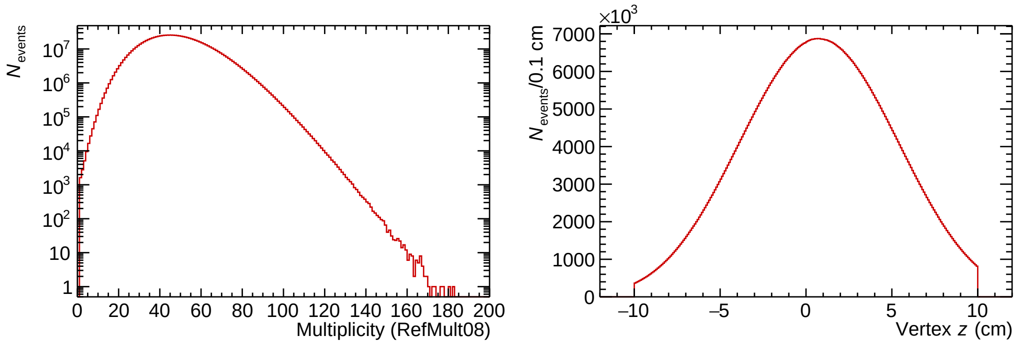

FIGURE B.1: The *left panel* shows the reference multiplicity Ref08 in $|\eta| < 0.8$. The *right panel* depicts the z-vertex distribution for HM pp collisions. Both observables are used for the event mixing.

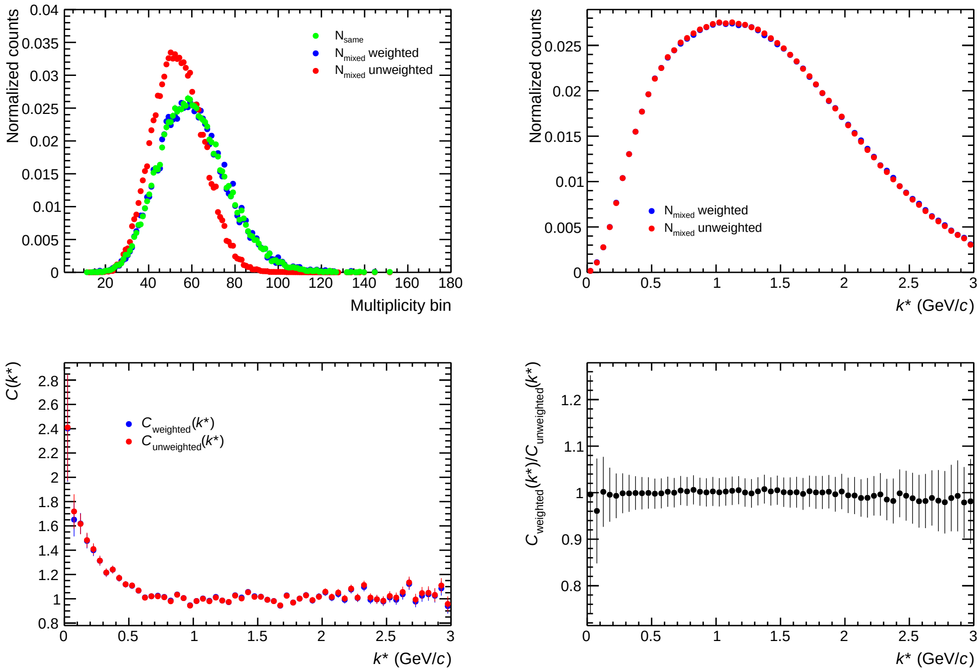

FIGURE B.2: (*Top left*) Multiplicity distribution in mixed and same event for the $\mathrm{D}^{-}\mathrm{K}^{+}$ correlation function before and after the re-weighting, (*top right*) mixed event k^* distribution before and after the re-weighting, (*bottom left*) the resulting $\mathrm{D}\pi$ correlation function before and after the re-weighting and (*bottom right*) the ratio of the two.

the same- (green) and mixed-event (red) distribution. The multiplicity distribution of the mixed event after the re-weighting is shown in blue. As can be seen, they are well in agreement. The top right panel of the same figures shows the effect on the multiplicity-integrated mixed-event distribution, and the effect on the respective correlation function is depicted in the bottom left panel. As can be seen from the ratio between the two, shown in the bottom right panel, the effect for $\mathrm{D}\pi$ and DK is negligible.

B.3 Detector effects

The experimental correlation function can be affected by the finite resolution of the momentum measurement, especially in the sensitive femtoscopic region of $k^* < 200\ \mathrm{MeV}/c$. The effect can be studied by comparing k^*_{Reco}, the relative momentum of pairs reconstructed within the ALICE detector, and the one obtained from the true single-particle momenta at the collision vertex, k^*_{Gen}, using HF MC generated data. The resulting momentum-resolution matrices are shown exemplarily in Figs. B.6a and B.7a for same-charge DK and $\mathrm{D}\pi$ pairs and are identical for opposite-charge pairs. As can be seen, the distribution is symmetrical, and the entries accumulate closely around the identity line. A potential impact of the finite momentum resolution of the ALICE detector on the analysis is further investigated by transforming a model correlation function to the reconstructed momentum basis using the momentum-resolution matrices. Figure B.6b and B.7b show such correlation functions of $\mathrm{D}^{+}\mathrm{K}^{+} \oplus \mathrm{D}^{-}\mathrm{K}^{-}$ and $\mathrm{D}^{+}\pi^{+} \oplus \mathrm{D}^{-}\pi^{-}$, respectively. They are computed with CATS [73] with (pink) and without (red) accounting for detector effects. The theory

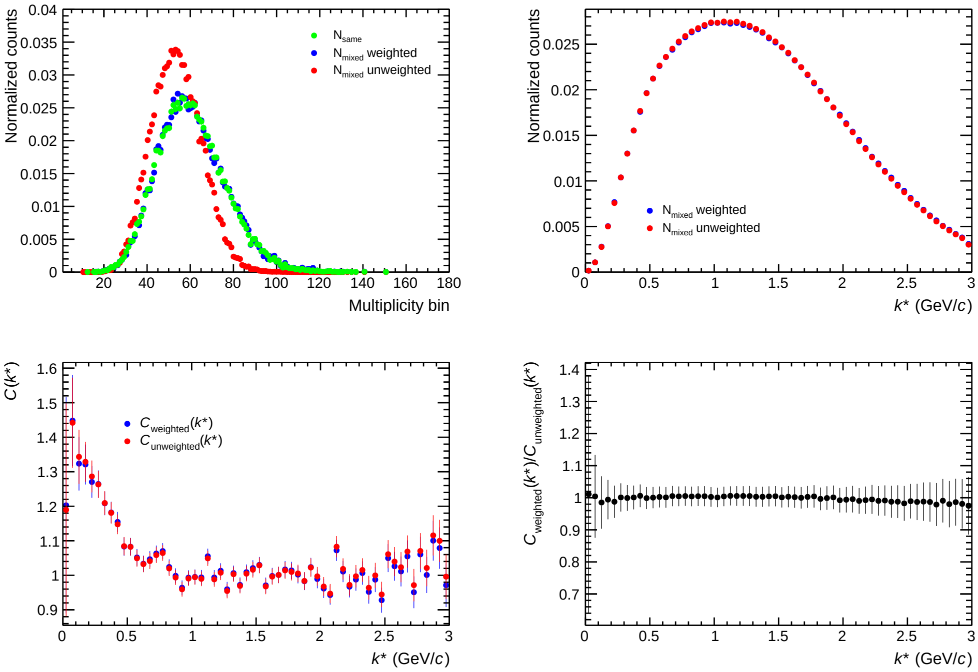

FIGURE B.3: (*Top left*) Multiplicity distribution in mixed and same event for the D^+K^+ correlation function before and after the re-weighting, (*top right*) mixed event k^* distribution before and after the re-weighting, (*bottom left*) the resulting $D\pi$ correlation function before and after the re-weighting and (*bottom right*) the ratio of the two.

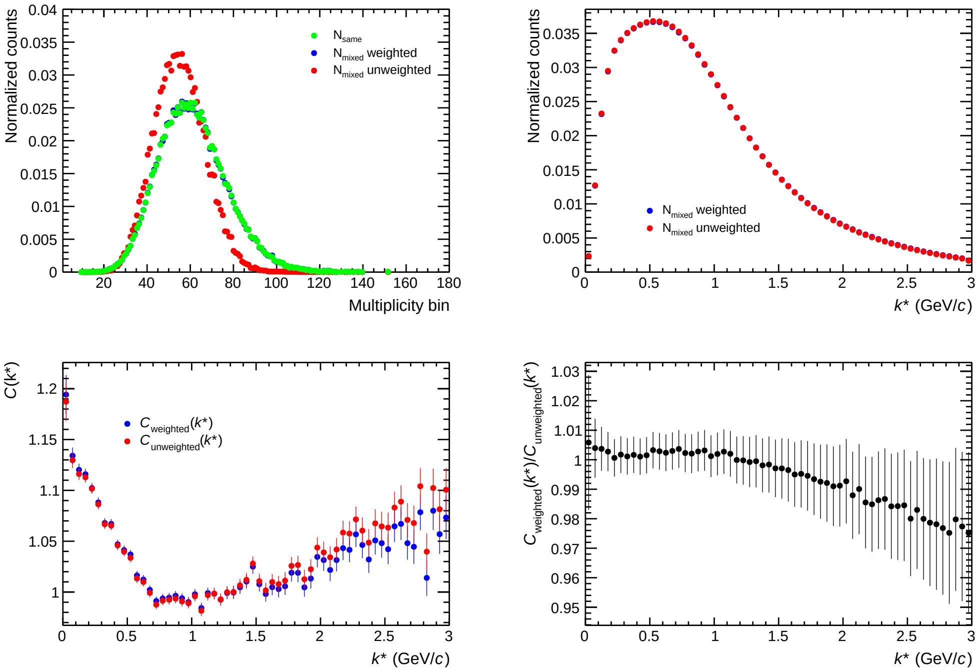

FIGURE B.4: (*Top left*) Multiplicity distribution in mixed and same event for the $D^-\pi^+$ correlation function before and after the re-weighting, (*top right*) mixed event k^* distribution before and after the re-weighting, (*bottom left*) the resulting $D\pi$ correlation function before and after the re-weighting and (*bottom right*) the ratio of the two.

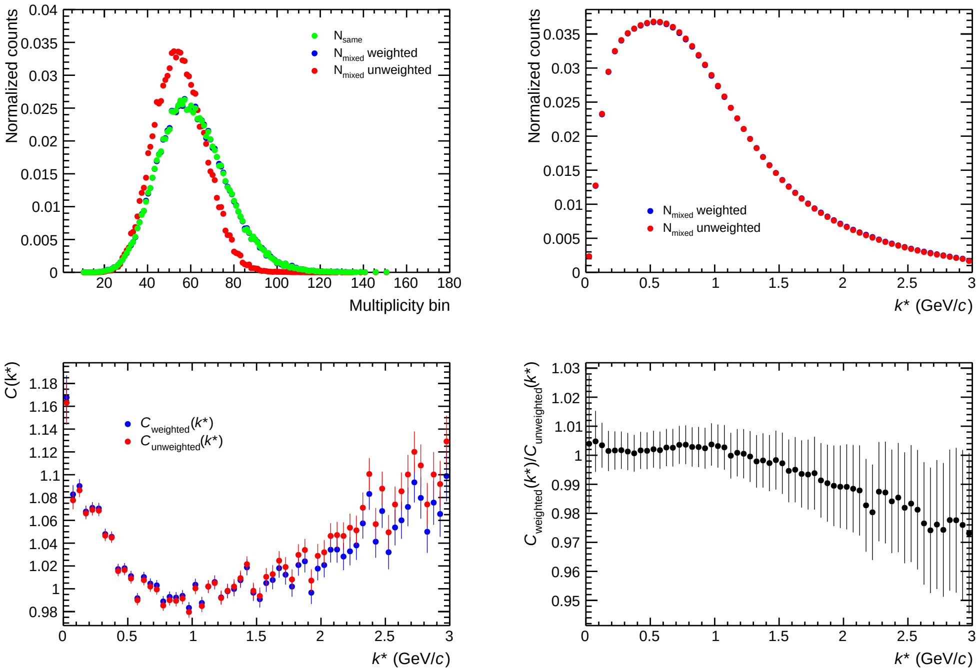

FIGURE B.5: (*Top left*) Multiplicity distribution in mixed and same event for the $D^+\pi^+$ correlation function before and after the re-weighting, (*top right*) mixed event k^* distribution before and after the re-weighting, (*bottom left*) the resulting $D\pi$ correlation function before and after the re-weighting and (*bottom right*) the ratio of the two.

curves are obtained using the scattering lengths predicted by the model of B. Huang *et al.* [196], listed in Tab. 4.15 and 4.14. Only at small k^* a deviation is visible. Such small relative momenta, however, are not resolved by the data. Therefore, no further correction is applied.

B.4 Contribution to the raw correlation functions from D mesons from beauty decays

The correlation of primary light-flavor mesons with non-prompt D$^+$ mesons is studied by employing the same approach used to determine the contribution from D$^+$ mesons from D* decays, presented in Sec. 4.3.1. As no experimental data is available on the Bπ and BK interaction, it is assumed to be dominated by the Coulomb force, as found for D$^*\pi$ and D*K [186]. The decay kinematics of the $B^+ \to D^+ + X$ decay is simulated and used to map the model BK and Bπ correlation functions into the one of the daughter D$^+$ and light-flavor mesons, respectively. The transformation matrices are shown in the left panel of Fig. B.9 and B.8. As the available phase space for the decay is much larger than in the $D^{*+} \to D^+$ case, the information on the interaction between beauty and light-flavor hadrons is lost, leading to a flat correlation. This can be seen by comparing the solid lines in the right panel of the same figure, which shows the genuine BK and Bπ correlation functions obtained from the Coulomb interaction potential, to the correlation functions after the mapping to the DK and Dπ system, which are depicted as dashed lines.

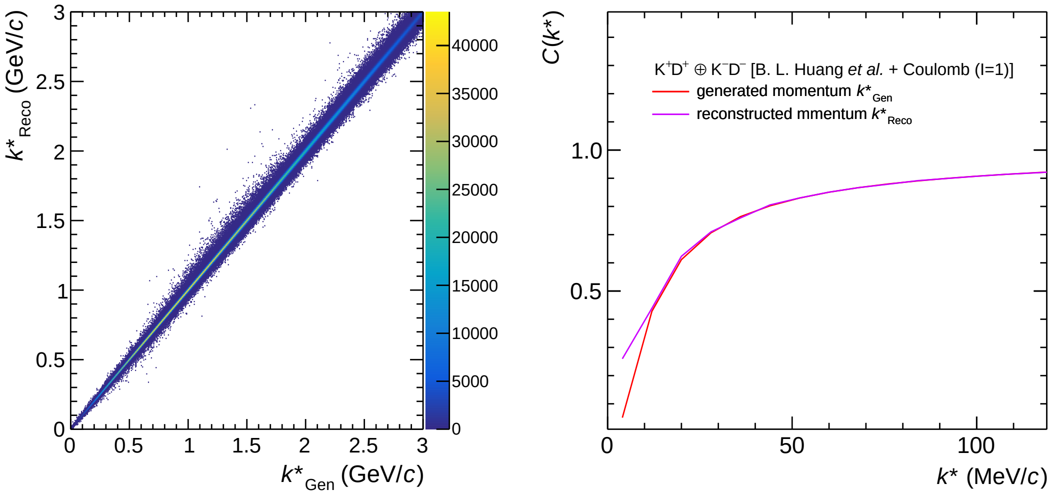

(A) Momentum resolution matrix from HF MC generated data.

(B) Correlation function obtained from the scattering length predicted by Ref. [196].

FIGURE B.6: Effect of the momentum resolution on the $D^+K^+ \oplus D^-K^-$ correlation function, estimated by transforming the model correlation function from the generated k^*_{Gen} to the reconstructed momentum basis k^*_{Reco}, using the momentum resolution matrix obtained from MC simulated data.

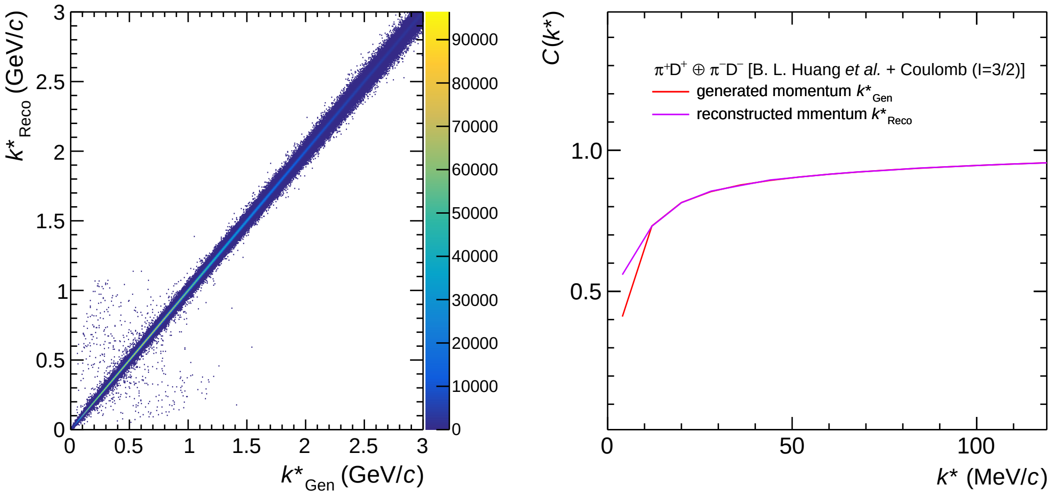

(A) Momentum resolution matrix from HF MC generated data.

(B) Correlation function obtained from the scattering length predicted by Ref. [196].

FIGURE B.7: Effect of the momentum resolution on the $D^+\pi^+ \oplus D^-\pi^-$ correlation function, estimated by transforming the model correlation function from the generated k^*_{Gen} to the reconstructed relative momentum k^*_{Reco}, using the momentum resolution matrix obtained from MC simulated data.

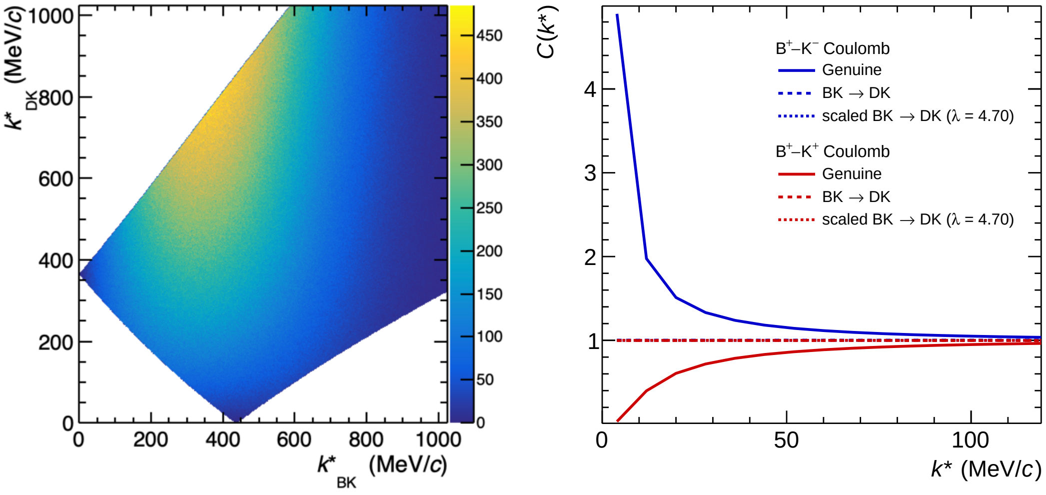

FIGURE B.8: The *left panel* shows the transformation matrix from the BK momentum basis to the one the DK system. The *right panel* depicts the BK correlation function modeled using the Coulomb potential (solid line), as well as the same correlation function after the transformation (dashed line) and additional re-weighting by $\lambda = 4.70\%$ (dotted line), for same- (red) and opposite-charge (blue) pairs.

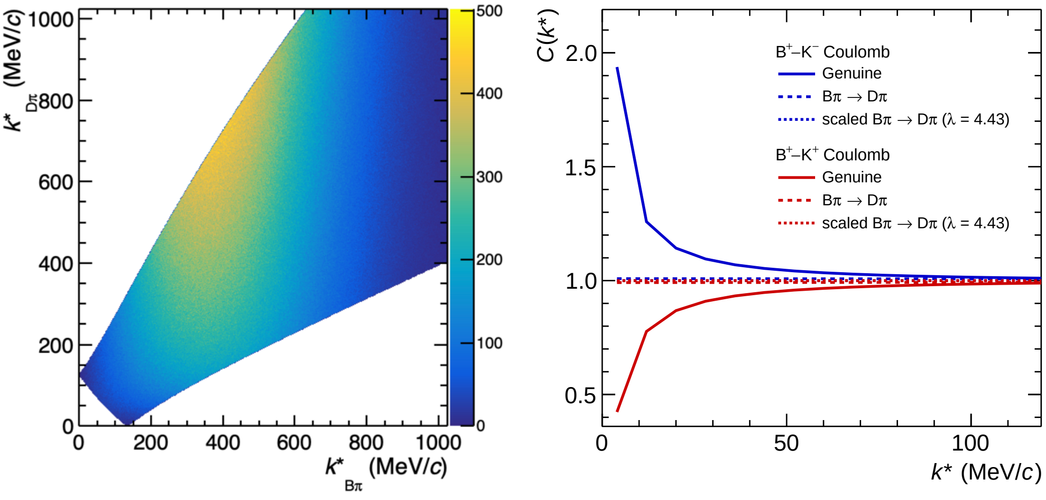

FIGURE B.9: The *left panel* shows the transformation matrix from the Bπ momentum basis to the one the Dπ system. The *right panel* depicts the Bπ correlation function modeled using the Coulomb potential (solid line), as well as the same correlation function after the transformation (dashed line) and additional re-weighting by $\lambda = 4.70\%$ (dotted line), for same- (red) and opposite-charge (blue) pairs.

Appendix C

The $\Lambda\mathrm{K}^+$correlation function

The $\Lambda\mathrm{K}^- \oplus \overline{\Lambda}\mathrm{K}^+$ and $\Lambda\mathrm{K}^+ \oplus \overline{\Lambda}\mathrm{K}^-$ correlation functions were studied in HM triggered pp collisions at $\sqrt{s} = 13$ TeV, measured by ALICE [52]. While the former provided crucial information on the properties and nature of the $\Xi(1620)$ state, which strongly couples to the measured pair, the latter, which I was directly involved in analyzing, is particularly interesting to this thesis as possible decay channel of the p–ϕ bound state.

The analysed events are selected using the same criteria as the ones given in Tab. 4.1 and explained in detail in Sec. 4.1. Also, the kaon candidate selection is equivalent to that in Sec. 4.1. The criteria are listed in Tab. 4.2 and result in a purity of $> 99\%$ and the primary fraction is found to be $\sim 94\%$. The Λ candidates are reconstructed from the weak decay $\Lambda \rightarrow \mathrm{p}\pi^-$ (BR $= (63.9 \pm 0.5)\%$ [122]) and its charge conjugate, characterized by a relatively long decay length of $c\tau = (7.89 \pm 0.06)$ cm, making them V_0 candidates. The kinematic and topological selection criteria related to the reconstruction of the Λ and $\overline{\Lambda}$ resonance follow Ref. [123] and are listed in Tab. C.1. Each V_0 is built from the invariant mass of two opposite charged tracks, which are reconstructed globally due to the better spatial resolution and from at least 70 clusters in the TPC. The daughter tracks are required to lie within a pseudorapidity interval of $|\eta| < 0.8$ and have a minimum distance of closest approach to the primary vertex of 0.05 cm. To reject Λ candidates with daughter tracks stemming from pile-up events, either the time information of the TOF is used to identify the bunch crossing in which the particle was produced, or the tracks need a hit in the SPD or SSD layers of the ITS. A loose PID selection employing only information provided by the TPC of $|n_{\sigma,\mathrm{TPC}}(\mathrm{p}, \pi)| < 5$ is applied to maximize the efficiency. The position and properties of the Λ decay vertex are restricted by several selection criteria, which were already introduced in Sec. 3.2.2. Additionally, the reconstructed Λ candidate need a transverse momentum $p_\mathrm{T} > 0.3$ GeV/c to reduce the contribution of fake candidates and lie within 4 GeV/c^2 around their nominal mass of $M_{\Lambda,\mathrm{PDG}} = (1115.683 \pm 0.006)$ MeV/c^2 [122]. Due to the rather wide PID selection of the daughter tracks, residual pions contaminate the proton sample. When paired with the charge-conjugate daughter pion, they lead to the misidentification of K^0_S as Λ candidates. This is accounted for by a cut in the invariant mass spectrum, obtained under the π^+–π^- daughter hypothesis. The resulting invariant mass spectrum is fitted with the sum of two Gaussian functions, which describe the signal S, and a spline function with 6 knots, which emulate the combinatorial background B. A total yield of 99.1×10^6 and 93.6×10^6, and purities of 94.2% and 95.1% are obtained for Λ and $\overline{\Lambda}$, respectively. The purities are determined by the ratio $S/(S+B)$. The primary fraction of the sample is found to be 57.6%, while 23.2% of Λ candidates are secondary particles from the weak decays of neutral and charged Ξ baryons. The remaining 19.2% are associated with Σ_0 particles. These fractions are determined by following the procedure described in Ref. [46]. The raw correlation functions of

Selection criterion	Value
Daughter selection criteria	
Track-type	global tracks
Pseudorapidity	$\|\eta\| < 0.8$
TPC cluster	$n_{\mathrm{TPC}} > 70$
Distance of closest approach	$\|\mathrm{DCA}\| > 0.05\,\mathrm{cm}$
Particle identification	$\|n_{\sigma,\mathrm{TPC}}(\mathrm{p},\pi)\| < 5$
Out-of-bunch pile-up removal	Hit in ITS SPD or SSD or TOF timing
V_0 selection criteria	
Transverse momentum	$p_{\mathrm{T}} > 0.3\,\mathrm{GeV}/c$
Λ decay vertex	$\|i_{\mathrm{vertex}_\Lambda}\| < 100$ cm with $i = x, y, z$
Transverse radius of the decay vertex	$0.2 < r_{xy} < 100$ cm
DCA of daughter tracks at the decay vertex	$\sigma_{\mathrm{vertex}} < 1.5$ cm
Cosine of pointing angle ff	$\cos\theta_{\mathrm{p}} > 0.99$
K^0 rejection	$0.48 < \mathrm{M}_{\pi^+\pi^-} < 0.515\,\mathrm{GeV}/c^2$
Λ selection	$\|\mathrm{M}_{\mathrm{p}\pi} - \mathrm{M}_{\Lambda,\mathrm{PDG}}\| < 4\,\mathrm{GeV}/c^2$

TABLE C.1: Λ selection criteria.

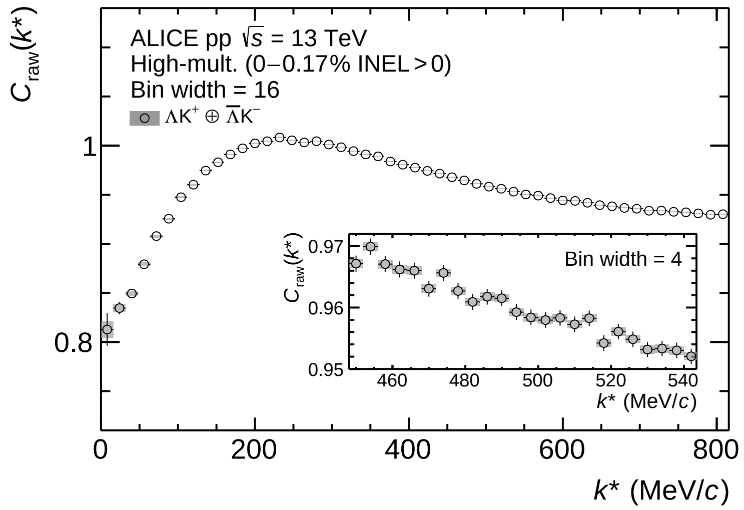

FIGURE C.1: The experimental ΛK$^-$ ⊕ $\overline{\Lambda}$K$^+$ correlation function with statistical (bars) and systematic uncertainties (boxes), evaluated in 16 MeV/c wide k^* intervals in the main panel. The sub-panel shows the k^* region of interest for a possible p–ϕ bound state decay in a finer bin width of 4 MeV/c.

Λ–K^+ and $\overline{\Lambda}$–K^- are obtained from Eq. 2.10, choosing $k^* \in [240, 340]$ MeV/c as normalization region. As they are compatible within the statistical uncertainties, they are combined to $\Lambda\mathrm{K}^+ \oplus \overline{\Lambda}\mathrm{K}^-$, with a total of 16.78×10^7 pairs out of which 4.45×10^6 contribute to the correlation signal in the femtoscopic region of $k^* < 200\,\mathrm{MeV}/c$. The systematic uncertainties of the raw data are estimated by simultaneously varying the selection criteria of kaon and Λ candidates. Each set of variations and their individual amount is chosen to not induce a modification larger than ±10% to N_{same} within $k^* < 200\,\mathrm{MeV/c}$ in order to retain the statistical significance. This leads to a relative systematic uncertainty of $2 - 4\%$ in the lower k^* bins. The resulting $\Lambda\mathrm{K}^+ \oplus \overline{\Lambda}\mathrm{K}^-$ correlation function is shown in Fig. C.1. The k^* value of the data points shown in the main panel is evaluated in intervals of 16 MeV/c width. The sub-panel shows the region of $k^* \in [479, 517]$ MeV/c in finer binning. It corresponds to the k^*-interval, where a p–ϕ bound state would appear as structure, given the binding energy of 12.8 to 56.1 MeV obtained from the analysis presented in Chapter 5. Even though a finer bin width of 4 MeV/c is chosen, no signs of a p–ϕ bound state, decaying into $\Lambda\mathrm{K}^+$ can be observed. The signal might, however, be washed out, and other decay channels favored. Also, no cusp at the opening of the p–ϕ channel is found at $k^* \sim 529$ MeV/c, indicating a shallow coupling between the two channels. All relevant k^* values related to the p–ϕ channel and bound state in the $\Lambda\mathrm{K}^+$ correlation function can be obtained from Eq. 2.38.

Bibliography

[1] Wikipedia. Standard model of elementary particles: the 12 fundamental fermions and 5 fundamental bosons. `https://commons.wikimedia.org/wiki/File:Standard_Model_of_Elementary_Particles.svg`, 2019. Accessed: 16th January, 2025.
Cited on page 2.

[2] Mark Thomson. *Modern particle physics*. Cambridge University Press, New York, 10 2013. ISBN 978-1-107-03426-6, 978-1-139-52536-7. doi: 10.1017/CBO9781139525367.
Cited on pages 3, 4, and 5.

[3] F. Halzen and Alan D. Martin. *QUARKS AND LEPTONS: AN INTRODUCTORY COURSE IN MODERN PARTICLE PHYSICS*. 1984. ISBN 978-0-471-88741-6.
Cited on page 4.

[4] S. Navas et al. Review of particle physics. *Phys. Rev. D*, 110(3):030001, 2024. doi: 10.1103/PhysRevD.110.030001.
Cited on page 4.

[5] W. Weise. Nuclear aspects of chiral symmetry. *Nucl. Phys. A*, 553:59C–72C, 1993. doi: 10.1016/0375-9474(93)90615-5.
Cited on page 5.

[6] Yoichiro Nambu. Quasiparticles and Gauge Invariance in the Theory of Superconductivity. *Phys. Rev.*, 117:648–663, 1960. doi: 10.1103/PhysRev.117.648.
Cited on page 5.

[7] J. Goldstone. Field Theories with Superconductor Solutions. *Nuovo Cim.*, 19: 154–164, 1961. doi: 10.1007/BF02812722.
Not cited.

[8] Jeffrey Goldstone, Abdus Salam, and Steven Weinberg. Broken Symmetries. *Phys. Rev.*, 127:965–970, 1962. doi: 10.1103/PhysRev.127.965.
Cited on page 5.

[9] Jeremy W. Holt, Norbert Kaiser, and Wolfram Weise. Nuclear chiral dynamics and thermodynamics. *Prog. Part. Nucl. Phys.*, 73:35–83, 2013. doi: 10.1016/j.ppnp.2013.08.001.
Cited on page 6.

[10] Hideki Yukawa. On the Interaction of Elementary Particles I. *Proc. Phys. Math. Soc. Jap.*, 17:48–57, 1935. doi: 10.1143/PTPS.1.1.
Cited on page 7.

[11] C. M. G. Lattes, H. Muirhead, G. P. S. Occhialini, and C. F. Powell. PROCESSES INVOLVING CHARGED MESONS. *Nature*, 159:694–697, 1947. doi: 10.1038/

159694a0.
Cited on page 7.

[12] Robert B. Wiringa, V. G. J. Stoks, and R. Schiavilla. An Accurate nucleon-nucleon potential with charge independence breaking. *Phys. Rev. C*, 51:38–51, 1995. doi: 10.1103/PhysRevC.51.38.
Cited on pages 7, 16, and 40.

[13] B. Holzenkamp, K. Holinde, and J. Speth. A Meson Exchange Model for the Hyperon Nucleon Interaction. *Nucl. Phys. A*, 500:485–528, 1989. doi: 10.1016/0375-9474(89)90223-6.
Cited on page 7.

[14] A. Reuber, K. Holinde, and J. Speth. Meson exchange hyperon - nucleon interactions in free scattering and nuclear matter. *Nucl. Phys. A*, 570:543–579, 1994. doi: 10.1016/0375-9474(94)90073-6.
Cited on page 9.

[15] T. A. Rijken, V. G. J. Stoks, and Y. Yamamoto. Soft core hyperon - nucleon potentials. *Phys. Rev. C*, 59:21–40, 1999. doi: 10.1103/PhysRevC.59.21.
Not cited.

[16] Th. A. Rijken and Y. Yamamoto. Extended-soft-core baryon-baryon model. II. Hyperon-nucleon interaction. *Phys. Rev. C*, 73:044008, 2006. doi: 10.1103/PhysRevC.73.044008.
Not cited.

[17] J. Haidenbauer and Ulf-G. Meissner. The Julich hyperon-nucleon model revisited. *Phys. Rev. C*, 72:044005, 2005. doi: 10.1103/PhysRevC.72.044005.
Cited on page 7.

[18] Th. A. Rijken and Y. Yamamoto. Extended-soft-core baryon-baryon model III: S=-2 hyperon-hyperon/nucleon interaction. 8 2006.
Cited on page 7.

[19] Y. Yamamoto and T. A. Rijken. S = -2 hypernuclei based on the ESC04 model. *Nucl. Phys. A*, 804:139–148, 2008. doi: 10.1016/j.nuclphysa.2007.12.005.
Cited on page 7.

[20] Rui Chen, Atsushi Hosaka, and Xiang Liu. Heavy molecules and one-σ/ω-exchange model. *Phys. Rev. D*, 96(11):116012, 2017. doi: 10.1103/PhysRevD.96.116012.
Cited on page 7.

[21] Yasuhiro Yamaguchi, Shigehiro Yasui, and Atsushi Hosaka. Open charm and bottom meson-nucleon potentials à la the nuclear force. *Phys. Rev. D*, 106(9):094001, 2022. doi: 10.1103/PhysRevD.106.094001.
Cited on page 7.

[22] Steven Weinberg. Phenomenological Lagrangians. *Physica A*, 96(1-2):327–340, 1979. doi: 10.1016/0378-4371(79)90223-1.
Cited on page 7.

[23] Steven Weinberg. Nuclear forces from chiral Lagrangians. *Phys. Lett. B*, 251:288–292, 1990. doi: 10.1016/0370-2693(90)90938-3.
Cited on page 7.

[24] R. Machleidt and D. R. Entem. Chiral effective field theory and nuclear forces. *Phys. Rept.*, 503:1–75, 2011. doi: 10.1016/j.physrep.2011.02.001.
Cited on pages 7 and 8.

[25] Kenneth G. Wilson. Confinement of Quarks. *Phys. Rev. D*, 10:2445–2459, 1974. doi: 10.1103/PhysRevD.10.2445.
Cited on page 9.

[26] T. Hatsuda. Hadron interactions from lattice QCD. *Prog. Part. Nucl. Phys.*, 67: 122–129, 2012. doi: 10.1016/j.ppnp.2011.12.005.
Cited on page 9.

[27] Martin Luscher. Two particle states on a torus and their relation to the scattering matrix. *Nucl. Phys. B*, 354:531–578, 1991. doi: 10.1016/0550-3213(91) 90366-6.
Cited on page 9.

[28] Martin Luscher. Signatures of unstable particles in finite volume. *Nucl. Phys. B*, 364:237–251, 1991. doi: 10.1016/0550-3213(91)90584-K.
Cited on page 9.

[29] N. Ishii, S. Aoki, and T. Hatsuda. The Nuclear Force from Lattice QCD. *Phys. Rev. Lett.*, 99:022001, 2007. doi: 10.1103/PhysRevLett.99.022001.
Cited on page 9.

[30] Tetsuo Hatsuda. Lattice quantum chromodynamics and baryon-baryon interactions. *Front. Phys. (Beijing)*, 13(6):132105, 2018. doi: 10.1007/ s11467-018-0829-4.
Cited on page 9.

[31] S. Aoki. Hadron interactions in lattice QCD. *Prog. Part. Nucl. Phys.*, 66:687–726, 2011. doi: 10.1016/j.ppnp.2011.07.001.
Cited on page 9.

[32] R. A. Arndt, W. J. Briscoe, I. I. Strakovsky, and R. L. Workman. Updated analysis of NN elastic scattering to 3-GeV. *Phys. Rev. C*, 76:025209, 2007. doi: 10.1103/PhysRevC.76.025209.
Cited on page 9.

[33] R. Navarro Pérez, J. E. Amaro, and E. Ruiz Arriola. Partial Wave Analysis of Nucleon-Nucleon Scattering below pion production threshold. *Phys. Rev. C*, 88:024002, 2013. doi: 10.1103/PhysRevC.88.024002. [Erratum: Phys.Rev.C 88, 069902 (2013)].
Cited on page 9.

[34] Terry S. Mast, Margaret Alston-Garnjost, Roger O. Bangerter, Angela S. Barbaro-Galtieri, Frank T. Solmitz, and Robert D. Tripp. Elastic, Charge Exchange, and Total K- p Cross-Sections in the Momentum Range 220-MeV/c to 470-MeV/c. *Phys. Rev. D*, 14:13, 1976. doi: 10.1103/PhysRevD.14.13.
Cited on page 9.

[35] J. Ciborowski et al. KAON SCATTERING AND CHARGED SIGMA HYPERON PRODUCTION IN K- P INTERACTIONS BELOW 300-MEV/C. *J. Phys. G*, 8:13–32, 1982. doi: 10.1088/0305-4616/8/1/005.
Cited on page 9.

[36] B. Sechi-Zorn, B. Kehoe, J. Twitty, and R. A. Burnstein. Low-energy lambda-proton elastic scattering. *Phys. Rev.*, 175:1735–1740, 1968. doi: 10.1103/PhysRev.175.1735.
Cited on page 9.

[37] R. Engelmann, H. Filthuth, V. Hepp, and E. Kluge. Inelastic Σ $-$p-interactions at low momenta . *Phys. Lett.*, 21(5):587–589, 1966. doi: 10.1016/0031-9163(66)91310-2.
Cited on page 9.

[38] F. Eisele, H. Filthuth, W. Foehlisch, V. Hepp, and Gunter Zech. Elastic sigma+-p scattering at low energies. *Phys. Lett. B*, 37:204–206, 1971. doi: 10.1016/0370-2693(71)90053-0.
Cited on page 9.

[39] A. Gal, J. M. Soper, and R. H. Dalitz. Shell-model analysis of lambda binding energies for p-shell hypernuclei. 1. Basic formulas and matrix elements for lambda N and lambda NN forces. *Annals Phys.*, 63:53–126, 1971. doi: 10.1016/0003-4916(71)90297-1.
Cited on page 9.

[40] O. Hashimoto and H. Tamura. Spectroscopy of Lambda hypernuclei. *Prog. Part. Nucl. Phys.*, 57:564–653, 2006. doi: 10.1016/j.ppnp.2005.07.001.
Cited on page 9.

[41] D. Gotta et al. Pionic hydrogen. *Lect. Notes Phys.*, 745:165–186, 2008. doi: 10.1007/978-3-540-75479-4_10.
Cited on page 9.

[42] M. Bazzi et al. A New Measurement of Kaonic Hydrogen X-rays. *Phys. Lett. B*, 704:113–117, 2011. doi: 10.1016/j.physletb.2011.09.011.
Cited on page 9.

[43] Shreyasi Acharya et al. p–p, p–Λ, and Λ–Λ correlations studied via femtoscopy in pp reactions at $\sqrt{s} = 7$ TeV. *Phys. Rev. C*, 99(2):024001, 2019. doi: 10.1103/PhysRevC.99.024001.
Cited on pages 10, 14, 15, 68, and 88.

[44] Shreyasi Acharya et al. Investigating the role of strangeness in baryon–antibaryon annihilation at the LHC. *Phys. Lett. B*, 829:137060, 2022. doi: 10.1016/j.physletb.2022.137060.
Cited on pages 10, 15, and 68.

[45] Shreyasi Acharya et al. Scattering studies with low-energy kaon-proton femtoscopy in proton–proton collisions at the LHC. *Phys. Rev. Lett.*, 124(9):092301, 2020. doi: 10.1103/PhysRevLett.124.092301.
Cited on pages 10 and 68.

[46] Shreyasi Acharya et al. Exploring the NΛ–NΣ coupled system with high precision correlation techniques at the LHC. *Phys. Lett. B*, 833:137272, 2022. doi: 10.1016/j.physletb.2022.137272.
Cited on pages 10, 15, and 115.

[47] Shreyasi Acharya et al. Investigation of the p–Σ^0 interaction via femtoscopy in pp collisions. *Phys. Lett. B*, 805:135419, 2020. doi: 10.1016/j.physletb.2020.

135419.
Cited on pages 10 and 15.

[48] Shreyasi Acharya et al. Study of the Λ–Λ interaction with femtoscopy correlations in pp and p–Pb collisions at the LHC. *Phys. Lett. B*, 797:134822, 2019. doi: 10.1016/j.physletb.2019.134822.
Cited on page 10.

[49] Shreyasi Acharya et al. First Observation of an Attractive Interaction between a Proton and a Cascade Baryon. *Phys. Rev. Lett.*, 123(11):112002, 2019. doi: 10.1103/PhysRevLett.123.112002.
Cited on pages 10 and 15.

[50] Alice Collaboration et al. Unveiling the strong interaction among hadrons at the LHC. *Nature*, 588:232–238, 2020. doi: 10.1038/s41586-020-3001-6. [Erratum: Nature 590, E13 (2021)].
Cited on pages 10, 15, and 33.

[51] Shreyasi Acharya et al. Experimental Evidence for an Attractive p–ϕ Interaction. *Phys. Rev. Lett.*, 127(17):172301, 2021. doi: 10.1103/PhysRevLett.127.172301.
Cited on pages 10, 68, 85, 87, 88, 93, 94, 97, 100, and 102.

[52] Shreyasi Acharya et al. Accessing the strong interaction between Λ baryons and charged kaons with the femtoscopy technique at the LHC. *Phys. Lett. B*, 845:138145, 2023. doi: 10.1016/j.physletb.2023.138145.
Cited on pages 10, 100, and 115.

[53] Shreyasi Acharya et al. First study of the two-body scattering involving charm hadrons. *Phys. Rev. D*, 106(5):052010, 2022. doi: 10.1103/PhysRevD.106.052010.
Cited on pages 10, 15, 44, 52, 57, 71, 81, and 105.

[54] Raffaele Del Grande, Laura Šerkšnytė, Laura Fabbietti, Valentina Mantovani Sarti, and Dimitar Mihaylov. A method to remove lower order contributions in multi-particle femtoscopic correlation functions. *Eur. Phys. J. C*, 82(3):244, 2022. doi: 10.1140/epjc/s10052-022-10209-z.
Cited on pages 10 and 63.

[55] Shreyasi Acharya et al. Towards the understanding of the genuine three-body interaction for p–p–p and p–p–Λ. *Eur. Phys. J. A*, 59(7):145, 2023. doi: 10.1140/epja/s10050-023-00998-6.
Cited on page 10.

[56] Shreyasi Acharya et al. Study of the p–p–K^+ and p–p–K^- dynamics using the femtoscopy technique. *Eur. Phys. J. A*, 59(12):298, 2023. doi: 10.1140/epja/s10050-023-01139-9.
Cited on page 10.

[57] R. Hanbury Brown and R. Q. Twiss. A New type of interferometer for use in radio astronomy. *Phil. Mag. Ser. 7*, 45:663–682, 1954. doi: 10.1080/14786440708520475.
Cited on page 11.

[58] R. Hanbury Brown and R. Q. Twiss. Correlation between Photons in two Coherent Beams of Light. *Nature*, 177:27–29, 1956. doi: 10.1038/177027a0.
Cited on page 11.

[59] R. Hanbury Brown and R. Q. Twiss. A Test of a new type of stellar interferometer on Sirius. *Nature*, 178:1046–1048, 1956. doi: 10.1038/1781046a0.
Cited on page 11.

[60] E. Brannen and H. Ferguson. The Question of Correlation between Photons in Coherent Light Rays. *Nature*, 178:481–482, 1956. doi: 10.1038/178481a0.
Cited on page 11.

[61] E. Purcell. The Question of Correlation between Photons in Coherent Light Rays. *Nature*, 178:1449–1450, 1956. doi: 10.1038/1781449a0.
Cited on page 11.

[62] Gerson Goldhaber, William B. Fowler, Sulamith Goldhaber, and T. F. Hoang. Pion-pion correlations in antiproton annihilation events. *Phys. Rev. Lett.*, 3: 181–183, 1959. doi: 10.1103/PhysRevLett.3.181.
Cited on page 11.

[63] Gerson Goldhaber, Sulamith Goldhaber, Won-Yong Lee, and Abraham Pais. Influence of Bose-Einstein statistics on the anti-proton proton annihilation process. *Phys. Rev.*, 120:300–312, 1960. doi: 10.1103/PhysRev.120.300.
Cited on page 11.

[64] G. I. Kopylov and M. I. Podgoretsky. Correlations of identical particles emitted by highly excited nuclei. *Sov. J. Nucl. Phys.*, 15:219–223, 1972.
Cited on page 11.

[65] G. I. Kopylov. Like particle correlations as a tool to study the multiple production mechanism. *Phys. Lett. B*, 50:472–474, 1974. doi: 10.1016/0370-2693(74)90263-9.
Cited on page 11.

[66] S. E. Koonin. Proton Pictures of High-Energy Nuclear Collisions. *Phys. Lett. B*, 70:43–47, 1977. doi: 10.1016/0370-2693(77)90340-9.
Cited on pages 11 and 13.

[67] S. Pratt. Pion Interferometry for Exploding Sources. *Phys. Rev. Lett.*, 53:1219–1221, 1984. doi: 10.1103/PhysRevLett.53.1219.
Cited on pages 11 and 12.

[68] S. Pratt, T. Csorgo, and J. Zimanyi. Detailed predictions for two pion correlations in ultrarelativistic heavy ion collisions. *Phys. Rev. C*, 42:2646–2652, 1990. doi: 10.1103/PhysRevC.42.2646.
Cited on page 13.

[69] S. Pratt. Validity of the smoothness assumption for calculating two-boson correlations in high-energy collisions. *Phys. Rev. C*, 56:1095–1098, 1997. doi: 10.1103/PhysRevC.56.1095.
Cited on pages 11 and 12.

[70] R. Lednický and V.L. Lyuboshits. Final State Interaction Effect on Pairing Correlations Between Particles with Small Relative Momenta. *Sov. J. Nucl. Phys.*,

35:770, 1982.
Cited on pages 11 and 107.

[71] Richard Lednicky. Femtoscopic correlations of nonidentical particles. *Acta Phys. Polon. B*, 40:1145–1154, 2009.
Cited on page 12.

[72] Richard Lednický. Femtoscopy: Theory. *AIP Conference Proceedings*, 828(1): 423–429, 2006. doi: 10.1063/1.2197450.
Cited on pages 11 and 12.

[73] D. L. Mihaylov, V. Mantovani Sarti, O. W. Arnold, L. Fabbietti, B. Hohlweger, and A. M. Mathis. A femtoscopic Correlation Analysis Tool using the Schrödinger equation (CATS). *Eur. Phys. J. C*, 78(5):394, 2018. doi: 10.1140/epjc/s10052-018-5859-0.
Cited on pages 13, 94, and 110.

[74] Ulrich W. Heinz and Barbara V. Jacak. Two particle correlations in relativistic heavy ion collisions. *Ann. Rev. Nucl. Part. Sci.*, 49:529–579, 1999. doi: 10.1146/annurev.nucl.49.1.529.
Cited on pages 14 and 16.

[75] T. Csorgo, S. Hegyi, and W. A. Zajc. Bose-Einstein correlations for Levy stable source distributions. *Eur. Phys. J. C*, 36:67–78, 2004. doi: 10.1140/epjc/s2004-01870-9.
Cited on page 14.

[76] Georges Aad et al. Two-particle Bose–Einstein correlations in pp collisions at $\sqrt{\mathbf{s}} = 0.9$ and 7 TeV measured with the ATLAS detector. *Eur. Phys. J. C*, 75(10): 466, 2015. doi: 10.1140/epjc/s10052-015-3644-x.
Cited on page 14.

[77] Albert M Sirunyan et al. Bose-Einstein correlations in pp, pPb, and PbPb collisions at $\sqrt{s_{NN}} = 0.9 - 7$ TeV. *Phys. Rev. C*, 97(6):064912, 2018. doi: 10.1103/PhysRevC.97.064912.
Not cited.

[78] Albert M Sirunyan et al. Bose-Einstein correlations of charged hadrons in proton-proton collisions at $\sqrt{s} = 13$ TeV. *JHEP*, 03:014, 2020. doi: 10.1007/JHEP03(2020)014.
Cited on page 14.

[79] Shreyasi Acharya et al. Constraining the $\overline{\mathrm{K}}$N coupled channel dynamics using femtoscopic correlations at the LHC. *Eur. Phys. J. C*, 83(4):340, 2023. doi: 10.1140/epjc/s10052-023-11476-0.
Cited on pages 15 and 40.

[80] Shreyasi Acharya et al. Kaon femtoscopy in Pb-Pb collisions at $\sqrt{s_{\mathrm{NN}}}$ = 2.76 TeV. *Phys. Rev. C*, 96(6):064613, 2017. doi: 10.1103/PhysRevC.96.064613.
Cited on page 15.

[81] Betty Bezverkhny Abelev et al. Multiplicity dependence of jet-like two-particle correlation structures in p–Pb collisions at $\sqrt{s_{NN}}$=5.02 TeV. *Phys. Lett. B*, 741: 38–50, 2015. doi: 10.1016/j.physletb.2014.11.028.
Cited on page 18.

[82] Bo Andersson, G. Gustafson, G. Ingelman, and T. Sjostrand. Parton Fragmentation and String Dynamics. *Phys. Rept.*, 97:31–145, 1983. doi: 10.1016/0370-1573(83)90080-7.
Cited on pages 18 and 68.

[83] Michael Creutz. *Quarks, Gluons and Lattices*. Oxford University Press, 1983. ISBN 978-1-009-29039-5, 978-1-009-29038-8, 978-1-009-29037-1, 978-0-521-31535-7. doi: 10.1017/9781009290395.
Cited on page 18.

[84] Mathias Macêdo-Lima and Lucas Madeira. Scattering length and effective range of microscopic two-body potentials. *Rev. Bras. Ens. Fis.*, 45:e20230079, 2023. doi: 10.1590/1806-9126-RBEF-2023-0079.
Cited on page 19.

[85] Jun John Sakurai and Jim Napolitano. *Modern Quantum Mechanics*. Quantum physics, quantum information and quantum computation. Cambridge University Press, 10 2020. ISBN 978-0-8053-8291-4, 978-1-108-52742-2, 978-1-108-58728-0. doi: 10.1017/9781108587280.
Cited on page 22.

[86] Leonard S. Rodberg, R. M. Thaler, and U. Fano. Introduction to the quantum theory of scattering. *American Journal of Physics*, 36(4):373–373, 1968. doi: 10.1119/1.1974532.
Cited on page 22.

[87] Lars Bojer Madsen. Effective range theory. *American Journal of Physics*, 70(8):811–814, 2002. doi: 10.1119/1.1473644.
Cited on page 22.

[88] N. G. Kelkar, K. P. Khemchandani, N. J. Upadhyay, and B. K. Jain. Interaction of eta mesons with nuclei. *Rept. Prog. Phys.*, 76:066301, 2013. doi: 10.1088/0034-4885/76/6/066301.
Cited on page 26.

[89] Yuki Kamiya, Tetsuo Hyodo, Kenji Morita, Akira Ohnishi, and Wolfram Weise. $K^- p$ Correlation Function from High-Energy Nuclear Collisions and Chiral SU(3) Dynamics. *Phys. Rev. Lett.*, 124(13):132501, 2020. doi: 10.1103/PhysRevLett.124.132501.
Cited on pages 25 and 26.

[90] Serguei Chatrchyan et al. Observation of a New Boson at a Mass of 125 GeV with the CMS Experiment at the LHC. *Phys. Lett. B*, 716:30–61, 2012. doi: 10.1016/j.physletb.2012.08.021.
Cited on page 29.

[91] Georges Aad et al. Observation of a new particle in the search for the Standard Model Higgs boson with the ATLAS detector at the LHC. *Phys. Lett. B*, 716:1–29, 2012. doi: 10.1016/j.physletb.2012.08.020.
Cited on page 29.

[92] S. Acharya et al. The ALICE experiment: a journey through QCD. *Eur. Phys. J. C*, 84(8):813, 2024. doi: 10.1140/epjc/s10052-024-12935-y.
Cited on page 29.

[93] LHC Machine. *JINST*, 3:S08001, 2008. doi: 10.1088/1748-0221/3/08/S08001.
Cited on page 29.

[94] M. Bajko et al. Report of the task force on the incident of 19th September 2008 at the LHC. 3 2009.
Cited on page 30.

[95] Francesco Bertinelli et al. Towards a Consolidation of LHC Superconducting Splices for 7 TeV Operation. *Conf. Proc. C*, 100523:MOPEB042, 2010.
Cited on page 30.

[96] Mike Lamont and Joachim Mnich. Foreword to "accelerator and experiments for lhc run3" special issue. *Journal of Instrumentation*, 19(05):P05060, may 2024. doi: 10.1088/1748-0221/19/05/P05060. URL `https://dx.doi.org/10.1088/1748-0221/19/05/P05060`.
Cited on page 30.

[97] Esma Mobs. The CERN accelerator complex. Complexe des accélérateurs du CERN. Jul 2016. URL `http://cds.cern.ch/record/2197559`. General Photo.
Cited on page 30.

[98] A. Kalweit. Highlights from the ALICE experiment. *Nucl. Phys. A*, 982:1–7, 2019. doi: 10.1016/j.nuclphysa.2018.10.015.
Cited on page 31.

[99] ALICE Collaboration. Recorded integrated luminosity in pp @ 13.6 tev, 2022-2024 comparison, as of 18.10.2024. `https://alice-figure.web.cern.ch/node/32193`, 2024. Accessed: 20th January, 2025.
Cited on page 31.

[100] John Jowett. Colliding Heavy Ions in the LHC. In *9th International Particle Accelerator Conference*, 6 2018. doi: 10.18429/JACoW-IPAC2018-TUXGBD2.
Cited on page 31.

[101] K. Aamodt et al. The ALICE experiment at the CERN LHC. *JINST*, 3:S08002, 2008. doi: 10.1088/1748-0221/3/08/S08002.
Cited on pages 32, 33, 34, 36, and 37.

[102] P Cortese et al. ALICE: Physics performance report, volume I. *J. Phys. G*, 30: 1517–1763, 2004. doi: 10.1088/0954-3899/30/11/001.
Not cited.

[103] Christian Wolfgang Fabjan et al. ALICE: Physics Performance Report, volume II. *J. Phys. G*, 32:1295–2040, 2006. doi: 10.1088/0954-3899/32/10/001.
Cited on page 37.

[104] Betty Bezverkhny Abelev et al. Performance of the ALICE Experiment at the CERN LHC. *Int. J. Mod. Phys. A*, 29:1430044, 2014. doi: 10.1142/S0217751X14300440.
Cited on pages 32, 36, 37, and 45.

[105] ALICE Collaboration. 3d alice schematic run2 - with description. `https://alice-figure.web.cern.ch/node/11218`, 2017. Accessed: 30th August, 2024.
Cited on page 33.

[106] E. Abbas et al. Performance of the ALICE VZERO system. *JINST*, 8:P10016, 2013. doi: 10.1088/1748-0221/8/10/P10016.
Cited on page 33.

[107] Jaroslav Adam et al. Enhanced production of multi-strange hadrons in high-multiplicity proton-proton collisions. *Nature Phys.*, 13:535–539, 2017. doi: 10.1038/nphys4111.
Cited on page 33.

[108] Jaroslav Adam et al. Measurement of charm and beauty production at central rapidity versus charged-particle multiplicity in proton-proton collisions at $\sqrt{s} = 7$ TeV. *JHEP*, 09:148, 2015. doi: 10.1007/JHEP09(2015)148.
Cited on page 33.

[109] Domenico Colella. ALICE ITS: the Run 1 to Run 2 transition and recent operational experience. *PoS*, VERTEX2015:003, 2015. doi: 10.22323/1.254.0003.
Cited on page 33.

[110] J. Alme et al. The ALICE TPC, a large 3-dimensional tracking device with fast readout for ultra-high multiplicity events. *Nucl. Instrum. Meth. A*, 622:316–367, 2010. doi: 10.1016/j.nima.2010.04.042.
Cited on page 35.

[111] W. Shockley. Currents to conductors induced by a moving point charge. *J. Appl. Phys.*, 9(10):635–636, 1938. doi: 10.1063/1.1710367.
Cited on page 35.

[112] S. Ramo. Currents induced by electron motion. *Proceedings of the IRE*, 27(9): 584–585, 1939. doi: 10.1109/JRPROC.1939.228757.
Cited on page 35.

[113] Alexander Philipp Kalweit. ALICE TPC dE/dx performace in Run2 13 TeV (0.2T), 2015. URL `https://alice-figure.web.cern.ch/node/8670`. Accessed: 4th September, 2024.
Cited on page 36.

[114] Bogdan Povh, Klaus Rith, Christoph Scholz, and Frank Zetsche. *Teilchen und Kerne: Eine Einführung in die physikalischen Konzepte; 8th ed.* Springer-Lehrbuch. Springer, Heidelberg, 2009. URL `https://cds.cern.ch/record/1494496`. Also available in English version.
Cited on page 35.

[115] Luigi Rolandi, Werner Riegler, and Walter Blum. *Particle Detection with Drift Chambers*. Particle Acceleration and Detection. Springer, 2008. ISBN 978-3-540-76683-4, 978-3-642-09538-2, 978-3-540-76684-1. doi: 10.1007/978-3-540-76684-1.
Cited on page 36.

[116] A. Akindinov et al. Performance of the ALICE Time-Of-Flight detector at the LHC. *Eur. Phys. J. Plus*, 128:44, 2013. doi: 10.1140/epjp/i2013-13044-x.
Cited on page 37.

[117] Tonatiuh Jimenez. TOF beta vs momentum performance in pp at 13 TeV (LHC15f), 2016. URL `https://alice-figure.web.cern.ch/node/9564`. Accessed: 4th September, 2024.
Cited on page 37.

[118] M. Ivanov, I. Belikov, P. Hristov, and K. Safarik. Track reconstruction in high density environment. *Nucl. Instrum. Meth. A*, 566:70–74, 2006. doi: 10.1016/j.nima.2006.05.029.
Cited on page 37.

[119] ALICE Collaboration. AliPhysics, 2020. URL `https://github.com/alisw/AliPhysics`. Accessed: 4th September, 2024.
Cited on page 39.

[120] Torbjörn Sjöstrand, Stefan Ask, Jesper R. Christiansen, Richard Corke, Nishita Desai, Philip Ilten, Stephen Mrenna, Stefan Prestel, Christine O. Rasmussen, and Peter Z. Skands. An introduction to PYTHIA 8.2. *Comput. Phys. Commun.*, 191:159–177, 2015. doi: 10.1016/j.cpc.2015.01.024.
Cited on page 39.

[121] R. Brun, R. Hagelberg, M. Hansroul, and J. C. Lassalle. Geant: Simulation Program for Particle Physics Experiments. User Guide and Reference Manual. 7 1978.
Cited on page 39.

[122] R. L. Workman et al. Review of Particle Physics. *PTEP*, 2022:083C01, 2022. doi: 10.1093/ptep/ptac097.
Cited on pages 39, 40, 52, 57, 64, 67, 88, 91, 100, and 115.

[123] Shreyasi Acharya et al. Search for a common baryon source in high-multiplicity pp collisions at the LHC. *Phys. Lett. B*, 811:135849, 2020. doi: 10.1016/j.physletb.2020.135849.
Cited on pages 39, 40, 41, 72, 81, and 115.

[124] F. Becattini, P. Castorina, A. Milov, and H. Satz. Predictions of hadron abundances in pp collisions at the LHC. *J. Phys.*, G38:025002, 2011. doi: 10.1088/0954-3899/38/2/025002.
Cited on page 39.

[125] T. Pierog, Iu. Karpenko, J.M. Katzy, E. Yatsenko, and K. Werner. EPOS LHC: Test of collective hadronization with data measured at the CERN Large Hadron Collider. *Phys. Rev. C*, 92(3):034906, 2015. doi: 10.1103/PhysRevC.92.034906.
Cited on page 40.

[126] ALICE Collaboration. Common femtoscopic hadron-emission source in pp collisions at the lhc. 2023.
Cited on pages 40, 41, 62, 63, 71, 72, and 81.

[127] Henk Polinder, Johann Haidenbauer, and Ulf-G. Meissner. Hyperon-nucleon interactions: A Chiral effective field theory approach. *Nucl. Phys. A*, 779:244–266, 2006. doi: 10.1016/j.nuclphysa.2006.09.006.
Cited on page 40.

[128] J. Haidenbauer, U. G. Meißner, and A. Nogga. Hyperon–nucleon interaction within chiral effective field theory revisited. *Eur. Phys. J. A*, 56(3):91, 2020. doi: 10.1140/epja/s10050-020-00100-4.
Cited on page 40.

[129] Kenji Aoki and Daisuke Jido. KN scattering amplitude revisited in a chiral unitary approach and a possible broad resonance in S = +1 channel. *PTEP*, 2019(1):013D01, 2019. doi: 10.1093/ptep/pty130.
Cited on page 40.

[130] Dimitar Mihaylov and Jaime González González. Novel model for particle emission in small collision systems. *Eur. Phys. J. C*, 83(7):590, 2023. doi: 10.1140/epjc/s10052-023-11774-7.
Cited on page 41.

[131] S. Godfrey and Nathan Isgur. Mesons in a Relativized Quark Model with Chromodynamics. *Phys. Rev. D*, 32:189–231, 1985. doi: 10.1103/PhysRevD.32.189.
Cited on page 43.

[132] B. Aubert et al. Observation of a narrow meson decaying to $D_s^+\pi^0$ at a mass of 2.32 GeV/c^2. *Phys. Rev. Lett.*, 90:242001, 2003. doi: 10.1103/PhysRevLett.90.242001.
Cited on page 43.

[133] P. Krokovny et al. Observation of the $D(SJ)(2317)$ and $D(SJ)(2457)$ in B decays. *Phys. Rev. Lett.*, 91:262002, 2003. doi: 10.1103/PhysRevLett.91.262002.
Not cited.

[134] D. Besson et al. Observation of a narrow resonance of mass 2.46 GeV$/c^2$ decaying to $D_s^{*+}\pi^0$ and confirmation of the $D_{sJ}^*(2317)$ state. *Phys. Rev. D*, 68:032002, 2003. doi: 10.1103/PhysRevD.68.032002. [Erratum: Phys.Rev.D 75, 119908 (2007)].
Cited on page 43.

[135] Hai-Yang Cheng and Wei-Shu Hou. B decays as spectroscope for charmed four quark states. *Phys. Lett. B*, 566:193–200, 2003. doi: 10.1016/S0370-2693(03)00834-7.
Cited on page 43.

[136] M. E. Bracco, A. Lozea, Ricardo D'Elia Matheus, F. S. Navarra, and M. Nielsen. Disentangling two- and four-quark state pictures of the charmed scalar mesons. *Phys. Lett. B*, 624:217–222, 2005. doi: 10.1016/j.physletb.2005.08.037.
Not cited.

[137] Veljko Dmitrasinovic. $D_{s0}^+(2317) - D_0(2308)$ mass difference as evidence for tetraquarks. *Phys. Rev. Lett.*, 94:162002, 2005. doi: 10.1103/PhysRevLett.94.162002.
Cited on page 43.

[138] T. Barnes, F. E. Close, and H. J. Lipkin. Implications of a DK molecule at 2.32 GeV. *Phys. Rev. D*, 68:054006, 2003. doi: 10.1103/PhysRevD.68.054006.
Cited on page 43.

[139] Adam P. Szczepaniak. Description of the D*(s)(2320) resonance as the D π atom. *Phys. Lett. B*, 567:23–26, 2003. doi: 10.1016/S0370-2693(03)00865-7.
Not cited.

[140] Yu-Qi Chen and Xue-Qian Li. A Comprehensive four-quark interpretation of $D_s(2317)$, $D_s(2457)$ and $D_s(2632)$. *Phys. Rev. Lett.*, 93:232001, 2004. doi:

10.1103/PhysRevLett.93.232001.
Not cited.

[141] Feng-Kun Guo, Peng-Nian Shen, Huan-Ching Chiang, Rong-Gang Ping, and Bing-Song Zou. Dynamically generated 0^+ heavy mesons in a heavy chiral unitary approach. *Phys. Lett. B*, 641:278–285, 2006. doi: 10.1016/j.physletb.2006.08.064.
Cited on page 44.

[142] Feng-Kun Guo, Peng-Nian Shen, and Huan-Ching Chiang. Dynamically generated 1^+ heavy mesons. *Phys. Lett. B*, 647:133–139, 2007. doi: 10.1016/j.physletb.2007.01.050.
Cited on page 43.

[143] Thomas E. Browder, Sandip Pakvasa, and Alexey A. Petrov. Comment on the new $\mathrm{D}_\mathrm{s}^{(*)+}\pi^0$ resonances. *Phys. Lett. B*, 578:365–368, 2004. doi: 10.1016/j.physletb.2003.10.067.
Cited on page 43.

[144] J. Vijande, F. Fernandez, and A. Valcarce. Open-charm meson spectroscopy. *Phys. Rev. D*, 73:034002, 2006. doi: 10.1103/PhysRevD.73.034002. [Erratum: Phys.Rev.D 74, 059903 (2006)].
Cited on page 43.

[145] Eef van Beveren and George Rupp. Observed $D_s(2317)$ and tentative $D(2100\text{–}2300)$ as the charmed cousins of the light scalar nonet. *Phys. Rev. Lett.*, 91:012003, 2003. doi: 10.1103/PhysRevLett.91.012003.
Cited on page 43.

[146] Stephen Godfrey. Testing the nature of the $D_s(2317)^+$ and $D(sJ)(2463)^+$ states using radiative transitions. *Phys. Lett. B*, 568:254–260, 2003. doi: 10.1016/j.physletb.2003.06.049.
Cited on page 43.

[147] William A. Bardeen, Estia J. Eichten, and Christopher T. Hill. Chiral multiplets of heavy - light mesons. *Phys. Rev. D*, 68:054024, 2003. doi: 10.1103/PhysRevD.68.054024.
Not cited.

[148] Fayyazuddin and Riazuddin. Some comments on narrow resonances D^*_{s1} (2.46 GeV/c^2) and D_{s0} (2.317 GeV/c^2). *Phys. Rev. D*, 69:114008, 2004. doi: 10.1103/PhysRevD.69.114008.
Not cited.

[149] P. Colangelo and F. De Fazio. Understanding D(sJ)(2317). *Phys. Lett. B*, 570: 180–184, 2003. doi: 10.1016/j.physletb.2003.08.003.
Not cited.

[150] P. Colangelo, F. De Fazio, and A. Ozpineci. Radiative transitions of $\mathrm{D}^*_{sJ}(2317)$ and $\mathrm{D}_{sJ}(2460)$. *Phys. Rev. D*, 72:074004, 2005. doi: 10.1103/PhysRevD.72.074004.
Not cited.

[151] Jie Lu, Xiao-Lin Chen, Wei-Zheng Deng, and Shi-Lin Zhu. Pionic decays of $\mathrm{D}_{sj}(2317)$, $\mathrm{D}_{sj}(2460)$ and $\mathrm{B}_{sj}(5718)$, $\mathrm{B}_{sj}(5765)$. *Phys. Rev. D*, 73:054012, 2006.

doi: 10.1103/PhysRevD.73.054012.
Cited on page 43.

[152] S. K. Choi et al. Observation of a narrow charmonium-like state in exclusive $B^{\pm} \to K^{\pm}\pi^{+}\pi^{-}J/\psi$ decays. *Phys. Rev. Lett.*, 91:262001, 2003. doi: 10.1103/PhysRevLett.91.262001.
Cited on page 43.

[153] Roel Aaij et al. Observation of an exotic narrow doubly charmed tetraquark. *Nature Phys.*, 18(7):751–754, 2022. doi: 10.1038/s41567-022-01614-y.
Cited on page 43.

[154] Roel Aaij et al. Study of the doubly charmed tetraquark T_{cc}^{+}. *Nature Commun.*, 13(1):3351, 2022. doi: 10.1038/s41467-022-30206-w.
Cited on page 43.

[155] Roel Aaij et al. Observation of $J/\psi p$ Resonances Consistent with Pentaquark States in $\Lambda_b^0 \to J/\psi K^- p$ Decays. *Phys. Rev. Lett.*, 115:072001, 2015. doi: 10.1103/PhysRevLett.115.072001.
Cited on page 43.

[156] Roel Aaij et al. Observation of a narrow pentaquark state, $P_c(4312)^+$, and of two-peak structure of the $P_c(4450)^+$. *Phys. Rev. Lett.*, 122(22):222001, 2019. doi: 10.1103/PhysRevLett.122.222001.
Cited on page 43.

[157] Hua-Xing Chen, Wei Chen, Xiang Liu, and Shi-Lin Zhu. The hidden-charm pentaquark and tetraquark states. *Phys. Rept.*, 639:1–121, 2016. doi: 10.1016/j.physrep.2016.05.004.
Cited on page 43.

[158] Nora Brambilla, Simon Eidelman, Christoph Hanhart, Alexey Nefediev, Cheng-Ping Shen, Christopher E. Thomas, Antonio Vairo, and Chang-Zheng Yuan. The XYZ states: experimental and theoretical status and perspectives. *Phys. Rept.*, 873:1–154, 2020. doi: 10.1016/j.physrep.2020.05.001.
Not cited.

[159] Yuki Kamiya, Tetsuo Hyodo, and Akira Ohnishi. Femtoscopic study on DD^* and $D\bar{D}^*$ interactions for T_{cc} and X(3872). *Eur. Phys. J. A*, 58(7):131, 2022. doi: 10.1140/epja/s10050-022-00782-y.
Cited on page 76.

[160] Nijiati Yalikun, Yong-Hui Lin, Feng-Kun Guo, Yuki Kamiya, and Bing-Song Zou. Coupled-channel effects of the Σc(*)D¯(*)-Λc(2595)D¯ system and molecular nature of the Pc pentaquark states from one-boson exchange model. *Phys. Rev. D*, 104(9):094039, 2021. doi: 10.1103/PhysRevD.104.094039.
Cited on page 43.

[161] Peter Braun-Munzinger, Volker Koch, Thomas Schäfer, and Johanna Stachel. Properties of hot and dense matter from relativistic heavy ion collisions. *Phys. Rept.*, 621:76–126, 2016. doi: 10.1016/j.physrep.2015.12.003.
Cited on page 43.

[162] John Adams et al. Experimental and theoretical challenges in the search for the quark gluon plasma: The STAR Collaboration's critical assessment of the

evidence from RHIC collisions. *Nucl. Phys. A*, 757:102–183, 2005. doi: 10.1016/j.nuclphysa.2005.03.085.
Not cited.

[163] B. B. Back et al. The PHOBOS perspective on discoveries at RHIC. *Nucl. Phys. A*, 757:28–101, 2005. doi: 10.1016/j.nuclphysa.2005.03.084.
Not cited.

[164] K. Adcox et al. Formation of dense partonic matter in relativistic nucleus-nucleus collisions at RHIC: Experimental evaluation by the PHENIX collaboration. *Nucl. Phys. A*, 757:184–283, 2005. doi: 10.1016/j.nuclphysa.2005.03.086.
Not cited.

[165] I. Arsene et al. Quark gluon plasma and color glass condensate at RHIC? The Perspective from the BRAHMS experiment. *Nucl. Phys. A*, 757:1–27, 2005. doi: 10.1016/j.nuclphysa.2005.02.130.
Cited on page 43.

[166] Markus H. Thoma and Miklos Gyulassy. Quark Damping and Energy Loss in the High Temperature QCD. *Nucl. Phys. B*, 351:491–506, 1991. doi: 10.1016/S0550-3213(05)80031-8.
Cited on page 43.

[167] Eric Braaten and Markus H. Thoma. Energy loss of a heavy fermion in a hot plasma. *Phys. Rev. D*, 44:1298–1310, 1991. doi: 10.1103/PhysRevD.44.1298.
Not cited.

[168] Eric Braaten and Markus H. Thoma. Energy loss of a heavy quark in the quark - gluon plasma. *Phys. Rev. D*, 44(9):R2625, 1991. doi: 10.1103/PhysRevD.44.R2625.
Cited on page 43.

[169] R. Baier, Yuri L. Dokshitzer, Alfred H. Mueller, S. Peigne, and D. Schiff. Radiative energy loss and p(T) broadening of high-energy partons in nuclei. *Nucl. Phys. B*, 484:265–282, 1997. doi: 10.1016/S0550-3213(96)00581-0.
Cited on page 43.

[170] Miklos Gyulassy and Michael Plumer. Jet Quenching in Dense Matter. *Phys. Lett. B*, 243:432–438, 1990. doi: 10.1016/0370-2693(90)91409-5.
Cited on page 43.

[171] Shreyasi Acharya et al. Transverse-momentum and event-shape dependence of D-meson flow harmonics in Pb–Pb collisions at $\sqrt{s_{NN}}$ = 5.02 TeV. *Phys. Lett. B*, 813:136054, 2021. doi: 10.1016/j.physletb.2020.136054.
Cited on page 43.

[172] Shreyasi Acharya et al. Prompt D^0, D^+, and D^{*+} production in Pb–Pb collisions at $\sqrt{s_{\mathrm{NN}}}$ = 5.02 TeV. *JHEP*, 01:174, 2022. doi: 10.1007/JHEP01(2022)174.
Cited on page 43.

[173] Min He, Rainer J. Fries, and Ralf Rapp. Thermal Relaxation of Charm in Hadronic Matter. *Phys. Lett. B*, 701:445–450, 2011. doi: 10.1016/j.physletb.2011.06.019.
Cited on page 43.

[174] Min He, Rainer J. Fries, and Ralf Rapp. Heavy Flavor at the Large Hadron Collider in a Strong Coupling Approach. *Phys. Lett. B*, 735:445–450, 2014. doi: 10.1016/j.physletb.2014.05.050.
Cited on page 43.

[175] E. E. Kolomeitsev and M. F. M. Lutz. On Heavy light meson resonances and chiral symmetry. *Phys. Lett. B*, 582:39–48, 2004. doi: 10.1016/j.physletb.2003.10.118.
Cited on page 44.

[176] A. Martínez Torres, E. Oset, S. Prelovsek, and A. Ramos. Reanalysis of lattice QCD spectra leading to the $D_{s0}^{*}(2317)$ and $D_{s1}^{*}(2460)$. *JHEP*, 05:153, 2015. doi: 10.1007/JHEP05(2015)153.
Cited on page 44.

[177] The ALICE definition of primary particles. 2017.
Cited on page 49.

[178] Xgboost. `https://xgboost.readthedocs.io/en/latest/`.
Cited on page 53.

[179] Fernando Nogueira. Bayesian Optimization: Open source constrained global optimization tool for Python, 2014–. URL `https://github.com/fmfn/BayesianOptimization`.
Cited on page 53.

[180] Trevor Hastie, Robert Tibshirani, and Jerome Friedman. *The Elements of Statistical Learning*. Springer Series in Statistics. Springer New York Inc., New York, NY, USA, 2001.
Cited on page 53.

[181] hipe4ml. `https://github.com/hipe4ml/hipe4ml`.
Cited on page 53.

[182] Shreyasi Acharya et al. Measurement of beauty and charm production in pp collisions at $\sqrt{s} = 5.02$ TeV via non-prompt and prompt D mesons. *JHEP*, 05:220, 2021. doi: 10.1007/JHEP05(2021)220.
Cited on pages 56 and 57.

[183] Shreyasi Acharya et al. Measurement of D^0 , D^+ , D^{*+} and D_s^+ production in pp collisions at $\sqrt{s} = 5.02$ TeV with ALICE. *Eur. Phys. J. C*, 79(5):388, 2019. doi: 10.1140/epjc/s10052-019-6873-6.
Cited on page 57.

[184] Michael Annan Lisa, Scott Pratt, Ron Soltz, and Urs Wiedemann. Femtoscopy in relativistic heavy ion collisions. *Ann. Rev. Nucl. Part. Sci.*, 55:357–402, 2005. doi: 10.1146/annurev.nucl.55.090704.151533.
Cited on pages 59 and 109.

[185] Volodymyr Vovchenko and Horst Stoecker. Thermal-FIST: A package for heavy-ion collisions and hadronic equation of state. *Comput. Phys. Commun.*, 244:295–310, 2019. doi: 10.1016/j.cpc.2019.06.024.
Cited on page 63.

[186] Shreyasi Acharya et al. Studying the interaction between charm and light-flavor mesons. *Phys. Rev. D*, 110(3):032004, 2024. doi: 10.1103/PhysRevD.110.032004.
Cited on pages 67, 81, 82, 83, and 112.

[187] F. James. Monte-Carlo phase space. 5 1968.
Cited on page 67.

[188] Betty Abelev et al. $\mathrm{K}^0_\mathrm{S} - \mathrm{K}^0_\mathrm{S}$ correlations in pp collisions at $\sqrt{s} = 7$ TeV from the LHC ALICE experiment. *Phys. Lett. B*, 717:151–161, 2012. doi: 10.1016/j.physletb.2012.09.013.
Cited on page 68.

[189] B. Abelev et al. Charged kaon femtoscopic correlations in pp collisions at $\sqrt{s} = 7$ TeV. *Phys. Rev.*, D87(5):052016, 2013. doi: 10.1103/PhysRevD.87.052016.
Not cited.

[190] K. Aamodt et al. Femtoscopy of pp collisions at $\sqrt{s} = 0.9$ and 7 TeV at the LHC with two-pion Bose–Einstein correlations. *Phys. Rev. D*, 84:112004, 2011. doi: 10.1103/PhysRevD.84.112004.
Cited on page 68.

[191] J. Adam et al. Two-pion femtoscopy in p–Pb collisions at $\sqrt{s_{\mathrm{NN}}} = 5.02$ TeV. *Phys. Rev. C*, 91:034906, 2015. doi: 10.1103/PhysRevC.91.034906.
Cited on page 68.

[192] Torbjorn Sjostrand. Jet Fragmentation of Nearby Partons. *Nucl. Phys. B*, 248: 469–502, 1984. doi: 10.1016/0550-3213(84)90607-2.
Cited on page 68.

[193] Liuming Liu, Kostas Orginos, Feng-Kun Guo, Christoph Hanhart, and Ulf-G. Meissner. Interactions of charmed mesons with light pseudoscalar mesons from lattice QCD and implications on the nature of the $D^*_{s0}(2317)$. *Phys. Rev. D*, 87(1):014508, 2013. doi: 10.1103/PhysRevD.87.014508.
Cited on pages 75, 76, 77, and 80.

[194] Xiao-Yu Guo, Yonggoo Heo, and Matthias F. M. Lutz. On chiral extrapolations of charmed meson masses and coupled-channel reaction dynamics. *Phys. Rev. D*, 98(1):014510, 2018. doi: 10.1103/PhysRevD.98.014510.
Cited on pages 75 and 77.

[195] Zhi-Hui Guo, Liuming Liu, Ulf-G Meißner, J. A. Oller, and A. Rusetsky. Towards a precise determination of the scattering amplitudes of the charmed and light-flavor pseudoscalar mesons. *Eur. Phys. J. C*, 79(1):13, 2019. doi: 10.1140/epjc/s10052-018-6518-1.
Cited on pages 76 and 77.

[196] Bo-Lin Huang, Zi-Yang Lin, and Shi-Lin Zhu. Light pseudoscalar meson and heavy meson scattering lengths to O(p4) in heavy meson chiral perturbation theory. *Phys. Rev. D*, 105(3):036016, 2022. doi: 10.1103/PhysRevD.105.036016.
Cited on pages 76, 77, 112, and 113.

[197] Juan M. Torres-Rincon, Àngels Ramos, and Laura Tolos. Femtoscopy of D mesons and light mesons upon unitarized effective field theories. *Phys. Rev. D*, 108(9):096008, 2023. doi: 10.1103/PhysRevD.108.096008.
Cited on pages 75, 76, 77, and 80.

[198] Daniel Mohler, C. B. Lang, Luka Leskovec, Sasa Prelovsek, and R. M. Woloshyn. $D_{s0}^{*}(2317)$ Meson and D-Meson-Kaon Scattering from Lattice QCD. *Phys. Rev. Lett.*, 111(22):222001, 2013. doi: 10.1103/PhysRevLett.111.222001.
Cited on page 76.

[199] Aurora Tumino et al. Coulomb-free ${}^{1}\mathrm{S}_{0}\mathrm{p}-\mathrm{p}$ scattering length from the quasi-free $\mathrm{p}+\mathrm{d}\to\mathrm{p}+\mathrm{p}+\mathrm{n}$ reaction and its relation to universality. *Commun. Phys.*, 6(1):106, 2023. doi: 10.1038/s42005-023-01221-0.
Cited on page 76.

[200] Xinwei Kong and Finn Ravndal. Proton proton scattering lengths from effective field theory. *Phys. Lett. B*, 450:320–324, 1999. doi: 10.1016/S0370-2693(99) 00144-6. [Erratum: Phys.Lett.B 458, 565–565 (1999)].
Not cited.

[201] D. E. Gonzalez Trotter et al. New Measurement of the S-10 Neutron-Neutron Scattering Length Using the Neutron-Proton Scattering Length as a Standard. *Phys. Rev. Lett.*, 83:3788–3791, 1999. doi: 10.1103/PhysRevLett.83.3788.
Cited on page 76.

[202] Tung-Mow Yan, Hai-Yang Cheng, Chi-Yee Cheung, Guey-Lin Lin, Y. C. Lin, and Hoi-Lai Yu. Heavy quark symmetry and chiral dynamics. *Phys. Rev. D*, 46:1148–1164, 1992. doi: 10.1103/PhysRevD.46.1148. [Erratum: Phys.Rev.D 55, 5851 (1997)].
Cited on page 81.

[203] Thomas Mannel. Spin effects in heavy quark processes. *Acta Phys. Polon. B*, 29:1413–1427, 1998.
Cited on page 81.

[204] Zhan-Wei Liu, Yan-Rui Liu, Xiang Liu, and Shi-Lin Zhu. The Pseudoscalar Meson and Heavy Vector Meson Scattering Lengths. *Phys. Rev. D*, 84:034002, 2011. doi: 10.1103/PhysRevD.84.034002.
Cited on pages 81 and 82.

[205] K. P. Khemchandani, Luciano M. Abreu, A. Martinez Torres, and F. S. Navarra. Can femtoscopic correlation function shed light on the nature of the lightest, charm, axial mesons? 12 2023.
Cited on page 81.

[206] Kazuo Abe et al. Study of $B^{-}\to D^{**0}\pi^{-}(D^{**0}\to D^{(*)+}\pi^{-})$ decays. *Phys. Rev. D*, 69:112002, 2004. doi: 10.1103/PhysRevD.69.112002.
Cited on page 83.

[207] Roel Aaij et al. Amplitude analysis of $B^{0}\to\bar{D}^{0}K^{+}\pi^{-}$ decays. *Phys. Rev. D*, 92 (1):012012, 2015. doi: 10.1103/PhysRevD.92.012012.
Cited on page 83.

[208] S. Okubo. ϕ meson and unitary symmetry model. *Phys. Lett.*, 5:165, 1963. doi: 10.1016/S0375-9601(63)92548-9.
Cited on page 85.

[209] G. Zweig. *An SU(3) model for strong interaction symmetry and its breaking. Version 2*, pages 22–101. 2 1964. doi: 10.17181/CERN-TH-412.
Not cited.

[210] Jugoro Iizuka. Systematics and phenomenology of meson family. *Prog. Theor. Phys. Suppl.*, 37:21–34, 1966. doi: 10.1143/PTPS.37.21.
Cited on page 85.

[211] Thomas Appelquist and W. Fischler. Some Remarks on Van Der Waals Forces in QCD. *Phys. Lett. B*, 77:405–410, 1978. doi: 10.1016/0370-2693(78)90587-7.
Cited on page 85.

[212] Vladimir B. Belyaev, Werner Sandhas, and Ivan I. Shlyk. New nuclear three-body clusters \\$\phi$NN. *Few Body Syst.*, 44:347–349, 2008. doi: 10.1007/s00601-008-0324-5.
Cited on pages 85, 99, 100, and 102.

[213] H. Gao, T. S. H. Lee, and V. Marinov. ϕ–N bound state. *Phys. Rev. C*, 63:022201, 2001. doi: 10.1103/PhysRevC.63.022201.
Cited on pages 85, 86, 99, 100, and 102.

[214] Jaume Tarrús Castellà and Gastão Krein. Effective field theory for the nucleon-quarkonium interaction. *Phys. Rev. D*, 98(1):014029, 2018. doi: 10.1103/PhysRevD.98.014029.
Cited on pages 85 and 91.

[215] Gyan Bhanot and Michael E. Peskin. Short Distance Analysis for Heavy Quark Systems. 2. Applications. *Nucl. Phys. B*, 156:391–416, 1979. doi: 10.1016/0550-3213(79)90200-1.
Not cited.

[216] H. Fujii and D. Kharzeev. Long range forces of QCD. *Phys. Rev. D*, 60:114039, 1999. doi: 10.1103/PhysRevD.60.114039.
Not cited.

[217] Nora Brambilla, Gastão Krein, Jaume Tarrús Castellà, and Antonio Vairo. Long-range properties of 1S bottomonium states. *Phys. Rev. D*, 93(5):054002, 2016. doi: 10.1103/PhysRevD.93.054002.
Cited on page 85.

[218] F. Huang, Z. Y. Zhang, and Y. W. Yu. $N\phi$ state in chiral quark model. *Phys. Rev. C*, 73:025207, 2006. doi: 10.1103/PhysRevC.73.025207.
Cited on pages 85, 99, 100, and 102.

[219] Sachiko Oshima, Takehisa Fujita, Naohiro Kanda, and Akihiro Yoshimi. Two pion versus σ-meson exchange potentials. *Journal of Modern Physics*, 06:927–936, 2015. doi: 10.4236/jmp.2015.67097.
Cited on page 85.

[220] S. Liska, H. Gao, W. Chen, and X. Qian. Search for the ϕN bound state from ϕ meson subthreshold production. *Phys. Rev. C*, 75:058201, 2007. doi: 10.1103/PhysRevC.75.058201.
Cited on page 85.

[221] Junko Yamagata-Sekihara, Daniel Cabrera, Manuel J. Vicente Vacas, and Satoru Hirenzaki. Formation of ϕ mesic nuclei. *Prog. Theor. Phys.*, 124:147–162, 2010. doi: 10.1143/PTP.124.147.
Not cited.

[222] S A Sofianos, G J Rampho, M Braun, and R M Adam. The ϕ–NN and $\phi\phi$–NN mesic nuclear systems. *J. Phys. G.*, 37(8):085109, 2010. doi: 10.1088/0954-3899/37/8/085109.
Cited on pages 85, 99, 100, and 102.

[223] J. J. Cobos-Martínez, K. Tsushima, G. Krein, and A. W. Thomas. ϕ-meson–nucleus bound states. *Phys. Rev. C*, 96(3):035201, 2017. doi: 10.1103/PhysRevC.96.035201.
Not cited.

[224] Haiyan Gao, Hongxia Huang, Tianbo Liu, Jialun Ping, Fan Wang, and Zhiwen Zhao. Search for a hidden strange baryon-meson bound state from ϕ production in a nuclear medium. *Phys. Rev. C*, 95(5):055202, 2017. doi: 10.1103/PhysRevC.95.055202.
Cited on pages 99, 100, and 102.

[225] Bao-Xi Sun, Ying-Ying Fan, and Qin-Qin Cao. The ϕp bound state in the unitary coupled-channel approximation. *Commun. Theor. Phys.*, 75(5):055301, 2023. doi: 10.1088/1572-9494/acc31d.
Cited on pages 85, 99, 100, and 102.

[226] Stanley J. Brodsky, I. A. Schmidt, and G. F. de Teramond. NUCLEAR BOUND QUARKONIUM. *Phys. Rev. Lett.*, 64:1011, 1990. doi: 10.1103/PhysRevLett.64.1011.
Cited on pages 85 and 100.

[227] Sourav Sarkar, Bao-Xi Sun, E. Oset, and M. J. Vicente Vacas. Dynamically generated resonances from the vector octet-baryon decuplet interaction. *Eur. Phys. J. A*, 44:431–443, 2010. doi: 10.1140/epja/i2010-10956-4.
Cited on page 85.

[228] D. Gamermann, C. Garcia-Recio, J. Nieves, and L. L. Salcedo. Odd Parity Light Baryon Resonances. *Phys. Rev. D*, 84:056017, 2011. doi: 10.1103/PhysRevD.84.056017.
Cited on pages 86, 97, and 102.

[229] E. Oset, A. Ramos, E. J. Garzon, R. Molina, L. Tolos, C. W. Xiao, J. J. Wu, and B. S. Zou. Interaction of vector mesons with baryons and nuclei. *Int. J. Mod. Phys. E*, 21:1230011, 2012. doi: 10.1142/S0218301312300111.
Not cited.

[230] A. Ramos and E. Oset. The role of vector-baryon channels and resonances in the $\gamma p \to K^0\Sigma^+$ and $\gamma n \to K^0\Sigma^0$ reactions near the $K^*\Lambda$ threshold. *Phys. Lett. B*, 727:287–292, 2013. doi: 10.1016/j.physletb.2013.10.012.
Cited on page 85.

[231] Yuji Koike and A. Hayashigaki. QCD sum rules for rho, omega, phi meson - nucleon scattering lengths and the mass shifts in nuclear medium. *Prog. Theor. Phys.*, 98:631–652, 1997. doi: 10.1143/PTP.98.631.
Cited on pages 86 and 87.

[232] F. Klingl, Norbert Kaiser, and W. Weise. Current correlation functions, QCD sum rules and vector mesons in baryonic matter. *Nucl. Phys. A*, 624:527–563, 1997. doi: 10.1016/S0375-9474(97)88960-9.
Cited on page 86.

[233] Yan Lyu, Takumi Doi, Tetsuo Hatsuda, Yoichi Ikeda, Jie Meng, Kenji Sasaki, and Takuya Sugiura. Attractive N-ϕ interaction and two-pion tail from lattice QCD near physical point. *Phys. Rev. D*, 106(7):074507, 2022. doi: 10.1103/PhysRevD.106.074507.
Cited on pages 86, 91, 92, 93, 94, 96, 97, 101, 102, and 106.

[234] Near-threshold diffractive ϕ-meson photoproduction from the proton. *Phys. Rev. Lett.*, 95:182001, Oct 2005. doi: 10.1103/PhysRevLett.95.182001.
Cited on page 87.

[235] A. I. Titov, T. Nakano, S. Daté, and Y. Ohashi. Differential cross section of ϕ-meson photoproduction at threshold. *Phys. Rev. C*, 76:048202, 2007. doi: 10.1103/PhysRevC.76.048202.
Cited on page 87.

[236] Igor I. Strakovsky, Lubomir Pentchev, and Alexander Titov. Comparative analysis of ωp, ϕp, and $J/\psi p$ scattering lengths from A2, CLAS, and GlueX threshold measurements. *Phys. Rev. C*, 101(4):045201, 2020. doi: 10.1103/PhysRevC.101.045201.
Cited on page 87.

[237] Takatsugu Ishikawaa and Hiroaki Ohnishi. Pion-induced phi-meson production on the proton. `http://j-parc.jp/researcher/Hadron/en/pac_2208/pdf/P95_2022-19.pdf`, 2022. Proposal for the J-PARC 30-GeV Proton Synchrotron.
Cited on page 87.

[238] E. L. Feinberg. Hadron Clusters and Half Dressed Particles in Quantum Field Theory. *Sov. Phys. Usp.*, 23:629–650, 1980. doi: 10.1070/PU1980v023n10ABEH005036.
Cited on page 87.

[239] Yin-Zhen Xu, Siyang Chen, Zhao-Qian Yao, Daniele Binosi, Zhu-Fang Cui, and Craig D. Roberts. Vector-meson production and vector meson dominance. *Eur. Phys. J. C*, 81(10):895, 2021. doi: 10.1140/epjc/s10052-021-09673-w.
Cited on page 87.

[240] Emma Chizzali. First experimental evidence of an attractive proton–ϕ interaction. Master's thesis, Munich, Tech. U., 2021.
Cited on pages 87 and 88.

[241] Betty Abelev et al. Transverse sphericity of primary charged particles in minimum bias proton-proton collisions at $\sqrt{s} = 0.9$, 2.76 and 7 TeV. *Eur. Phys. J. C*, 72:2124, 2012. doi: 10.1140/epjc/s10052-012-2124-9.
Cited on page 88.

[242] A. Feijoo, M. Korwieser, and L. Fabbietti. Relevance of the coupled channels in the ϕp and ρ0p correlation functions. *Phys. Rev. D*, 111(1):014009, 2025. doi: 10.1103/PhysRevD.111.014009.
Cited on page 102.